TECHNISCHE UNIVERSITÄT MÜNCHEN

Physik-Department
Lehrstuhl für Funktionelle Materialien

Nanostructure-Performance Relationship in Polymer-Based Solar Cells

Weijia Wang

Vollständiger Abdruck der von der Fakultät für Physik der Technischen Universität München zur Erlangung des akademischen Grades eines

Doktors der Naturwissenschaften (Dr. rer. nat.)

genehmigten Dissertation.

Vorsitzende:	Prof. Christine Papadakis, Ph.D.
Prüfer der Dissertation:	1. apl. Prof. Dr. Peter Müller-Buschbaum
	2. Prof. Dr. Friedrich Simmel

Die Dissertation wurde am 26.10.2016 bei der Technischen Universität München eingereicht und durch die Fakultät für Physik am 08.12.2016 angenommen.

Abstract

Within the scope of this thesis, polymer-based films were investigated regarding their potential application as active layers in organic solar cells. The focus lies on the influence of external factors, such as solvent additives, cell architecture or annealing conditions, on the active layer. Aside from surface sensitive imaging techniques, advanced X-ray and neutron scattering methods were applied to probe the inner film morphology. The photovoltaic performance of the solar cells was examined in terms of efficiency and stability which in turn could be correlated to the morphology of the active layers. Polymer/titania hybrid films were explored as promising base for flexible, polymer-based hybrid solar cells. Their flexibility was tested via cyclic bending and correlated to their surface and inner morphology as well as their material compositions.

Zusammenfassung

Im Rahmen der vorliegenden Arbeit wurden polymerbasierte Filme bezüglich ihrer potenziellen Anwendung als aktive Schichten in organischen Solarzellen untersucht. Der Fokus liegt auf dem Einfluss externer Faktoren, wie beispielsweise Lösungsmittelzusätzen, Zellarchitektur oder Temperbedingungen, auf die aktive Schicht. Neben oberflächensensitiven Bildgebungsverfahren wurden moderne Röntgen- und Neutronenstreumethoden eingesetzt, um die innere Morphologie der Filme zu ermitteln. Die photovoltaische Leistung der Solarzellen wurde hinsichtlich ihrer Effizienz und Stabilität untersucht, welche wiederum mit der Morphologie der aktiven Schichten korreliert werden konnte. Polymer-Titandioxid-Hybridfilme wurden als vielversprechende Basis für flexible, polymerbasierte Hybridsolarzellen untersucht. Ihre Flexibilität wurde mit Hilfe von zyklischen Biegetests betrachtet und mit ihrer (Oberflächen-)Morphologie sowie ihrer Materialzusammensetzung korreliert.

Contents

List of abbreviations

AFM:	atomic force microscopy
BHJ:	bulk heterojunction
DOS:	density of states
DWBA:	distorted wave Born approximation
FF:	fill factor
FTO:	fluorine doped tin oxide
FWHM:	full width at half maximum
GISAXS:	grazing incidence small angle X-ray scattering
GIWAXS:	grazing incidence wide angle X-ray scattering
HOMO:	highest occupied molecular orbital
J_{SC}:	short circuit current
J-V curve:	current-voltage curve
ITO:	indium tin oxide
LMA:	local monodisperse approximation
LUMO:	lowest unoccupied molecular orbital
M_n:	number average molecular weight
M_w:	weight average molecular weight
ODT:	1,8-octanedithiol
OPV:	organic photovoltaic
PCE:	power conversion efficiency
PCBM:	[6,6]-phenyl-C61 butyric acid methyl ester
PEDOT:PSS:	poly(3,4-ethylenedioxythiophene):poly(styrenesulfonate)
P3HT:	poly(3-hexylthiophene-2,5-diyl)
SDD:	sample detector distance
SEM:	scanning electron microscope
SLD:	scattering length density
TOF-GISANS:	time-of-flight grazing incidence small angle neutron scattering
UV/Vis:	ultraviolet/visible spectroscopy
V_{OC}:	open circuit voltage
XRD:	X-ray diffraction

1 Introduction

The demand for energy is ever-increasing to sustain human civilization with the progress of the industrialization and electrification. The traditional energy resources including oil, coal, and natural gas are readily combustible and still dominant in the world energy consumption so far [1]. However, they are likely to be exhausted within a couple of decades due to increasing requirements and a limited amount on earth. Thus, renewable energies like sunlight, wind, water, and geothermal energy rise as an alternative in response to the shortage of the traditional energy resources, among which solar energy shows a great potential. In addition to sustainability, solar energy is available worldwide, environment-friendly, and free of charge.

Conversion of light into electricity is one of the most important applications of harvesting solar energy. This application was initiated by the observation of the photovoltaic effect in 1839 by the French experimental physicist Becquerel. Followed by this finding, the first solar cell using selenium as a functional layer was fabricated by Fritts in 1883, showing an efficiency of around 1%. Afterwards, explorations on new materials and manufacturing processes were dedicated to improving the efficiency of solar devices by industries and research institutes. Until now, crystalline-silicon solar cells, chalcogenide thin film solar cells, and III-V cells are the most efficient and mature devices with efficiencies over 20% (in general) [2]. Among them, silicon-based solar cells dominate the market today. However, the silicon-based solar cells suffer from the strictly-controlled fabrication processes with high energy consumption. The rigidity and heavy weight of silicon-based solar cells strongly limit applications regarding flexible and lightweight products.

The first discovery of conductive polymers was in the mid-20th century. The breakthrough leading to applications in organic semiconductors came by the discovery of highly conductive polyacetylene (PA) by Heeger, Shirakawa, and MacDiarmid in 1977 which was awarded the Nobel Prize in Chemistry in 2000. Since then, researches on conductive and semiconductive polymers boosted. Among all promising outcomes, polymer-based solar cells establish themselves as new excellent candidates for use in photovoltaics. These solar cells are better suited to be used in flexible and lightweight applications than silicon solar cells. In addition, polymer-based solar cells are potentially cheap and have less environmental impact. Another benefit is the solution processing, which allows the development

of device fabrication approaches like printing or spray deposition as well as a large scale production.

Polymer:fullerene solar cells constitute a type of polymer-based solar cells, where semiconductive polymers act as the electron donor and fullerenes (or its derivatives) act as the electron acceptor. The typical structural layout of the active layer is the so-called bulk heterojunction (BHJ) morphology. Within such layout, the donor and the acceptor materials spatially interpenetrate one another and therefore allow excitons to be generated allover the active layer and then dissociated very efficiently [3]. A good control of the morphology of the BHJ active layer is important. In general, an ideal BHJ layer exhibits the phase separation between two components within length scales similar to the exciton diffusion length ($\sim$ 10-20 nm for polymer). A great deal of work is dedicated to make the active layer approach this ideal morphology. Thermal annealing of the polymer:fullerene BHJ solar cells is widely used, which leads to a more favorable inner structure for an efficient exciton dissociation [4]. In addition, the solvent for active layer preparation shows a strong influence on the morphology of the active layer and accordingly on the photovoltaic performance of the final devices [5]. However, so far, most structural characterizations merely focus on surface morphology of the active layer, which sometimes does not coincide with the inner morphology. Therefore, surface morphology can not be directly linked to the photovoltaic behavior without understanding the corresponding inner morphology. Furthermore, besides an optimized inner morphology, crystallinity, molecular miscibility between two components, and the configuration of the solar cells play an important role in photovoltaic performance as well. In order to understand the true mechanism with respect to final photovoltaic performance, a systematic study of all these aspects is necessary. Additionally, the short lifetime is another disadvantage of the polymer:fullerene solar cells. Thus, understanding the influence of external environment on their stability has a great significance in fabrication processes and further applications. Therefore, obtaining long-term stable polymer:fullerene solar cells is highly desirable.

Hybrid solar cells are another type of polymer-based solar cells. Instead of using fullerenes (or its derivatives) as the electron acceptor material, inorganic semiconductors are used. Hybrid solar cells provide a huge opportunity to fabricate cheap and stable devices via various production routes. However, manufacturing hybrid devices toward highly flexible applications still faces two challenges. The first one is that the inorganic semiconductor usually requires a high-temperature sintering step (above 400 °C) during fabrication, which is necessary to obtain highly crystallized metal oxides and to burn away organic residuals. The other challenge is caused by the brittle nature of the metal oxides.

In the present thesis, the nanostructure-performance correlation in polymer-based solar cells is investigated. For the polymer:fullerene solar cells, the focus lies on the influence

of the external parameters, such as processing solvent additive and using different configurations of the solar cells, on the photovoltaic performance. In addition, the stability of the active layers and the final devices is covered. For the hybrid solar cells, the main aim is to establish a straightforward routine to obtain flexible active layers at low temperature. Followed by this concept, the corresponding mechanical properties of the hybrid films are investigated. Overall, the following questions are tackled in this thesis: How to improve the photovoltaic performance of the polymer:fullerene solar cells? How do external parameters tune the morphology of the active layer and accordingly, impact on the efficiency? How to improve the stability of the solar cells and what is the mechanism behind? Can hybrid films be fully flexible, and is there a common rule to evaluate the flexibility of the hybrid films with various morphologies and constituents?

To start with, chapter 2 provides the theoretical aspects with respect to the basics of polymers and sol-gel synthesis. Also, individual processes accounting for photo-electricity conversion occurring in a polymer-based solar cell are presented. The fundamentals of the scattering methods for detecting the inner structures and probing methods for mechanical properties are included in this chapter as well. Thereafter, a description of used characterization equipments as well as the parameters set for experiments are detailed in chapter 3 followed by the sample preparation in chapter 4. As the main part of this thesis, different research subjects are presented from chapter 5 to chapter 8 as schematically displayed in figure 1.1, respectively.

In chapter 5, the influence of the solvent additive 1,8-octanedithiol (ODT) on poly(3-hexylthiophene-2,5-diyl):[6,6]-phenyl-C61-butyric acid methyl ester (P3HT:PCBM) BHJ system is studied as schematically illustrated in figure 1.1a. The volume concentration of ODT is varied from 0% to 9%. Through the investigation on morphology and crystallinity of the P3HT:PCBM BHJ active layers, the resulting nanostructure-efficiency correlation is addressed.

Chapter 6 (represented as figure 1.1b) elucidates the stability of the P3HT:PCBM BHJ solar cells in the host solvent vapor. Different solvents such as chlorobenzene, toluene, xylene, and dichlorobenzene are selected as the host solvent to prepare P3HT:PCBM BHJ active layers. Afterward, the stability of each solar cell is investigated via exposure to its respective host solvent vapor for a long period. The resulting morphology, crystallinity, and optical property of all active layers are thoroughly investigated. Consequently, these properties are correlated to stability of the solar cells which are aged in different solvent vapors.

Chapter 7 (shown as figure 1.1c) introduces an inverted geometry to significantly improve the efficiency and stability of P3HT:PCBM BHJ solar cells. At first, the morphological evolution during functional stack build-up of the P3HT:PCBM BHJ solar cell is

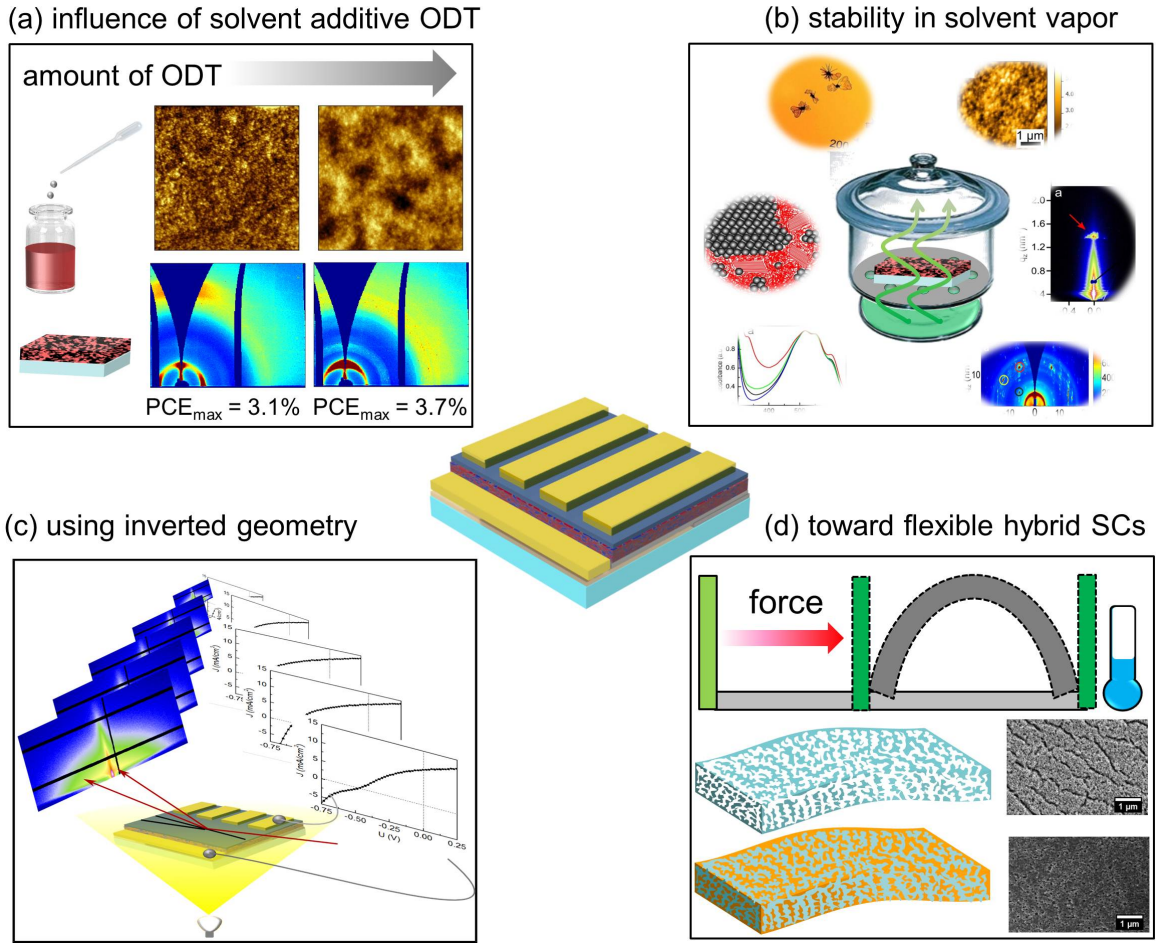

Figure 1.1: *Schematic illustration of a P3HT:PCBM bulk heterojunction organic solar cell. An overview of different research subjects included in the present thesis is represented from (a) to (d), with correspondence to the chapter from 5 to 8, respectively. Description of each topic is detailed in the text.*

investigated. In order to explain the enhancement of the efficiency of inverted solar cells, the domain sizes of the individual functional stacks are compared to those of the standard solar cells. Then, the direct correlation between the morphology of the active layer and the photovoltaic performance is studied during continuous operation under illumination.

In chapter 8 (schematically illustrated in figure 1.1d), a low temperature route towards flexible P3HT/titania hybrid films is introduced. Different methods to remove the polymer template, which is used as the structure directing agent for synthesis of nanostructured titania, are compared. Afterward, a successful P3HT backfilling is evidenced. The most interesting feature is the high flexibility of the P3HT/titania hybrid films. In order to understand the increase of the flexibility, a proper model for the P3HT/titania

film is introduced, from which the effective elastic modulus is derived and correlated to its corresponding high flexibility.

The thesis is concluded in chapter 9, giving a systematical response to the questions raised in this section. A short outlook for further projects on the basis of this thesis is presented at the end of chapter 9 as well.

2 Theoretical aspects

In this chapter, the theoretical background for all investigations is introduced. The basic knowledge of polymers is presented in section 2.1. Then the theory of sol-gel chemistry is thoroughly described in section 2.2. Thereafter, in section 2.3 the working principles of solar cells are explained systematically. In section 2.4, the advanced X-ray (or neutron) scattering techniques using grazing incidence geometry are elucidated. Finally, the basis about mechanical properties is illustrated in section 2.5.

2.1 Polymer basics

A basic introduction of polymers is presented in this section. First, general definitions are described. A detailed discussion about the polymer crystalline order is introduced in section 2.1.1. Afterwards, phase separation and diblock copolymer are discussed in section 2.1.2 and section 2.1.3, respectively. In the end, in section 2.1.4, the fundamentals of conductive polymers are illustrated.

Basic definitions

The term polymer refers to a macromolecule which is made up of many repeating subunits. A subunit is called monomer. Individual monomers are covalently bound to each other. According to the molecular weight M_w, the molecules are categorized into micromolecule, oligomers, and polymers. For polymers, the molecular weight needs to be larger than 10 kg/mol, whereas oligomers have a molecular weight between 1 kg/mol and 10 kg/mol.

Taking a monomer A as an example, the related polymer A-A-A-...-A-A-A can be named polyA or abbreviated as PA. In order to depict the polymer chain, different methods are employed as illustrated in figure 2.1. Polystyrene (PS) has the molecular formula $(C_8H_8)_n$, where the formula C_8H_8 denotes the monomer styrene and n indicates the number of total monomers, also called degree of polymerization. A visual and simple representation for a PS chain is using a curled curve (figure 2.1a). Alternatively, a detailed description for its monomer is given by the Lewis structure formula (figure 2.1b),

including the information of bonds and atoms. The most common way to represent the polymer is its skeletal formula, as in figure 2.1c. According to the rule of Lewis structure, each joint marks the position of one carbon atom with maximal four bonds (H atoms are not drawn). The carbon atom locates at each joint and the remaining positions are filled by hydrogen atoms. In total, each carbon atom can provide four bounds.

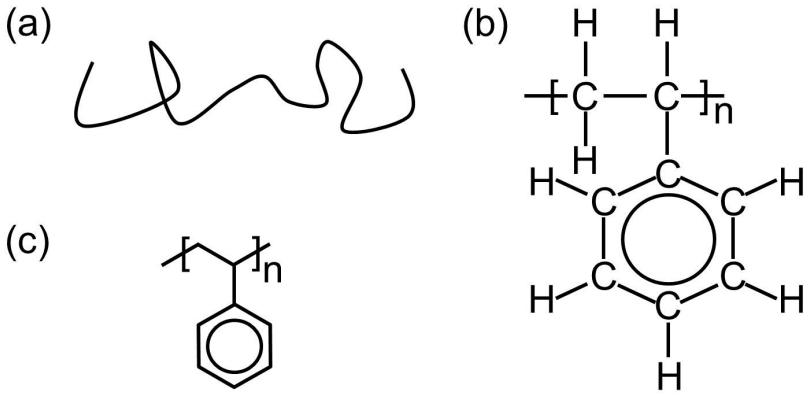

Figure 2.1: *Three methods for polymer representation: (a) a curled line, (b) Lewis structure formula, and (c) skeletal formula. The polymer PS is used as the example in this figure.*

Polymers either exist in nature or are fabricated by artificial polymerization. Some natural polymers are monodisperse, such as proteins and enzymes. However, artificial polymers never have only one defined chain length. Therefore, a statistical mean value is used to describe these polymers. The number average molecular weight M_n is derived from the first moment of the statistical distributions of molar mass, as shown below:

$$M_n = \frac{\sum_i n_i M_i}{\sum_i n_i} \tag{2.1}$$

M_i is the molar mass of one polymer chain and n_i is the number of polymer chains for component i. Then the total mass of all polymer chains for component i can be represented with $w_i = \sum_i n_i M_i$. The weight average molecular weight M_w, always simplified as molecular weight, can be calculated by the formula:

$$M_w = \frac{\sum_i w_i M_i}{\sum_i w_i} = \frac{\sum_i n_i M_i^2}{\sum_i n_i M_i}. \tag{2.2}$$

With both M_n and M_w, the polydispersity index P and the inconsistency U can be derived by

$$P = \frac{M_w}{M_n} = U + 1 \tag{2.3}$$

It is noticeable that the polydispersity index is always larger than 1 for artificially synthesized polymers. Moreover, it strongly depends on the method of synthesis. Two types of molar mass distribution are frequently used. One is Schulz-Zimm distribution, accounting for a broad molar mass dispersity. These polymers can be yielded by step polymerization or poly-condensation methods, meaning random monomers or fragments can react with each other. Due to the low cost, this method is widely used in industry. The other one is Poisson distribution, which refers to a more narrow molar mass dispersity. These polymers are generally obtained by chain polymerization (anionic polymerization). Normally, it is costly with a limited yield. Therefore, these polymers are mainly used in research.

Furthermore, three aspects are of great importance for defining polymer structures, including constitution, configuration, and conformation. The constitution describes the basic architecture of the polymer chains, such as the type and the sequence of monomers. Homopolymer is the simplest, which only constitutes of one type of monomer, such as A-A-A-...-A-A-A. If the polymer is build up with more than one type of monomers, it is called copolymer. Depending on the arrangement of different monomers, copolymers are subdivided into different categories, such as alternating copolymers, diblock copolymers, and graft copolymers. In terms of diblock copolymer, polyA-block-polyB can be shortened as PA-b-PB, describing the polymer chain A-A-A-...-A-B-...-B-B-B, with covalent bound blocks A and B.

The configuration of the polymer chain can be simply understood as the geometrical arrangement of the substituents within the molecule. Taking a double bond as an example, if all the side groups are located on the same side relative to the double bond, it is called *cis*, while if the side groups are arranged at opposite sides of the double bond the *trans*-configuration is obtained. In more general cases, for a polymer chain tacticity is used to describe the ordering of the configurationally repeating units in the main chain. If the substituents are linked in the same order, the so-called isotactic is obtained. Otherwise, a syndiotactic configuration denotes alternative arrangement and atactic configuration random alignment. Additionally, if the polymer is produced from the same isomers of the monomer, it is called regioregular, otherwise regiorandom. Normally, a higher regioregularity of the conjugated polymer is prone to result in a higher crystallinity.

The term conformation refers to the ordering that arises from the rotation of molecules around single bonds. It is noteworthy that double bonds cannot rotate. In short, conformation describes the overall shape of the polymer chain. This property is mainly dependent on the environment around the polymer chains. In a good solvent with a high dilution, polymer chains are stretched. On the contrary, in a bad solvent the polymer

chain is tightly coiled in order to reduce the interface to the solvent. In order to obtain the characteristic length scales, several different calculations are used, such as mean-square end-to-end distance, the contour length, and radius of gyration. Among these methods, the radius of gyration R_g is widely used in terms of Gaussian coil conformation (in a Θ-solvent). It can be written as:

$$R_g = \frac{1}{M} \sum_i m_i(\vec{r_i} - \vec{r_c}) \tag{2.4}$$

M is the total mass of the chain, $\vec{r_c}$ denotes the center of the mass, and $\vec{r_i}$ represents the position of the single monomers with mass m_i. Typically, the values of R_g are in the order of several nanometers.

2.1.1 Conductive polymers

Polymers are conventionally considered as electrical insulators due to their intrinsic properties. However, in 1977, Heeger, Shirakawa, and MacDiarmid discovered conductive polyacetylene (PA) after doping with a high dopant concentration [6]. Due to this significant finding, they were rewarded the Nobel Prize in Chemistry in 2000. Since then, interests in conductive polymer have dramatically boosted. The basic principle accounting for polymer conductivity is based on the delocalized π electrons. With overlapping and merging the π orbitals, electrons can move freely. For example, π orbitals are formed in a benzene ring. From the perspective of energy, the overlap of π orbitals forms a binding π band and an energetically unfavorable anti-binding π^* band. They are named the highest occupied molecular orbital (HOMO) and the lowest unoccupied molecular orbital (LUMO), respectively. In addition, if the length of a polymer chain with alternating single and double bonds is extended, a conjugated π-system is formed, which allows for charge transport. In the following part, the band structure and doping will be introduced in details.

Band structure of polymers

The band structure of conjugated polymers can be understood by Peierl's instability theorem [7]. Generally, for a 1D chain with all atoms located with a periodic distance of d between each other, the band is half-filled up to Fermi level E_f as illustrated in figure 2.2a. The system shows metallic properties. However, if the periodic distance is slightly distorted, such as in case of conjugation or dimerization, a new periodic distance would be formed (figure 2.2b). Accordingly, the Brioullin zone is broken and an energy gap ΔE_{gap}

is formed. This material is then considered as an insulator or semiconductor depending on the width of ΔE_{gap}. Therefore, Peierl's instability theorem is frequently used to understand the formation of a bandgap and the intrinsic insulating or semiconducting behavior of polymers. The bandgap of polymers greatly depends on the degree of polymerization, morphology, crystallinity, or doping of the polymer. Generally, the bandgaps of polymers are in the range from 1.5 eV to 3 eV, for example 1.9-2 eV for P3HT, 1.64 eV for low bandgap polymer PTB7, and 1.58 eV for PTB7-Th [8, 9].

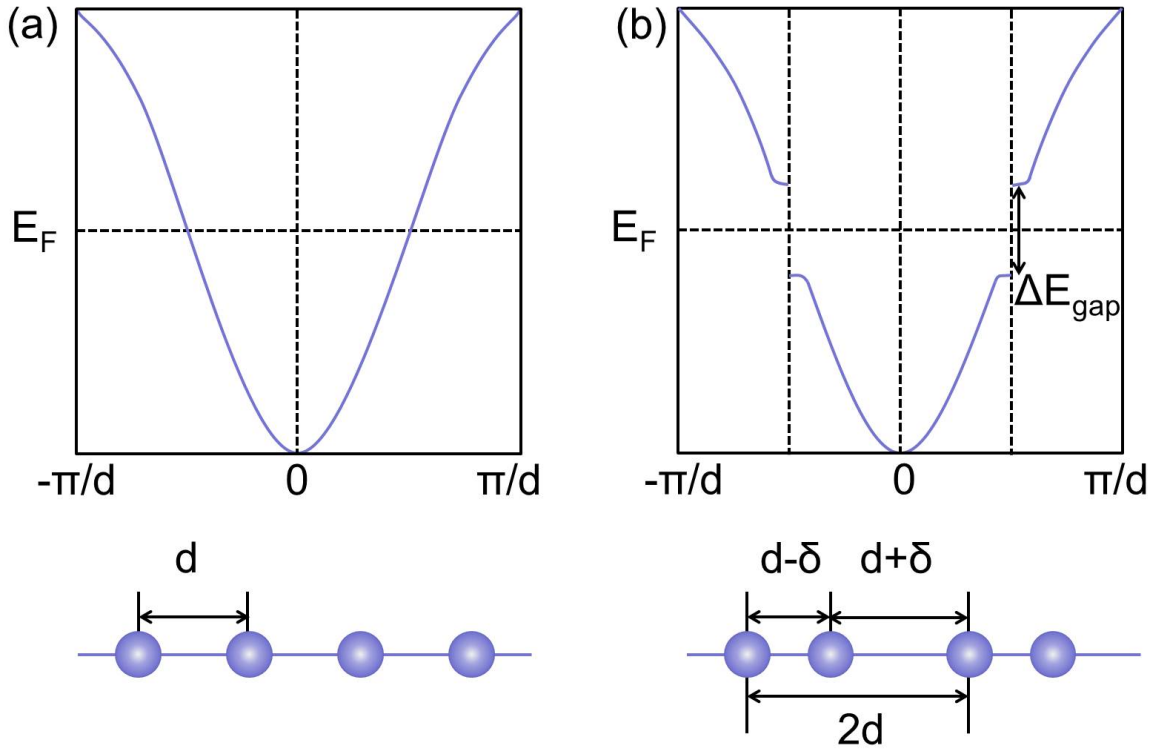

Figure 2.2: *Illustrations of Peierl's instability theorem: band structures and sketches of the 1D chain with (a) all atoms located with a periodic distance of d, and (b) the periodic distance slightly distorted by δ.*

In conducting polymers, charge carriers consist of quasiparticles which include the charges and lattice distortion. The lattice distortion is much more prominent in polymers as compared to inorganic systems, because atoms can move more freely. Solitons, polarons, and bipolarons are three types of quasiparticles in polymers with an energetically degenerated ground state. Taking PA as an example, these three quasiparticles with their net charge and respective energetic state are schematically illustrated in figure 2.3. In general, charge carriers like electrons or holes have half-integer spin. On the contrary, solitons with positive or negative charge are spin-zero, while neutral solitons have half-integer spin, as illustrated in figure 2.3a. Moreover, in reality solitons are not

localized, but distributed over the main chain over e.g. 14 carbon atoms in PA. Polarons are charged and have half-integer spin (figure 2.3b), whereas bipolarons are charged and spin-zero (figure 2.3c).

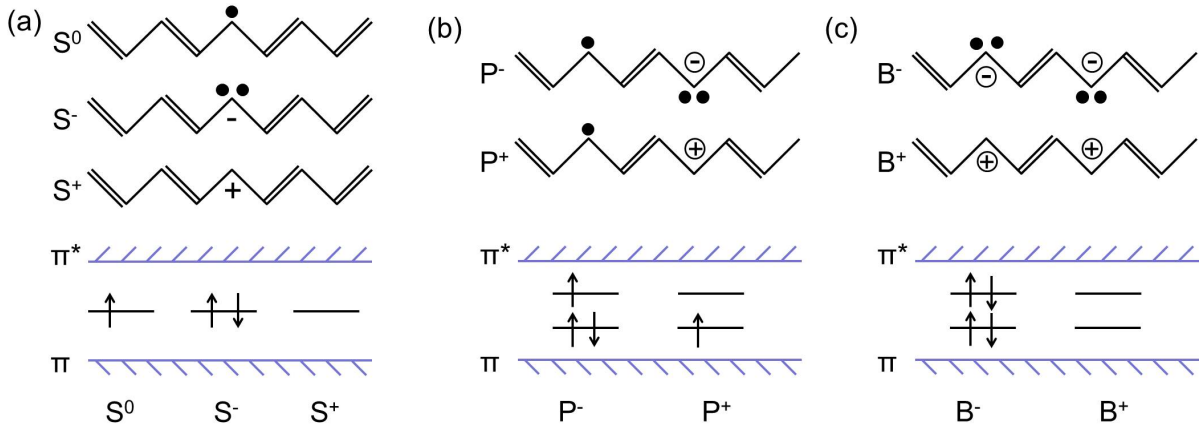

Figure 2.3: *Schematic illustrations of (a) solitons, (b) polarons, and (c) bipolarons, together with their respective energetic band states.*

Doping

Doping of polymers is attained by oxidation or reduction, which is different from inorganic semiconductors. Taking PA as an example, the iodide ion has strong oxidation potential and therefore is used as dopant. If the PA chain has a neutral soliton already, iodine would take the electron and locate at that place. Accordingly, a charged soliton is formed. However, if the PA chain does not have any solitons, the oxidation could still occur. In this case, the iodide ion would take one electron from the π bond. Thereafter, a positively charged polaron is generated. In terms of the chain with multiple polarons already, further oxidation or reduction creates bipolarons, such as in P3HT [10].

2.1.2 Polymer crystalline order

The physical properties of crystals and amorphous phases of the same polymer sometimes are significantly different. Taking P3HT as an example, the hole mobility in crystals is orders of magnitude higher than in amorphous phases. Therefore, understanding the crystallization behaviour of polymers is of great importance. As opposed to small molecules, crystallizable polymers always end up in a semicrystalline state rather than a perfect crystal. The term semicrystalline refers to a composite of lamellar stacked polymers (crystals) surrounded by amorphous or coiled chains. The existence of the semicrystalline state is

related to the fact that the polymer chains are polydisperse, showing a relatively low regularity as compared to small molecules. Moreover, the polymer chains are entangled, and it is entropically unfavorable to fully disentangle the chains to achieve full crystallization. Therefore, instead of being in thermal equilibrium, the semicrystalline phase is kinetically determined. Crystallinity is frequently used to evaluate the degree of crystallization, defined as the volume fraction of the crystalline phases. It is influenced by many aspects, such as backbone flexibility, the configuration of the polymer chains, the polydispersity, and the functional groups. For example, the crystallinity of high-density polyethylene, having a low degree branching, can be up to 85%, while the low-density polyethylene, owning to a high degree branching, only achieves the crystallinity from 35% to 55%.

Before discussing the polymer crystallization in details, three temperatures are essential to know. The first one is the melting temperature (T_m) of polymer crystals. At this temperature, the polymer chains leave from the crystalline phases and start to behave like a disordered liquid. Another parameter is the glass transition temperature (T_g), which refers to the amorphous regions. When approaching T_g, chain segments in amorphous phase start to move. In brief, below T_g a polymer can be considered as hard and brittle material, while above T_g it is still in solid state but soft and flexible. Finally, at the crystallization temperature (T_c), polymer chains gain enough energy to organize themselves in an ordered structure and crystallization occurs. T_c always lies between T_m and T_g.

In amorphous phase, chain ends, impurities, defects, and entangled chains are more common. In crystalline regions, polymer chains form layered structures with a layer thickness d_c (figure 2.4). It is noted that d_c is normally in the range of tens of nanometers, and strongly depends on the crystallization temperature rather than the molecular weight. These layered structures continuously grow laterally (perpendicular to the polymer chains) up to micrometers [11]. Furthermore, the crystals arrange in the form of so-called spherulites. Since in the application of organic photovoltaics, the exciton diffusion length is within tens of nanometers, micrometer-sized crystals are unfavorable and avoided. Therefore, the focus lies on the early stages of polymer crystallization, mainly including the nucleation and initial crystal growth. Moreover, polymer crystallization can be initiated in a solution, or a melt. In this thesis, the crystallization of P3HT is initiated in the solution and then, the crystals grow via post-treatment of the thin film.

Nucleation

Polymer crystallization starts from nucleation, as is addressed by Hoffman nucleation theory. Nucleation occurs at the temperature range between T_g and T_m. Typically, one differentiates between two types of nucleation, the first being heterogenous nucleation.

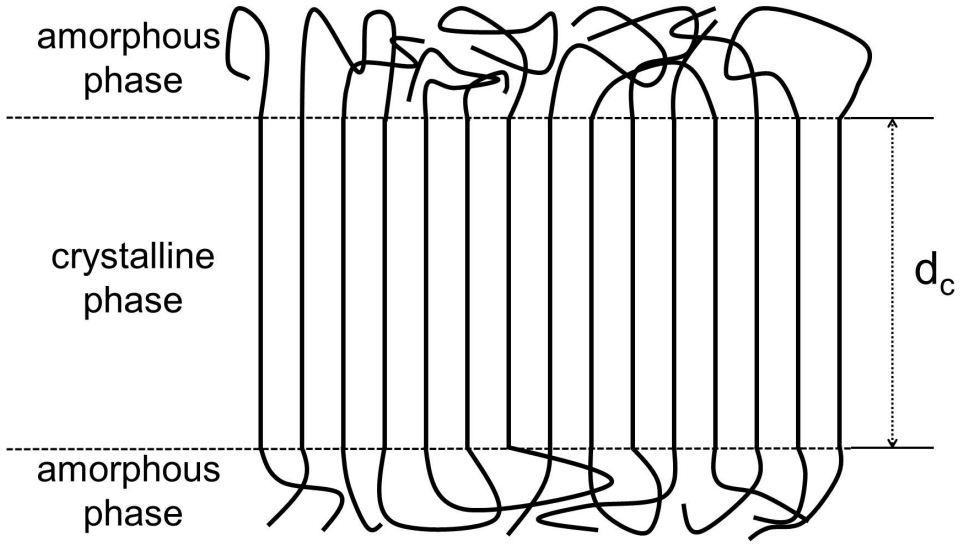

Figure 2.4: *The model of a semicrystalline phase in polymers thickness d_c. All the lines represent the polymer backbones. The middle region (straight lines) represents the crystalline phase, also called crystalline lamellae. The top and bottom regions (crooked lines) depict the amorphous phase.*

Dust particles, impurities, and defects can act as the pre-existing nuclei. The polymer chains then attach to the surface of the nuclei in an ordered structure, and then the crystal starts to grow. The other type is homogeneous nucleation, in which polymer chains arrange themselves in an ordered structure due to thermal fluctuations. This type of nucleation is a dynamic process, with the possibility that nuclei disappear again or growth is initiated.

Growth

The growth mechanism of crystalline lamellae from a nucleus is schematically illustrated in figure 2.5 [12, 13]. It is noted that crystallization is not a one-step transition from the melt to the crystalline phase. Instead, an intermediate state is observed in prior to the final crystal, called mesomorphic phase [14]. During this stage, the chains in the melt are aligned by epitaxial forces [15]. It can be considered as a densification procedure, where the defects are expelled out and the preliminary lamellar stacks are formed. As shown in figure 2.5a, chains are much more stretched in crystalline phase as compared to melts, but still slightly helical. Meanwhile, the thickness of lamellas increases due to a high inner mobility. When it reaches the critical value, the increase in thickness stops, and a transition towards more ordered lamellar structure occurs. The core solidification

leads to the formation of a block, as depicted in figure 2.5b. Finally, the surface ordering occurs in order to further stabilize the crystals (figure 2.5c).

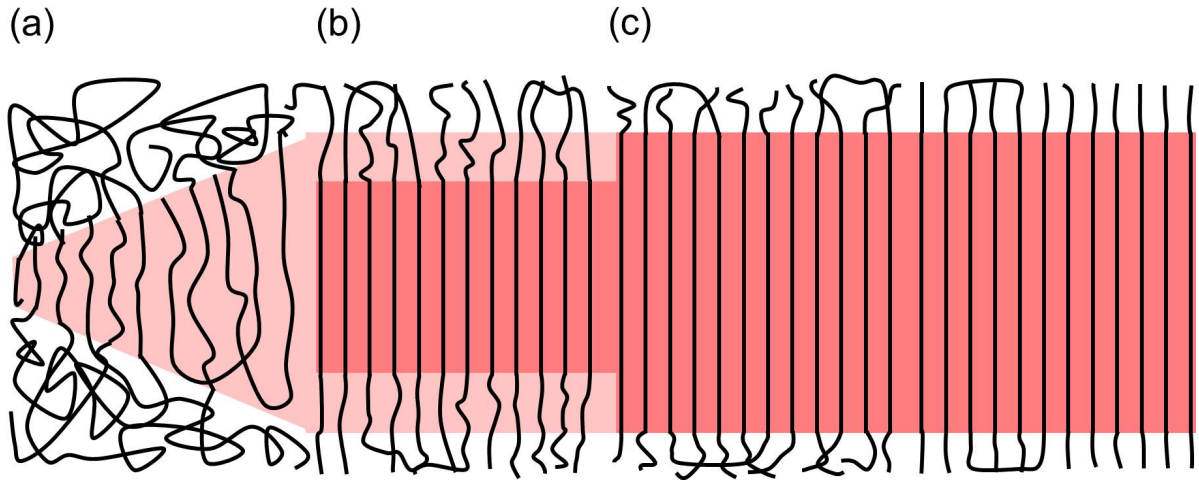

Figure 2.5: *The sketch of the multistage model describing growth of polymer crystals. It starts from a polymer melt by the formation of (a) mesomorphic phase, and then approaches the state of (b) core solidification. Finally, the (c) surface ordering occurs in order to stabilize the crystals. The light pink region indicates the region in which the polymer chains are stretched but still slightly crooked. In the dark pink region, the polymer chains are well aligned in lamellar structures.*

The rate of polymer crystallization is determined by the crystallization temperature. However, the rate-dependency is different in nucleation and growth. On one hand, homogeneous nucleation is suppressed at high temperature due to the high thermal activation. Accordingly, an increase in the nucleation rate occurs with lowering temperature. On the other hand, the growth rate of crystals is promoted at a higher temperature since the motion of the chains is facilitated. Taking both rate-dependence of nucleation and growth into account, the rate-temperature diagram of polymer crystallization can be divided into four regions, as illustrated in figure 2.6. Region I shows almost no crystallization due to an extremely low nucleation rate. Then in region II a prominent increase in the crystallization rate occurs with lowering the temperature, where the nucleation rate is dominant. The maximal crystallization rate is presented in region III. Finally, the rate decreases with increasing temperature, where the growth rate is determinant (region IV). The rate-temperature dependence ($G(T)$) can be described by the formula below:

$$G(T) \propto exp\left(\frac{-\Delta F_N}{RT}\right) exp\left(\frac{-\Delta F_G}{RT}\right) \tag{2.5}$$

ΔF_N represents free energy variance via the critical free energy barrier for nucleation. ΔF_G describes activation energy barrier which enables chains to fold and arrange themselves in lamellar crystals. In brief, the first term accounts for nucleation, which is inverse proportional to $T_m - T$, while the second term addresses motion of chains, which is inverse proportional to $T - T_g$. In correlation with figure 2.6, at the temperature around T_m the nucleation is dominant, while at the temperature about T_g the motion of chains is prominent.

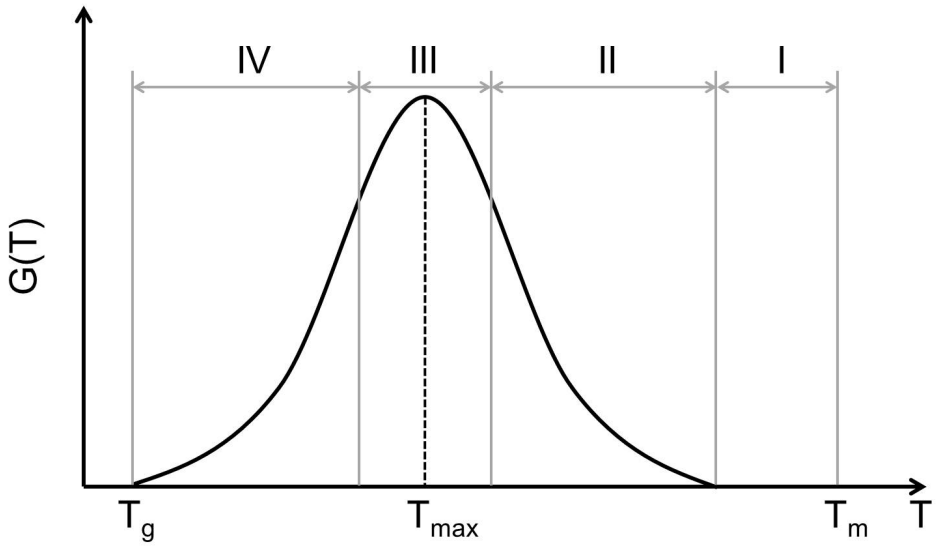

Figure 2.6: *Schematic diagram of $G(T)$.*

2.1.3 Diblock copolymer

Diblock copolymers constitute of two different homopolymer subunits linked by a covalent bond. In case of the subunits A and B, the resulting polymer is named polyA-block-polyB, abbreviated as PA-b-PB. Normally, each homopolymer block of the copolymers has a different degree of polymerization N_A and N_B. Then the block ratio f_A and f_B can be calculated by:

$$f_A = \frac{N_A}{N_A + N_B} \tag{2.6}$$

$$f_B = \frac{N_B}{N_A + N_B} = 1 - f_A \tag{2.7}$$

Generally, different polymers are incompatible and therefore, phase separation occurs. Instead of a macro-phase separation as in polymer blends, micro-phase separation is present in block copolymers, because homopolymer chains are connected by covalent bonds in the diblock copolymer. The sizes of the domains are determined by the chain fractions of each block. Detailed introduction about the phase separation of block copolymers will be introduced in section 2.1.4.

2.1.4 Phase separation

Understanding the behavior when different polymers are blended with each other is of great importance, since the obtained new system might have the different properties from individual polymers, such as mechanical properties and crystallinity. In the field of organic photovoltaics, the combination of donor and acceptor materials enables effective working devices. Phase separation frequently occurs in polymer blends and is generally driven by minimizing free energy of the whole system. The Gibbs free energy of mixing two polymers is described by Flory-Huggins theory:

$$\Delta G = nk_BT[\frac{\phi_1}{N_1}ln\phi_1 + \frac{\phi_2}{N_2}ln\phi_2 + \chi\phi_1\phi_2] \tag{2.8}$$

Here, ϕ_1 and ϕ_2 indicate the volume fractions of polymer 1 and 2. N_1 and N_2 represent their respective degrees of polymerization, n is the total number of polymer chains, χ is the Flory-Huggins interaction parameter. The first two terms of this formula describe the entropy and the last term addresses the enthalpy. If N_1 (or N_2) is equal to 1, the component$_1$ (or component$_2$) can be considered as a solvent and therefore, the equation resembles a polymer solution. The Flory-Huggins interaction parameter can be expressed by:

$$\chi = \chi_S + \frac{\chi_H}{T} \tag{2.9}$$

with two constants χ_H and χ_S, determined by the polymers. This description is slightly different from the original Flory-Huggins interaction parameter. In the original simple model it is a purely enthalpic term, while empiric corrections motivated the addition of a entropic parameter χ_S.

Polymer blend

In a polymer blend, where only one phase exists, the Gibbs free energy is shortened to $\Delta G(\phi)$. However, if demixing happens, two phases show up with each Gibbs free energy $\Delta G(\phi_\alpha)$ and $\Delta G(\phi_\beta)$, respectively. The miscibility of two polymers is determined by the Gibbs free energy of mixing. For example, no phase separation takes place only if:

$$\Delta G < \alpha \Delta G(\phi_\alpha) + \beta \Delta G(\phi_\beta) \tag{2.10}$$

where $\phi = \phi_\alpha + \phi_\beta$, and $\alpha + \beta = 1$. α and β indicate two phases, with their volume fractions ϕ_α and ϕ_β.

The dependence of the Gibbs free energy on the volume fraction is depicted in figure 2.7a and 2.7b. The blue lines describe $\Delta G(\phi)$, and the red lines represent the energy of two phases of α and β, weighted average of $\Delta G(\phi_\alpha)$ and $\Delta G(\phi_\beta)$. In figure 2.7a, $\Delta G(\phi)$ is a concave-shaped curve. The Gibbs free energy of the mixture is lower than that of the average value between phase α and β. Therefore, the blend is stable. On the contrary, in figure 2.7b, a convex-shaped curve of $\Delta G(\phi)$ suggests that the blend is not stable and phase separation is desired.

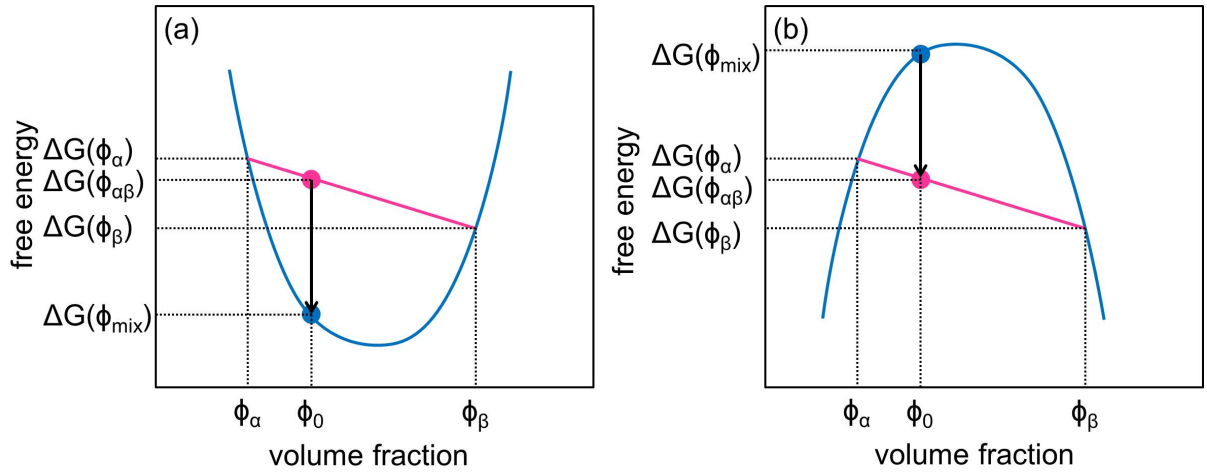

Figure 2.7: *(a) An exemplary concave-shaped Gibbs free energy curve. In this case, the blend with volume fraction ϕ_0 is stable since phase separation would increase the Gibbs free energy. While (b) a convex-shaped Gibbs free energy curve. Its blend with volume fraction ϕ_0 is unstable as phase separation would reduce the corresponding Gibbs free energy.*

The phase diagram of a polymer blend can be expanded to include the dependency on other parameters. Figure 2.8a displays the Gibbs free energy as function of the volume fraction obtained at different temperatures. It is noted that the curves taken at high

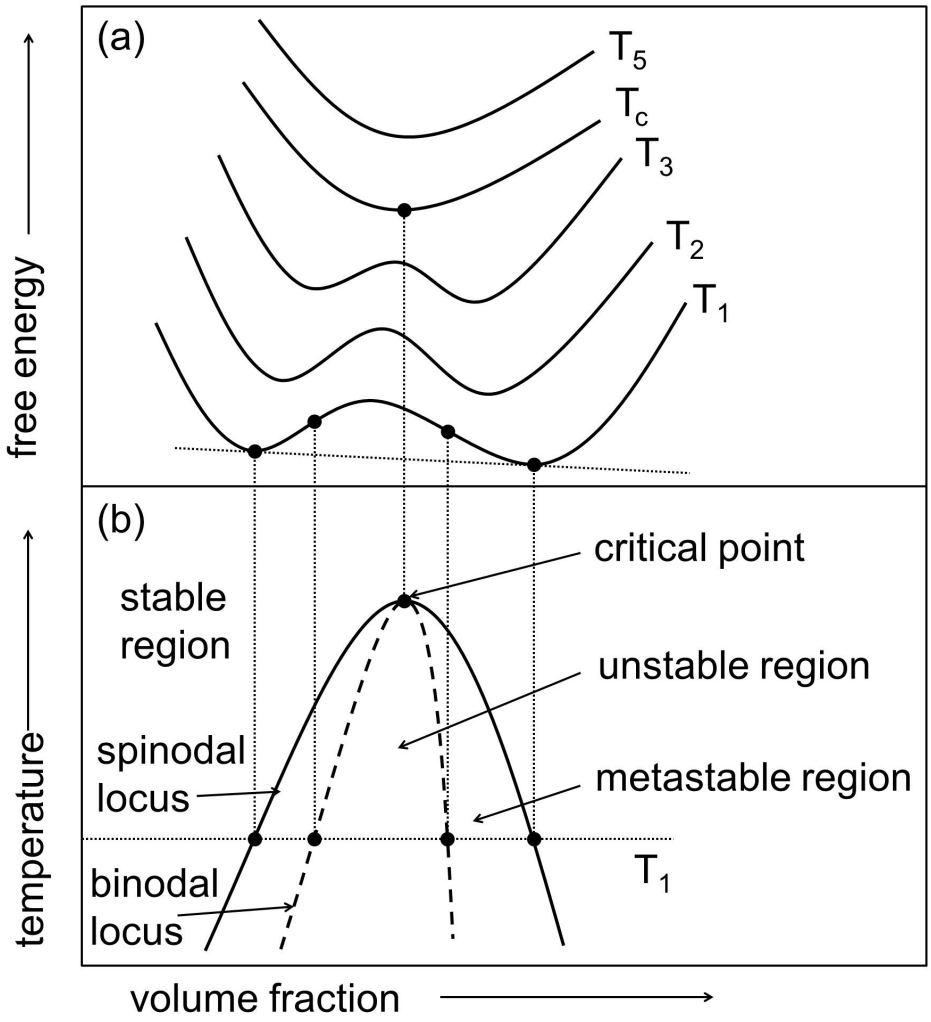

Figure 2.8: *(a) An example of Gibbs free energy as a function of volume fraction obtained at different temperatures. (b) Corresponding phase diagram derived from (a), with all phases labeled. The binodal locus is obtained from the tangential construction and the spinodal locus is derived from the second derivative of the free energies at different temperatures.*

temperatures of T_c and T_5 are concave, suggesting that the homogeneous mixture is stable. However, when the temperature decreases to T_1, T_2, and T_3, the curves show both convex- and concave-shape. It indicates that in certain volume fractions phase separation is desired, while in the other regions the blend is stable. In order to clearly depict the stable and unstable regions, the projection to the temperature-volume fraction is built as shown in figure 2.8b. The binodal locus is constructed by the tangent of the $\Delta G(\phi)$ trajectories, denoted by the black solid line. It is the separation between the homogeneous mixture (stable region) and the two phase system. The spinodal line (black dashed line) is obtained from the inflection points of the $\Delta G(\phi)$, further dividing the two phase system into meta-

stable and phase-separated states (unstable region). The blend in meta-stable region could enter the stable region or unstable region due to fluctuation. The common point between binodal and spinodal lines is called critical point, which is obtained when the third derivative of $\Delta G(\phi)$ is equal to 0. The critical volume fraction ϕ_c can be described from the degree of polymerization N for a solution:

$$\phi_c = \frac{1}{1+\sqrt{N}} \tag{2.11}$$

if ϕ_c is known, the interaction parameter χ_c is calculated by:

$$\chi_c = \frac{1}{2}\left(1+\frac{1}{\sqrt{N}}\right)^2 \tag{2.12}$$

In the case of two different polymers, with their respective degrees of polymerization N_1 and N_2, the critical point is determined by

$$\frac{\partial^3}{\partial\phi^3}\frac{\Delta G}{nk_BT} = 0 \tag{2.13}$$

then

$$\phi_c = \frac{1}{1+\sqrt{N_2/N_1}} \tag{2.14}$$

Moreover, the critical polymer-polymer interaction parameter χ_c is determined by

$$\frac{\partial^2}{\partial\phi^2}\frac{\Delta G}{nk_BT} = 0 \tag{2.15}$$

then

$$\chi_c = \frac{1}{2N_2}(1+\sqrt{N_2/N_1})^2 \tag{2.16}$$

If the two polymers have the same polymerization N, the phase diagram is symmetric with the point ϕ_c. In this case, ϕ_c is equivalent to $1/2$, and χ_c is equal to $2/N$. Then the critical value is $\chi_c N = 2$. If $\chi_c N$ is above 2 the blends demix, while if $\chi_c N$ is below 2 the blends form an intermixed phase.

Diblock copolymers

Diblock copolymer commonly tends to spontaneously self-assemble into a diversity of meso-phases (order), but an intermixed phase (disorder) can be also formed if it is at a sufficiently high temperature or in sufficiently diluted solution. The critical value for symmetric diblock copolymer is $\chi_c N = 10.5$, which is much larger than the value for polymer blends [16]. When the χN is far below 10.5, for example in case of low polymerization, a mixed phase is established. With increasing χN, the two blocks start to repel each other and therefore, a composition fluctuation is formed in the disordered melt. When χN approaches 10.5, the so-called weak segregation limit (WSL) is reached. The repulsion between two blocks is large enough to form phase separation. The so-called order-disorder phase transition (ODT) occurs. Upon continuously increasing χN, the system attains to the strong segregation limit (SSL). Strong demixing happens, resulting in a sharp interface between blocks.

Taking a conformationally symmetric diblock copolymer PA-b-PB as an example, the corresponding theoretic phase diagram is schematically illustrated in figure 2.9. First of all, depending on χN and f_A, the whole area can be divided into two regions by the orange line in figure 2.9. The region above this line indicates an ordered structure while the region below the line describes the disordered structure. Moreover, different structures stay in the ordered region, including sphere, cylinder, gyroid, and lamella, with their structures schematically shown in figure 2.9. Therefore, the morphology of the resulting sample can be tuned by χN and f_A. However, in reality, the long-range highly ordered structure is hard to achieve. The two blocks normally have quite different monomer structures and properties which strongly influence the development of an ordered structure. Moreover, the real phase diagram is commonly asymmetric, and varies from the bulk material to thin films [17].

2.2 Sol-gel synthesis

Titania, also known as titanium dioxide, has been widely used in academic and industrial applications. In this thesis, it has been utilized as the electron acceptor, together with the corresponding electron donor P3HT showing a great potential for the flexible hybrid solar cells. The basic properties of titania are discussed in section 2.2.1. Nanostructured titania films are obtained by the so-called block copolymer assisted sol-gel synthesis. After this process, the polymer template is removed to obtain an interconnected titania network with adjustable porosity and pore size. A detailed introduction about the basics of sol-gel

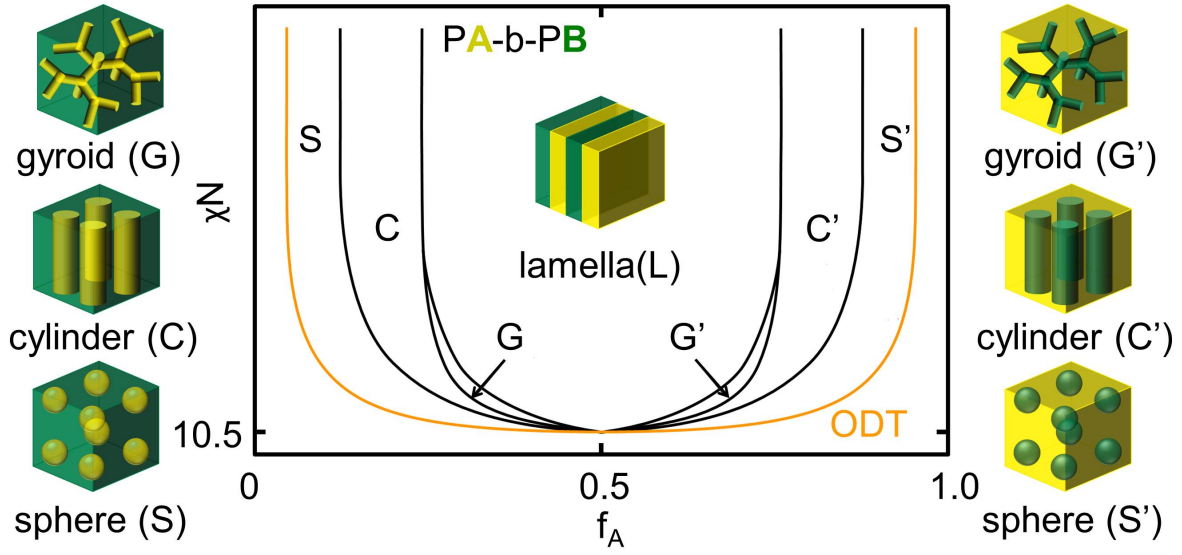

Figure 2.9: *Schematic of an exemplary symmetric phase diagram of a diblock copolymer melt of PA-b-PB. Block A and B are described by yellow and green colors, respectively. In detail, with increasing block ratio f_A, the structure of A in B matrix undergoes a transition from sphere (S), cylinder (C), and gyroid (G). When f_A is equivalent to f_B, a lamella structure (L) is formed. With continuously increasing f_A, the structure, with B in matrix A, changes from gyroid (G') to cylinder (C'), and then to sphere (S'). The orange line indicates the boundary between ordered and disordered phases. The transition from the region above the orange line towards the area below it is called order-disorder transition (ODT). The image is adapted from [18].*

chemistry is described in section 2.2.2, and the further structure direction with polymer template is presented in section 2.2.3.

2.2.1 Properties of titania

Titania (TiO_2) is a natural form of oxidized titanium. Besides the amorphous phase, it has three main different crystalline forms, namely anatase, rutile, and brookite. Anatase has been successfully used as a photocatalyst for photodecomposition and as a photoanode for photovoltaics due to its high photoactivity. The rutile is the most thermodynamically stable phase, and it has also been widely utilized for applications in photovoltaics. The brookite phase is not thermodynamically stable as compared to other phases. Nevertheless, all these three phases exhibit high refractive indexes, high densities, and large bandgaps, with all the values listed in table 2.1. The absorption edges of anatase and rutile are 388 nm and 413 nm, respectively, suggesting that both phases have a great UV

absorbing ability. Therefore, it is believed that titania, as a hole blocking layer or an electron acceptor, can protect the photoactive polymers from UV degradation.

	refractive index	**density (g cm^{-3})**	**bandgap (eV)**
anatase	2.57	3.83	3.2
rutile	2.95	4.24	3.0
brookite	2.81	4.17	3.1-3.4

Table 2.1: Crystal phases of titania, with their corresponding refractive index, density, and energy bandgap [19–22].

2.2.2 Principles of sol-gel synthesis

The sol-gel process is a typical method for fabricating metal oxides from a homogeneous alkoxide solution in organic media. The process converts the precursor monomers into an oligomer solution (sol), and then develops an integrated network (gel) with further chemical reactions. For titania sol-gel, the chemical formula of the precursor is given by $Ti(OR)_4$, where R represents alkyl groups. Sol-gel chemistry is based on hydrolysis and polycondensation of $Ti(OR)_4$. The titania precursor starts reacting readily with water molecules. This reaction is called hydrolysis, as hydroxide anions become attached to Ti atom rather than OR groups:

$$Ti(RO)_4 + mH_2O \leftrightharpoons (HO)_m - Ti - (OR)_{4-m} + mR - OH \tag{2.17}$$

where m is not larger than 4. Depending on the amount of water and catalyst in the solution, the hydrolysis degree (partially or completely) could be tuned easily.

After hydrolysis, a polycondensation process take place through the reaction of hydroxyl groups. Two partially hydrolyzed titania monomers polymerize via a Ti-O-Ti bond by the elimination of a H_2O or ROH molecule. Two mechanisms are shown in the following equations.

$$(RO)_3Ti - OH + HO - Ti(OR)_3 \leftrightharpoons (RO)_3 - Ti - (OR)_3 + H_2O \tag{2.18}$$

$$(RO)_3Ti - OR + HO - Ti(OR)_3 \leftrightharpoons (RO)_3 - Ti - (OR)_3 + R - OH \tag{2.19}$$

With this process going on, the titania precursors can be transformed into 1−, 2−, or 3− dimensional oxide networks accompanied by the production of H_2O and ROH species. Therefore, those main parameters, including the type of titania precursor, amount of water, catalyst, reactants molar ratio, temperature, have a significant effect on the hydrolysis and polycondensation reactions and thereby, the properties of synthesized titania nanostructures.

In this thesis, ethylene glycol-modified titanate (EGMT) is used as the titania precursor, which has already been applied successfully for the fabrication of titania nanostructures at low temperatures [23]. During EGMT hydrolysis and polycondensation reactions, the crystal phase of titania (anatase or rutile) can be tuned by changing of pH values.

2.2.3 Structure direction with polymer template

In order to further control the nanomorphology of titania, a structure directing material can be incorporated into the sol-gel process [24]. In this thesis, the block copolymer PS-b-PEO is used. It is an amphiphilic diblock copolymer, which comprises a hydrophobic block PS and a hydrophilic block PEO. As described in section 2.1.4, block copolymers tend to phase separate in case of $\chi N > 10.5$. Through adjustment of degree of polymerization N or interaction parameter χ, the corresponding morphology can be tuned, as illustrated in figure 2.9. In solution, the polymer chains form micellar morphologies which are influenced by the molecular weight and weight ratio of the two blocks, the selected solvent and their corresponding solubilities, and the experimental conditions such as temperature, humidity, and pressure [18, 25]. Most importantly, the titania precursor has to be selectively incorporated into one block of the copolymer. For PS-b-PEO, titania precursor coordinates to the hydrophilic block PEO.

The principle of the diblock copolymer assisted sol-gel process is schematically illustrated in figure 2.10. The block copolymer is first dissolved in a good solvent and then the precursor and a selective solvent are added. Thereafter, micellar structures are formed due to the presence of the selective solvent. Meanwhile, the titania precursor starts to hydrolyze and incorporate into the desired block. During this process, the self-assembly of the block copolymer, titania incorporation, and the gelation of titania all determine the phase separation in the solution. Towards thin films, different deposition methods are available. Depending on the selected casting method, the resulting morphology can be further tuned, either freezing the morphology immediately with a fast deposition process like spin coating or rearranging the morphology with a relatively slow deposition method like solution casting. Finally, to obtain porous titania films, the polymer template has to be removed. A calcination process is a common method to achieve the highly crys-

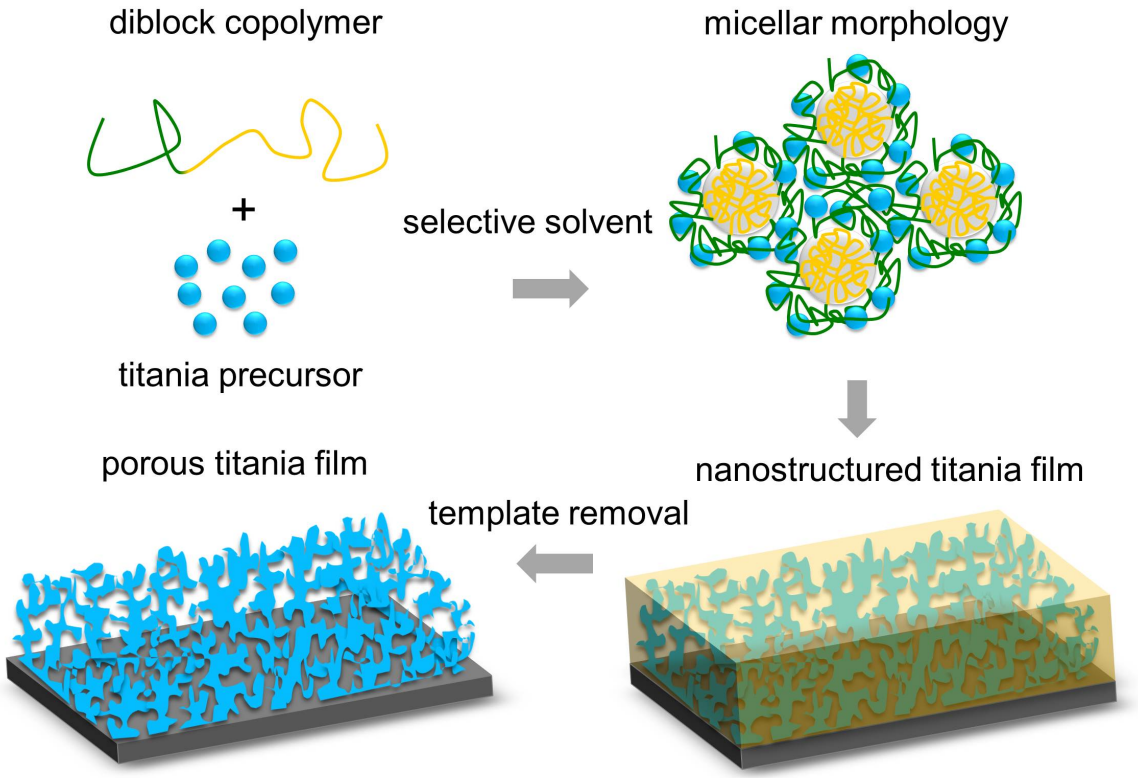

Figure 2.10: *Schematic illustration of the diblock copolymer assisted sol-gel process.*

tallized and purified titania films. However, it costs energy and limits the application based on flexible polymer substrates. Therefore low temperature methods are intensively investigated in this thesis, with all details described in section 8.1.

2.3 Organic solar cells

Solar cells constitute a type of optoelectronic devices, which can directly convert light into electricity. Specifically, the term organic solar cells refers to the main functional layer (active layer) comprising at least one organic semiconductor. In the present work, P3HT:PCBM organic solar cells are mainly discussed, which employ the semiconductor polymer P3HT as electron donor and the organic small molecule PCBM as electron acceptor. Moreover, the active layer forms a so-called bulk heterojunction (BHJ) structure. The basic principle of light-electricity conversion process will be introduced in section 2.3.1. Afterwards, detailed descriptions for each step will be presented in the following order:

light absorption (section 2.3.2), exciton diffusion (section 2.3.3), exciton dissociation (section 2.3.4), charge transport (section 2.3.5), and charge extraction (section 2.3.6). Finally, the possible loss mechanisms during these processes are discussed in section 2.3.7.

2.3.1 Basic principles

Organic solar cells are normally thin films, with thicknesses in the range of several nanometers up to hundreds of nanometers. The devices are built up by several functional layers as shown in figure 2.11. In principle, the active layer is the main functional layer, where the photovoltaic conversion takes place. In order to extract the charge carriers, the active layer is sandwiched between two electrodes. Depending on the direction of positive charge collection, two geometries are commonly investigated. One is the standard geometry, as shown in figure 2.11a. In such a device, the light passes through the bottom electrode before being absorbed by the active layer. Holes are collected at the bottom electrode while electrons are collected at the top electrode. Accordingly, the top electrode is called cathode and the bottom one is called anode. On the contrary, an inverted solar cell (figure 2.11b) has its anode at the top of the device and cathode at the bottom. In more advanced devices, blocking layers are incorporated in solar cells to improve efficiency. In this thesis, we only use the electron blocking layer in standard solar cells because the hole blocking layer is not necessary to obtain well functional P3HT:PCBM solar cells [26]. But both, electron and hole blocking layers, are used in inverted devices in order to obtain properly working devices. The sketches of both architectures are shown in figure 2.11 with all the details labeled.

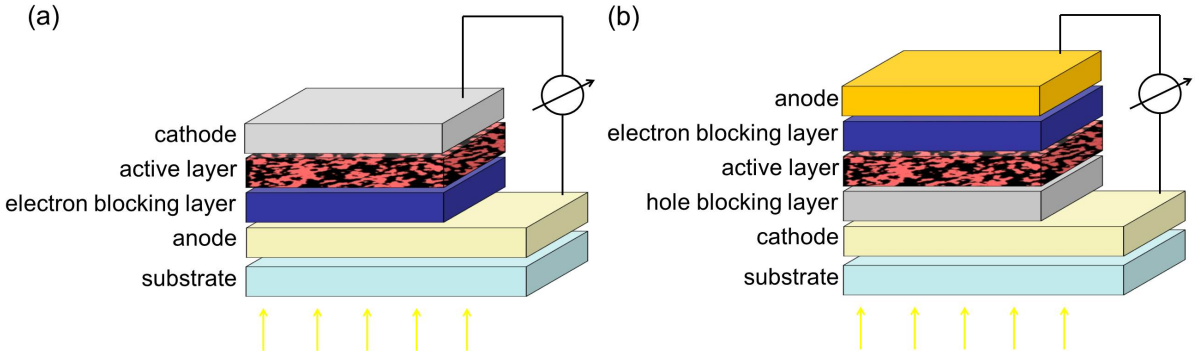

Figure 2.11: *Device architectures of organic BHJ solar cells with (a) a standard geometry and (b) an inverted geometry. Yellow arrows denote the direction of illumination.*

The active layer consists of at least one organic semiconductor as donor material which generates excitons. An exciton is a neutral quasi-particle, with no charge. The exciton

binding energy of around 0.5 eV in polymers is much higher than in inorganic semiconductors [27]. Thermal energy at room temperature is not enough to separate these excitons. Therefore, a second material with different LUMO level is necessary to provide a potential difference to dissociate the excitons. In the present thesis, PCBM is used as the acceptor material. Moreover, due to the small exciton diffusion length of around 10 nm, bilayer structures of donor and acceptor are unlikely to achieve an efficient exciton dissociation. As the exciton needs to reach an interface within its lifetime to be dissociated, the inner morphology of the active layer is of great importance for the solar cell performance. The so-called bulk heterojunction (BHJ) structure as depicted in the active layer in figure 2.11 has proven to be more efficient.

The light-electricity conversion is a complicated process, including several steps. In figure 2.12, all these steps are listed schematically. In general, the active layer absorbs a photon and then generates an exciton. The exciton diffuses to the interface of donor and acceptor materials and dissociates into free charge carriers. Afterwards, the charge carriers are transported towards the corresponding electrodes and are eventually extracted at the electrodes. Each individual step is described in detail in the following sections.

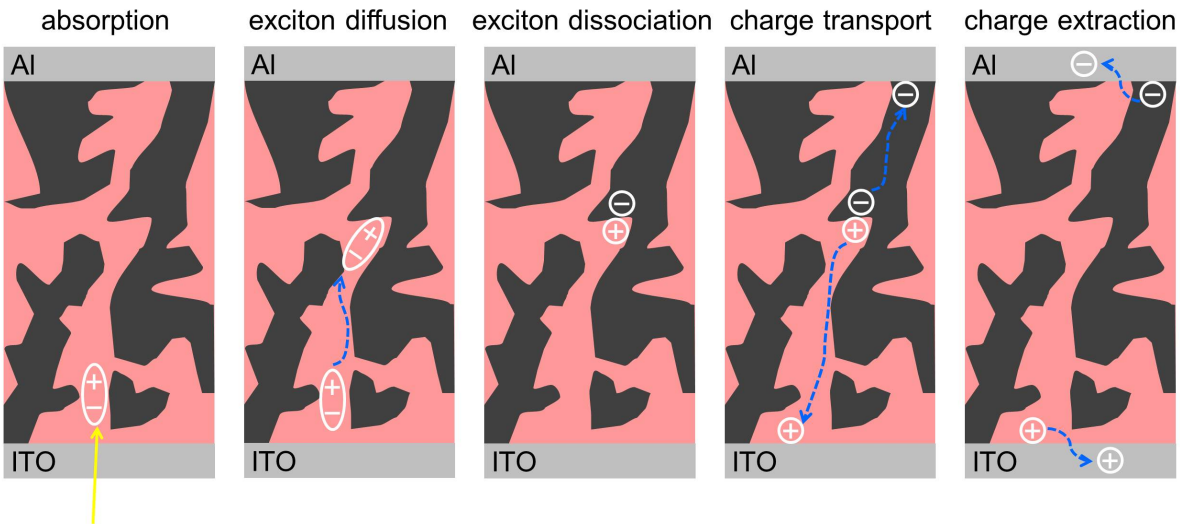

Figure 2.12: *Schematic illustration of light-electricity conversion process. The pink and black colors indicate the donor and acceptor materials, respectively.*

2.3.2 Absorption

The first step of the photovoltaic conversion is light absorption. A photon can be absorbed if its energy is larger or equal to the bandgap of the polymer. The electron is then excited from the HOMO level to the LUMO level. The excitation to different vibrational states is

possible in organic materials due to a mean nuclear distance Q_{12} as depicted in figure 2.13. According to the Franck-Condon principle, the electronic transition is much faster than the movement of the nucleus, accordingly the excitation is regarded as a straight line which is perpendicular to the vibrational state (figure 2.13).

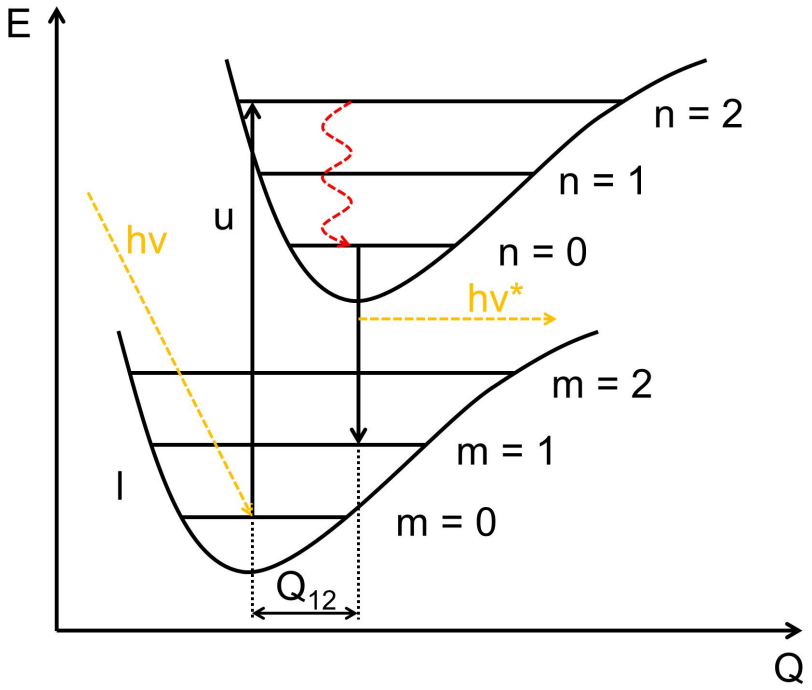

Figure 2.13: *An example of band profile of organic semiconductor. The lower and higher electronic states are denoted as l and u, respectively. Each electronic state is divided into different vibrational states m,n = 0, 1, 2... Q_{12} is the spatial displacement in the organic semiconductor.*

As an example shown in figure 2.13, the photon with energy $h\nu$ is absorbed by the polymer. The excitation is initiated from the electronic and vibrational ground state, indicated by $m = 0$. The electron is excited to the vibrational state of $n = 2$ of the electronic state u, leaving a hole behind. Afterwards, the excited electron can be relaxed to the ground vibrational state ($n = 0$) of the electronic state u via non-radiative relaxation, as illustrated by the red arrow in figure 2.13. Thereafter, the excited electron might transit back to the ground state (electronic state l) via luminescence. During this process, a photon is emitted with the frequency ν^*. So far, only the generation of a singlet exciton (electrons and holes have an opposite spin) is discussed since it accounts for the majority of transitions. Moreover, in the case of organic semiconductors, the exciton is considered to be a tightly bound Frenkel exciton, which refers to a high binding energy typically in the order of 0.5 eV and resulting in strong localization [28]. On the contrary, binding

energy of the Wannier-Mott exciton, which is typical for inorganic semiconductors is only around 20 meV. This kind of exciton can be easily separated via thermal energy at room temperature ($\sim$ 25 meV). However, the necessary energy for dissociating the Frenkel exciton is significantly higher than the thermal energy at room temperature. Therefore, additional energy is needed. For example, blending of the polymer with an acceptor material provides the essential energy via the potential difference between donor and acceptor materials.

The absorption spectrum is correlated to the structures of semiconducting polymers. Normally, the absorption spectra of these materials contain several peaks due to vibrational excitations. The shape of the spectrum is mainly determined by the type of the monomer. Moreover, a red shift is observed with increasing numbers of monomers of this material [29]. It results from overlapping of binding and anti-binding states, and accordingly narrowing of the bandgap. Thus, inter- and intrachain ordering can be revealed by absorption measurements. Taking P3HT aggregates as an example, the absorbance with its fit is shown in figure 2.14. The main peak 0-1 is correlated to the 0-1 transition, which refers to the π-π^* intrachain absorption in P3HT [30]. Its position is determined by the conjugation length of the main chain. In reality, the conjugation length of the polymer chain is much shorter than its chain length due to kinks, defects, etc. Generally, an increased conjugation length results in a red shift. The shoulder at around 600 nm (2.06 eV) is correlated to the 0-0 transition, which is an optical transition between states of the interchain [30]. It has been reported that the absorbance spectra of P3HT can be analyzed using the weakly coupled H-aggregate model, with more details shown in reference [31]. From the ratio between the amplitude of transition 0-0 to 0-1, the free exciton bandwidth W can be calculated by the equation:

$$\frac{A_{0-0}}{A_{0-1}} \approx \frac{n_{0-0}}{n_{0-1}} \left(\frac{1 - 0.24W/E_P}{1 + 0.073W/E_P} \right)^2 \tag{2.20}$$

A_{0-0} and A_{0-1} indicate the absorbance of the transition 0-0 and 0-1, respectively. n_{0-0} and n_{0-1} are the real parts of the refractive indexes at the wavelengths of transition 0-0 and 0-1. For P3HT, E_P was reported as 0.18 eV and the ratio between n_{0-0} to n_{0-1} as 0.97 [30]. In general, the smaller the value of W indicates a higher crystalline order of P3HT [32].

2.3.3 Exciton diffusion

In order to obtain free charges, the exciton dissociation is necessary. As explained in section 2.3.2, the Frenkel exciton cannot dissociate at room temperature due to the high

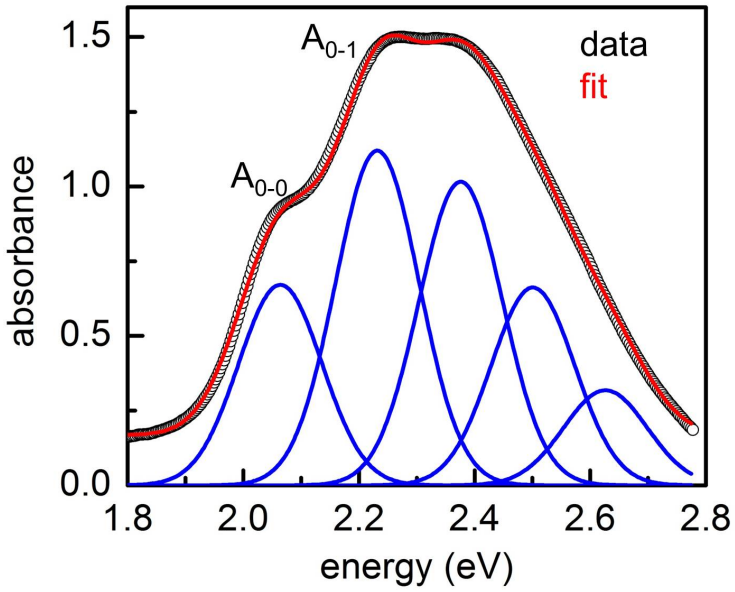

Figure 2.14: *An example of the absorbance spectrum of aggregated P3HT (black symbols) with its fit (red curve). Five Gaussians (blue curves) with equal FWHM are used for fitting. The amplitudes of the 0-0 and 0-1 transitions are labeled as A_{0-0} and A_{0-1}, respectively.*

binding energy. The potential difference between donor and acceptor materials provides the energy for exciton dissociation. Therefore, the exciton has to diffuse towards the interface between donor and acceptor materials. The motion of the exciton is enabled by several energy transfer processes between donor molecule and acceptor molecules. It is of importance to clarify that in the present section the so-called donor or acceptor molecule is a different concept from the donor or acceptor material. For instance the exciton in a polymer phase, the donor molecule is the site where the exciton sits and the acceptor molecule refers to the site to which the exciton is transferred. Generally for singlet exciton created in conjugated polymer, two types of energy transfer exist, including the trivial energy transfer and the Förster resonant energy transfer depicted in figure 2.15a and 2.15b, respectively.

Taking an example that exciton generates in a conjugated polymer, the trivial energy transfer represents the process that a photon is emitted via fluorescence by the donor molecule and then reabsorbed by the acceptor molecule. It means another exciton is created in the acceptor molecule. The trivial energy transfer mainly occurs when the distance of donor and acceptor molecules is larger than 10 nm. Briefly, the trivial energy transfer can be considered as an excitation transfer among molecules. Accordingly, it significantly

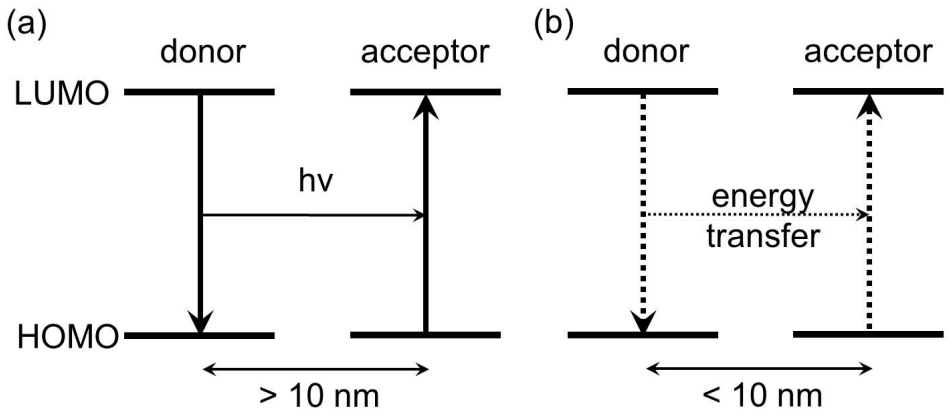

Figure 2.15: *Sketches of (a) the trivial energy transfer and (b) the Förster resonant energy transfer.*

enhances the lifetime of the exciton [7]. The transfer rate $k_{D\to A}^{ET}$ can be described by the equation 2.21, where R represents the distance between donor and acceptor molecules:

$$k_{D\to A}^{ET} \propto \frac{1}{R^2} \tag{2.21}$$

The Förster resonant energy transfer is a radiationless process, also known as fluorescence resonance energy transfer (FRET). It is carried out by dipole-dipole coupling. Contrary to the trivial energy transfer, the Förster resonant energy transfer occurs when the distance of donor and acceptor molecules is short, typically less than 10 nm. The transfer rate $k_{D\to A}^{FRET}$ can be calculated by:

$$k_{D\to A}^{FRET} = \frac{1}{\tau_D}\left(\frac{R_0}{R}\right)^6 \tag{2.22}$$

where τ_D is the natural lifetime of the donor and R_0 the critical transfer distance between donor and acceptor. Exciton diffusion correlates to several energy transfer processes, which can be considered as a random hopping-like motion along different directions. Therefore, the effective distance, also named diffusion length, is significantly smaller than the sum of all moved distances. The diffusion length l_d can be calculated by the formula:

$$l_d = \sqrt{ZD\tau_D} \tag{2.23}$$

where Z is a parameter, which describes the dimensionality of the diffusion, D is the diffusion coefficient, and τ_D is lifetime of the exciton. l_d depends on the material, the sample preparation, the crystallinity, etc. For example, the diffusion length of P3HT was reported from 4 nm to 12 nm [33, 34], while a larger diffusion length of around 40 nm was found for the thin films of C_{60} fullerene [35].

2.3.4 Exciton dissociation

Exciton dissociation occurs when an exciton diffuses to an interface between electron donor and electron acceptor materials. In theory, excitons can be generated both in donor and acceptor materials. However, for the P3HT:PCBM system the excitation in P3HT is dominant. Because the light absorption of P3HT is in the visible spectrum, while PCBM mainly absorbs light in UV range that only has a small overlap with the solar spectrum. Therefore, in the following parts P3HT is assumed as donor material and PCBM as acceptor material.

When the exciton arrives at an interface, exciton dissociation takes place. It is a very fast process as compared to some decay processes, around 10 fs for the P3HT:PCBM system [36]. Two types of exciton dissociation are known. One is direct charge transfer and the other one is the charge transfer following an initial energy transfer. After charge transfer, no matter which type occurs, positive and negative charge carriers reside within donor and acceptor materials, respectively. In this case, a charge carrier refers to a polaron which consists of a charge and the caused polarization of the surroundings. These two polarons are still Coulomb bound rather than free polarons. Therefore, this polaron pair needs to be separated eventually, in order to obtain free charges. The Braun-Onsager model describes the separation of a polaron pair, which considers the possibilities of polaron dissociation with a rate k_d, the recombination to the ground state with a rate k_f, and a chance of free polarons forming a polaron pair again with a rate k_r [37, 38]. A brief illustration for the Braun-Onsager model is shown in figure 2.16.

Polaron separation yield $P(F)$ can be expressed by the formula below:

$$P(F) = \frac{\kappa_d(F)}{\kappa_d(F) + (\mu\tau_f)^{-1}} \tag{2.24}$$

where $\kappa_d(F)$ can be calculated by $k_d(F)/\mu$. μ is electron charge carrier mobility. τ_f is polaron pair lifetime, following the relationship with k_f ($k_f \propto \tau_f^{-1}$). Therefore, polaron separation yield depends strongly on the electron charge carrier mobility and polaron pair lifetime [3].

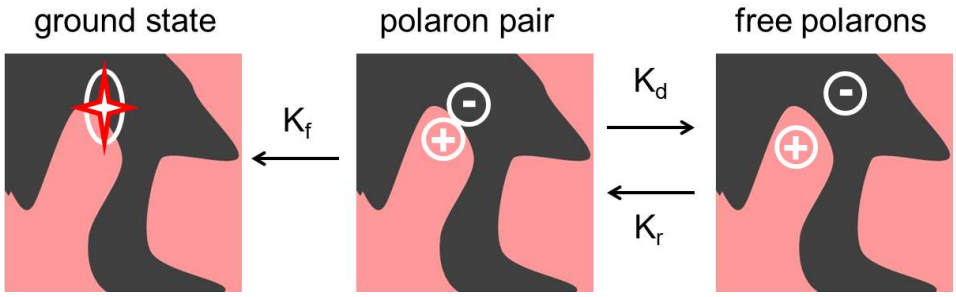

Figure 2.16: *Illustration for Braun-Onsager model, describing the polaron dissociation with a rate k_d, the recombination to the ground state with a rate k_f, and the chance of free polarons forming a polaron pair with a rate k_r.*

2.3.5 Charge transport

After exciton dissociation, charge carriers (polarons) need to be transported to the corresponding electrodes. As introduced in section 2.1.1, the polarons can move freely along the chain backbone in a conjugated polymer. However, charge transport between chains is also of great importance since most polymer chains are not directly connected to the electrode. Conducting polymers are spatially and energetically disordered, therefore, interchain charge transport mainly occurs by the so-called hopping process, which can be understood by the combination of tunneling from one localized state to the next, and thermal activation. Tunneling happens in case the wavefunctions of the two states overlap weakly.

Figure 2.17 schematically presents the concept of hopping transport. A Gaussian distribution is used to describe the energetic disorder of density of state, indicated by the purple curve in figure 2.17. Its width σ is also called disorder parameter. Thermal activation energy $-\sigma^2/k_BT$ for the charge density defines the transport energy, as indicated by the black dashed line. A charge carrier is generated at an exited state and then transports towards the states with low energy via relaxation. For the states located near transport energy, charge carrier either hops from one state to another via thermal activation, or continuously relaxes down to a trap state. Generally the charge carrier mobility of polymers is much less than metals. Moreover, the charge carrier mobility of polymers depends strongly on the crystallinity. For example, the hole mobility of crystal P3HT is around 10^{-1} cm^2/Vs and for amorphous P3HT is less than 10^{-3} cm^2/Vs [39].

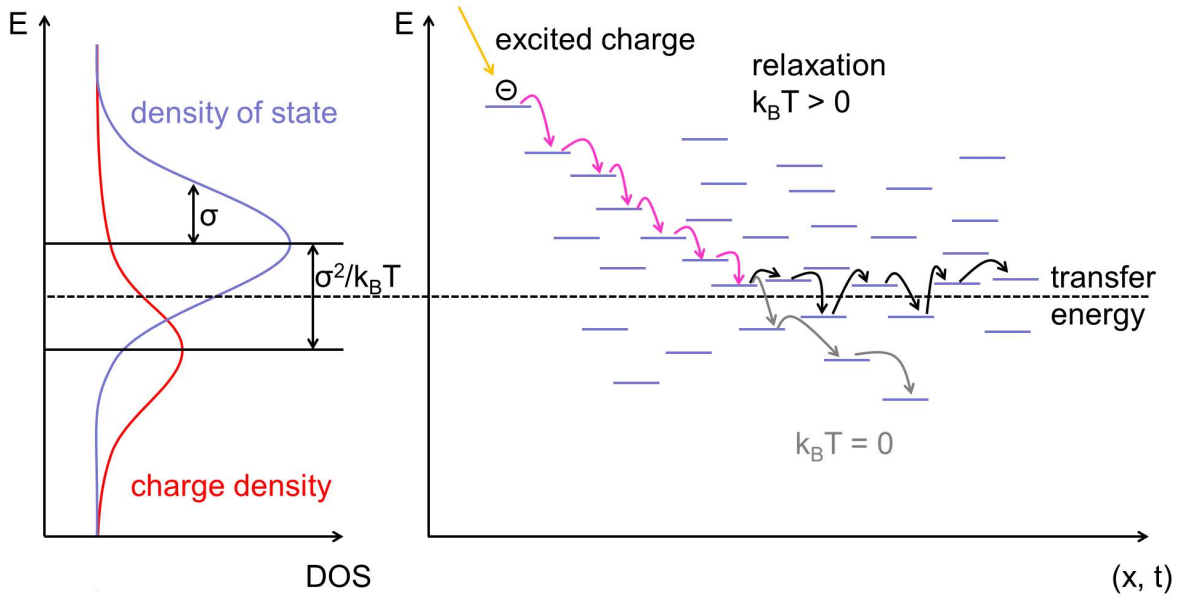

Figure 2.17: *Schematic presentation of the concept of hopping transport. Density of states are indicated by purple lines, which follows a Gaussian distribution (purple) with width σ. The red line represents charge density, which is also described by Gaussian function. The exited charge relaxes to a quasi-equilibrium (magenta arrows), and then either hops along the transfer energy with thermal activation (black arrows) or continuously relaxes down to a trap state (grey arrows).*

2.3.6 Charge extraction

When the charge carriers reach the interface between the active layer and the electrode, they have to be extracted by the corresponding electrode. The charge extraction rate is strongly influenced by the charge carrier accumulation at the interface, the device architecture, and the energy levels of the device. Deposition of interlayers which block charge carriers traveling to a wrong electrode is of great importance. This prevents non-geminate recombination of holes and electrons at the polymer-electrode interface, and optimizes the energy level alignment. Taking an inverted P3HT:PCBM as an example, a TiO_2 layer works as a hole blocking layer, which is deposited onto the FTO bottom electrode, and PEDOT:PSS is employed as an electron blocking layer, which is cast on top of the active layer and beneath the adjacent gold top electrode.

So far, the most applied model accounting for the extracted photocurrent J_{ph} is the combination between the Braun-Onsager model and the Sokel and Huges model, and is expressed by the formula:

$$J_{ph} = qP(F)G_{pp}L\left(\frac{exp(qV/kT)+1}{exp(qV/kT)-1} - \frac{2kT}{q}\right) \tag{2.25}$$

where q is the elementary charge, $P(F)$ is the polaron dissociation yield as discussed in section 2.3.4, G_{pp} is the generation rate of polaron pairs, L is the thickness, V indicates internal voltage, and kT/q denotes thermal voltage. The first factor is derived from the Braun-Onsager model, which depicts the field-dependence of charge carrier generation, while the second factor is evolved from Sokel and Huges model, depicting the voltage dependence [3].

2.3.7 Loss mechanisms

The basics of single processes in an organic solar cell have been explained in previous sessions. However, the final electricity generation is constrained by loss mechanisms. In general, loss mechanisms include losses of excitons and free charge carriers. It can be subdivided into different loss mechanisms (1-5) as depicted in figure 2.18.

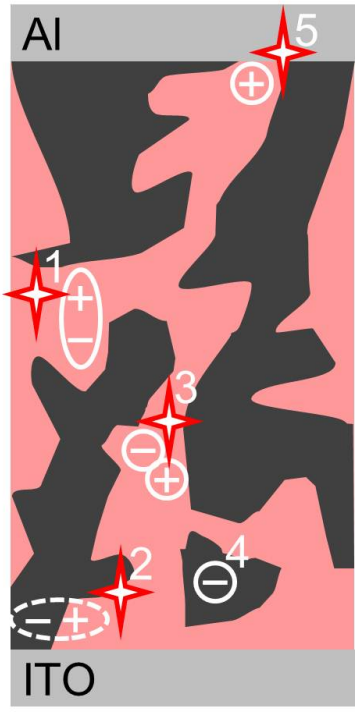

Figure 2.18: *Illustration of the possible loss mechanisms as depicted from 1 to 5. The full sketch refers to an organic BHJ solar cell, where pink color indicates the donor and black color for the acceptor material. Possible recombinations are denoted by red stars. Detailed descriptions of processes from 1 to 5 are presented in text.*

For an exciton, if it does not reach a donor-acceptor interface within the lifetime τ_f, recombination would occur as depicted in process 1 in figure 2.18. As mentioned before (section 2.3.3), the lifetime and the diffusion length of the exciton depends strongly on the type of exciton and the material. For P3HT the lifetime of a singlet exciton is several hundreds of picoseconds while the lifetime of a triplet exciton is tens of microseconds [40, 41]. If an exciton arrives at a donor-acceptor interface, recombination of polarons could also occur. As introduced in section 2.3.4, before an exciton is dissociated into completely free polarons, formation of a Coulomb bound polaron pair is the intermediate step [3]. The so-called geminate recombination of this Coulomb bound polaron pair is possible (process 2 in figure 2.18), for example in the case of a low charge charrier mobility or a very short polaron pair lifetime. On the other hand, two already separated polarons could also recombine, which is named a non-geminate recombination and is shown in figure 2.18 process 3. Briefly, the word non-geminate refers to the separated polarons that do not belong to the common exciton precursor. Another probable recombination is caused by the trapped polaron that is either in a deep energetic state or in a defect. The example is shown as process 4 in figure 2.18. The island-like structure has no connection with either of the electrodes and therefore, this polaron recombines with an oppositely-charged free polaron. Finally, if the polaron migrates to the wrong electrode as demonstrated in process 5 in figure 2.18, it will be recombined at the donor-cathode or acceptor-anode interface.

All loss mechanisms affect solar cell performance. Many methods have been proposed to reduce recombinations in organic solar cells. For example, by incorporating metal nanoparticles in active layer, the lifetime of excitons can be prolonged and accordingly the recombination directly from exciton would be restrained [41]. In addition, an interdigitate heterojunction can effectively lower the recombination caused by the trapped polarons at the island-like defects [42].

2.4 Scattering methods

In addition to real space measurements such as AFM and SEM, scattering methods using X-rays or neutrons are employed to characterize the inner morphology of the samples with a resolution ranging from a few to hundreds of nanometers. One of the biggest advantages of scattering techniques is the high statistical relevance as compared to real space measurements. In the following part, the basic principles of scattering techniques are introduced in section 2.4.1, then detailed explanation of grazing incidence small angle X-ray (or neutron) scattering (section 2.4.2) and X-ray diffraction in particular in a grazing incidence geometry (section 2.4.3) are presented.

2.4.1 Principles

X-rays are imagined as a plane electromagnetic wave which impinges on a medium. The electric field vector $\vec{E}(\vec{r})$ can be described via the Helmholtz equation [43]

$$\Delta\vec{E}(\vec{r}) + k^2 n^2(\vec{r}) E(\vec{r}) = 0 \tag{2.26}$$

where $\vec{r}$ is the position of the wave vector $\vec{k}$ of the electromagnetic wave. $k = 2\pi/\lambda$ is the modulus of $\vec{k}$. λ indicates X-ray wavelength. n is the refractive index of the investigated material, and given by the formula

$$n = 1 - \delta(\vec{r}) + i\beta(\vec{r}) \tag{2.27}$$

with δ representing the dispersive part and β the absorbing part. Both parameters depend on wavelength λ of X-rays and can be given by

$$\delta = \rho_e r_e \frac{\lambda^2}{2\pi} = \rho\frac{\lambda^2}{2\pi} \tag{2.28}$$

$$\beta = \mu\frac{\lambda}{4\pi} \tag{2.29}$$

where r_e is the classical electron radius equal to $2.814 \cdot 10^{-5}$ Å and ρ_e the electron density of the investigated material. ρ is the scattering length density (SLD), and μ is the absorption coefficient. SLD represents the scattering power of a material, which depends on the material's density and the electron density of the elements in it. Generally, the dispersive part δ is in the range from 10^{-5} to 10^{-6} and therefore, the refractive index for X-rays is only slightly smaller than 1. In the case of a film composed by two materials, the contrast of scattering originates from the difference in SLD between them.

For thin films, the scattering signal is quite low in the traditional transmission experiment, because very little material is in the beam path. To compensate for this issue, incident angle α_i, as illustrated in figure 2.19, is typically chosen below 1°, resulting in a large footprint on the sample and accordingly, reasonable scattering signal is emanated. This geometry is called grazing incidence geometry, which is schematically illustrated in figure 2.19. The incident X-ray $\vec{k_i}$ impinges on the sample with the angle α_i, and then is scattered under an exit angle α_f with an out of plane angle ψ. In order to record the scattering signal, a two-dimensional (2D) detector is typically used. When the exit angle α_f is equal to the incident angle α_i, specular reflection occurs. The scattering wave vector $\vec{q}$ is the momentum transfer from incident beam to exit beam, defined by

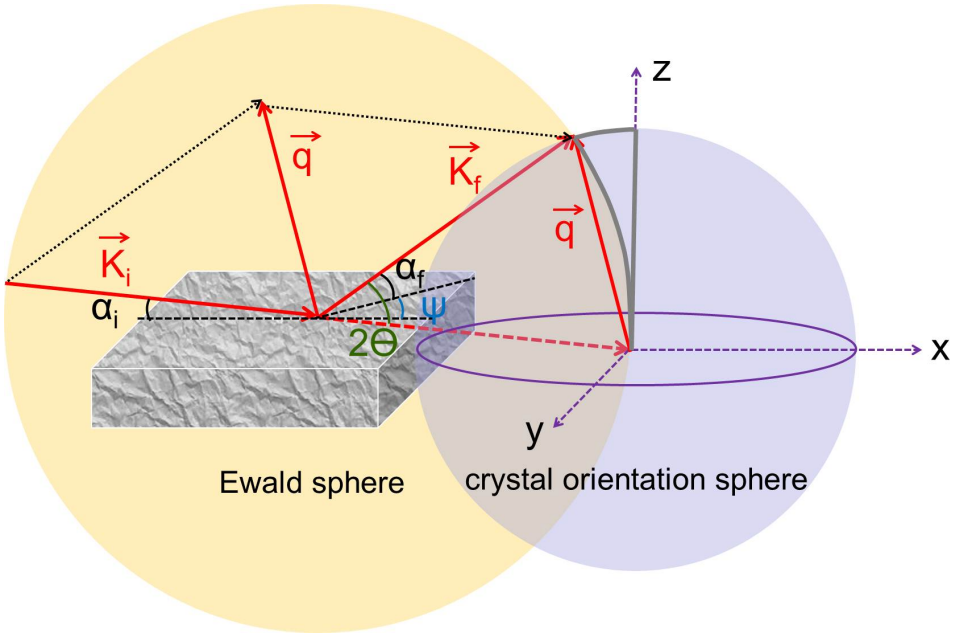

Figure 2.19: *Schematic geometry of diffuse scattering with incident angle α_i, exit angle α_f, out of plane angle ψ, and solid angle 2Θ. The distortion of 2D GIWAXS pattern originates from the intersection of the Ewald sphere (yellow) and the crystal orientation sphere (lilac).*

$$\vec{q} = \vec{q}(x, y, z) = \vec{k_f} - \vec{k_i} \tag{2.30}$$

Since grazing incidence small angle scattering (GISAXS) is an elastic scattering experiment, the scattering wave vector $\vec{q}$ only counts the change in direction of the beam rather than the energy exchange. Its components can be represented by the formulae

$$\vec{q_x} = \frac{2\pi}{\lambda}[\cos(\alpha_f)\cos(\psi) - \cos(\alpha_i)] \tag{2.31}$$

$$\vec{q_y} = \frac{2\pi}{\lambda}[\cos(\alpha_f)\sin(\psi)] \tag{2.32}$$

$$\vec{q_z} = \frac{2\pi}{\lambda}[\sin(\alpha_f) + \sin(\alpha_i)] \tag{2.33}$$

A total reflection occurs when the incident angle α_i is lower than the critical angle α_c. Neglecting absorption effects, α_c as given by

$$\alpha_c \approx \sqrt{2\delta} = \lambda\sqrt{\frac{\rho}{\pi}} \tag{2.34}$$

Diffuse scattering occurs from the rough interfaces and also from lateral structures. The most pronounced diffuse scattering is located at the position of the critical angle, which is called Yoneda peak [44]. In terms of total reflection, evanescent X-rays can still penetrate the sample to a certain depth. The depth where the intensity of the wave declines to $1/e$ of its original intensity is defined as penetration depth. Moreover, considering the damping of the scattered waves on the way out of the sample, the concept of escape depth is proposed. Generally, the real scattering depth is correlated to both penetration depth and escape depth, which is considered as approximately half of the penetration depth [45]. By selecting the incident angle below α_c, the scattering depth is around several nanometers and therefore, the diffuse scattering is surface sensitive. Whereas for the incident angle above α_c, the waves can penetrate the whole sample (i.e. several hundreds of nanometers) and the obtained scattering results are bulk sensitive.

2.4.2 Grazing incidence small angle X-ray (or neutron) scattering

For characterization on nanostructures at surface or in bulk, grazing incidence small angle X-ray (or neutron) scattering (GISAXS or GISANS) is a powerful technique. The diffuse scattering is commonly treated within the framework of the distorted wave Born approximation (DWBA), considering the scattering as a perturbation of an ideal system for example a smooth single layer. The interface roughness and lateral structures are treated as perturbations and therefore, the differential cross section is given by the formula:

$$\frac{d\sigma}{d\Omega} = \frac{A\pi^2}{\lambda^4}(1-n^2)^2 \mid T_i \mid^2 \mid T_f \mid^2 P_{diff}(\vec{q}) \propto P_{diff}(\vec{q}) \tag{2.35}$$

where A is the illuminated area, $T_{i,f}$ are the respective Fresnel transmission coefficients, and $P_{diff}(\vec{q})$ is the diffuse scattering factor which accounts directly for the scattered intensity. When the α_i (or α_f) is equal to the critical angle of the probed material, the Fresnel transmission coefficients have the maximum value. This maximum value is material sensitive and correlated to the Yoneda peak in the 2D GISAXS data. Nevertheless, $T_{i,f}$ act only as an overall scaling factor and therefore, the scattered intensity is proportional to the diffuse scattering factor $P_{diff}(\vec{q})$. In terms of N identical and centrosymmetric objects without preferred orientation, the diffuse scattering factor $P_{diff}(\vec{q})$ can be described by the form factor of each object $F(\vec{q})$ and the structure factor $S(\vec{q})$:

$$P_{diff}(\vec{q}) \propto NS(\vec{q})F(\vec{q}) \tag{2.36}$$

This approximation is used to analyze lateral structures of the sample. Therefore, instead of the whole 2D GISAXS (or GISANS) data, a horizontal line cut is extracted at the position of the Yoneda peak of the investigated material. The diffuse scattering is usually treated within the framework of DWBA, which includes the different modes of reflection and scattering [46]. The form factor $F(\vec{q})$ refers to the Fourier transformation of the shape of object [47]. Typical object shapes include cylinder, cone, sphere, and ellipsoid. In most sample systems, a cylinder form factor is most common due to the rotational isotropy of the film. A one-dimensional paracrystalline lattice (1DDL) accounts for the spatial distribution of objects, which is described by the structure factor $S(\vec{q})$. Paracrystalline lattice represents a local short-range-ordered structure. With increasing crystal neighbour order, the deviation of the theoretical position rises and therefore, the higher orders are strongly damped out. This behavior is quite common for nanostructured polymer thin films [48]. In a 1DDL, the arrangement of the objects is independent on the orientation within the crystal, meaning that the system is invariant when it is rotated.

Generally, diffuse scattering of nanostructured films is determined by the size and shape of form factors and the structure factors. In this work, local monodisperse approximation (LMA) is applied. With this approximation, each object scatters with the same-sized objects most powerfully and does not interact with objects with different sizes. Individual form factors and structure factors follow a Gaussian distribution. Finally, the overall scattered intensity can be obtained by the sum of the intensities obtained from all these objects [49].

2.4.3 X-ray diffraction

Generally, X-ray diffraction is a powerful tool to probe the crystalline structures also for thin films and with increased surface sensitivity. In principle, the atoms in a crystal lattice can be considered as periodic gratings for X-rays. The incoming X-rays are scattered by the lattice planes and then travel out of the lattice. Afterwards, exit waves interfere and form a scattering pattern. According to the scattering information, the type of the material and its specific crystalline phase can be identified. If the lattice planes fulfill Bragg equation as graphically illustrated in figure 2.20, the lattice spacing d_{hkl} can be obtained by [49]

$$d_{hkl} = \frac{n\lambda}{2\sin(\theta)} \tag{2.37}$$

The corresponding average crystal size D_{hkl} can be estimated from the width of Bragg peak by the Scherrer equation

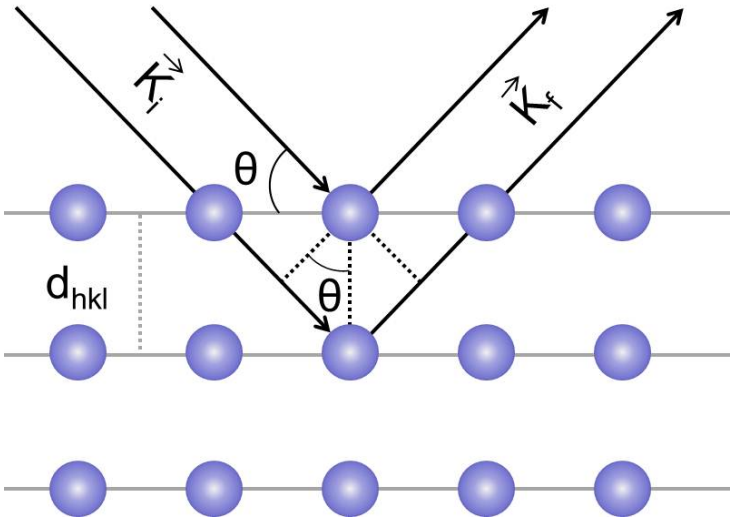

Figure 2.20: *Bragg equation is graphically illustrated. The positions of atoms are represented by blue spheres, which constitute the lattice planes. The incoming X-ray beam $\vec{k_i}$ impinges on the lattice planes and are scattered out as illustrated by $\vec{k_f}$. The spacing between adjacent lattice planes is denoted as d_{hkl} and the incident angle is labeled as θ.*

$$D_{hkl} = \frac{K\lambda}{\Delta(2\theta)\cos(\theta_0)} \tag{2.38}$$

where K is the Scherrer form factor, often assumed to be 0.9 - 1. $\Delta(2\theta)$ is the full width half maximum (FWHM) of the Bragg peak located at the positon of 2θ. In terms of $\vec{q}$, the Scherrer equation can also be represented by

$$D_{hkl} = \frac{2\pi}{\Delta q_{hkl}} \tag{2.39}$$

where Δq_{hkl} is the integral line width, equal to $FWHM$ of the Bragg peak at the position of q. However, for conjugated polymers, the crystal size cannot be accurately calculated by Scherrer equation. Rivnay et al. reported that paracrystalline order strongly affects the width of the Bragg peak, which are quite common in $\pi-\pi$ stacked polymers [50]. Decoupling the contributions from crystal size and paracrystallinity is one method, which needs to detect several higher order peaks. However, for most conjugated polymer films, only the first order of the $\pi-\pi$ stacking Bragg peak can be detectable and the scattering intensity is quite low. In addition, the resolution of the setup broadens the Bragg peaks. For instance, Oesinghaus found that a larger slit size increased the scattering intensity and significantly broadened the peak [51]. Therefore, only rough estimations of the coherence length and the qualitative comparison between samples are accessible.

Grazing incidence wide angle X-ray scattering

Grazing incidence wide angle X-ray scattering (GIWAXS) can be considered as a similar technique to GISAXS but recording wide scattering angles. Therefore, the setup is the same as the one used for GISAXS, except for the much shorter sample-detector distance. One of the biggest advantages of GIWAXS is that the preferred orientation of the crystals inside the film is accessible. For organic photovoltaics, understanding of the crystalline orientation is significant. For example, in terms of P3HT, a face-on dominated crystalline orientation is preferred, which refers that the π plane stacks along the film normal direction. Such a crystalline orientation facilitates charge carriers transport towards the corresponding electrode.

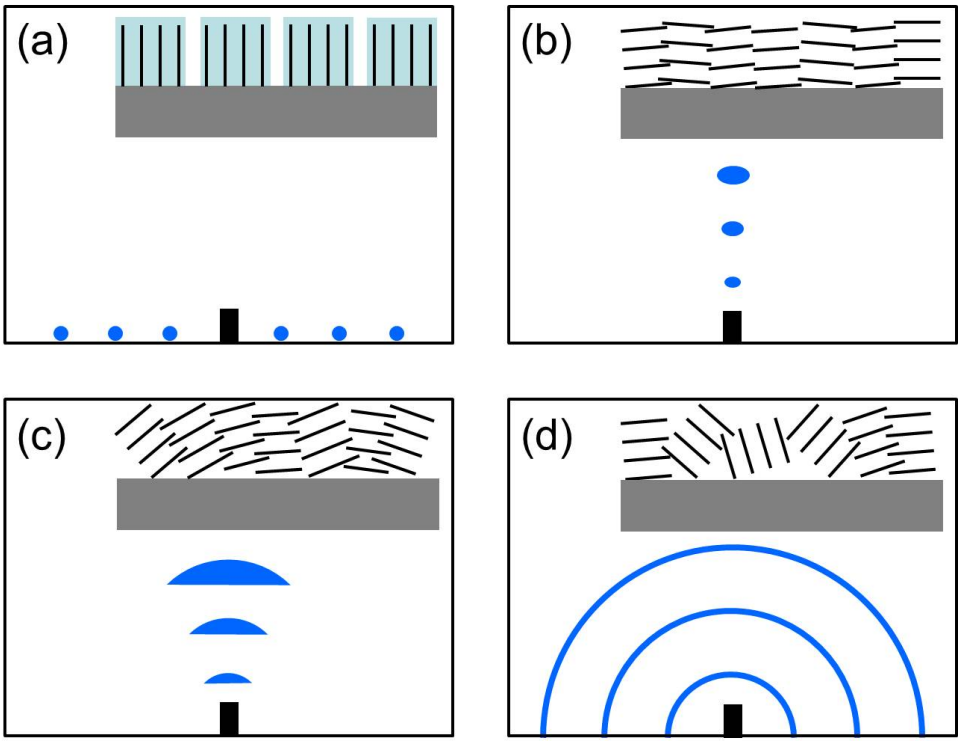

Figure 2.21: *Sketches of different lamellar stackings in films with their corresponding 2D GIWAXS data in terms of (a) ideally vertical lamellar stacking, (b) slightly and (c) strongly disordered horizontal lamellar stacking, and (d) stacking without any preferential crystalline orientation. The turquoise backgrounds in (a) are guide to the eyes for each of the lamellar stacks.*

For an easy understanding, the ideal case of vertical lamellar stacking is illustrated with its resulting GIWAXS pattern in figure 2.21a. If the film is highly crystalline and with all crystal planes aligned in direction perpendicular to the substrate surface, accordingly well-defined Bragg peaks appear on the 2D detector only in vertical direction, as illustrated in

figure 2.21a. However, most polymer thin films do not have ideally aligned crystals and therefore, in its GIWAXS pattern the Bragg peaks are broadened. Taking the slightly and strongly disordered horizontal lamellar stackings as examples, their corresponding GIWAXS patterns are illustrated in figure 2.21b and 2.21c, respectively. In case of powder-like films without any preferential crystalline orientation, instead of Bragg peaks, so-called Debye-Scherrer-like rings are observed (figure 2.21d) [52].

Concerning GIWAXS pattern recorded on a 2D detector, the image is distorted because the area detector does not directly represent the information in reciprocal space. Moreover, the contribution from q_x is nonnegligible in GIWAXS measurements, especially for large exit angle (illustrated in figure 2.19). Therefore, 2D GIWAXS pattern needs to be reconstructed into the natural reciprocal space coordinates [53, 54], assigned to (q_{xy}, q_z). q_{xy} can be calculated by

$$q_{xy} = \sqrt{{q_x}^2 + {q_y}^2} \tag{2.40}$$

At a first step, a flat field correction is done via the calibration file provided by the company of the used detector, which deals with the difference in sensitivity of the individual pixel in the detector. Afterwards, the absorption efficiency has to be corrected for the attenuation of the beam intensity caused by different path lengths through the medium between the sample and detector (represented by E_m) and within individual pixels of the detector at small and large angles (represented by E_d). They can be calculated by

$$E_m = \frac{1}{1 - exp(\mu_m SDD/\cos 2\Theta_i)} \tag{2.41}$$

$$E_d = \frac{1}{1 - exp(-\mu_d t_d/\cos 2\Theta_i)} \tag{2.42}$$

where μ_m and μ_d represent the absorption attenuation coefficients of the medium and the detector, respectively. t_d describes the thickness of a pixel in the detector. In brief, increasing the solid angle $2\Theta_i$ (illustrated in figure 2.19) induces an increase of attenuation in the path and of absorption by the detector pixels.

In addition, a solid angle correction, accounting for the difference in solid angle relative to the beam, is done by the equation:

$$C_s = \frac{\Omega_0}{\Omega_i} = \cos^{-3}(2\Theta_i) \tag{2.43}$$

Ω_0 and Ω_i denote the solid angle subtended under the direct beam and under the solid angle $2\Theta_i$.

Furthermore, since the synchrotron radiation is almost horizontally polarized, scattering intensity shows an angular dependence on the detector. Polarization correction can be done by [55]

$$C_p = p_h(1 - \cos^2 \alpha_f \sin^2 \psi) + (1 - p_h)(1 - \sin^2 \alpha_f) \tag{2.44}$$

where p_h is the fraction of the radiation polarized in horizontal direction, in terms of synchrotron, p_h approximating 98%. α_f and ψ are the exit angle and out of plane angle, as labeled in figure 2.19.

In total, all correction factors are multiplied with the raw data [51, 53, 54]:

$$reconstruction = raw\ data \cdot flat\ field \cdot \frac{1}{C_p} \cdot \frac{E_m E_d}{max(E_m E_d)} \cdot C_s \tag{2.45}$$

Examples of the 2D GIWAXS data as recorded on the 2D detector and after reconstruction are shown in figure 2.22a and 2.22b. The reshaped 2D GIWAXS data exhibits a missing wedge as denoted by the red curves in figure 2.22b, which is an inaccessible q space under a fixed incident angle with the grazing incidence geometry. As indicated in figure 2.19, a region (highlighted by grey lines in crystal orientation sphere) located at the crystal orientation sphere does not interact with the Ewald sphere. Since the Ewald sphere describes all the possibly detectable scattering events and therefore, this q range ($q_{xy} = 0$) is not accessible. Briefly, the missing wedge in figure 2.22b can be correlated to the wedge indicated by grey lines in figure 2.19. One solution proposed by Baker and coworkers for constructing the missing wedge is to perform a series so-called "local-specular" scans near the angle for Bragg diffraction conditions [55].

2.5 Mechanical properties

Generally, photovoltaic devices are assembled by several layers. The mechanical stability of each thin layer plays an important role in maintaining the performance of the whole device. In order to understand the mechanical stability of thin films, the elastic behavior, and the material failure properties are of importance. Moreover, the deformation mechanisms are different between bulk and thin films. For material failure, crack initiations are dominant in bulk materials, while crack propagations are more common in thin films [56]. In this thesis, the mechanical properties are not measured directly since they are difficult to probe in thin films. However, according to the types of thin films, different models are applied to derive corresponding elastic parameters of the thin films from their bulk

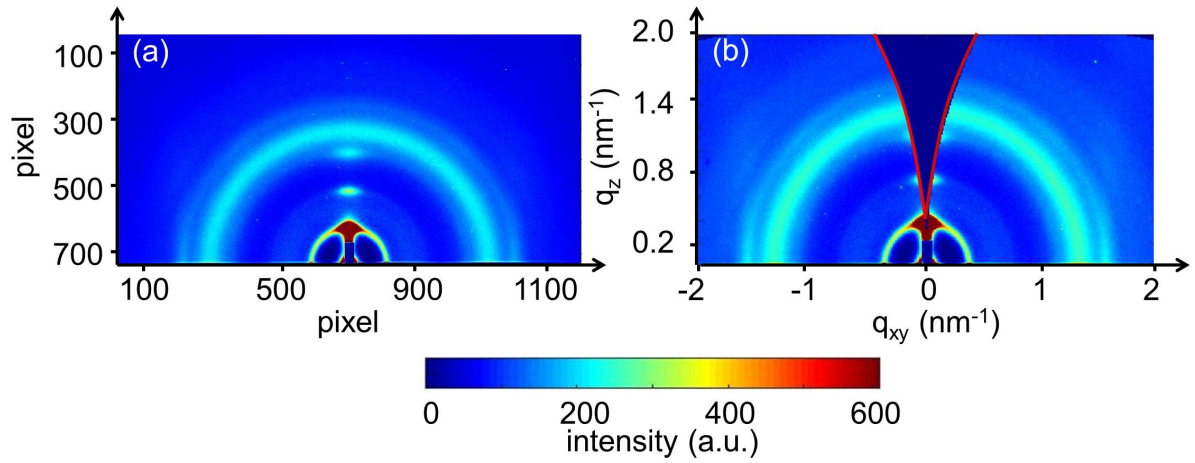

Figure 2.22: *(a) 2D GIWAXS data of P3HT:PCBM film directly recorded on the detector in pixels. (b) Reconstructed 2D GIWAXS data as a function of q_{xy} and q_z, with inaccessible q range denoted by the red curves.*

counterparts. Furthermore, the responses of a thin film to a cyclical bending are examined and studied.

The probing method for titania-based thin film is introduced in section 2.5.1. Afterwards, in section 2.5.2 the bending of titania-based films is first described, and then different models are compared and descried according to the investigated titania-based films.

2.5.1 Probing method for titania-based thin film

Bending tests are widely used to characterize the mechanical stability of thin films, such as flexural strength and material fatigue. Three point bending test and two point bending test are common methods. Their sketches are shown in figure 2.23. Three point bending test (figure 2.23a) is normally used for large objects, for example wooden beams and steel rods. The specimen is placed on two supporting pins with a third load pin in its center. With this design, the sample surface is frequently contacted by the load pin. Moreover, in this contact region, shear forces are formed in the film. In order to avoid the invasive influence from three point bending design, two point bending setup is employed to investigate the mechanical properties of thin films in this thesis. As illustrated in the sketch shown in figure 2.23b, the sample is fixed between two blades. One blade is fixed and the other blade can be move horizontally, which allows the film to bend. With this method, the stress can be uniformly loaded along entire sample without any contacts on

the sample surface. The stress generated from bending can be either tensile stress (on the convex surface) or compressive stress (on the concave surface).

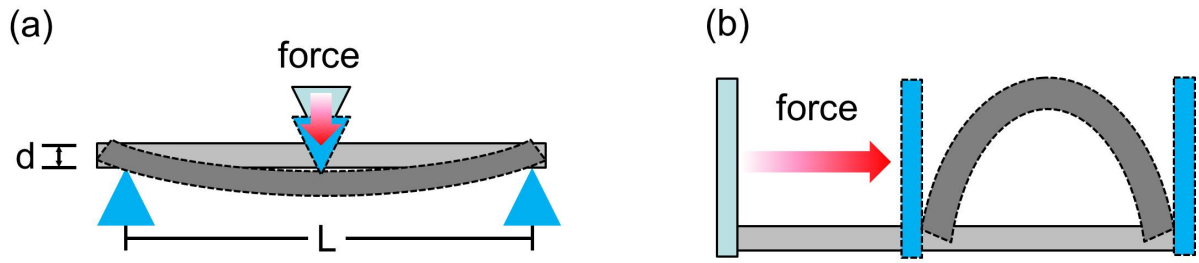

Figure 2.23: *Sketches of (a) three point bending setup and (b) two point bending setup.*

Theoretical aspects

The mathematical framework for strength measurements with two point bending setup was first described by John Matthewson et al. for glass fibers [57]. Later on, Gulati et al. promoted this method for thin glass sheets [58]. The method from Gulati et al. is used to determine the maximal strain and stress of the titania-based thin films in this thesis. The sketch of an ideal two point bending measurement at the strongest bending state is shown in figure 2.24a. The stress σ along the convex surface can be obtained from the equation [57]

$$\sigma = \sigma_{max}\sqrt{(\sin(\theta))} \tag{2.46}$$

with

$$\sigma_{max} = 1.198E\frac{d}{L} \tag{2.47}$$

where σ_{max} denotes the maximal stress at the center of the film. All the SEM measurements for characterization of materials failure are performed at this position. E is the elastic modulus of the film. d is the thickness of the investigated sample and L is the distance between two blades when the maximal strain is induced in the sample. All the parameters are labeled in figure 2.24a. The elastic modulus can be calculated by

$$E = \frac{\sigma}{\varepsilon} \tag{2.48}$$

where ε is strain in the film. Therefore, the maximal strain on the film can be derived from above equations:

$$\varepsilon_{max} = 1.198\frac{d}{L} \tag{2.49}$$

since the film thickness of the PET substrate is three orders of magnitude higher than the titania-based film, the d is approximated to the film thickness of PET. However, an additional factor should be included in above equation, since the sample is not fully in contact with the blades [58]. The adapted formula is

$$\varepsilon_{max} = \frac{1.198d}{L\sqrt{\cos\psi}} \tag{2.50}$$

with ψ equal to the angle between the end of the sample and the blade, as labeled in figure 2.24b.

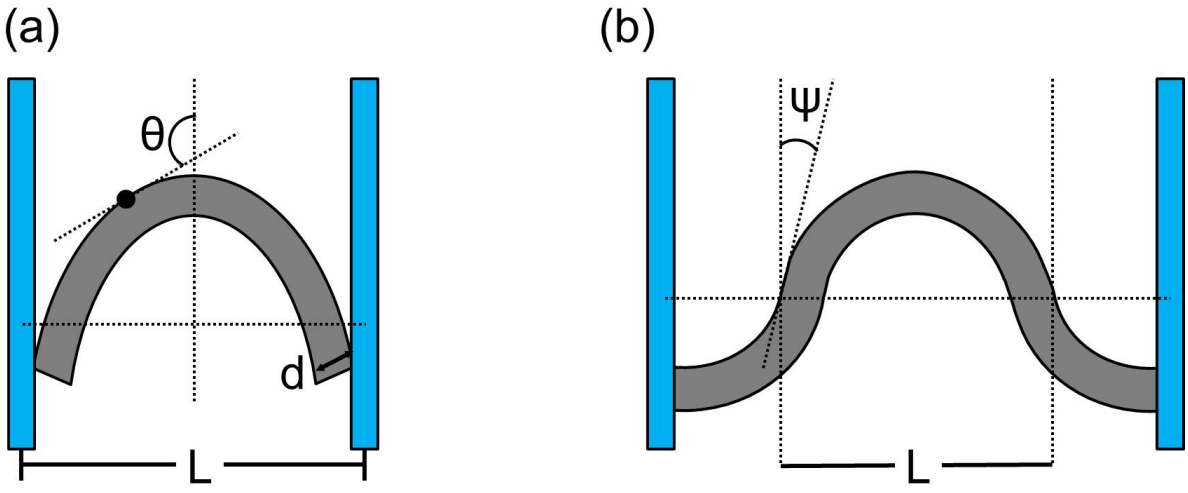

Figure 2.24: *Sketches of (a) ideal two point bending measurement at the strongest bending. The distance between two blades is L and sample thickness is d. θ refers to the angle between the vertical and tangent lines at the position denoted by a black dot. (b) The sketch of a real measurement, with two ends of the sample clamped on a stage. ψ counts for the angle between the vertical and the tangent of the point with zero curvature.*

The sketch of two point bending in the present thesis (figure 2.24b) is slightly different from the one described by Gulati et al.. In order to prevent any slips of the sample during cyclic bends, the sample is clamped by two blocks at its edges. The position for determining angle ψ is located at the point with zero curvature, as labeled in figure 2.24b. Furthermore, L is determined as the distance between the two points, which have zero curvature. The formulae for strain and stress are still applicable to this measurement, especially for analyzing the maximal strain and stress.

Failure mechanisms

Mechanical properties are strongly influenced by film thickness. In theory, sufficient thin films of any materials are flexible, since the bending strain declines with reducing film thickness [59]. In addition, the film elastic modulus and the adhesion to the substrates play an important role in the mechanical characteristics, which are closely correlated to the surface strain, interfacial shear stress, and interfacial normal stress when the samples are subjected to two point bending tests.

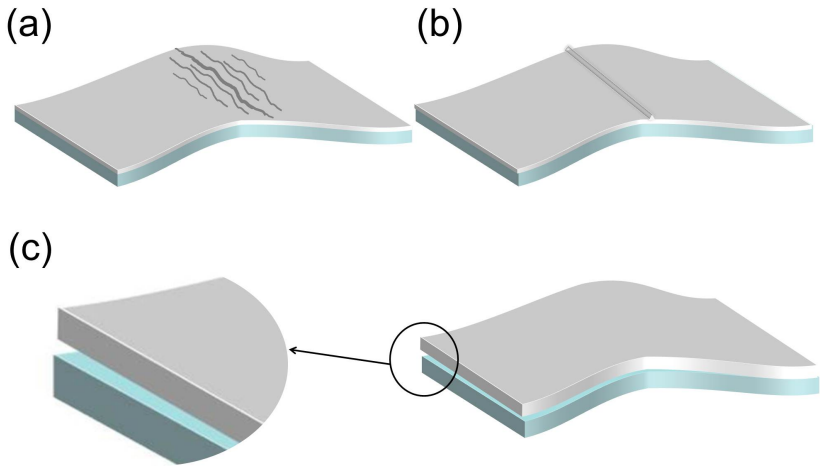

Figure 2.25: *Sketches of different failure modes. When the film is overloaded under bending condition, (a) cracks may form in the sample, (b) the film slips along the substrate to form buckles, or (c) the film delaminates from the substrate with its zoom-in image, especially in the case of thick film.*

Two main categories of failure modes are schematically illustrated in figure 2.25 [60]. The first case corresponds to the formation of cracks as illustrated in figure 2.25a, which is the mostly common type of failure for a thin film under cyclic tension. When the applied stress is over a certain threshold, the strain is concentrated in several positions such as persistent slip bands, defects, boundaries, and surface, where the cracks initiate and then some of them develope into micro cracks with cyclic bending [61, 62]. Thereafter, the micro cracks continuously spread with deepening and broadening until certain sizes of the cracks are reached. Finally, the cracks propagate quickly along the sample surface and the film fractures. On the other hand, if the stress for crack formation is larger than the adhesion between the film and substrate, the film slips along the substrate to release the stress inside it. When the stress is unloaded, the substrate returns to its original shape, however the sample often does not slip back to its previous location on the substrate. Consequently, the film buckles and forms ripple-like structures (figure 2.25b). In the case

of thick film, delamination mostly happens (figure 2.25c), which is mainly driven by the interface-normal stresses.

In addition to the innate properties of the sample as discussed above, other factors can be taken into account for contracting the failure behaviors. Examples range from the small sample dimension that leads to more robust bending properties, to additional mechanical plane layout that could further enhance the pliability [60].

2.5.2 Micromechanical models

When a solid bulk sample is converted into a thin film with nanostructures, the innate properties such as stiffness, strength, optical performance, and electrical conductivity are changed [63]. Direct measurements for certain parameters like the optical performance and electrical conductivity are available, however characterizations for mechanical characteristics like elastic modulus of the nanostructured thin film face certain challenges. Therefore, according to the type of thin films, an applicable micromechanical model is selected to estimate their mechanical properties. In this section, the open-cell foam model for cellular solid and Halpin-Tsai model for composite film are introduced, which model the porous titania film and titania-based hybrid film, respectively.

Open-cell foam model

The nanoporous titania is considered as a cellular solid, which can be described by a lattice with a certain unit cell. In order to understand the mechanical performance of the cellular film, three main factors are necessary. The first dominant parameters are the innate properties of the solid material, of which the cellular sample is made. For example, the elastic modulus of the bulk titania is of great importance for the final elastic modulus of a porous titania film. Then, determination of the appropriate model to describe the topology and the shape of the network structure. There are different lattice types for modelling the cellular solid, such as the woven structure, the pyramidal lattices, and the foams [63]. In the present thesis, following the nanostructure of the porous titania layer as illustrated by an SEM image (figure 2.26a), an open-cell foam model is selected with the sketch of its unit cell shown in figure 2.26b. In general, the lattice can be described by the struts which are connected at nodes and accordingly, the network is formed. For the open-cell foam model, the deformation of the sample is usually considered to be bending-dominated [64]. Lastly, the relative density of the cell, meaning the density difference between the solid and foam-like nanostructured sample, plays an important role for the mechanical properties of the cellular film. For the open-cell foam model, the relative

density is determined by cell edge length L and the cell wall thickness t ($t < L$) (labeled in figure 2.26b), described by the formula:

$$\frac{\rho}{\rho_s} \propto \left(\frac{t}{L}\right)^2 \tag{2.51}$$

where ρ and ρ_s are the density of the foam and solid materials, respectively. For the uniform porous structures, the relative density can also be obtained via the porosity Θ of the film, as described by:

$$\frac{\rho}{\rho_s} \propto 1 - \Phi \tag{2.52}$$

Furthermore, for the bending-dominated deformation the elastic modulus of the sample is approximated by the formula:

$$E \propto E_s \left(\frac{\rho}{\rho_s}\right)^2 \tag{2.53}$$

where E_s is the elastic modulus of the solid material. Since E is equal to E_s when ρ is equal to ρ_s, the constant of proportionality is approximated to be a unity, which has been verified by experiments and numerical calculations [63].

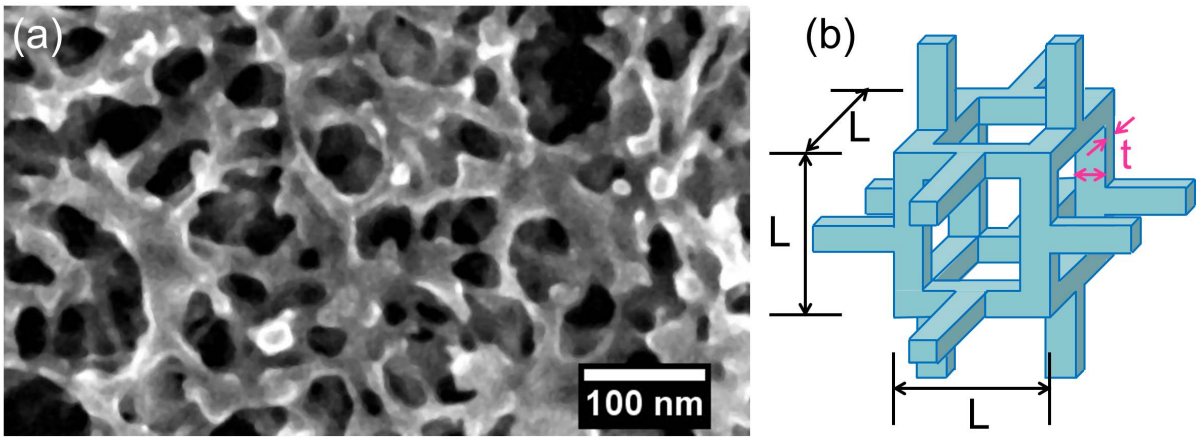

Figure 2.26: *(a) An example of the SEM image of the porous titania film. (b) The sketch of a unit cell for the ideal open-cell model.*

Composite model

The titania-based hybrid films, containing the titania and polymer either PS-b-PEO or P3HT, can be regarded as a composite. In general, the composite material is made from several constituent materials which have different properties. When the composite material is fabricated, its properties are generally different from the individual component. Meanwhile, all components remain distinct in the final structure. Examples range from reinforced plastics to the engineering materials concrete that commonly composes of aggregates embraced in a matrix of cement. Generally, two main types of constituents are necessary for a composite, matrix and reinforcement. Common matrix are ceramics, polymers, cement, mud, and metals, while the most popular reinforcements are fibers, aggregates, steel mesh, and wires. In this thesis, a P3HT/TiO_2 film is prepared in the way that the porous TiO_2 is backfilled with P3HT, which appears to be a composite based on a ceramic matrix. However, such composite material is generally believed as a polymer matrix reinforced with ceramic fibers [65, 66].

In order to estimate the elastic properties of the composite, two simplified analogs are mostly utilized according to the microstructures and orientations of the ceramic filler. One analog is the unidirectional, long fiber reinforced polymer and the other one is the particulate reinforced polymer, with their sketches illustrated in figure 2.27a and 2.27b, respectively.

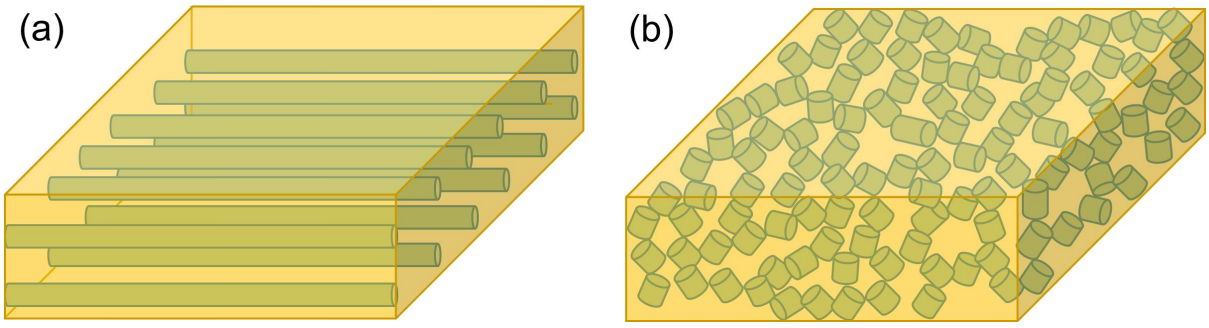

Figure 2.27: *Sketches of composite models with (a) unidirectional fibers and (b) particulates.*

For an unidirectional long fiber reinforced composite, the most commonly used models are developed by Voigt and Reuss [67]. Voigt model assumes the strain is uniformly distributed along the two constituent materials of the composite. This is described by the formula:

$$E = E_m V_m + E_f V_f \tag{2.54}$$

where E_m and E_f are the elastic moduli of matrix and filler materials, with their respective volume fractions of V_m and V_f. This model approximates an upper limit of the elastic modulus of the composite. On the contrary, Reuss model presumes a constant stress throughout the whole sample, which predicts a lower limit of the elastic modulus. The elastic modulus can be calculated by the formula:

$$E = \frac{E_m E_f}{E_m V_f + E_f V_m} \tag{2.55}$$

Particulate reinforced composite accounts for randomly distributed short fibers or other types of particulates. The semi-empirical Halpin-Tsai model is well known for prediction of the elastic modulus [68]. The analytical equation is:

$$E = \frac{E_m(1 + \xi\eta V_f)}{1 - \eta V_f} \tag{2.56}$$

with

$$\eta = \frac{E_f - E_m}{E_f + \xi E_m} \tag{2.57}$$

where ξ is an empirical parameter, which depends on the geometry, arrangement, and loading conditions of the fillers. Regarding to a short fiber, it can be described by:

$$\xi = 2\frac{l}{d} \tag{2.58}$$

with l the length and d the diameter of the fiber. In comparison with unidirectional long fiber reinforced composite, the particulate reinforced composite is closer to the real case of titania-based hybrid film, especially holding the truth for the distribution of random orientation. Although the Halpin-Tsai model yields the closest condition, it is accurate only under the assumption of fully-filled particle-polymer composite. For PS-b-PEO/TiO_2 system, the film is fully meet the Halpin-Tsai model. However, for P3HT/TiO_2 hybrid films, the fact that around 84% backfilling degree [69] requires a new model for accounting for the porosity. Therefore, the Halpin-Tsai model is further adapted by Bert et al. [70] for the composite with three phase materials, including two solid materials and air:

$$E = E_m \frac{1 + \xi\eta V_f}{1 - \eta V_f} \left(1 - \frac{\rho}{1 - V_f}\right)^{K_0(1-V_f)} \tag{2.59}$$

where η has been defined in formula 2.57. In formula 2.59, ρ is the porosity of the composite and K_0 refers to the shape and relative space of the pores in the sample. For example, K_0 is set to 2 for spherical pores [71].

3 Characterization methods

In the present thesis, solar cells and their active layers are prepared. In order to address the correlation between the morphology and physical properties, different characterization techniques are employed to examine the spectroscopy, the structures, and the device performance. Furthermore, the mechanical properties of TiO_2-related samples are investigated via a custom-made bending test setup. In this chapter, all used instruments and the methods for data analysis are presented.

3.1 Spectroscopic and electronic characterizations

UV/Vis spectroscopy (section 3.1.1) is used to probe the absorption of light within the active layer and to obtain information about the molecular ordering of the conjugated polymer P3HT. In order to determine the performance of the solar cell, the J-V curves are recorded under dark and AM 1.5G illumination (1000 W/m^2) (section 3.1.2). Then EQE measurements are carried out to investigate the photon-charge conversion external quantum efficiency as a function of wavelength, as detailed in section 3.1.3.

3.1.1 UV/Vis spectroscopy

To measure the absorption within the active layer, a Perkin Elmer Lambda 35 UV/Vis spectrometer is used. The light source includes one deuterium lamp and one halogen lamp for a wavelength range of 190 nm - 326 nm and 326 nm - 1100 nm, respectively. The lamps are automatically switched at a wavelength of 326 nm. Since the measurement is carried out in transmission mode, a transparent substrate such as glass or PET is needed for sample preparation. An optical grating and a slit system enable a monochromatic beam. The beam is split into two parallel beams by a half-transparent mirror before it reaches the sample. One beam passes through the sample and the other one through an identically cleaned reference substrate. Then, the intensity of both transmitted beams is measured by two photodiode detectors. Through comparing these two intensities, the transmission intensity of the sample is obtained. The spectra, shown in this thesis, are

recorded from 290 nm to 1100 nm as glass is not transparent for wavelengths below 290 nm. The scan speed is 120 nm/min and the slit width is 1 nm. The spectrometer is controlled via the software UV-Winlab, provided by PerkinElmer as well. The wavelength dependent absorbance (A) of the sample can be converted from the output transmission via the Lambert-Beer law:

$$A(\lambda) = -log_{10}\left(\frac{I_t(\lambda)}{I_0(\lambda)}\right) = a(\lambda)hlog_{10}e \tag{3.1}$$

with the initial beam intensity $I_0(\lambda)$, transmitted intensity $I_t(\lambda)$, linear absorption coefficient $\alpha(\lambda)$, and film thickness h. In this case, the reflection and scattering of the sample are not taken into account.

Furthermore, information of the molecular ordering of P3HT can be obtained from the measured spectrum. For example, red shift of the main absorption peak indicates an increased conjugation length [30,72]. In addition, the crystalline order can be extracted by applying the weakly coupled H-aggregate model [31, 32, 73]. The theoretical background of this model is described in section 2.3.2. In order to use this model, amorphous P3HT and PCBM contributions are subtracted from the original P3HT:PCBM spectra because this model is suitable for aggregated polymer crystals only. Then the resulting curve is converted into an energy scale. The resulting curve is fitted with 5 Gaussians of equal width via the software PeakFit (version 4.12).

3.1.2 J-V characterization

In order to determine the photovoltaic performance, J-V curves of the solar cells are recorded under dark and illumination conditions. The solar simulator SolarConstant 1200 (K. H. Steurnagel Lichttechnik GmbH) is used as the illumination source. A halide lamp with rare earth metals provide a spectrum, which is similar to the solar spectrum of AM 1.5G conditions with a standard light intensity of 1000 W/m^2. Before the measurements, the silicon based reference solar cell (WPVS-ID3, ISE) is probed to calibrate the intensity of the lamp. The J-V curve is recorded by a Keithley 2400 sourcemeter.

A custom-made sample holder is used to enclose the solar cells during the measurements, which includes a mask to limit the illumination to the area of the individual pixels. The distance between the solar cell and light source is 320 mm. For the measurements, the voltage sweeps from -1 V to 1 V with 0.01 V increment and 0.01 s delay. The standard P3HT:PCBM solar cells are measured once for each pixel, while the inverted solar cells are examined by loop measurements with a time interval 20 s to probe the best efficiency and the further degradation. Each pixel is measured via optical microscopy and the

size is extracted via the software ImageJ. From the J-V curve under illumination, the photovoltaic properties such as open circuit voltage (V_{OC}), short circuit current density (J_{SC}), fill factor (FF), serial resistance (R_s), and shunt resistance (R_{sh}) are obtained. An exemplary J-V curve under illumination is shown in figure 3.1. The V_{OC} and J_{SC} are extracted by the interception with their respective axes. In general, the V_{OC} is determined by the donor and acceptor materials, while the J_{SC} is correlated to the charge carrier generation, transportation, and extraction. The FF is the ratio between the product of V_{OC} and J_{SC} and the maximal output power, which is descripted by the ratio of the red and blue rectangles denoted in figure 3.1. It reflects the quality of the solar cell, which is equal to 100% in an ideal case. The R_s and R_{sh} are inversely proportional to the differential coefficient at the interception with voltage and the current axes, respectively. The low R_s and high R_{sh} indicate a high FF.

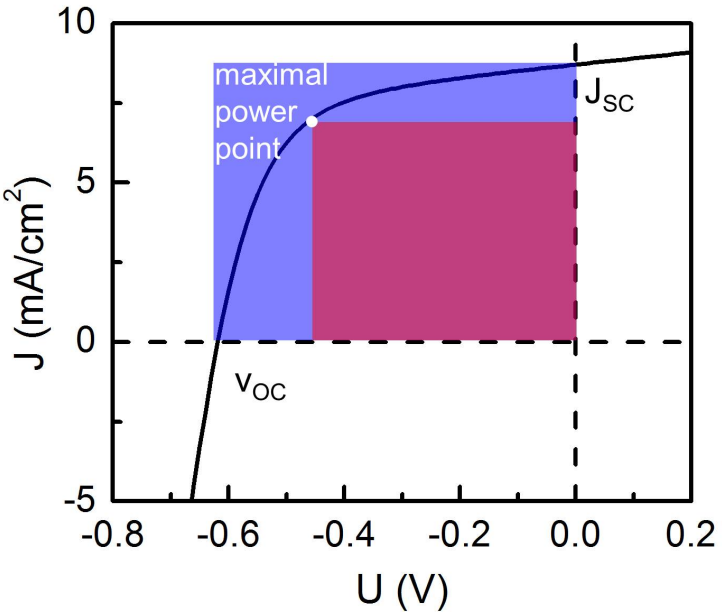

Figure 3.1: *An exemplary J-V curve under standard illumination AM1.5 (1000W/m^2). The V_{OC}, J_{SC} and maximal power point (white dot) are depicted. The blue and red rectangles indicate the product of V_{OC} and J_{SC} and the maximal output power, respectively. The ratio between these two areas is defined as FF.*

The overall power conversion efficiency PCE is defined as the extracted power P_{out} and the input power P_{in}. In this thesis, P_{in} is equal to the illumination power $P_{AM1.5}$ (1000 W/m^2):

$$PCE = \frac{P_{out}}{P_{in}} = \frac{J_{SC} V_{OC} FF}{P_{AM1.5}} \tag{3.2}$$

3.1.3 External quantum efficiency

In order to determine the external quantum efficiency as a function of the wavelength, EQE is characterized. The "Quantum Efficiency/IPCE Measurement Kit" developed by Newport, Corporation (Irvine, CA, USA) is employed for the measurements. A xenon arc lamp is used as the light source. The light is preliminary filtered through a fully automated filter wheel and pulsed by a chopper wheel at a frequency of 27 Hz. Afterwards, the beam is collimated at the monochromator (CornerstoneTM 260, 74125) and then illuminates the sample. The same sample holder as described for the J-V characterization is used. The electrical signal generated by the solar cell is recorded and the frequency provided by the chopper is filtered via a digital Lock-In amplifier. The Oriel's TracQ Basic software is employed to configure instrument parameters and process the data. A preliminary calibration of the EQE system is done with a silicon reference diode (Newport, 70356). The range of the wavelength is selected from 300 nm to 800 nm for P3HT:PCBM based solar cells.

An example of an EQE measurement of a P3HT:PCBM solar cell is shown in figure 3.2. The ideal case is illustrated by the green area. However, the EQE of all solar cells is smaller compared to the ideal case due to recombination effects. Moreover, the bandgap of donor material could be estimated from the energy cutoff as denoted by the white dashed line in figure 3.2 [74]. The J_{SC} can be evaluated by integrating the EQE over the solar spectrum.

3.2 Structural characterizations

Two main types of structural characterization techniques are employed in this thesis. The first type investigates the surface morphology, which includes real space techniques such as optical microscopy (section 3.2.1), atomic force microscopy (AFM) (section 3.2.2), and scanning electron microscopy (SEM) (section 3.2.3). White light interferometry is used to examine the film thickness and porosity of TiO_2-related samples (section 3.2.4). The other techniques are focusing on inner morphological characterization. Grazing incidence scattering (GIS) examines the structural information in reciprocal space (section 3.2.5).

3.2.1 Optical microscopy

Optical microscopy is preliminarily used to check the sample quality. Additionally, it is employed to determine surface structures in the micrometer range and the pixel area of

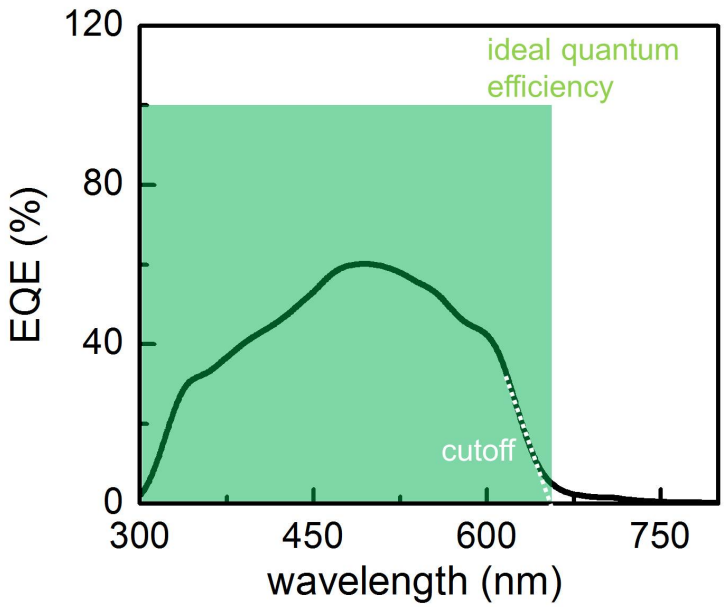

Figure 3.2: *An exemplary EQE curve of a P3HT:PCBM solar cell. The cutoff energy is depicted as the white dashed line. The green rectangle indicates the ideal EQE of this solar cell.*

solar cells. An Axiolab A microscope produced by Carl Zeiss is used, in combination with a PixeLink USB Capture BE 2.6 CCD camera and five different objectives. The dimension of the configured image is 1280 × 1024 pixels. The magnification can be selected as 1.25 × , 2.5 × , 10 × , 50 × , and 100 × , with a corresponding pixel size of 6.258 μm, 3.2 μm, 0.8 μm, 160 nm, and 80 nm, respectively. For the solar cell pixel size measurement, the 1.25 × objective is selected.

3.2.2 Atomic force microscopy

Atomic force microscopy (AFM) is used to investigate the topography and phase contrast of the thin films at the nanoscale. The surface structure and root mean squared roughness can be obtained from the topography images, while the phase image provides information about for example the hardness of the materials. Accordingly, phase images can be used to identify different blocks of a diblock copolymer.

The Autoprobe CP Research (Veeco Metrology group) is employed for all AFM measurements in this thesis. The sketch of the AFM setup is shown in figure 3.3. The AFM tip, laser system, photodiode, and the feedback controller are the main parts for scanning. The AFM tip is a gold covered silicon tip with curvature radius of 10 nm, which

is mounted face down on a silicon cantilever. The resonance frequency is in the range from 60 kHz to 90 kHz. Depending on the tip-sample distance, contact, tapping, and non-contact scanning modes are possible. According to the Lennard-Jones potential, the contact mode works in the Pauli repulsive range due to the short distance, whereas the tapping and non-contact mode are in the attractive range. In this thesis, the tapping mode is chosen for polymer-based samples, because most polymers are soft materials. Contact mode will induce sample damage due to artificial scans caused by the tip-sample adhesion. Before the measurement starts, the laser is focused onto the topside of the cantilever and reflected to the segmented photodiode. When the tip approaches the sample surface, the cantilever deflection due to the repulsive force is recorded through the reflected laser. During the scanning, the sample stage positions the sample in all three spacial directions under the tip. The deflection of the tip is detected and a feedback software controls the sample stage to keep the distance between sample and tip constant. Finally, according to the changes, the topography and phase images are constructed.

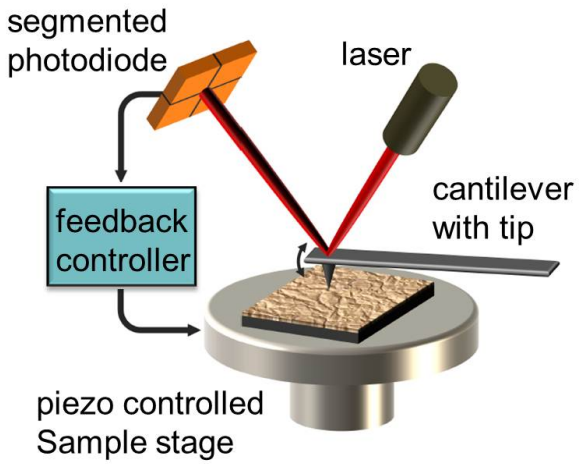

Figure 3.3: *Typical sketch of AFM setup with its main components. Image is adapted from [18].*

Generally, the samples are scanned over an area of 1×1 μm^2, 2×2 μm^2, 4×4 μm^2, and 8×8 μm^2. Two topography images with opposite scanning direction and a phase image are obtained from a single measurement. Conical shaped cantilevers with gold coating are used. The excitation frequency for the tip is set slightly above the resonant frequency (60-90 kHz), corresponding to non-contact mode condition. All 2D images are probed with 256 lines and each line consists of 256 data points. For better statistics, different spots are measured for each sample. The software Gwyddion 2.31 is used to analyze the AFM images.

3.2.3 Scanning electron microscopy

Scanning electron microscopy (SEM) is used to probe the surface and the cross sectional morphology of thin films in the nanometer range. Additionally, it is the main technique to examine cracks in titania-related samples with different bend times. SEM uses electrons as the illumination source, analogous to light in the optical microscope, but with much higher resolution due to the short wavelength of the electrons.

The SEM measurements are performed via a FESEM Gemini NVision 40 by Carl Zeiss, which is controlled by the software SmartSEM. The electron beam is emitted in a strong field from a field emission gun with tungsten filament. Subsequently, the electrons are accelerated by a voltage in the order of several kV. Through the magnetic and electrostatic lenses, the beam gets focused. The primary beam reaches the sample surface and interacts with the material. Accordingly, secondary electrons are emitted from the sample surface and collected by a detector. By recording the intensity of secondary electrons on the corresponding location of the sample surface, the resulting surface map is constructed with a resolution of 1 nm to 10 nm. The image is in a grey scale, which shows different brightness depending on the probed signal. The intensity of secondary electrons is correlated to the materials, the distance from the sample surface to the detector, and the surface morphology. For example, the smaller distance from sample surface to detector results in a higher density of detected secondary electrons, displayed with a white color. In addition, more secondary electrons can escape from a convex surface than a concave surface.

For all investigated samples, the values of working distance and acceleration voltage are set differently, as summarized in table 3.1. It is worthwhile to note that the low electrical conductivity of P3HT:PCBM films and PET substrates induce charging up over short time. In order to conquer this problem, the acceleration voltage is set much lower than for inorganic semiconductor films on silicon substrates. Likewise, the working distance is shorten in this case. However, the measurements performed on P3HT:PCBM films and the samples on PET substrates still show signs of static charge agglomeration, which in turn affects the quality of the taken images.

To measure cross sectional images with SEM, the backside of the sample is first scratched with a diamond cutter. Liquid nitrogen is used to obtain a sharp edge, which is especially important for polymer-based samples. During the scanning process, the sample is tilted by 60° along the x-axis and the tilt correction of 30° is applied by the software. The working distance and acceleration voltage for these measurements are also summarized in table 3.1. All the SEM images obtained directly from the measurements are analyzed by the image processing software ImageJ.

sample	measurement	working distance (mm)	acceleration voltage (kV)
P3HT:PCBM	surface	1.5	1
TiO_2/PET	surface	2.5	1.5
TiO_2/Si	surface	3	5
TiO_2/Si	cross-section	2	1
solar cell	cross-section	3.5	5

Table 3.1: *Parameters used for SEM measurements.*

3.2.4 White light interferometry

White light interferometry is a common technique to probe the film thickness and the refractive index of thin films. It is based on the interference of the light originating from two reflections at different interfaces. Incident light can be reflected partially at the film surface and partially at the film-substrate interface. According to the difference in optical path length, the two resulting reflected light rays interfere with each other constructively or destructively. In general, optical observations are determined depending on refractive index n(λ), extinction coefficient k(λ), and film thickness d. If the optical length difference is an even multiple of $\lambda/2$, the interference is constructive, while if it is an odd multiple of $\lambda/2$, the interferencce is destructive.

All white light interferometry measurements presented in this work are performed on a F20-UV thin-film analyzer (Filmetrics Inc.). The white light, supplied by a deuterium and tungsten halogen light source, illuminates the sample surface under 90°. The wavelength-sensitive point detector is employed to probe the intensity of reflected light in the range from 400 nm to 1100 nm. Investigated samples should be transparent to this wavelength regime. For example, optically active materials like P3HT or dye molecules are not suitable for these measurements performed in the range of visible light. Moreover, a silicon substrate is commonly used due to its high reflectivity and smooth surface. When the measurement is done, the resulting reflectivity curve is constructed. A fitting algorithm based on film thickness and refractive index is run until a successful fitting is obtained. Then the film thickness and refractive index are obtained.

Furthermore, the porosity of TiO_2 film can be calculated from the probed refractive index. Basically, a porous TiO_2 film can be considered as the composite, consisting of TiO_2 and air. The so-called Bruggeman effective medium approximation is used to obtain the porosity [75]:

$$(1 - f_b)\frac{n_a^2 - n_{eff}^2}{n_a^2 + 2n_{eff}^2} + f_b\frac{n_b^2 - n_{eff}^2}{n_b^2 + 2n_{eff}^2} = 0 \tag{3.3}$$

Where n_a and n_b refer to the refractive indexes of the respective material components a and b. The effective refractive index of the composite is n_{eff}, which is the value obtained directly from the white light interferometry measurements. The volume fraction of component b is denoted by f_b. In terms of the porous TiO_2 film, the n_{TiO_2} of 2.49 is taken from literature and n_{air} equals to 1. Then, the porosity is represented by the corresponding volume fraction of air f_{air}.

3.2.5 Grazing incidence scattering

In order to characterize the nanomorphology within the thin film, grazing incidence scattering (GIS) methods are employed. Contrary to transmission geometry used in standard small angle scattering (SAS), the GIS measurement is performed in reflection geometry, schematically shown in figure 3.4. In comparison to transmission geometry, this technique has the advantage of higher statistics due to the large footprint of X-ray beam on the sample. The sample-detector distance (SDD) limits the accessible angles and thereby the resolved structural length scales of the sample which could vary from several nanometers up to micrometer range. The incident angle α_i of the X-ray determines whether the measurements are surface or volume sensitive. For example, if the incident angle is above the critical angle, the structural information inside the film can be detected. While with an incident angle smaller than the critical angle, surface related information can be obtained. The theoretical background of GIS is described in section 2.4.

Grazing incidence small angle X-ray scattering

Within the frame of this thesis, the grazing incidence small angle X-ray scattering (GISAXS) experiments are carried out at different synchrotron beamlines. In general, the incident angle is set above the critical angle of the investigated materials to ensure that the X-rays fully penetrate the film. Detailed information such as wavelength, incident angle, SDD, and the detector properties are described in the respective chapters.

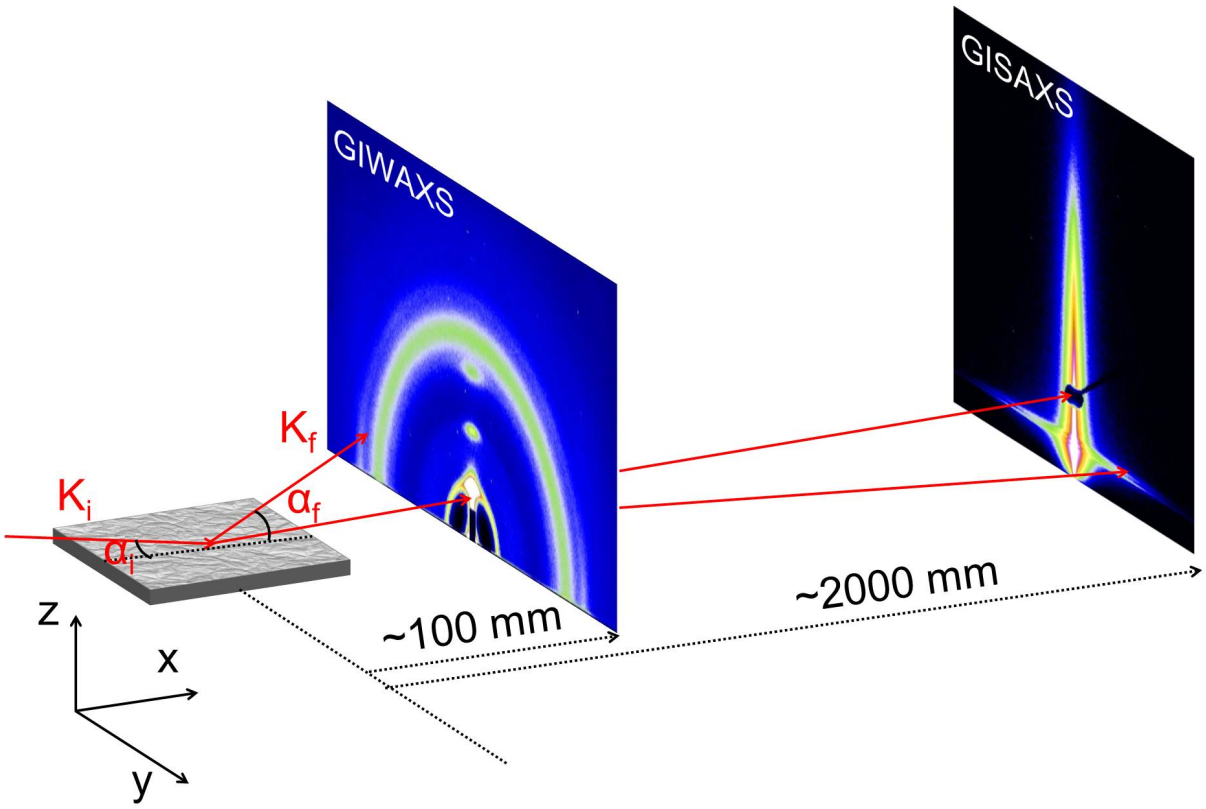

Figure 3.4: *Schematic presentation of a grazing incidence X-ray scattering setup. The X-ray beam with a wavevector K_i (red arrow) impinges on the sample with the incident angle α_i and then is scattered under an angle of α_f. 2D detectors with short and long sample-detector distances record wide angle and small angle X-ray scattering, respectively.*

Exemplary 2D GISAXS data are shown in figure 3.5a, which is obtained from a typical P3HT:PCBM thin film after thermal annealing. The specularly reflected beam is shielded by a beamstop to protect the detector from oversaturation, as denoted by the white arrow. In order to analyze GISAXS data, vertical and horizontal line cuts are performed at the positon of $q_y = 0$ and the critical angle of the studied material, respectively. The obtained vertical and horizontal line cuts are revealed in figure 3.5b and 3.5c. The cuts are extracted from the 2D GISAXS data via the software Fit2D (software by Andy Hammersley, 1987-2005, ESRF, Grenoble). The vertical line cut provides information about the vertical material composition in the film and the correlated roughness at the interface between two layers. The horizontal line cut reveals the lateral structural information of the film.

In order to obtain quantitative information about lateral structures, a custom-made program is used to fit the horizontal line cuts. First of all, the resolution is fitted with a Lorentzian function at the position of $q_y = 0$ and the background is fitted with a constant. Furthermore, both, form and structure factors, are assigned to the structure in the sam-

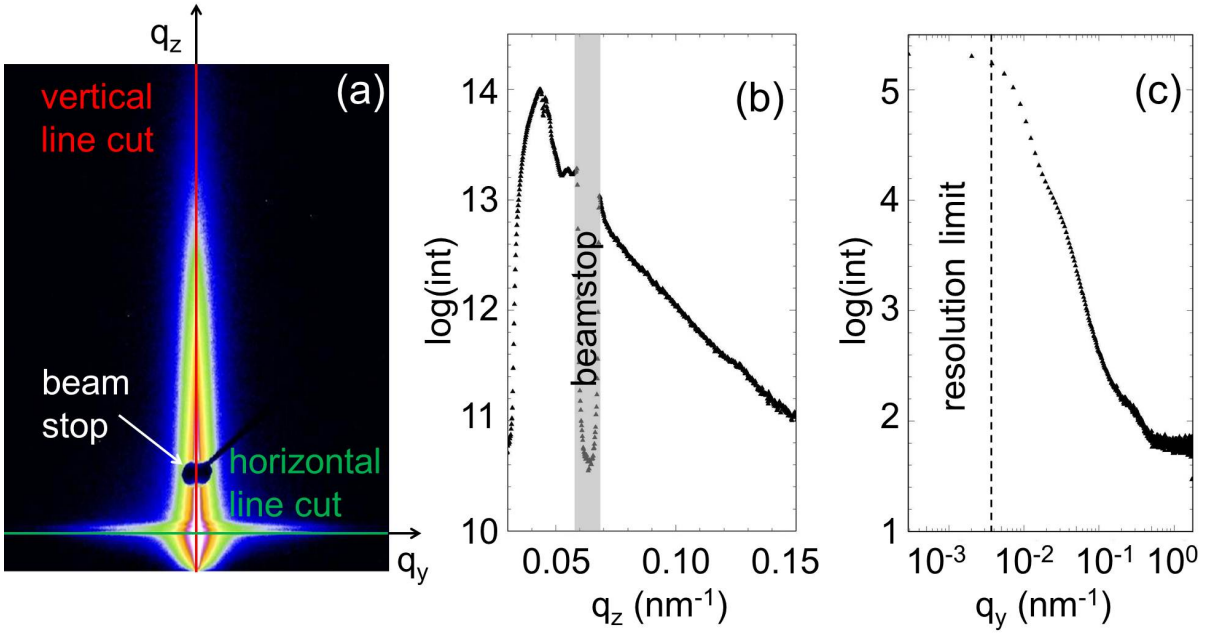

Figure 3.5: *(a) Exemplary 2D GISAXS data with illustration of the position where vertical (red line) and horizontal (green line) line cuts are taken. The specularly reflected beam is shielded by a beamstop, as denoted by the white arrow. Corresponding (b) vertical and (c) horizontal line cuts are shown with beamstop area and resolution area.*

ple. The model assumes either one, two, or three form factors, including the information of geometry (cylinder or sphere) and radii with a Gaussian distribution. Corresponding structure factors represent the distances between two neighboring scattering centers within the model of a one-dimensional paracrystal [76]. The structure factor follows the local monodisperse approximation (LMA), assuming the respective object types scatter independent from each other. The exemplary image of the horizontal line cut together with all fitting components is shown in figure 3.6. The sketch of the fitting model with three cylindrical form factors is shown as an inset in figure 3.6.

Grazing incidence wide angle X-ray scattering

The crystalline order (such as molecular stacking, crystal orientations, and estimation of crystal sizes) can be revealed by grazing incidence wide angle X-ray scattering (GIWAXS) measurements with an SDD in the order of 10 cm and an incident angle of 0.2°. GIWAXS and GISAXS experiments using the same detector can be conducted by a change of the SDD. For both, GISAXS and GIWAXS, the wavelength is kept constant.

Before analyzing 2D GIWAXS data, a sequence of data corrections is needed to account for detection efficiency, flat-field, X-ray polarization, solid angle variation, and reshaping

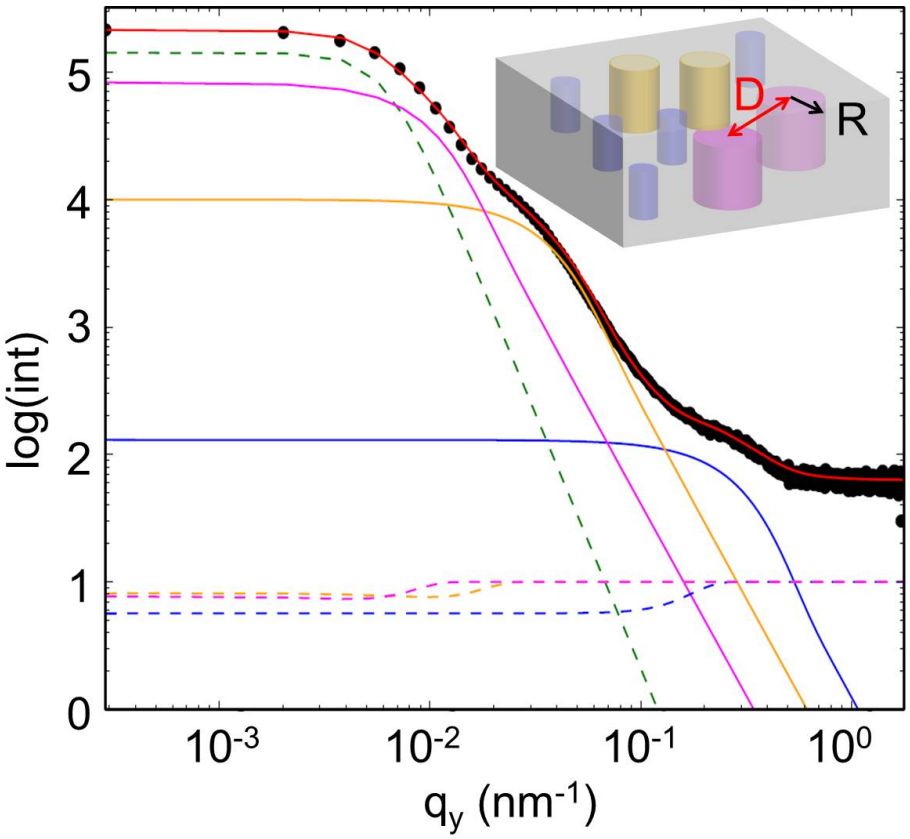

Figure 3.6: *Exemplary horizontal line cut (black dots) of GISAXS data with fit (red line). Green dashed line is used for fitting the resolution, whereas the yellow, blue, and magenta lines indicate three different form factors and the corresponding dashed lines indicate respective structure factors. The sketch of three structures in the film is shown as the inset.*

2D GIWAXS patterns. All the corrections are implemented in the software Grazing-incidence X-ray Scattering Graphical User Interface (GIXSGUI), which is an open source program developed by Advanced Photon Source, Argonne National Laboratory, USA. Afterwards, for a quantitative analysis, the sector integrals of 10° in vertical and horizontal directions are taken, which provide crystalline information along the direction perpendicular and parallel to the sample surface, respectively. These two sector integrals are displayed in figure 3.7a. The resulting curves (figure 3.7c and 3.7cd) are fitted with Gaussian functions. Peak positions and FWHM reveal the lattice constant and allow to estimate the size of crystals. Moreover, the tube integral along the specific q value (figure 3.7e) is also extracted from 2D GIWAXS data, referring to information about crystal orientations. The edge-on P3HT crystal structure is schematically represented in figure 3.7b, which is based on information extracted from tube integrals. The direction along the side chain, the π- π stacking, and the polymer backbone are denoted as (100), (010) and (001) directions, respectively.

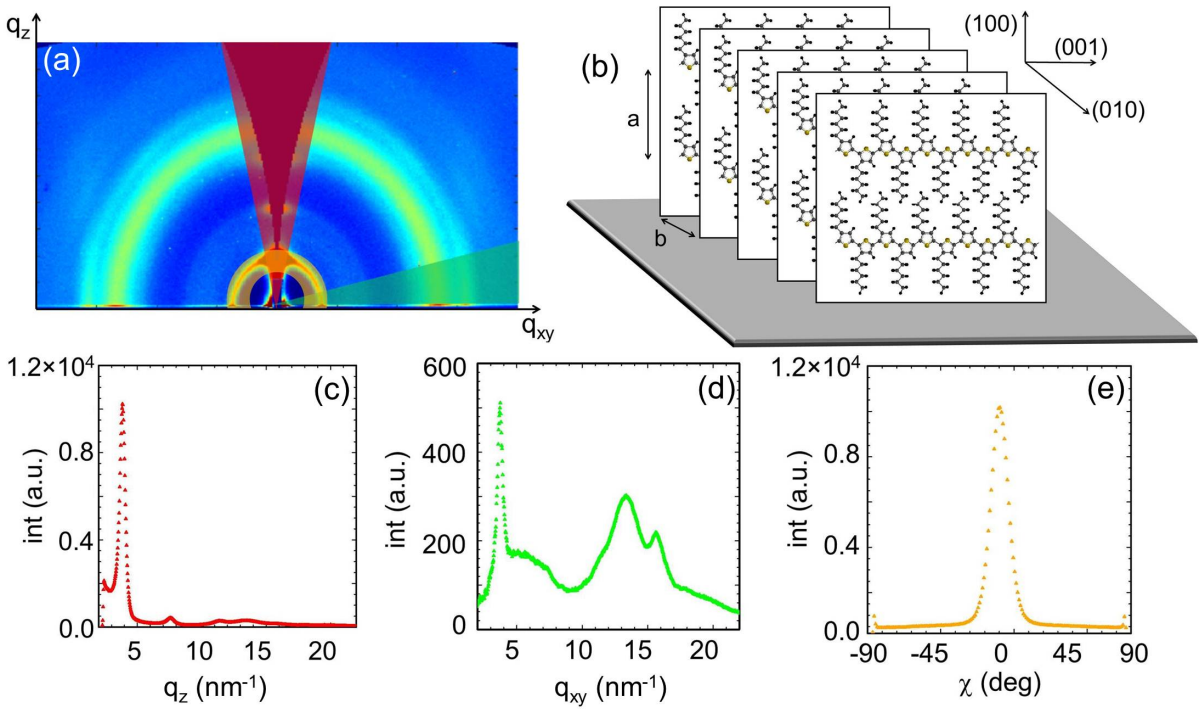

Figure 3.7: *(a) Exemplary 2D GIWAXS data of P3HT:PCBM thin film after correction, with highlighted vertical (red) and horizontal (green) sector integration area and tube integration area (orange). (b) Schematic representation of P3HT crystals with an edge-on orientation, suggested by the 2D GIWAXS data. Corresponding (c) vertical and (d) horizontal sector integrals and (e) tube integral.*

Time-of-flight grazing incidence small angle neutron scattering

Time-of-flight grazing incidence small angle neutron scattering (TOF-GISANS) measurements are performed at the beamline REFSANS at the Munich neutron research reactor FRM II of MLZ in Germany [77,78]. The TOF mode refers to the neutrons with different velocities and accordingly different arriving times at the detector. The pulsed neutrons with wavelengths from 2 Å to 15 Å are available by employing the chopper system. According to the different arrival times of the neutrons on the detector, the data are rebinned in the certain range of wavelengths with the resolution $\Delta\lambda/\lambda$ of 10% to obtain the best tradeoff between resolution and intensity. In this experiment, the selected binning of wavelengths is 2.21 Å, 2.44 Å, 2.7 Å, 2.98 Å, 3.3 Å, 3.65 Å, 4.03 Å, 4.45 Å, 4.92 Å, 5.44 Å, 6.01 Å, 6.65 Å, 7.35 Å, 8.12 Å, 8.97 Å, 9.92 Å, 10.96 Å, 12.12 Å, and 13.39 Å. A 2D ^{3}He detector with the active area of 500 mm^2 containing 340 × 340 pixels is used to record the scattering signal. The pixel size is 1.378 × 1.378 mm^2 wit a SDD of 10.52 m. An incident angle of 0.46° for short wavelengths and from 0.46° to 0.5° for long wavelengths is used. The variation of the incident angles in the long wavelength regime is

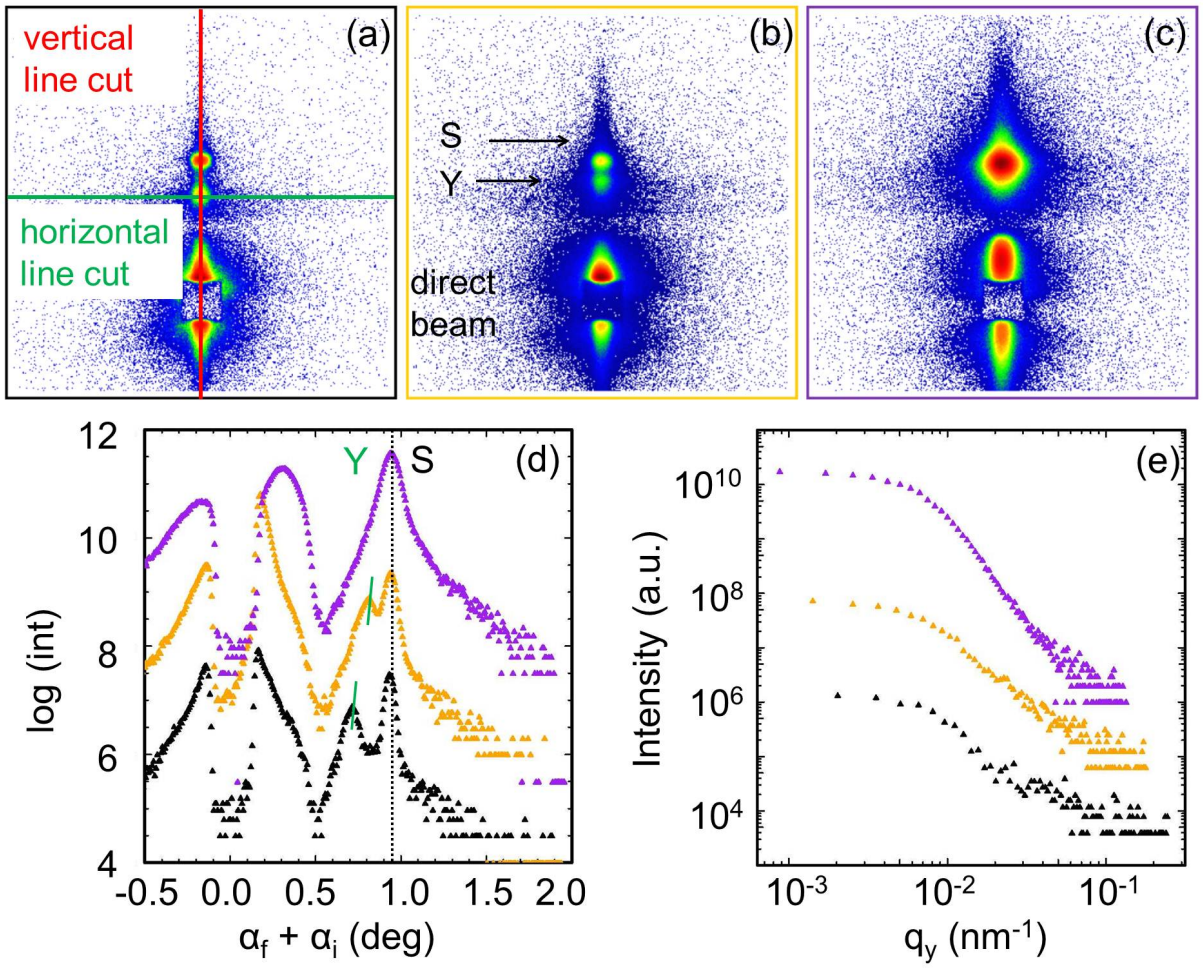

Figure 3.8: *Exemplary 2D TOF-GISANS data of P3HT:PCBM thin film with illustration the positions where vertical (red line) and horizontal (green line) line cuts are taken. Selected average wavelength of neutrons is (a) 5.44 Å, (b) 7.35 Å, and (c) 9.92 Å, respectively. The (d) vertical and (e) horizontal line cuts of these three data sets are shown. The black, yellow, and purple color denote the corresponding wavelength of 5.44 Å, 7.35 Å, and 9.92 Å, respectively. The curves are shifted along y direction for clarity.*

caused by non negligible gravitation effects acting on the neutron beam [69]. In order to obtain sufficient statistics, each sample is measured for 18 h.

An example of 2D GISANS data at selected wavelength of 5.44 Å, 7.35 Å, and 9.92 Å is shown in figure 3.8a, 3.8b, and 3.8c, respectively. The transmitted signal is visible around the beamstop, as denoted in figure 3.8b). The region near the transmitted beam provides information about the distribution of the grains and the structural ordering in vertical direction [79,80]. In order to analyze the TOF-GISANS data, the vertical and horizontal line cuts are performed on the 2D data for each wavelength as shown in figure 3.8d and 3.8e. For the vertical line cuts all specular peaks are located at the same position.

The Yoneda peak shifts towards the specular peak with increasing wavelengths, since the critical angle depends on the wavelength. By fitting the change of the critical angle for a certain wavelength, a precise determination of the SLD of the investigated material and accordingly information about the mixture of two components on a molecular level is obtained [69]. Once the position of the Yoneda peak is determined, the horizontal line cut is performed. These horizontal line cuts of 2D GISANS data are fitted with the same procedure as being used for the GISAXS profiles. Corresponding structure information such as form factors and structure factors are obtained.

3.3 Mechanical characterization

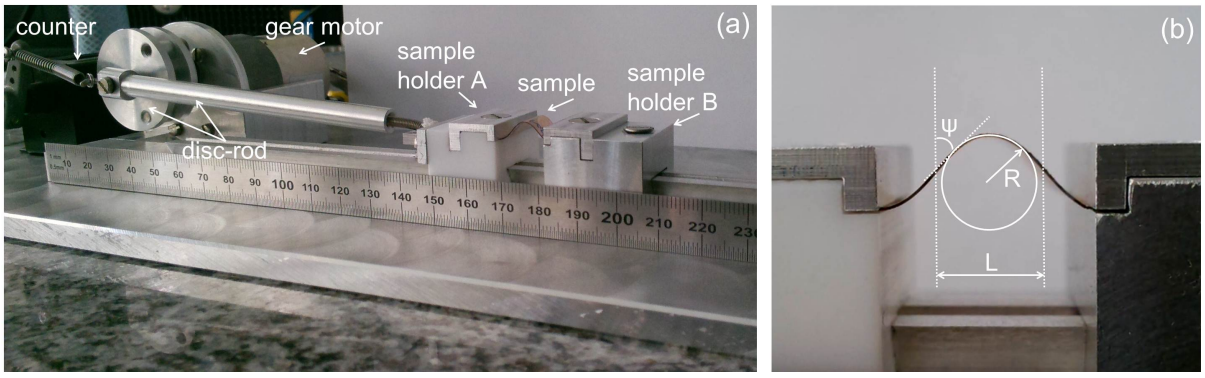

Figure 3.9: *(a) Bending test setup, with all components labeled. (b) Photograph of the sample with maximal bending. The stress and strain are determined in this condition. The bending radius R is extracted by the best fitting of the curved sample. The distance between the two points on the sample where the curvature is zero is labeled as L. ψ is the angle between the sample and the vertical plane.*

In order to characterize the mechanical properties of titania-related samples, bending tests are performed for thin films on flexible PET substrates. A custom-made bending test setup is employed to examine the fatigue and eventual failure of the thin films [25]. The bending test setup is shown in figure 3.9a. The sample is mounted between the sample holder A and B. The holder A is connected to the aluminum disc-rod, which is driven by the gear motor to bent the sample periodically, while the holder B is fixed during the measurements. The load speed can be tuned by adjusting the voltage applied to the gear motor. The mechanical counter is connected to the aluminum disc-rod to count the cycle numbers. In order to avoid slippage, the sample is clamped with two aluminum plates on the blocks.

For the bending experiments included in this thesis, six samples on PET substrates with 20 × 20 mm^2 area are equally prepared for the bending tests. Directly after the preparation, the samples are measured with bending 0, 10, 100, 500, 1000 and 5000 times, respectively. The voltage is set to (3.8 ± 0.1) V to apply a cycle frequency ω of (0.3 ± 0.1) s^{-1}. In order to record the maximal bending radius, a video within several cycles is taken during the test. The bending radius R of (3.0 ± 0.2) mm is extracted from the best fitting of the strongest curved sample as shown in figure 3.9b. It is correlated to the maximum strain of (2.8 ± 0.2) %. The method for calculating the strain is described in section 2.5.1.

4 Sample preparation

In this chapter different routines for preparation of the corresponding samples are described. In section 4.1, information about the materials and solvents is given. Afterwards, the film preparation for different substrates, including glass, silicon, and PET is described in section 4.2, where as well the process for polymer blend film (P3HT:PCBM) fabrication and the sol-gel synthesis for TiO_2 based samples is discussed. Finally, the assembly of solar cells with standard and inverted geometries is introduced in section 4.3.

4.1 Materials and solvents

Materials are described in two sections: the first section includes materials used for polymer BHJ films and corresponding solar cells, whereas the second section includes TiO_2-related materials. Accordingly, section 4.1.1 refers to the electron donor, electron acceptor, electron blocking layer and hole blocking layer materials as well as solvents. The second section (section 4.1.2) comprises polymer template and hole conductor materials in addition to the modified titania precursor and corresponding solvents.

4.1.1 Polymer blends

For polymer solar cells a thiophene derivative poly(3-hexylthiophene-2,5-diyl) (P3HT) was selected as electron donor and a fullerene derivative [6,6]-phenyl-C61-butyric acid methyl ester (PCBM) as electron acceptor. In addition, a poly(3,4-ethylenedioxythiophene):poly-(styrenesulfonate) (PEDOT:PSS) layer was applied as the electron blocking layer. Detailed parameters of these materials including the suppliers, molecular masses M_n and M_w, polydispersity PDI, and purity are listed in table 4.1.

material	supplier	M_n (kg/mol)	M_w (kg/mol)	PDI	purity
P3HT	Rieke Metals, Inc.	23	53	2.3	n.a.
PCBM	Nano-C, Inc.	911	n.a.	n.a.	99.5%
PEDOT:PSS (PH1000)	Ossila	n.a.	n.a.	n.a.	99%

Table 4.1: *The parameters of all involved materials, including supplier, number average molar mass M_n and weight average molar mass M_w, polydispersity PDI, and purity. M_n is calculated by the formula $M_n = M_w/PDI$.*

Electron donor

The semiconducting polymer P3HT is a commonly employed and broadly studied donor material for organic solar cells. As a result physical processes taking place in a P3HT based solar cell are often referred to as a paradigm for alike systems [81–83]. The chemical structure of P3HT is displayed in figure 4.1. Mainly the backbone facilitates the hole transportation. Furthermore, P3HT has a LUMO energy level of -3.3 eV and a HOMO energy level of -5.2 eV. As a result the energy bandgap is 1.9 eV, corresponding to the absorption in visible light [84]. In addition, P3HT molecules tend to crystallize [85]. Organic solvents like chlorobenzene, dichlorobenzene, toluene, and xylene can be used to dissolve P3HT, yielding a homogeneous solution.

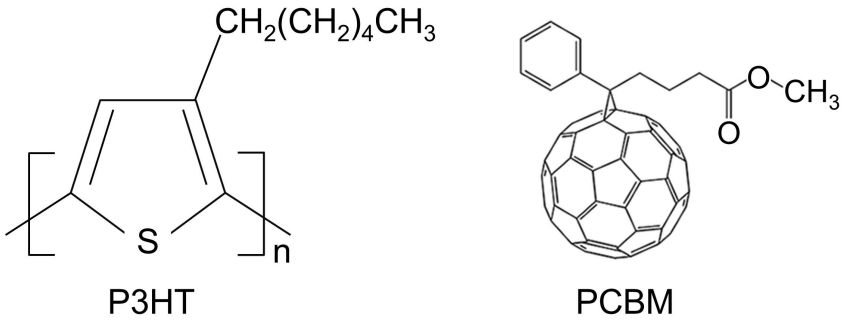

Figure 4.1: *The chemical structures of P3HT and PCBM.*

Electron acceptor

The small organic molecule $PC_{60}BM$, abbreviated as PCBM within this thesis, was used as the electron acceptor material. The molecular structure of this fullerene derivative is displayed in figure 4.1. The buckminsterfullerene derivate represents the functional part

for electron transportation, while the attached side chain serves to enhance solubility in organic solvents. The combination of P3HT and PCBM is the most broadly investigated system which is commonly selected for fabricating polymer solar cells, especially for a BHJ structure.

Electron blocking materials

PEDOT:PSS is a well-established material for application as an electron blocking layer in organic photovoltaics. The corresponding chemical structure is shown in figure 4.2. PEDOT:PSS PH1000 was bought from Ossila, with a weight ratio of 1:2.5 between PEDOT and PSS and a solid content of 1 wt.% to 1.3 wt.% in water was used within the frame of this thesis. The conjugated polymer PEDOT allows hole-transport through the layer, whereas the PSS component improves the limited solubility of PEDOT in an aqueous suspension. The conductivity is given as 918 S/cm. The final PEDOT:PSS film has a blueish color, which has little effect on the light absorption of the active layer due to a small film thickness of around 40 nm.

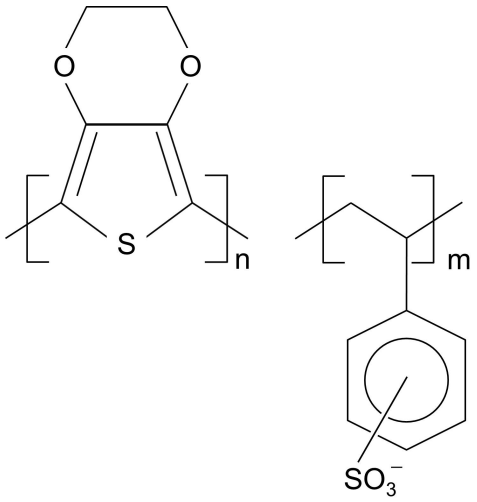

Figure 4.2: *The chemical structures of individual components of PEDOT:PSS. Holes can be transported along the thiophene backbone of PEDOT (left), whereas PSS (right) enhances solubility in water.*

Solvents

Chlorobenzene, dichlorobenzene, toluene, and xylene were used to dissolve P3HT and PCBM. All these solvents were purchased from Carl Roth and were used without further treatment. The chemical structure of these solvents is depicted in figure 4.3 and detailed

parameters including the molecular formula, density, boiling point, and vapor pressure are listed in table 4.2. Successful fabrication of solar cells based on each of the above mentioned solvents is frequently reported in literature [5, 26]. Further elaborative investigation about the influence of solvent vapor on solar cell stability will be presented in chapter 6.

solvent	**molecular formula**	**density (g/cm^3)**	**boiling point (°C)**	**vapor pressure (mm·Hg)**
chlorobenzene	C_6H_5Cl	1.11	132	11.8
dichlorobenzene	$C_6H_4Cl_2$	1.31	180	1.3
toluene	C_7H_8	0.87	110-111	22
xylene	C_8H_{10}	0.87	137-140	7.5

Table 4.2: *Detailed parameters of all host solvents for dissolving P3HT and PCBM, including molecular formula, density, boiling point, and vapor pressure.*

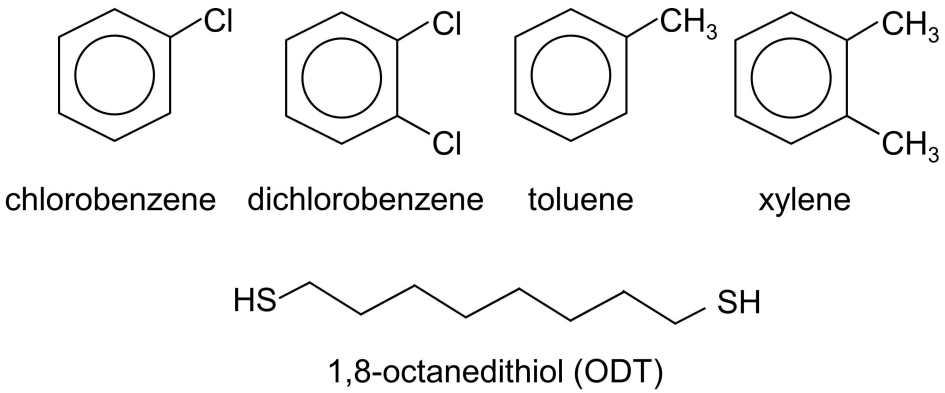

Figure 4.3: *The chemical structures of the solvents.*

Solvent additive

1,8-octanedithiol (ODT) was purchased from Sigma-Aldrich and used as supplied. The density is 0.97 g/ml at 25 °C and the boiling point is 269 - 270 °C. Its molecular formula is $HSCH_2(CH_2)_6CH_2SH$. This processing solvent additive has been widely utilized to tune the morphology in terms of BHJ systems due to its selective solubility for donor and acceptor materials [86,87]. In chapter 5, the influence of ODT addition on the morphology of P3HT:PCBM BHJ films will be discussed.

4.1.2 Sol-gel synthesis

The low temperature sol-gel synthesis, aiming for fabrication of porous titania films, is based upon a diblock copolymer as a template and a modified titania precursor. To obtain the complete active layer of a hybrid solar cell, the titania matrix obtained by this routine is backfilled with the electron donor P3HT which has been introduced in section 4.1.1. The present section will show detailed information about the diblock copolymer poly(styrene-block-ethylene oxide) (PS-b-PEO) and the titania precursor ethylene glycol modified titanate (EGMT).

Polymer template

In combination with various metal oxide precursors, a polymer template allows for the fabrication of precisely controllable nanostructures. In present thesis the amphiphilic diblock copolymer PS-b-PEO, purchased from Polymer Source Inc., Canada, was used as the polymer template. Detailed parameters like molar mass, polydispersity, and glass transition temperature are listed in table 4.3. Its chemical structure is shown in figure 4.4, containing a hydrophobic block PS and a hydrophilic block PEO.

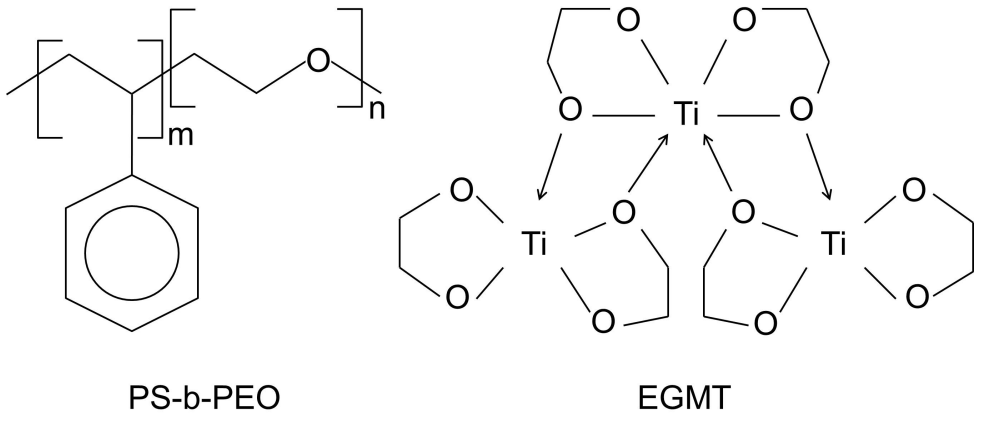

Figure 4.4: *The chemical structure of the polymer template PS-b-PEO and the titania precursor EGMT.*

Titania precursor

EGMT was used as the titania precursor. Combined with PS-b-PEO, nanostructured titania film can be produced. The EGMT was synthesized by Thomas Fröschl, in the group of Prof. Nicola Hüsing from the University of Salzburg. The detailed process of

polymer	M_n **(kg/mol)**	**polymer block**	**PDI**	M_n **(kg/mol)**	$\mathbf{T}_g$ **(°C)**
PS-b-PEO	28.5	PS	1.01	20.5	107
		PEO	1.02	8	-65

Table 4.3: *Properties of PS-b-PEO, including number average molar mass M_n of the block copolymer, polydispersity index PDI, number average molar mass M_n, and glass transition temperature T_g of each polymer block.*

synthesis is described in reference [88]. The molecular formula of EGMT is $C_4H_8O_4Ti$ with a chemical structure as shown in figure 4.4. The unit cell of EGMT is based on TiO_6 octaedrons. As an octahedral orientation has been achieved inside EGMT, the crystallization of titania can take place at low temperature (below 150 °C). The material itself is supplied as a white powder. In order to properly dissolve EGMT, an acidic environment is required. Moreover, by adjusting the pH value, the crystalline phase of anatase and rutile could be tuned [89].

4.2 Thin films

As the active layer is normally sandwiched in between other functional layers in a solar cell, a direct measurement of the active layer is difficult for a complete solar device. In order to focus on the functional layer of interest, individual thin films are prepared. Instead of ITO or FTO substrates, silicon, glass, or PET is used as the substrate according to the requirements of different sample characterization techniques. In this section, different thin film preparations will be introduced, starting with the substrate cleaning (section 4.2.1). Afterwards, solution preparation and deposition of P3HT:PCBM BHJ films are discussed in section 4.2.2. Finally, section 4.2.3 describes the sol-gel synthesis, film deposition, polymer template removal, and P3HT backfilling.

4.2.1 Substrate cleaning

Before thin film deposition the silicon, glass or PET substrates were cut to 20 × 20 cm^2 pieces, while for characterization with neutron scattering silicon substrates with a size of 70 × 70 cm^2 were prepared in order to enhance the statistics of the measurements.

Silicon and glass substrates

All silicon and glass substrates were cleaned in a hot acidic bath at 80 °C for 15 min. The acid bath contained 54 ml deionized water (H_2O), 84 ml hydrogen peroxide (H_2O_2), and 198 ml sulfuric acid (H_2SO_4). Afterwards, the substrates were taken out of the acid bath and were immersed in a deionized water bath for temporary storage. Then, each sample was thoroughly rinsed with deionized water and dried with nitrogen.

Polyethylene terephthalate (PET) substrates

In order to test the mechanical properties of hybrid films, PET foils were used as flexible substrates. Since they were not chemically stable in the acid bath, four organic solvent baths were employed for the cleaning procedure. PET substrates were subsequently cleaned with a detergent solution (alconox solution, 16 g/l), ethanol, acetone, and isopropanol for 10 min in an ultrasonic bath, respectively. Before changing to another solvent bath, PET substrates were always dried with nitrogen to remove solvent remains. After the last cleaning step, they were rinsed with isopropanol and dried with nitrogen. As PET substrates were highly hydrophobic, a further cleaning step with oxygen plasma was applied to ultraclean the surface and improve the wettability. All the substrates were placed in the plasma oven (Nano by Diener electronics). Then the oxygen plasma was generated with 250 W at a pressure of 0.4 mbar. The plasma treatment lasted for 10 mins. Afterwards, the substrates were directly used for film deposition.

4.2.2 P3HT:PCBM BHJ film preparation

Solution preparation

Chlorobenzene, dichlorobenzene, toluene, and xylene were used to dissolve P3HT and PCBM. In order to achieve similar film thickness, different concentrations were used as shown in table 4.4 with the constant weight ratio 1:1 between P3HT and PCBM. P3HT was firstly dissolved in the solvent till complete dissolution and then the P3HT solution was added to the PCBM powder. The glass vial was sealed with parafilm and covered by a piece of aluminum foil to prevent P3HT degradation induced by light. Afterwards, the P3HT:PCBM solution was stirred overnight till complete dissolution at room temperature. For the solvents with low PCBM solubility, the solution was heated in a sand bath to 60 °C for half an hour to enhance the solubility of PCBM.

solvent	concentration (mg/ml)
chlorobenzene	24
dichlorobenzene	30
toluene	18
xylene	24

Table 4.4: *Concentrations of P3HT:PCBM in different solvents, which enables to achieve similar film thickness. The weight ratio between P3HT and PCBM is kept as 1:1.*

P3HT:PCBM film deposition

In this thesis, all P3HT:PCBM films were deposited via spin coating. The prepared solution was dripped on top of the pre-cleaned substrate, which was fixed on the stage of the spin coater by vacuum. Then, the lid of the spin coater was closed and the spinning process was started immediately. Parameters like revolutions per minute, acceleration time, and spinning time can be adjusted. The relationship between film thickness and relevant parameters is described by Schubert's formula [90]. To obtain the film thickness of around 100 nm, the rotational speed of 2000 rpm, the acceleration time of 4.5 s, and spinning time of 30 s were selected for all used solvents. After spin coating the films were annealed in a glove box at 140 °C for 10 min.

4.2.3 TiO_2-related hybrid film preparation

The preparation of TiO_2-related hybrid films was a complex process. A detailed description is be presented in this section, including sol-gel synthesis, film deposition, polymer template extraction in a low temperature regime, and P3HT backfilling.

Sol-gel synthesis

The sol-gel synthesis at a low temperature was used to fabricate nano-structured TiO_2, which were based on EGMT as a TiO_2 precursor and the amphiphilic block copolymer PS-b-PEO as a structure-directing template. To prepare the sol-gel, PS-b-PEO was firstly dissolved in N,N-dimethylformamide (DMF), which was a good solvent for both blocks. The polymer solution was then stirred by a magnetic string fish for 30 min at room temperature. Subsequently, EMGT was added to the polymer solution and HCL was dropped in as the poor solvent to enable the microphase separation of the PS-b-PEO. Afterwards, the solution was stirred at room temperature for 30 min and then placed

on a heating stage at 90 °C for 15 min. The used weight ratio between all components (W_{DMF}:$W_{PS-b-PEO}$:W_{EGMT}:W_{HCL}) was set to 20:1:1:2.

PS-b-PEO/TiO_2 film deposition

All PS-b-PEO/TiO_2 films are prepared via spin coating. Basic knowledge of spin coating has been introduced in section 4.2.2. In terms of sol-gel solution, the spin coating parameters of rotational speed, acceleration and spinning time were set to 2000 rpm, 4.5 s and 60 s, respectively. After spin coating, the films were annealed at 90 °C for 30 min to prevent PEO crystallization on the surface [91]. Note that PET substrates cannot be directly fixed on the stage inside the spin coater by vacuum due to their highly flexibility. Therefore, the PET substrate is always attached to a glass slide using a droplet of water, whose capillary force enables the PET substrate to stick tightly to the glass.

In order to achieve thicker films beyond the film thickness limit for single spin coating, multiple spin coating can be performed. For this purpose, the sample was spin coated several times as described above. However, the annealing process was necessary after the deposition of each layer to stabilize the film and prevent it from being dissolved. The number of repetitions depends on the desired film thickness.

Polymer template extraction

The removal of the polymer template PS-b-PEO from hybrid films was necessary for porous TiO_2 films. In this thesis, different extraction methods were carried out and compared.

Calcination is the most widely used method to burn away the polymer template and to enable TiO_2 to crystallize. It was used as a reference method. Therefore, a tube furnace was heated up to 400 °C with a heating ramp 375 °C/h and then kept at this temperature for 4 h. The samples were taken out after the furnace was cooled down to room temperature.

As an alternative method for polymer removal, UV irradiation was performed in a metal chamber for 20 h, where the UV lamp was 15 cm above the sample stage. The sample was heated up to around 90 °C after 20 h irradiation. Oxygen plasma was also used as another method to remove PS-b-PEO, with the pressure of 0.4 mbar for 30 min. The plasma was generated at 200 W. Additionally, solvent treatment was used. The PS-b-PEO/TiO_2 sample was immersed in a DMF bath for 10 min and then in a chlorobenzene bath for 60 min. Afterwards, the sample was taken out of the solvent and dried by spin coating (4000 rpm for 30 s).

P3HT backfilling

After the polymer template PS-b-PEO was extracted from the hybrid film, a porous TiO_2 film was formed. In order to finalize the whole active layer, the porous TiO_2 film was backfilled with the electron donor P3HT. The P3HT was firstly dissolved in chlorobenzene with the concentration of 20 mg/ml. Then the glass vial was sealed with a parafilm and covered by a piece of aluminum foil. The solution was placed on a shaker overnight. The next day, before the P3HT deposition, the TiO_2 film was pre-soaked in a chlorobenzene bath for 1 h. Afterwards, the sample was placed in a spin coater. Before chlorobenzene fully evaporated, the P3HT solution was dropped on top of the sample and kept for 60 s. Two steps of spin coating followed (first with 900 rpm for 10 s and then 2500 rpm for 50 s). Finally, the P3HT/TiO_2 hybrid samples were annealed at 140 °C under constant nitrogen flow for 10 min to enhance the crystallinity of P3HT.

4.3 Organic solar cell preparation

P3HT:PCBM solar cells are multiple layer devices, including both electrodes, blocking layers, and the active layer, which have been carefully introduced in chapter 2. In this thesis, two types of solar cells were prepared, one with standard geometry and the other one with the inverted geometry. For both types of solar cells the active layers were made out of a P3HT:PCBM BHJ film. The standard solar cell had indium tin oxide (ITO) and aluminum layers as electrodes, while the FTO and the gold electrodes were used in the inverted solar cell. Moreover, a compact TiO_2 (hole blocking layer) was utilized in the inverted geometry.

The solar cell preparation procedures for both standard and inverted solar cells are presented in figure 4.5. For a standard solar cell, the ITO-covered glass (SOLEMS) was partially etched away via a combination of zinc and hydrochloric acid. Afterwards, the patterned ITO substrates were subsequently cleaned with a detergent solution (alconox solution, 16 g/l), ethanol, acetone, and isopropanol for 10 min in an ultrasonic bath, respectively. Oxygen plasma at 0.4 mbar for 10 min was followed to ultraclean the sample and increase the hydrophilicity of the ITO surface. Then the ITO substrate, as shown in figure 4.5a, is ready to be used for the following processes. Before spin coating (3000 rpm for 60 s) on top of the patterned ITO substrate, the PEDOT:PSS aqueous solution was placed in an ultrasonic bath for 15 min and then filtered by a PVDF filter (0.45 µm). The obtained PEDOT:PSS layer, denoted by the blue color in figure 4.5b, was annealed under ambient condition at 150 °C for 10 min. The P3HT:PCBM active layer was prepared as described in section 4.2.3 (red and black blends in figure 4.5c). Afterwards, the aluminum

layer was thermally deposited on top of the P3HT:PCBM layer under vacuum conditions of around 3×10^{-5} mbar in an evaporation chamber. Finally, the device was transferred to a glove box for annealing at 140 °C for 10 min. The complete device is illustrated in figure 4.5d.

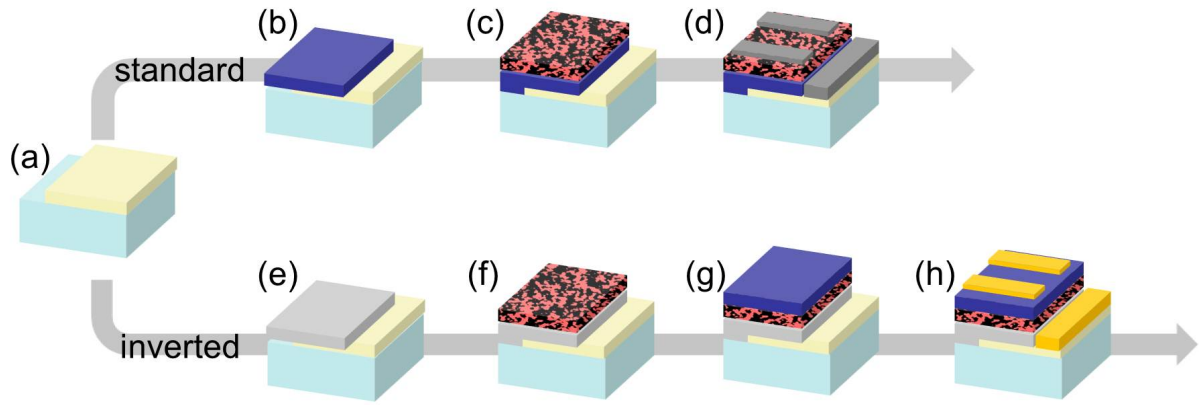

Figure 4.5: *The sketch of solar cell preparation procedures for both standard ((a), (b), (c), and (d)) and inverted solar cells ((a), (e), (f), (g), and (h)). Light yellow denotes ITO or FTO electrodes. Blue and light gray describe PEDOT:PSS and TiO_2 blocking layers. P3HT:PCBM active layer is represented by red and black blends. Aluminum and gold electrodes are illustrated by dark gray and golden layers.*

For the inverted solar cell preparation, a FTO-covered glass substrate was used. The etching, cleaning, and oxygen plasma process were the same as for ITO. After all these processes (figure 4.5a), a compact TiO_2 layer was deposited on top of FTO and then converted to a denser TiO_2 layer via a titanium tetrachloride ($TiCl_4$) bath treatment according to the procedure reported in reference [92]. The resulting TiO_2 blocking layer is indicated by a light gray film in figure 4.5e. The P3HT:PCBM layer (black and red blends in figure 4.5f) was spin coated on top of the dense TiO_2 layer as described in section 4.2.3. Afterwards, the PEDOT:PSS layer (the blue film in figure 4.5g) was deposited by spray coating. The filtered PEDOT:PSS was diluted with isopropanol at a volume ratio of 1:10 and spray coated on top of the active layer with a constant rate of 70 µl/s by a commercial airbrush gun placed 18 cm above the sample. After the spray deposition the sample is spin dried. Afterwards, the gold layer was deposited on top of the PEDOT:PSS layer in an evaporation chamber. To finalize the whole solar cell, thermal annealing at 140 °C for 10 min was performed in a closed environment under a constant nitrogen flow. The final device is sketched in figure 4.5h.

5 Influence of solvent additive on P3HT:PCBM films

Recent studies on OPVs revealed that processing additives, for instance 1,8-octanedithiol (ODT) and 1,8-diiodooctane (DIO), are able to tune the morphology of the active layer of organic solar cells [86,87,93]. Chen et al. reported that an enhanced PCE of P3HT:PCBM solar cell was obtained using 3 vol% ODT [94]. They attributed this enhancement to the interpenetrating P3HT:PCBM networks which were formed in an early stage of film deposition. Furthermore, Razzell-Hollis and coworkers found that the P3HT molecular ordering improves significantly with an ODT concentration of 3 vol% [87]. Likewise, it was shown that fibrilla structures were formed in the ODT additive-assisted P3HT, which led to an enhanced hole mobility [86]. These investigations focused on the local surface morphology, which were mainly revealed by AFM measurements, but inner structural information with a high statistic relevance is not available. Moreover, most studies only emphasized that solvent additive induces demixing between two components, whereas a quantitative understanding of the miscibility of both materials is still missing.

In the present chapter, the inner film structures are characterized via time of flight grazing incidence small angle neutron scattering (TOF-GISANS). As explained in section 3.2.5, such single measurement is equivalent to a set of GISANS measurements performed under a single incident angle with different wavelengths [79]. By selecting a proper incident angle, a part of the measurements is done with its critical wavevector larger than the incident one and a part with its critical wavevector smaller than the incident one. Accordingly, surface- and bulk-sensitive scattering can be obtained simultaneously. Another advantage of TOF-GISANS is a precise determination of the scattering length density (SLD) of the investigated materials, which can be extracted from the wavelength dependence of the Yoneda peak position [91]. The achieved SLD allows for a quantitative analysis of the molecular miscibility between P3HT and PCBM in the present study.

P3HT:PCBM BHJ films are prepared with different volume concentrations of ODT. At first, the microscopic morphologies of these films are discussed in section 5.1. The absorption behavior is investigated via UV/Vis spectroscopy in section 5.2 followed by the

results of crystalline order extracted from GIWAXS measurements (section 5.3). Finally, the performances of the corresponding solar cells are characterized and correlated to the morphology and the crystalline order of the active layers, as shown in section 5.4.

The results presented in this chapter have been summarized in a manuscript and submitted to a journal.

5.1 Mesoscopic morphology

The P3HT:PCBM BHJ films investigated in this chapter are prepared using the solvent additive ODT with varied concentrations. Five different volume concentrations of ODT in the host solvent toluene are chosen: 1 vol%, 3 vol%, 5 vol%, 7 vol%, and 9 vol%. Moreover, a typical P3HT:PCBM BHJ film, without ODT, is prepared as a reference sample.

To characterize the surface morphology of the P3HT:PCBM films processed with different amounts of ODT, AFM and SEM are chosen (section 5.1.1). In addition, the inner morphology and the molecular miscibility between P3HT and PCBM are investigated using TOF-GISANS (section 5.1.2).

5.1.1 Surface morphology

In order to observe the influence of ODT on the surface morphology of P3HT:PCBM BHJ films, AFM measurements are carried out. The obtained AFM topographic data are presented in figure 5.1. The reference film without ODT processing reveals a typical uniform structure consisting of fine grains, as shown in figure 5.1a. With 1 vol% ODT (figure 5.1b), the surface morphology of the P3HT:PCBM film is nearly unchanged. However, inhomogeneous films with significantly larger grains are observed in the samples with ODT of larger or equal to 3 vol% (figure 5.1c, 5.1d, 5.1e, and 5.1f), suggesting a large scale phase separation occurring. The films with ODT of 3 vol% and 5 vol% have isolated island-like structures as shown in figure 5.1c and 5.1d (indicated by red circles). However, the general grain sizes of the films with 5 vol% ODT are significantly larger than those of the films with 3 vol% ODT. With a further increasing amount of ODT volume concentration to 7 vol%, the film starts to show another distinct surface morphology. Elongated worm-shaped domains are observed for this sample, as indicated by red curve in figure 5.1e. For the films with the highest ODT volume concentration of 9 vol%, the bicontinuous worm-shaped large structures are still clearly seen as highlighted in figure 5.1f, showing a similar feature to the sample with 7 vol% ODT. Moreover, the fine structures arise

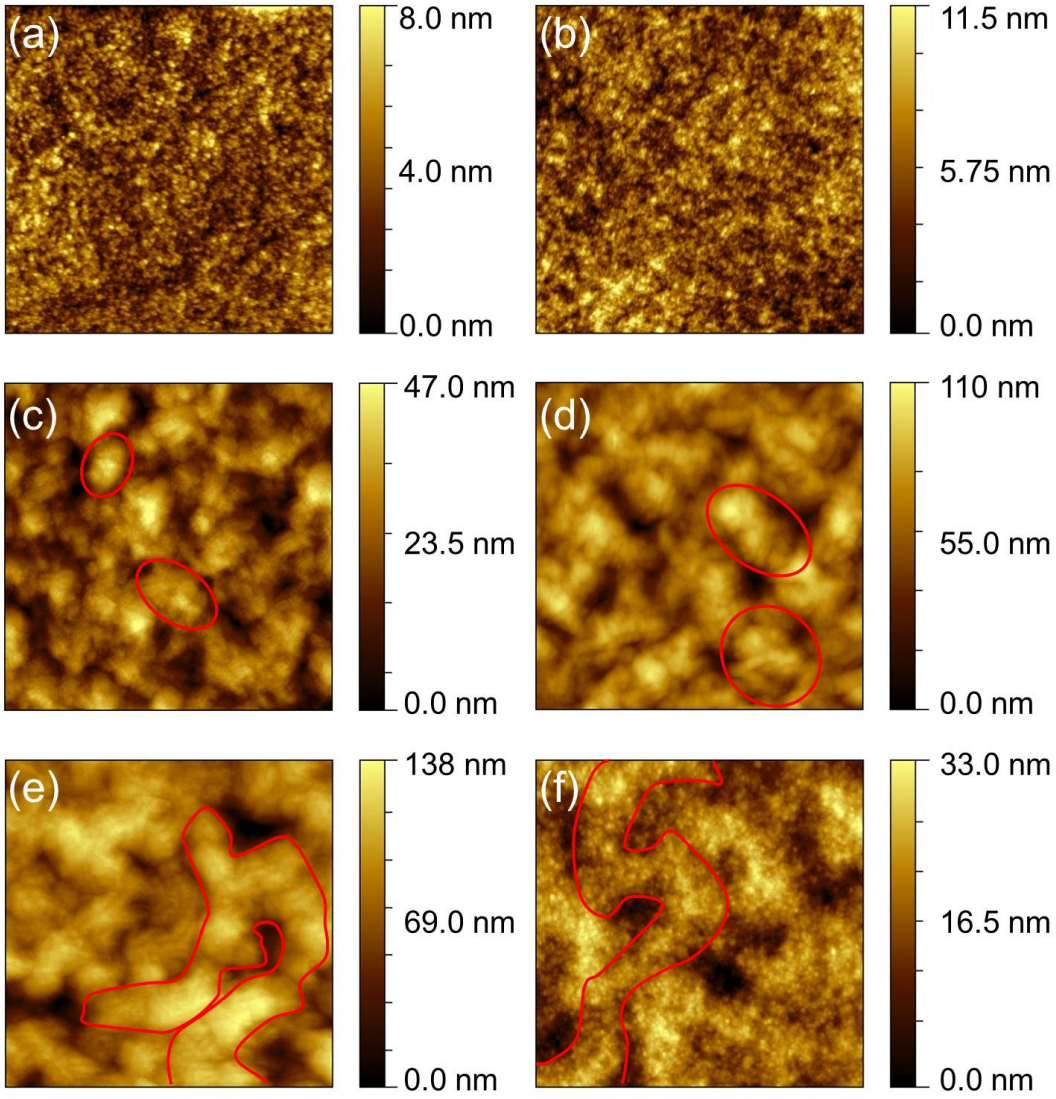

Figure 5.1: *AFM topographic data ($4 \times 4\ \mu m^2$) of the P3HT:PCBM films with different volume concentrations of ODT: (a) 0 vol%, (b) 1 vol%, (c) 3 vol%, (d) 5 vol%, (e) 7 vol%, and (f) 9 vol%. The exemplary large structures are indicated by red lines in (c), (d), (e) and (f), respectively.*

again at the top of the worm-shaped large structures. These tiny dot-shaped features are inferred to be small PCBM aggregates precipitated from the P3HT:PCBM blends. The surface rms-roughnesses of all these samples, extracted from the AFM topographic data, are 1 nm (0 vol%), 2 nm (1 vol%), 8 nm (3 vol%), 19 nm (5 vol%), 23 nm (7 vol%), and 6 nm (9 vol%), respectively, showing a growth trend with increasing amount of ODT up to 7 vol%, but a further increase of ODT to 9 vol% induces a smoother surface. An increased surface roughness of P3HT:PCBM film indicates a stronger phase separation

and an enhancement of ordered structure, which has been frequently observed for typical working solar cells after thermal annealing and solvent annealing [95, 96].

Generally, the influence of ODT on the surface morphology of the P3HT:PCBM films originates from the selective solubility of ODT towards P3HT and PCBM components. It was reported by Shin and coworkers that the solubilities of P3HT and PCBM in ODT were 0.5 mg/ml and 30 mg/ml, respectively [97]. The difference in solubility facilitates a demixing between P3HT and PCBM, thereby inducing phase separations. Chen and coworkers have also found a coarsening of the structure in the P3HT:PCBM films with ODT processing [94]. On the other hand, excess ODT shows an opposite impact on the surface structures. Liu et al. found that with an excess of solvent additive 4-bromoanisole (13%), large features of P3HT:PCDTBT film were replaced by finer structures, which was ascribed to a suppression of demixing by an earlier aggregation of P3HT [98]. This argument also holds true for the sample with 9 vol% ODT in the present work.

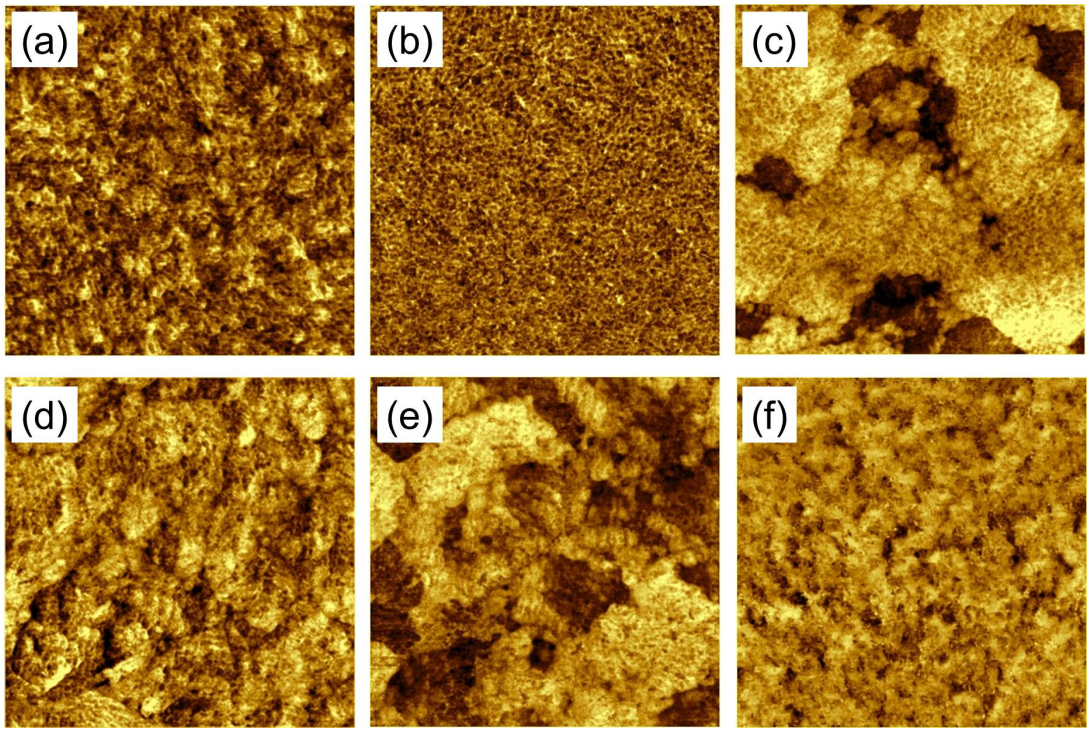

Figure 5.2: *AFM phase data ($1 \times 1\ \mu m^2$) of the P3HT:PCBM films with different volume concentrations of ODT: (a) 0 vol%, (b) 1 vol%, (c) 3 vol%, (d) 5 vol%, (e) 7 vol%, and (f) 9 vol%.*

The corresponding AFM phase data of the P3HT:PCBM BHJ films with different amounts of ODT is shown in figure 5.2. For the samples without ODT (figure 5.2a) and with 1 vol% of ODT (figure 5.2b), P3HT and PCBM are finely interpenetrated into each other. With increasing amount of ODT up to 7 vol%, large separation of the P3HT-rich

phase and the PCBM-rich phase is observed in figure 5.2c, 5.2d, and 5.2e. However, the sample with ODT of 9 vol% does not show prominent phase separation (figure 5.2f). Jin and coworkers reported a similar AFM phase image of the sample with grain-featured PCBM layer on top of P3HT [99]. Thus, it is inferred that the top surface of the sample with 9 vol% ODT might be a PCBM enrichment layer. A more direct evidence will be discussed in the following TOF-GISANS analysis (section 5.1.2). For applications in organic solar cells with a standard geometry, this PCBM enrichment layer would act as a hole blocking layer, which is beneficial for the photovoltaic performance.

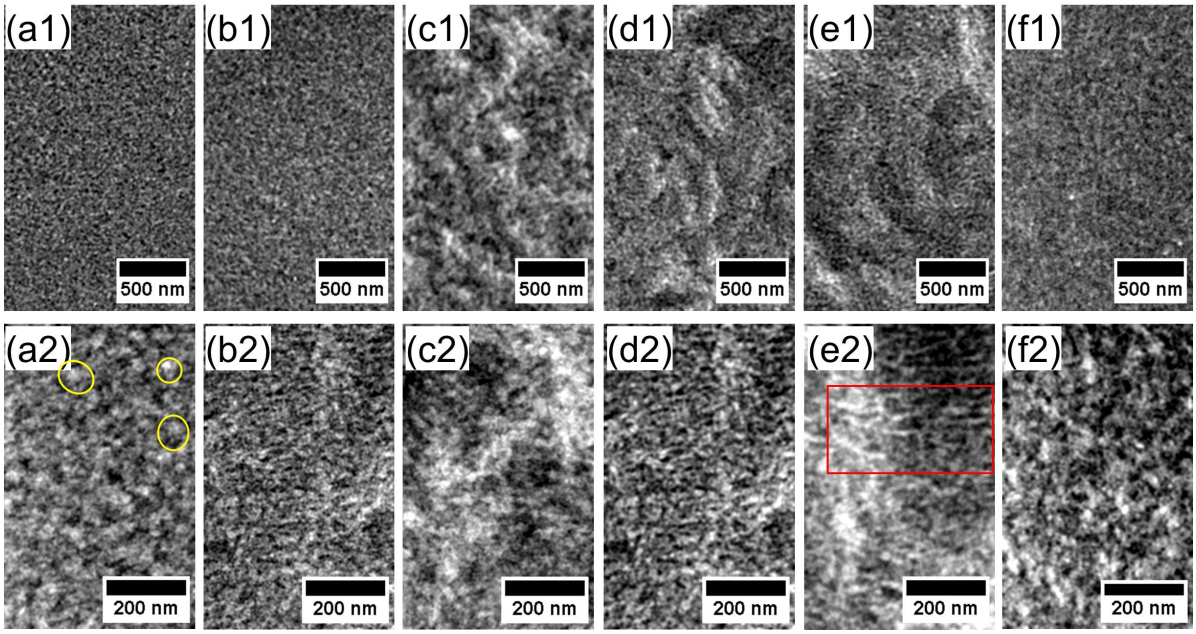

Figure 5.3: *SEM images of the P3HT:PCBM films with different volume concentrations of ODT: (a) 0 vol%, (b) 1 vol%, (c) 3 vol%, (d) 5 vol%, (e) 7 vol%, and (f) 9 vol% in two different magnifications each, which are denoted as 1 and 2, respectively. The spherical structures in (a2) and the area with prominent fibril-like structures in (e2) are indicated by yellow circles and red rectangle, respectively.*

Due to the high surface roughnesses of the films with ODT processing, detailed structural information might be suppressed in AFM measurements. Hence, SEM measurements are carried out as a supplementary study of surface morphology at a smaller length scale. The SEM images of all samples are shown in figure 5.3. Similar to the observation from AFM data, large features appear in the samples with ODT content of 3 vol% to 7 vol%, (figure 5.3c1, 5.3d1, and 5.3e1). For the sample without ODT, the isolated spherical objects are visible as indicated in figure 5.3a2, while these spherical objects are replaced by the fibril-like structures by use of more ODT as highlighted in figure 5.3e2 as an example. These fibril-like structures are generally associated to P3HT crystals [94]. A similar obser-

vation was also reported by Yao et al., who assigned these structures to P3HT crystalline domains in the ODT-processed P3HT:PCBM BHJ films [95]. Hence, it is deduced that the ODT induces the segregation of P3HT and therefore, the crystallinity of P3HT is enhanced [100].

5.1.2 Inner morphology

Since AFM and SEM only reveal surface morphology, TOF-GISANS is employed to gain information about composition as well as the inner morphology. These measurements were performed at the beamline REFSANS of the Helmholtz Zentrum Geesthacht, FRM II, Garching. A fixed incident angle of 0.46° was set for all measurements. Due to gravity for neutrons, the real incident angle is corrected to be 0.46° to 0.50° for various wavelengths (2-14.8 Å). The sample-detector distance was 10.52 m. During data processing a resolution in wavelength $\Delta\lambda/\lambda = 10\%$ was selected.

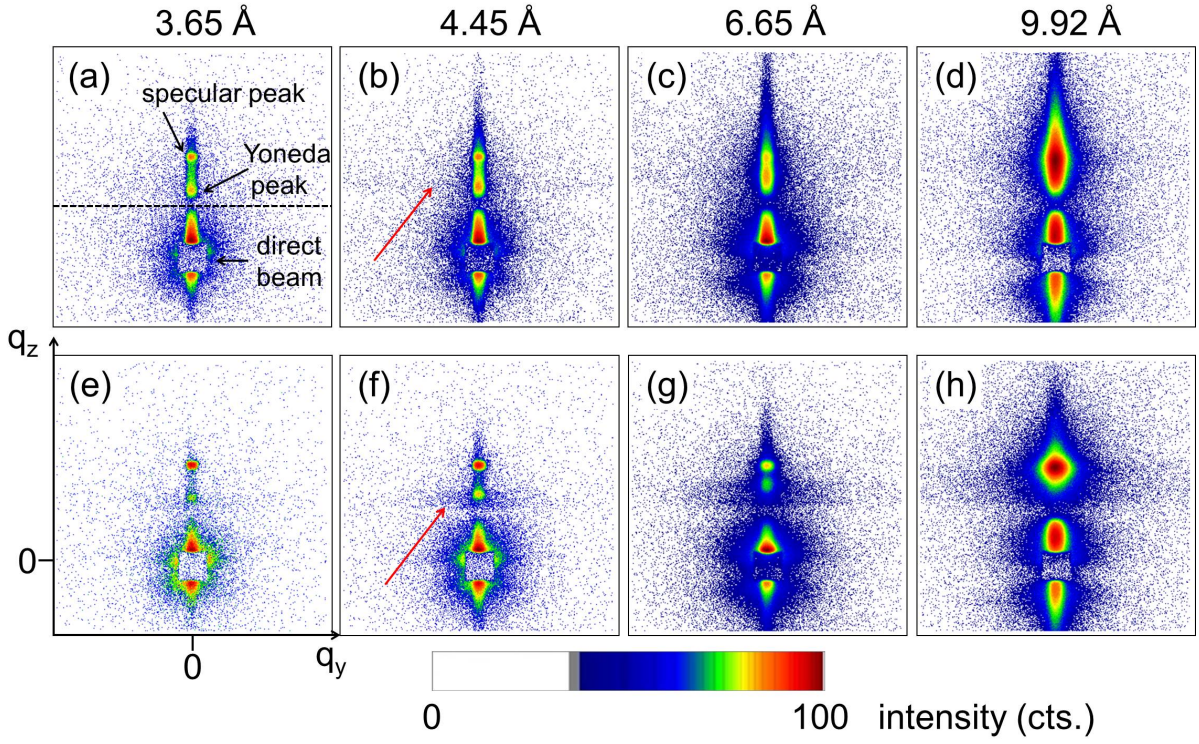

Figure 5.4: *Exemplary presentations of 2D GISANS data of the P3HT:PCBM films (a-d) without ODT and (e-h) with 5 vol% of ODT. From the left to right images, the corresponding average wavelengths are 3.65 Å, 4.92 Å, 6.65 Å, and 9.92 Å, respectively. The specular peak, the Yoneda peak, and the transmitted signal are labeled in (a). The horizon is indicated by the dashed line in (a).*

2D GISANS data with a selection of neutron wavelengths of the P3HT:PCBM films without ODT and with 5 vol% ODT are presented in figure 5.4. These data with different neutron wavelengths of 3.65 Å, 4.92 Å, 6.65 Å, and 9.92 Å are obtained simultaneously for each measurement and selected from the total wavelengths band (2-14.8 Å). The specular peak, the Yoneda peak, and the transmitted signal are labeled in figure 5.4a.

The overall intensity of the scattering data varies with wavelengths (figure 5.4) because of the distribution of the incoming neutron flux as a function of wavelength. Moreover, the position of the Yoneda peak moves upwards with increasing wavelength because the critical angle of the material is proportional to the wavelength (see equation 2.34 in section 2.4.1). Weak intensity side maxima are located at the Yoneda peak position (indicated by red arrows in figure 5.4b and 5.4f). For the sample with 5 vol% of ODT, more intense side maxima are seen in figure 5.4e, 5.4f, 5.4g, and 5.4h compared to the sample without ODT processing (figure 5.4a, 5.4b, 5.4c, and 5.4d). The increase of scattering intensity is caused by an increased number of P3HT and PCBM pure phases.

The vertical line cuts extracted from the 2D TOF-GISANS measurments of all P3HT: PCBM films are shown in figure 5.5 for probed wavelengths of 3.65 Å, 4.03 Å, 4.45 Å, 4.92 Å, 5.44 Å, 6.01 Å, 6.65 Å, 7.35 Å, 8.12 Å, 8.97 Å, 9.92 Å, 10.96 Å, and 12.12 Å, respectively. The specular peaks (indicated by grey dashed lines in figure 5.5) are located at the same position versus neutron wavelengths, while the Yoneda peaks (for example P3HT:PCBM blend as indicated by magenta arrows) shift towards larger $\alpha_i + \alpha_f$ values with increasing neutron wavelengths.

Individual Yoneda peaks of P3HT and silicon are determined from each vertical line cut and respectively remarked by blue and light green crosses in figure 5.5. The critical angles derived from the Yoneda peak positions are displayed in figure 5.6 (blue and light green squares). However, the PCBM Yoneda peak can not be precisely determined and therefore, they are not shown here. The theoretical values of the critical angles of P3HT, PCBM, and silicon are calculated from the scattering length density (SLD) ($6.76 \cdot 10^{-7}$ Å^{-2} for P3HT, $4.34 \cdot 10^{-6}$ Å^{-2} for PCBM, and $2.07 \cdot 10^{-6}$ Å^{-2} for silicon) and displayed in figure 5.6 (blue, green and red lines), showing a good agreement with the experimentally determined values. The critical angles of ODT is not discussed in the present chapter because it can not be detected due to the negative SLD ($-2.8 \cdot 10^{-7}$ Å^{-2}).

Another type of Yoneda peak located between the P3HT and silicon Yoneda peak is observed, as indicated by magenta arrows in figure 5.5. These Yoneda peaks are correlated to the phase consisting of P3HT and PCBM. More specifically, PCBM is molecularly dispersed in the amorphous P3HT phase and therefore, the mixture behaves like one material instead of P3HT or PCBM phase alone. In order to distinguish this mixture from P3HT phase and PCBM phase, the term P3HT:PCBM blend is used in the present

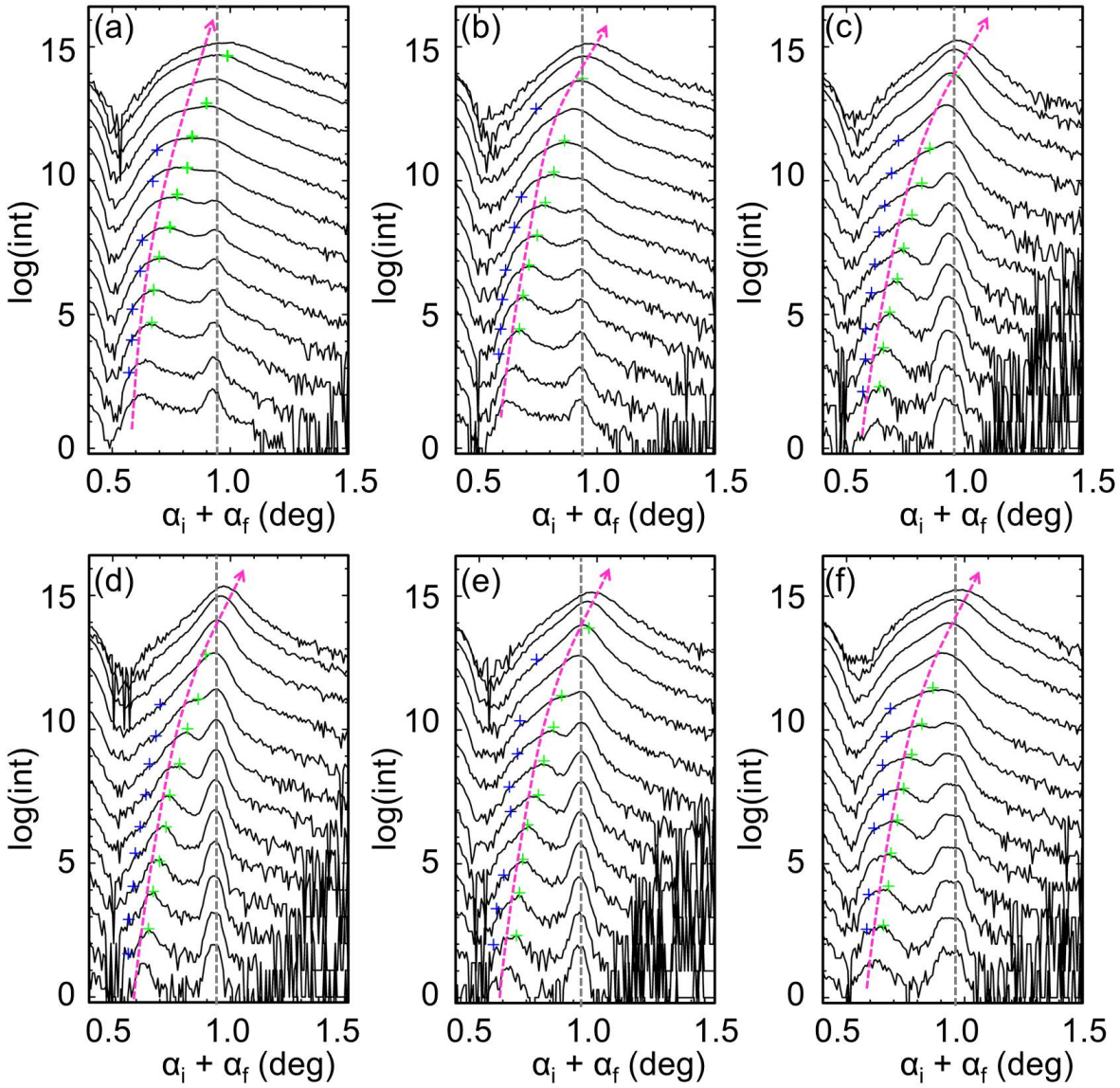

Figure 5.5: *Vertical line cuts extracted from the 2D TOF-GISANS data of the P3HT:PCBM films with different volume concentrations of ODT: (a) 0 vol%, (b) 1 vol%, (c) 3 vol%, (d) 5 vol%, (e) 7 vol%, and (f) 9 vol%. For all vertical line cuts in each image, the corresponding wavelengths are 3.65 Å, 4.03 Å, 4.45 Å, 4.92 Å, 5.44 Å, 6.01 Å, 6.65 Å, 7.35 Å, 8.12 Å, 8.97 Å, 9.92 Å, 10.96 Å, and 12.12 Å, from bottom to top. The specular peaks are indicated by grey dashed lines. The determined Yoneda peaks of P3HT and silicon are marked by blue and light green crosses, respectively. The shift of Yoneda peaks of P3HT:PCBM blend is indicated by the magenta arrows. In each image, the curves are shifted along intensity axis for clarity.*

chapter. Similarly, Ruderer and coworkers found that besides pure phases of P3HT and PCBM the phase of P3HT:PCBM mixture at a molecular level exists in P3HT:PCBM

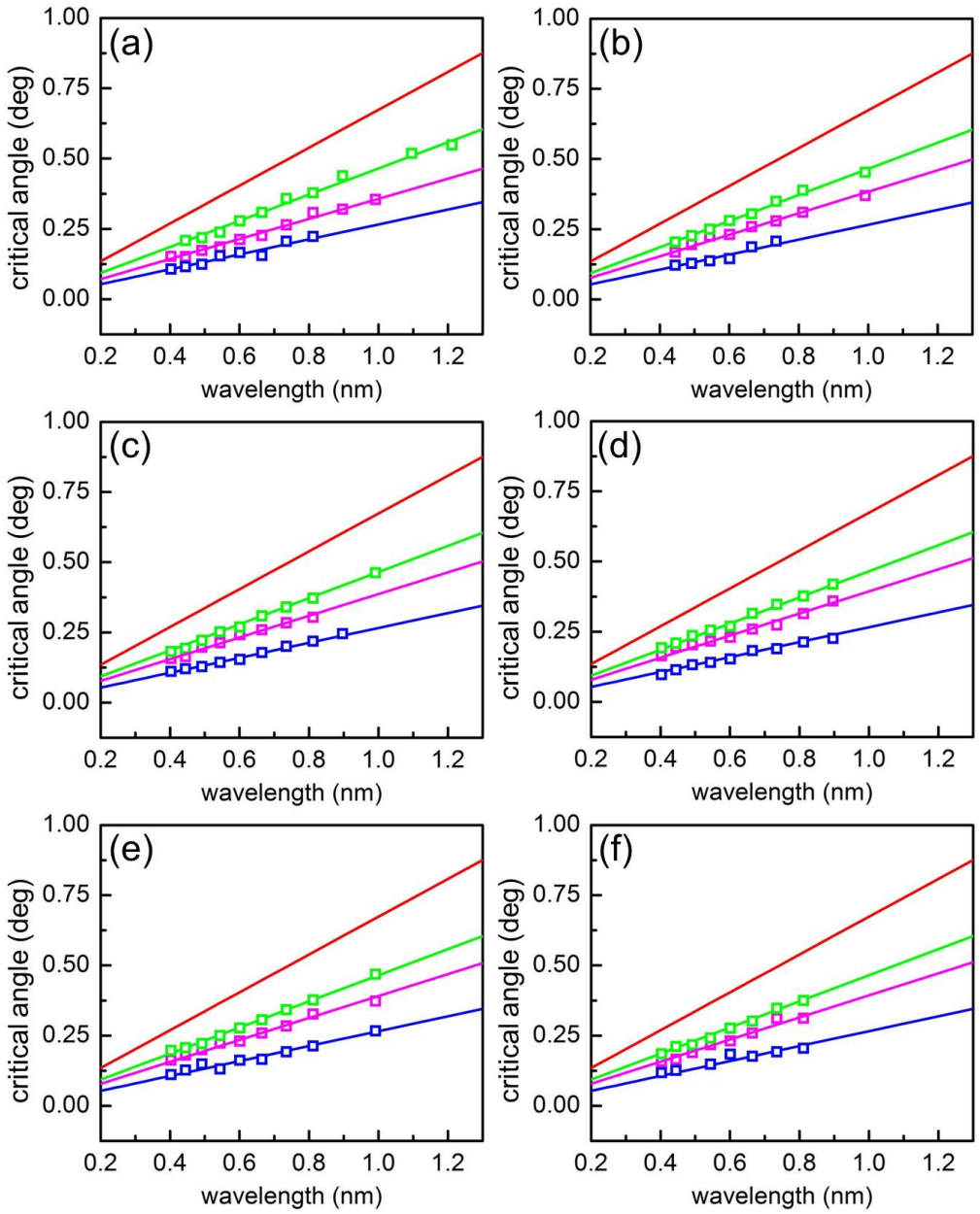

Figure 5.6: *Linear fits (magenta lines) to the critical angles of P3HT:PCBM blend (magenta squares) versus wavelength of neutrons for the P3HT:PCBM films with different amounts of ODT: (a) 0 vol%, (b) 1 vol%, (c) 3 vol%, (d) 5 vol%, (e) 7 vol%, and (f) 9 vol%. The theoretical values of P3HT (blue), PCBM (red), and silicon (green) and the corresponding experimentally determined values are indicated by lines and squares. All the experimentally determined values are calculated from the Yoneda peak positions. The experimental PCBM Yoneda peaks can not be precisely determined and therefore, they are not shown in this figure.*

BHJ films [101]. They further confirmed that PCBM is molecularly dispersed in the

amorphous P3HT matrices for the mixture phase. The critical angles of P3HT:PCBM blend are derived from the Yoneda peak positions for different neutron wavelengths and represented by magenta squares in figure 5.6. By fitting a linear function through the critical angles of P3HT:PCBM blend versus neutron wavelengths, the corresponding SLD is obtained from the slope via the equation 2.34 described in section 2.4.1. Through the usage of the individual SLD of P3HT ($6.76{\cdot}10^{-7}$ Å^{-2}) and PCBM ($4.34{\cdot}10^{-6}$ Å^{-2}), the SLD of the P3HT:PCBM blend is calculated to be around $1.22{\cdot}10^{-6}$ Å^{-2}, $1.41{\cdot}10^{-6}$ Å^{-2}, $1.43{\cdot}10^{-6}$ Å^{-2}, $1.48{\cdot}10^{-6}$ Å^{-2}, $1.46{\cdot}10^{-6}$ Å^{-2}, and $1.48{\cdot}10^{-6}$ Å^{-2} for the P3HT:PCBM films with ODT from 0 vol% to 9 vol%, respectively.

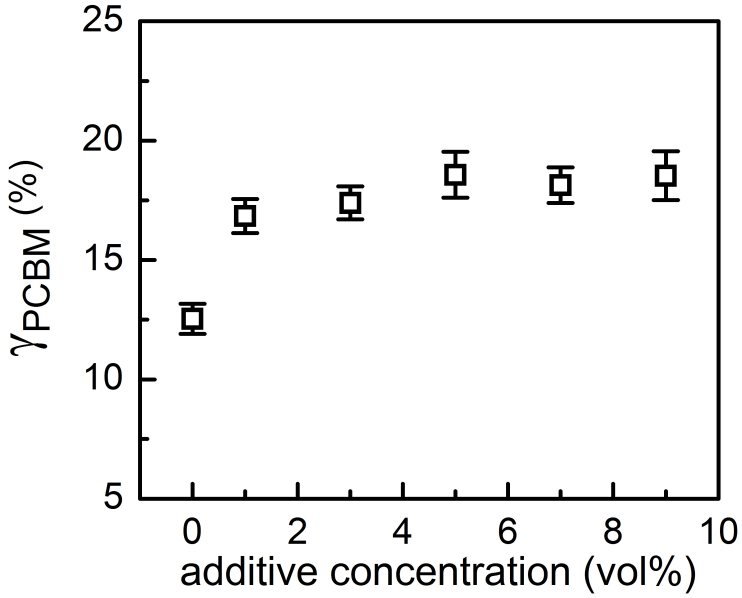

Figure 5.7: *The fraction γ_{PCBM} of molecularly dispersed PCBM in P3HT matrices for the P3HT:PCBM films with various volume concentrations of ODT.*

Looking into the phase of P3HT:PCBM blend, the fraction γ_{PCBM} of molecularly dispersed PCBM in P3HT matrices is further derived from the formula (SLD_{P3HT} + $\gamma_{PCBM}\mathrm{SLD}_{PCBM} = \mathrm{SLD}_{P3HT:PCBM\ blend}$) and depicted in figure 5.7. For the P3HT:PCBM film without ODT processing, the dispersed PCBM fraction γ_{PCBM} is about 12.5%. From literature, a smaller value of around 9% was reported for a P3HT:PCBM BHJ film prepared from chlorobenzene [101], suggesting that the molecular miscibility between P3HT and PCBM is influenced by the host solvent. Whereas, for the samples with ODT processing the γ_{PCBM} increases significantly up to (16.8-18.5) %. The increase of γ_{PCBM} is directly correlated to the use of ODT. During film deposition, P3HT is more easily expelled from the solution than PCBM at an early stage as toluene evaporates much faster

than ODT and P3HT has an extremely low solubility in ODT. Accordingly, more PCBM remains in the mixture of P3HT and PCBM. Shin et al. proposed a two-step drying model to blade-coated P3HT:PCBM films deposited from an ODT-assisted chlorobenzene solution [97]. They observed a complete evaporation of chlorobenzene within 30 s while more than 300 s for the removal of ODT. However, with further increasing volume concentration of ODT, no strong influence on the dispersed PCBM fraction γ_{PCBM} is found. This might be due to a saturation of the solubility of PCBM in P3HT matrices.

In order to obtain information about lateral structures for all P3HT:PCBM films, horizontal line cuts are taken at the theoretical position of the PCBM Yoneda peak. The selected horizontal line cuts are displayed in figure 5.8 with probed wavelengths of 6.01 Å, 6.65 Å, 7.35 Å, 8.12 Å, 8.97 Å, 9.92 Å, 10.96 Å, and 12.12 Å, respectively. The cuts obtained for smaller wavelengths are not shown here due to extremely low intensities. The horizontal line cuts are fitted within the framework of DWBA, with detailed description shown in section 3.2.5. In short, two times cylinder shaped objects are selected with Gaussian size distribution. From the fits, two substructures are found in all P3HT:PCBM films. Notably, substructures with structure sizes up to 10 nm are not detectable in the measurements, because REFSANS measurements are more sensitive to large substructures for the chosen settings [91]. Therefore, the structural information in terms of sizes of molecularly dispersed PCBM and the corresponding distances within the phase of P3HT:PCBM blend cannot be extracted from the measurements. However, the substructures in a larger scale (tens hundreds of nanometers) are investigated in the following.

For each of the samples with volume concentration of ODT from 0 vol% to 7 vol%, all horizontal line cuts obtained under various wavelengths can be fitted with the same substructures. For the sample with 9 vol% of ODT, the values from the fits for wavelengths above and below 8.12 Å are different. The change in structure sizes versus wavelengths is generally caused by the depth-sensitivity of neutrons [79]. The incident angle and critical angles of P3HT, PCBM, and P3HT:PCBM blend are drawn as a function of wavelengths in figure 5.9. For wavelengths below 7 Å, the incident angle is above all critical angles, suggesting that the sample is always penetrated by the neutrons no matter which material is enriched at the surface. Thus, the structural information is from the volume. However, for the probed wavelengths above 7 Å, only the critical angle of PCBM is above the incident angle. This indicates that if PCBM is enriched at the surface, neutrons can not penetrate the whole sample and therefore the structural information is from the surface. Based on this, it is inferred that the sample with 9 vol% of ODT has an PCBM enrichment layer at the surface. This inference also proves that the fine graining structures observed in its AFM topographic image (figure 5.1f) is PCBM, which is not observed for other samples. The PCBM enrichment layer at the top of the active layer can act as a hole

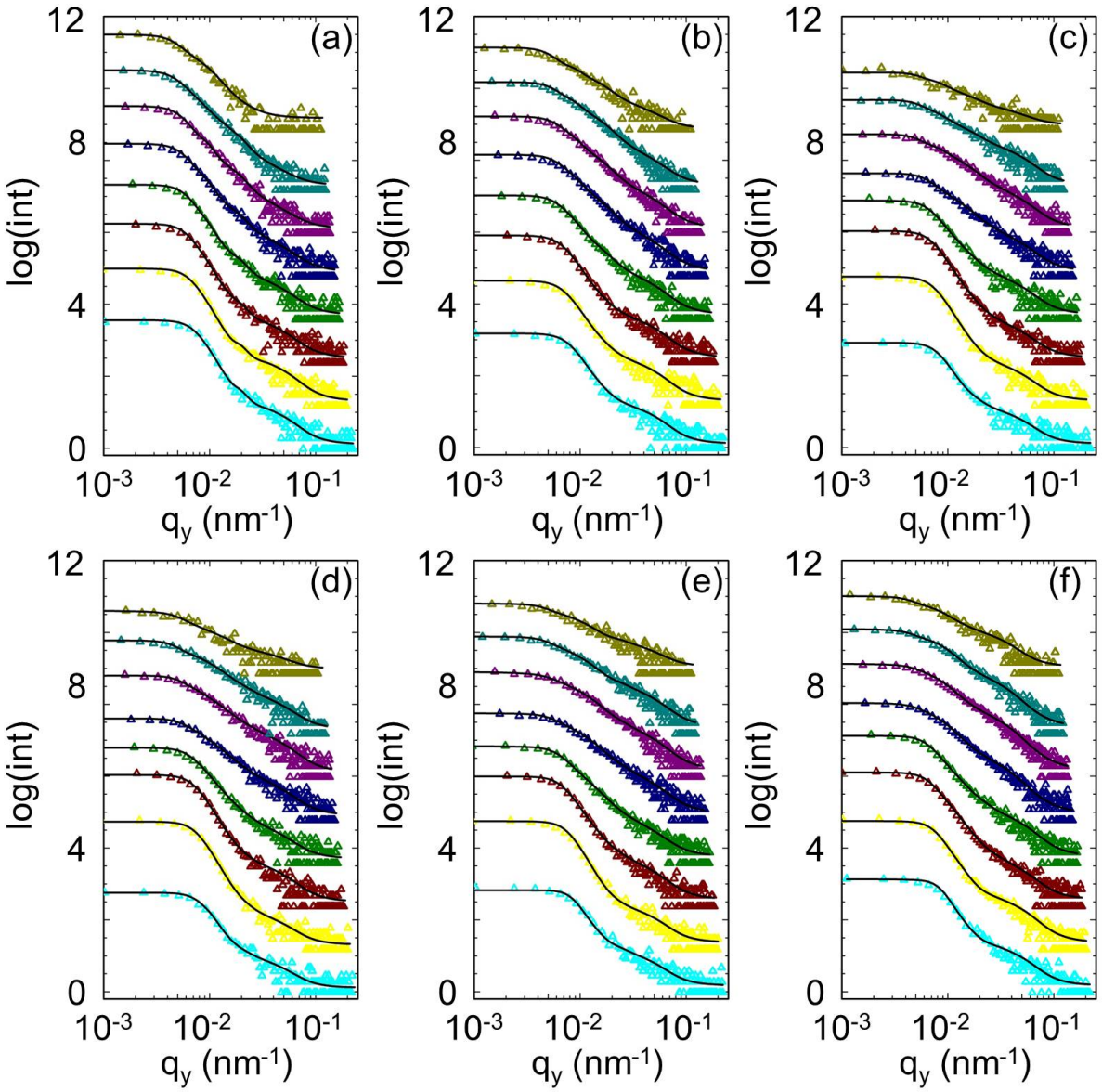

Figure 5.8: *Selected horizontal line cuts (symbols) extracted from the 2D TOF-GISANS data of the P3HT:PCBM films with different volume concentrations of ODT: (a) 0 vol%, (b) 1 vol%, (c) 3 vol%, (d) 5 vol%, (e) 7 vol%, and (f) 9 vol% are shown together with the fit (lines). The corresponding wavelengths are 6.01 Å, 6.65 Å, 7.35 Å, 8.12 Å, 8.97 Å, 9.92 Å, 10.96 Å, and 12.12 Å, from bottom to top in each image. In each image, the curves are shifted along intensity axis for clarity.*

blocking layer and therefore ensures efficient charge extraction and prevents recombination at the interface with top electrodes for solar cells with a standard geometry.

The inner structures in terms of domain sizes and distances extracted from the fitting results are displayed as a function of volume concentration of ODT in figure 5.10.

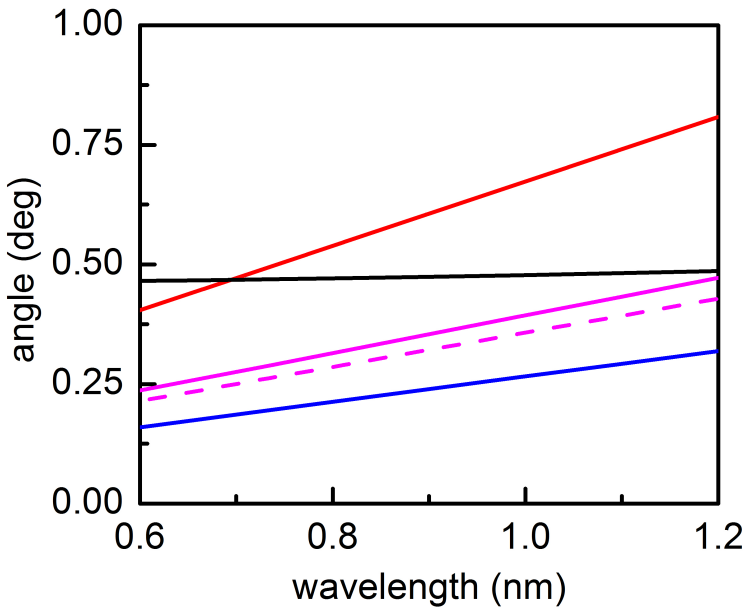

Figure 5.9: *The incident angle and critical angles of P3HT, PCBM, and P3HT:PCBM blend as a function of wavelength. The incident angle is indicated by black line. The theoretical critical angles of PCBM and P3HT are indicated by red and blue lines, respectively. The critical angles of P3HT:PCBM blend for the samples without ODT and with 9 vol% ODT are indicated by magenta dashed and solid lines, respectively. Since the critical angles of P3HT:PCBM blend for other ODT contents are very close to each other, only the bottom (without ODT) and top (9 vol% ODT) lines are shown here.*

Since the horizontal line cuts are taken at the PCBM Yoneda peak position, the domains are assumed to be of PCBM and the region between two PCBM domains are assumed to be either P3HT or P3HT:PCBM blends. For smaller inner substructures (indicated by black symbols in figure 5.10), no obvious change occurs to the structure size while a prominent decrease of the distance is observed with increasing amount of ODT. For larger substructures, a gradual increase of structure size and a significant decrease of the distance are found with increasing amount of ODT. Decrease of the distances indicates a reduction of P3HT domain sizes. Therefore, with increasing ODT concentration, the sizes of P3HT domains gradually decrease, from which an enhancement of charge generation in corresponding active layers is expected.

In conclusion, it is found that the ODT processing improves the fraction γ_{PCBM} in the phase of P3HT:PCBM blend. Furthermore, from the fits of horizontal line cuts substructures in a larger length scale is obtained. It is found that the sizes of pure PCBM phases are increased with increasing amount of ODT, whereas the sizes of pure P3HT phases are decreased. Moreover, for the sample with 9 vol% of ODT it is deduced that

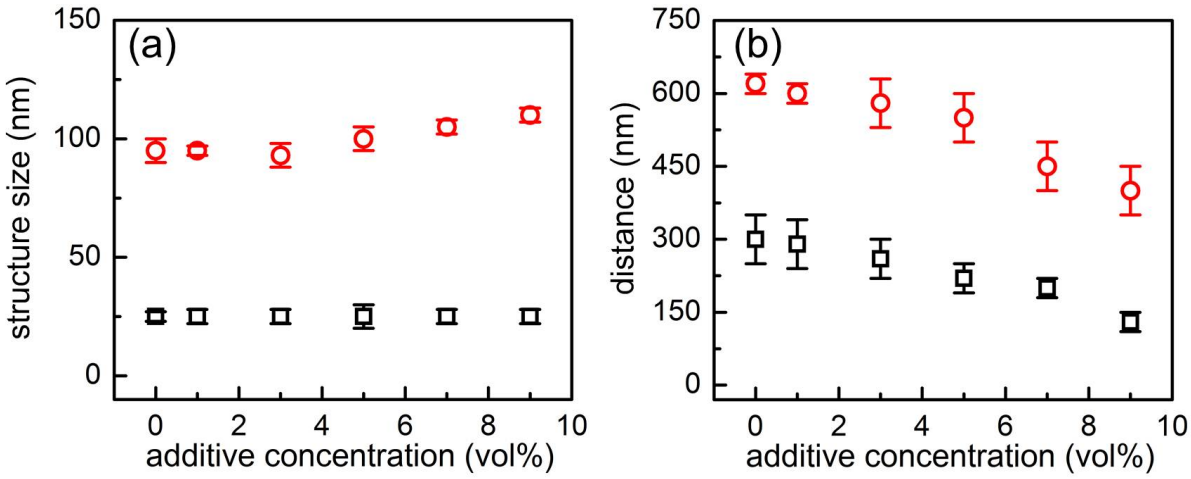

Figure 5.10: *(a) Structure sizes and (b) distances extracted from the fits of the horizontal line cuts of 2D TOF-GISANS data for the P3HT:PCBM films with various volume concentrations of ODT. Two inner substructures are found for all samples. The small and large substructures are represented by black squares and red circles, respectively.*

a PCBM enrichment layer is formed at the top surface. Hence, in summary, the use of ODT as solvent additive significantly reduces P3HT domain sizes and consequently, exciton dissociation is more efficient.

5.2 Absorption behavior

The normalized UV/Vis absorption spectra of the P3HT:PCBM films with different volume concentrations of ODT are shown in figure 5.11a. The absorbance of the P3HT:PCBM film reveals two main features: characteristic PCBM absorption peak at around 335 nm and the P3HT absorption peaks at around 500 nm, 550 nm, and 600 nm. The position of the characteristic PCBM absorption peak stays unchanged for all samples. However, a drop in relative intensity is found with increasing amounts of ODT. This phenomenon has been previously reported and correlated to the formation of PCBM aggregates in micrometer scale [102, 103].

The main P3HT absorption peak (at around 500 nm) redshifts with increase of ODT, suggesting an increased conjugation length of the P3HT chains [30, 72]. In addition, an increment of intensities of the shoulder-like absorption peaks located at around 550 nm and 600 nm is an indication for enhancement of the P3HT ordering [73]. In order to obtain detailed parameters regarding the free exciton bandwidth W and the main peak position of P3HT, the contributions of PCBM and P3HT are extracted from the absorbance spectra.

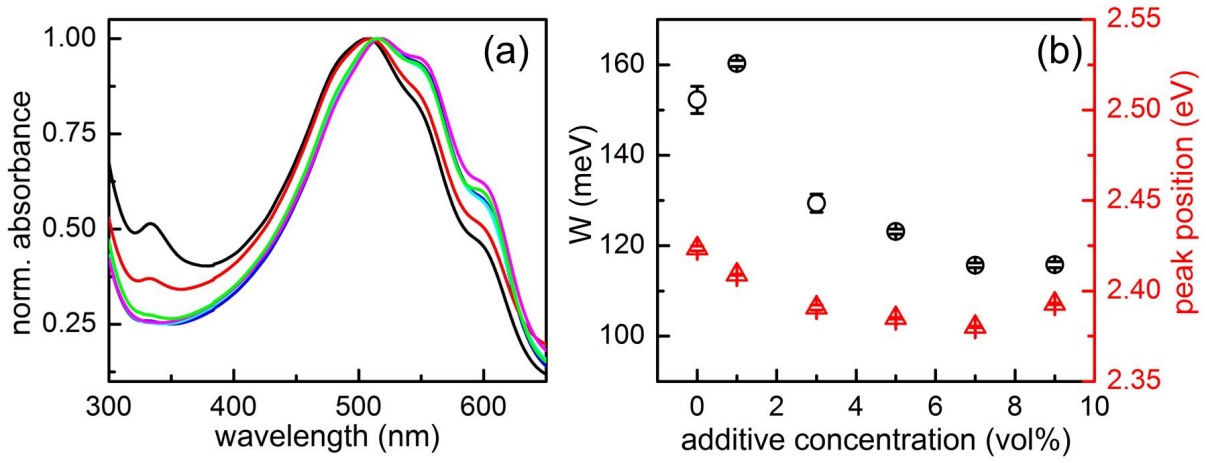

Figure 5.11: *(a) The normalized UV/Vis absorption spectra of the P3HT:PCBM films with different volume concentrations of ODT: 0 vol% (black), 1 vol% (red), 3 vol% (cyan), 5 vol% (blue), 7 vol% (magenta), and 9 vol% (green). (b) Calculated free exciton bandwidth W (black dots) and main peak position (red triangles) of the P3HT:PCBM films as a function of amount of ODT.*

Afterwards, each spectrum is fitted using five Gaussian peaks with equal width. The free exciton bandwidth is calculated using the model of weakly coupled H-aggregates as explained in section 2.3.2, and the main peak position of P3HT is obtained directly from the fit.

From the plot of the free exciton bandwidth W (black symbols in figure 5.11b), it is noted that for the sample with 1 vol% of ODT the free exciton bandwidth is of 160 meV which stays quite similar to the sample without ODT processing (152 meV). With further increase of ODT to 3 vol%, a significant drop of the free exciton bandwidth is found. This is attributed to a strong enhancement of the P3HT molecular ordering. The free exciton bandwidth decreases steadily with a further increase of ODT to 7 vol% but much less pronouncedly. In the end, the value of free exciton bandwidth is almost maintained for the samples with ODT of 7 vol% and 9 vol%.

The main peak position of the P3HT for all P3HT:PCBM films are presented by red symbols in figure 5.11b. The position of this peak clearly redshifts for the samples with ODT from 0 vol% to 3 vol%. When the volume concentration of ODT exceeds 3 vol% (except for 9 vol%), the peak position stays almost unchanged. While, the sample with 9 vol% of ODT exhibits an opposite trend as the main peak position of P3HT is shifted to a higher energy.

In conclusion, the ODT processing is beneficial for improving the P3HT molecular

ordering, indicated by the reduced free exciton bandwidth and the red-shift of the P3HT main absorption peak. Besides the information about the molecular ordering, the red-shift of the P3HT absorbance spectrum is correlated to a change in the bandgap of the P3HT. Accordingly, a potential influence on the V_{OC} of the corresponding solar cells is expected.

5.3 Crystalline order

For a more quantitative information about the crystalline order in the P3HT:PCBM BHJ films with different volume concentrations of ODT, GIWAXS measurements are carried out. Lattice constants and crystalline orientation of P3HT can be precisely determined, and the P3HT crystal size can be roughly estimated (section 2.4.2). The measurements were performed at an in-house device GANESHA 300 XL SAXS SYSTEM by JJ X-Ray Systems ApS. The X-ray wavelength was 0.154 nm. The sample-detector distance and incident angle were set to be 106 mm and 0.2°, respectively. In addition, due to a relatively low X-ray flux compared to that from synchrotron facilities, a larger beam size of 0.3 × 0.3 mm^2 was selected using a set of horizontal and vertical slits.

Figure 5.12 displays the 2D GIWAXS data of the P3HT:PCBM BHJ films with different volume concentrations of ODT. The (010), (100), (200), and (300) Bragg peaks are highlighted by the white dashed circles in figure 5.12a and 5.12e, which are assigned to P3HT crystals. For the P3HT:PCBM film without ODT processing, only the (100) and (010) Bragg peaks are clearly visible (figure 5.12a), while the higher orders of the (100) Bragg peak gradually appear with the addition of ODT (figure 5.12b, 5.12c, 5.12d, 5.12e, and 5.12f), indicating an enhancement of the P3HT crystallization along the (100) planes. Moreover, for the sample without ODT, the (100) Bragg peak is pronounced in both vertical and horizontal directions (figure 5.12a), indicating an co-existence of edge-on and face-on orientations. Whereas, for the samples with ODT processing (figure 5.12b, 5.12c, 5.12d, 5.12e, and 5.12f), (100) Bragg peaks are only clearly observed in the vertical direction, indicating an edge-on dominated orientation. Furthermore, the arc-like feature (indicated by the arrow in figure 5.12d) is visible for all 2D GIWAXS data, which is known to be random orientated PCBM [104].

In figure 5.13, the vertical and horizontal sector integrals extracted from the reconstructed 2D GIWAXS data are shown. It has to be mentioned at first that the peak widths and intensities obtained from these measurements can not be directly compared to those obtained from the GIWAXS measurements in the synchrotron facilities. It has been reported that the widths and intensities of the characteristic diffraction peaks also

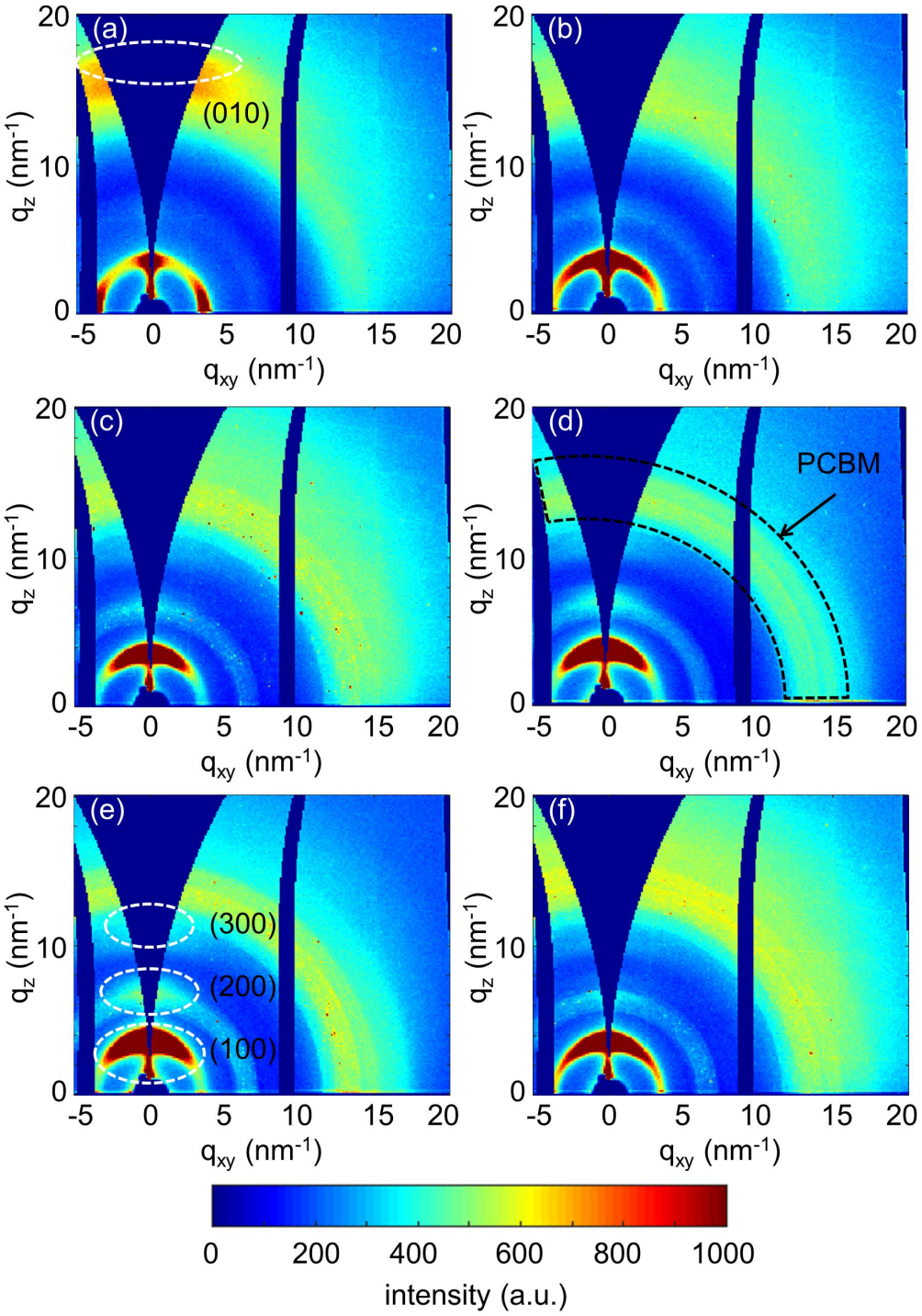

Figure 5.12: *2D GIWAXS data of the P3HT:PCBM films with different volume concentrations of ODT: (a) 0 vol%, (b) 1 vol%, (c) 3 vol%, (d) 5 vol%, (e) 7 vol%, and (f) 9 vol%. The (010), (100), (200), and (300) Bragg peaks of the P3HT crystals are highlighted by the white dashed circles in (a) and (e).*

depend on the X-ray beam size and the scattering setup in addition to the intrinsic parameters of the crystals themselves [51, 104]. Nevertheless, a comparison among all the samples which were measured under the same conditions is reliable.

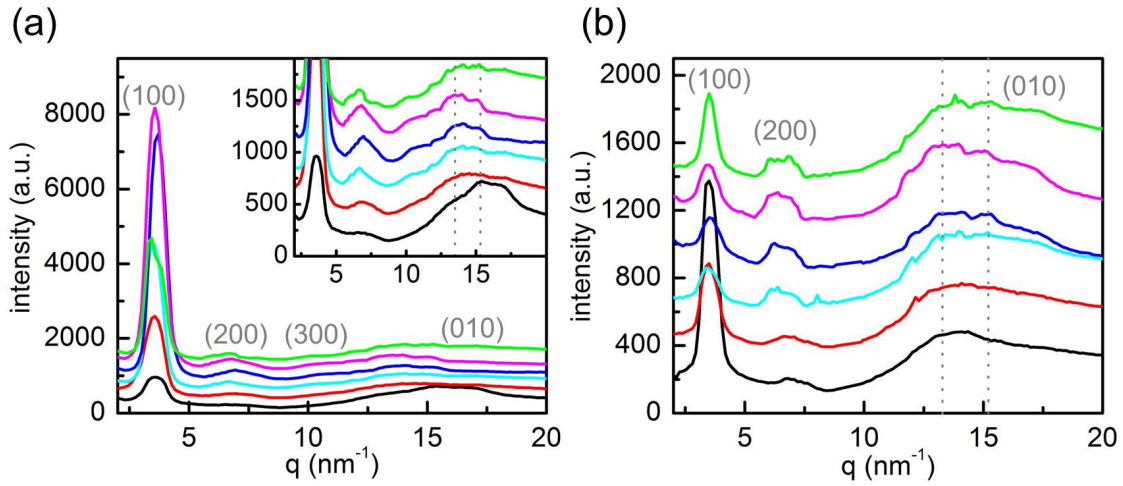

Figure 5.13: *The (a) vertical and (b) horizontal sector integrals extracted from the reconstructed 2D GIWAXS data of the P3HT:PCBM films with different volume concentrations of ODT: 0 vol% (black), 1 vol% (red), 3 vol% (cyan), 5 vol% (blue), 7 vol% (magenta), and 9 vol% (green). In order to clearly visualize the features in high q values in (a), an incomplete figure focused on the q range above 5 nm^{-1} is shown as an inset in (a). The curves are shifted along the intensity for clarity.*

At first, the crystalline information about P3HT is discussed. It is found that the (100) Bragg peak (located at around 3.5 nm^{-1}) in the vertical sector integral (figure 5.13a) gets more pronounced with increasing ODT content up to 5 vol% (indicated by blue line). The increase of intensity is due to the development of the (100) plane of P3HT crystals in vertical direction. In contrast, for the sample with 7 vol% of ODT, the intensity of the (100) Bragg peak maintains similar to that for the sample with 5 vol% of ODT. With further increasing to 9 vol%, a strong decrease of the (100) Bragg peak is observed, indicating an inverse impact of overdosed ODT on the crystallization along the (100) plane. An opposite trend is observed for the intensity of the (100) Bragg peak in the horizontal sector integral when the volume concentration of ODT is increased (figure 5.13b). This suppression in the intensity of the (100) Bragg peak is resulted from a decrease of the crystallization along the (100) plane in horizontal direction. In addition, the inverse tendencies in vertical and horizontal directions confirm that with ODT processing the crystalline orientation of the P3HT is changed from the co-existence of edge-on and face-on to the edge-on.

Information about the molecular packing of PCBM can also be extracted from the GIWAXS measurements. Two peaks indicated by grey dotted lines in figure 5.13 correspond

to PCBM. The peak located at around 13.4 nm^{-1} originates from the amorphous PCBM, which is frequently observed for P3HT:PCBM BHJ films [105]. The other peak observed at around 15.1 nm^{-1} comes from PCBM nanocrystals. A similar d-spacing of the PCBM nanocrystals was found using TEM by Yang and coworkers, who found that both the amorphous PCBM and the densely packed PCBM nanocrystals were obtained from thin film made out of toluene [106]. However, this feature is rarely observed from GIWAXS measurements. In general, the nanocrystals-related peak becomes more pronounced with increasing volume concentration of ODT, meaning an increase in the number of PCBM nanocrystals. This is probably caused by a slow evaporation rate of ODT as well as a large amount of ODT used, which allows more PCBM to self-assemble into nanocrystals during a longer period. It is generally believed that the solvent evaporation rate strongly influences the crystallization behavior of P3HT and PCBM from a film solidification [107].

The P3HT (100) lattice constant is derived from the position of the (100) Bragg peak and summarized in table 5.1. The lattice constants are found to to be 1.7-1.8 nm for both horizontal and vertical directions, which are quite close to the values reported in other references [41, 104]. The corresponding crystal sizes are estimated using the Scherrer equation and listed in table 5.1 as well. For the horizontal direction, meaning the information about P3HT crystals with a face-on orientation, the crystal size decreases from (8.6 $\pm$ 0.2) nm to (7.2 $\pm$ 0.2) nm with increasing volume concentration of ODT to 7 vol%. It corresponds in average to a reducing stacking from 5 to 4 (100) backbones. On the contrary, with further increasing of ODT content (9 vol%), crystal size increases to (9.7 $\pm$ 0.3) nm, which is even larger than that of the reference sample. The edge-on P3HT crystals show a first increase in size from (6.6 $\pm$ 0.1) nm to (8.3 $\pm$ 0.2) nm and then a decrease in size to (7.2 $\pm$ 0.3) nm.

The maximum difference of the average size of P3HT crystals is only one lattice plane among all samples and therefore, it is concluded that the influence of ODT on the crystal size is not significant. However, as discussed before, the scattering intensity of P3HT crystals increases dramatically with increasing the volume concentration of ODT except for the sample with 9 vol% ODT. Therefore, the increase in scattering intensity is mainly ascribed to the increasing amount of P3HT nanocrystals. Moreover, the sizes of these nanocrystals are generally in the range of exciton diffusion length ($\sim$ 10 nm), which is beneficial for an efficient exciton dissociation and also charge transportation.

In summary, ODT processing has mild influence on the crystal size. But the amount of the nanocrystals of P3HT and PCBM dramatically increases with increasing volume concentration of ODT. Therefore, the use of ODT as solvent additive predicts an enhancement of the solar cell efficiency from a perspective of the crystallinity.

additive	lattice constant (nm)		crystal size (nm)	
concentration (vol%)	(100)h	(100)v	(100)h	(100)v
0	1.8 ± 0.1	1.8 ± 0.1	8.6 ± 0.2	6.6 ± 0.1
1	1.8 ± 0.1	1.8 ± 0.1	7.5 ± 0.2	6.9 ± 0.1
3	1.8 ± 0.1	1.8 ± 0.1	7.3 ± 0.2	8.3 ± 0.2
5	1.8 ± 0.1	1.7 ± 0.1	7.2 ± 0.3	8.2 ± 0.1
7	1.8 ± 0.1	1.8 ± 0.1	7.2 ± 0.2	7.8 ± 0.1
9	1.8 ± 0.1	1.8 ± 0.1	9.7 ± 0.3	7.2 ± 0.3

Table 5.1: *Lattice constants and crystal sizes of the P3HT crystals extracted from the vertical and horizontal sector integrals of 2D GIWAXS data of of the P3HT:PCBM films with different volume concentrations of ODT: 0 vol%, 1 vol%, 3 vol%, 5 vol%, 7 vol%, and 9 vol%. h and v refer to horizontal and vertical sector integrals, respectively.*

5.4 Solar cell performance

P3HT:PCBM solar cells (standard geometry) with various volume concentrations of ODT are prepared. It needs to be mentioned that the thickness of the active layers in the solar cells is slightly thinner than those used for the TOF-GISANS measurements, in order to achieve a good efficiency. However, it is believed that the information about morphology and crystallinity obtained from the relatively thicker films can still predict the influence of the ODT processing on the photovoltaic performance.

The obtained J_{SC}, V_{OC}, FF, and PCE values of all P3HT:PCBM solar cells with different amounts of ODT are shown in figure 5.14. Generally, J_{SC} (figure 5.14a) and PCE (figure 5.14d) are both improved with increasing volume concentration of ODT. On the contrary, a decrease in V_{OC} with respect to the sample without ODT processing is found (figure 5.14b). For P3HT:PCBM solar cells using chlorobenzene as the main solvent, Chen and coworkers also found that V_{OC} dropped with increasing amount of ODT [94].

For J_{SC}, the improvement with increasing amount of ODT can be ascribed to a more optimized inner morphology and higher crystallinity. For the samples with volume concentrations of ODT from 0 vol% to 7 vol%, the sizes of P3HT domains are decreased and the amounts of the P3HT and PCBM nanocrystals are increased, which lead to the gradual increase in J_{SC}. For the sample with 9 vol% of ODT, besides the smaller P3HT domain sizes, a compact PCBM enrichment layer at the top of the active layer is beneficial for charge collection at the interface with top electrodes in standard solar cells. In order to confirm the role of a PCBM enrichment layer, inverted P3HT:PCBM solar cells with

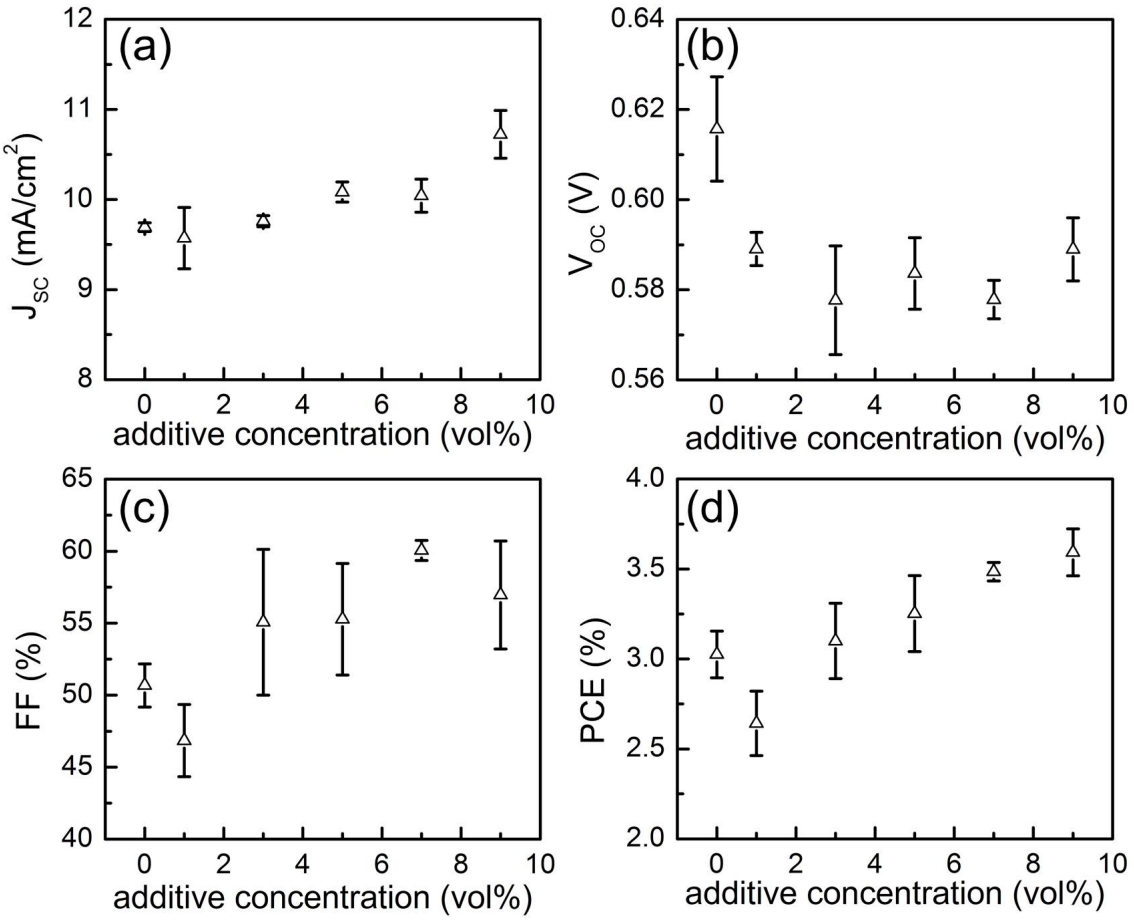

Figure 5.14: *(a) J_{SC}, (b) V_{OC}, (c) FF, and (d) PCE of the P3HT:PCBM films with various volume concentrations of ODT.*

9 vol% of ODT are built. The solar cells show J_{SC} of (9.08 ± 0.08) mA/cm^2, FF of (35 ± 1) %, V_{OC} of (0.43 ± 0.01), and PCE of (1.39 ± 0.01) %, suggesting the active layer with 9 vol% of ODT is unfavorable for an inverted geometry. Most studies found a P3HT enrichment layer near the surface due to the surface free energy [5, 108]. However, in this thesis, an opposite feature is observed for the sample with 9 vol% of ODT, which is probably caused by a low evaporation rate of ODT and a large solubility for PCBM.

The trend of V_{OC} with increasing amount of ODT is similar to that of the main absorption peak position of P3HT (figure 5.11b). Therefore, the variations in V_{OC} is correlated to the changes of the energy levels of P3HT. As a result, it is concluded that ODT processing improves J_{SC} and accordingly PCE of P3HT:PCBM BHJ solar cells, which is mainly caused by changes in the domain size, crystallinity, and enrichment layers.

5.5 Summary

In this chapter, the influence of the solvent additive ODT on the P3HT:PCBM BHJ system is investigated. It is found that the photovoltaic performance of P3HT:PCBM BHJ solar cells is improved with increasing amount of ODT. The increase in efficiency is mainly ascribed to the higher J_{SC}. The UV/Vis absorption measurements of all P3HT:PCBM BHJ films revealed that the crystalline order of P3HT is improved with ODT. Detailed information about P3HT crystals is further obtained by GIWAXS measurements. It is noted that ODT processing does not significantly alter the crystal size or stack distances of P3HT crystals but crystal quantity as higher Bragg peaks become visible. The surface morphology is probed using AFM and SEM. Both measurements reveal more pronounced surface structures due to phase separation between P3HT and PCBM induced by low miscibility of P3HT in ODT.

For the first time, the influence of ODT processing on the fraction of molecularly dispersed PCBM in P3HT matrices γ_{PCBM} is confirmed using the advanced scattering technique TOF-GISANS. A mixture phase between amorphous P3HT and PCBM molecules is found, from which the fraction γ_{PCBM} is quantified. It is found that the fraction γ_{PCBM} first increases and then stays almost constant with increasing ODT amount. In addition, the inner structures in terms of PCBM objects on a larger length scale (tens hundreds of nanometers), is obtained. PCBM object sizes increase for large ones and distances decrease, showing a signature of phase separation. Moreover, it is deduced from TOF-GISANS that a PCBM enrichment layer is formed at the top of the film with maximal amount of ODT (9 vol%).

In conclusion, ODT processing has a strongly positive impact on the photovoltaic performance of P3HT:PCBM BHJ solar cells. Although large phase separation occurs by ODT, its negative influence on efficiency is canceled out by other aspects. Higher crystallinity with reasonable crystal sizes are beneficial for efficient charge transport and accordingly results in a higher J_{SC}. Moreover, in the mixed phase (P3HT:PCBM blend) ODT induces a higher fraction of γ_{PCBM}. On the one hand, the molecularly dispersed PCBM could be beneficial for exciton dissociation. On the other hand, isolated PCBM objects would act as trap centers and induce recombination. On a larger length scale, pure PCBM object sizes increase while the distances (P3HT sizes) decrease, lowering geminate recombination. Especially for the sample with 9 vol% of ODT, a PCBM enrichment top layer enables a optimized vertical composition gradient, which facilitates an efficient charge extraction for the top electrodes. Consequently, the maximal efficiency is found for the sample with 9 vol% of ODT.

6 Exposure to solvent vapor induced degradation of P3HT:PCBM films

Parts of this chapter have been published in the article: Investigation of morphological degradation of P3HT:PCBM bulk heterojunction films exposed to long-term host solvent vapor [109] (W. Wang et al., J. Mater. Chem. A, 4, 3743-3753, 2016, DOI: 10.1039/c5ta09873d).

Over the last few decades, OPV devices have been intensively investigated due to their potential application in large areas, flexibility, light weight, low environmental impact, and low-cost production (such as roll-to-roll printing and spray coating) [110–112]. Major efforts have focused on the development of organic solar cells, with continual improvements of the overall device performance. Most significantly, PCE values above 10% in champion single-junction polymer solar cells have been achieved by utilizing novel conjugated polymers as donor materials [113, 114].

Up to now, P3HT:PCBM BHJ solar cells have been the mostly investigated organic system, which frequently serve as a paradigm to get a basic understanding of the solar cell performance. It is generally known that the inner morphology of the P3HT:PCBM active layer is crucial for the solar cell performance [115]. Via applying an external treatment, such as thermal annealing, solvent annealing, a solution processing additive, or a third component incorporation, the BHJ morphology can be optimized [73, 116]. Correspondingly, the performance of the final device is improved. In literature, most investigations are mainly focused on the surface morphology of the active layer. However, from previous work, it was found that the inner morphology is different from the surface morphology for P3HT:PCBM BHJ films [5]. So far, studies about inner morphology are still very few. Typically, if the obtained structural information is in the nanometer scale, the investigated areas are limited to several micrometers. Therefore, in this thesis, besides local surface characterization, we select a promising scattering technique as the complementary characterization method to reveal the inner morphology of active layers. The probed area is on the length scale of several millimeters, and accordingly the resulting information about the nanostructures is attained with a high statistic relevance.

Most studies have revealed that moderate solvent vapor post-treatments are beneficial for the solar cell performance [117–119]. However, these investigations only payed close attention to the improvement of the solar cell performance by strictly controlling the conditions of the solvent vapor annealing. In contrast, the knowledge of an unintended exposure to the host solvent vapor is limited. As is known, solar cell preparations are typically done in a glove box or closed environment by solution-based processing procedures. During fabrication and handling, solar cells are frequently exposed to a solvent atmosphere which is generated by its processing solvent. Therefore, knowledge about the stability of solar cells in such solvent atmosphere is important.

In this chapter, chlorobenzene, toluene, xylene, and dichlorobenzene are used individually as the host solvent for preparing the P3HT:PCBM active layer and subsequently employed to form a solvent vapor for post-treatment of the samples. After this vapor treatment, the evolution of the active layers and the final solar cells are studied. First, stability of P3HT:PCBM BHJ solar cells prepared out of different solvents is investigated via a long-term solvent vapor treatment (section 6.1). Afterwards, in order to understand the degradation of photovoltaic performance, the influence of solvent vapor on the morphology of P3HT:PCBM layer is studied, as shown in section 6.2. The absorption behavior of these samples are further discussed in section 6.3. Finally, the resulting crystalline order of the degraded active layers is investigated (section 6.4).

6.1 Solar cell performance

P3HT:PCBM solar cells consist of a multi-layer architecture (glass/ITO/PEDOT:PSS/-P3HT:PCBM/aluminum) with a standard geometry. For this style of solar cell, holes are transported through the PEDOT:PSS layer towards the bottom ITO electrode, while electrons are extracted by the top aluminum electrode. Two series of devices are fabricated. In the first series, freshly prepared solar cells are produced following the procedure as described in section 4.3. In order to obtain a similar film thickness for P3HT:PCBM layers prepared out of different solvents, the total concentrations of P3HT and PCBM are adapted to 20 mg/ml for chlorobenzene, 18 mg/ml for toluene, 24 mg/ml for xylene, and 30 mg/ml for dichlorobenzene. These pristine solar cells are used as references. In another series, the long-term solvent vapor post-treated solar cells are fabricated in a way analogous to the reference devices. Before the deposition of the top electrode, they are placed in four separated glass desiccators, into which 10 ml of the corresponding solvent is injected to generate a saturated vapor at 25 °C. The vapor pressures are 12.0 mmHg for chlorobenzene, 28.4 mmHg for toluene, 6.6 mmHg for xylene, and 1.4 mmHg for dichlorobenzene. All devices are stored in their individual desiccators for 5 days.

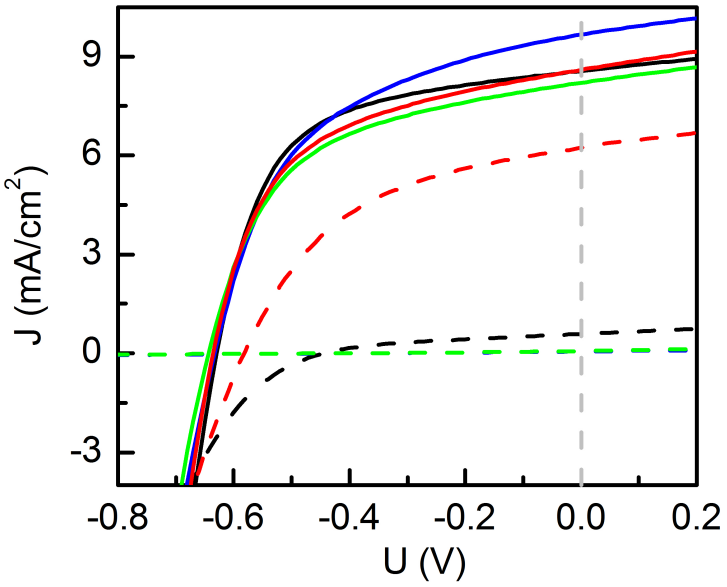

Figure 6.1: *J-V curves of pristine (solid lines) and solvent vapor post-treated (dashed lines) P3HT:PCBM solar cells. Chlorobenzene (black), toluene (blue), xylene (green) and dichlorobenzene (red) are used as host solvent for pristine devices and subsequently to form the solvent vapor for degradation.*

The performance of pristine and solvent vapor post-treated solar cells are examined via J-V characterization, with their results shown in figure 6.1. The photovoltaic performance of all devices is characterized by J_{SC}, V_{OC}, FF, and PCE, which are extracted from the corresponding J-V curves and summarized in table 6.1. All pristine solar cells are shown to function normally. Although efficiency values are moderate as compared to those reported in literature [120], the focus of the present work lies on the solvent vapor induced degradation as compared by a relative loss in device performance.

Compared to the pristine devices, all solar cells demonstrate a dramatic degradation after long-term solvent vapor treatment. On the one hand, toluene vapor and xylene vapor treated-solar cells malfunction completely, acting like large value resistors as illustrated by blue and green dashed curves in figure 6.1. On the other hand, chlorobenzene- and dichlorobenzene-related devices still work, as represented by the remaining J-V performance curves (black and red dashed lines in figure 6.1). Most significantly, the dichlorobenzene-based device shows the best preserved efficiency. Its PCE drops from (2.85 $\pm$ 0.12) % to (1.66 $\pm$ 0.07) %, which is still above 50% of the pristine values. Although the chlorobenzene-based sample still behaves like a solar cell, its PCE sustains only 3% of the original values. Upon a closer look to each photovoltaic parameter

solvent	**device**	J_{SC} **(mA/cm^2)**	V_{OC} **(V)**	FF **(%)**	PCE **(%)**
chlorobenzene	pristine	8.41 ± 0.12	0.63 ± 0.01	58 ± 1	3.09 ± 0.06
	post-treated	0.56 ± 0.03	0.41 ± 0.01	41 ± 1	0.09 ± 0.01
toluene	pristine	9.71 ± 0.06	0.61 ± 0.01	50 ± 2	2.99 ± 0.16
	post-treated	0.05 ± 0.01	0.36 ± 0.03	23 ± 1	0.01 ± 0.01
xylene	pristine	8.16 ± 0.37	0.63 ± 0.01	52 ± 1	2.71 ± 0.19
	post-treated	0.08 ± 0.01	0.40 ± 0.01	20 ± 1	0.01 ± 0.01
dichlorobenzene	pristine	8.47 ± 0.18	0.64 ± 0.01	53 ± 1	2.85 ± 0.12
	post-treated	6.15 ± 0.22	0.58 ± 0.01	47 ± 1	1.66 ± 0.07

Table 6.1: *Comparisons of photovoltaic parameters of pristine and solvent vapor post-treated P3HT:PCBM BHJ organic solar cells prepared out of different solvents, including chlorobenzene, toluene, xylene, and dichlorobenzene.*

as listed in table 4.1, J_{SC}, V_{OC}, FF, and PCE similarly degrade after 5 days of solvent vapor treatments. The significant decline of J_{SC} is mainly ascribed to failure of the solar cells.

In summary, the type of host solvent rarely affects the photovoltaic performance of the freshly prepared solar cells. However, when devices are long-term subjected to the vapor generated by the host solvent, the type of the solvent vapor has a strong impact on the device stability.

6.2 Mesoscopic morphology

It is well known that the morphology of the active layer is of the utmost importance for OPV [121]. On the one hand, a small phase separation within the scale of the exciton diffusion length is necessary for an efficient exciton dissociation. For instance, P3HT has an exciton diffusion length of about 10 nm to 20 nm [40, 115]. On the other hand, relatively large structures can minimize a non-geminate recombination during the charge carrier transport towards the electrodes. Hence, the phase separation of the active layer strongly influences the photovoltaic performance.

Since the effect of different host solvents on the morphology of pristine P3HT:PCBM films has been thoroughly studied in our previous work [5, 26], the focus of this chapter is to investigate the morphology of degraded samples obtained from 5 days of solvent vapor

treatment. For the morphological investigation, P3HT:PCBM films on silicon substrates are prepared following the procedure described in section 4.2.2.

In the present section, surface morphologies of the degraded films are firstly investigated via optical microscopy and AFM in section 6.2.1. Afterwards, their inner structure is studied via GISAXS measurements in section 6.2.2.

6.2.1 Surface morphology

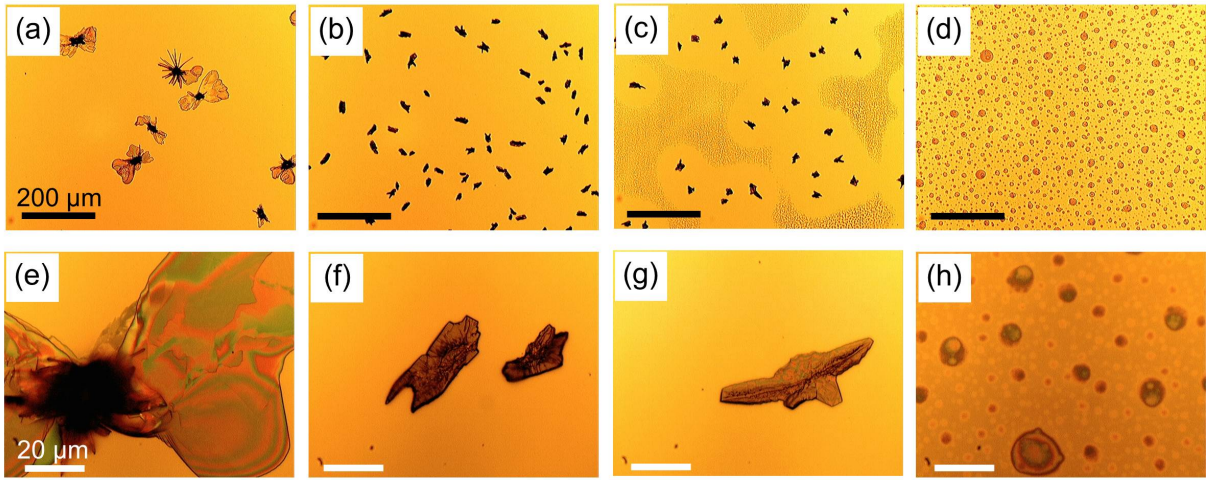

Figure 6.2: *Optical microscopy images of P3HT:PCBM films degraded in (a) and (e) chlorobenzene vapor, (b) and (f) toluene vapor, (c) and (g) xylene vapor, and (d) and (h) dichlorobenzene vapor. Two series of images are shown. One was recorded under a low magnification, with the scale bar (black) of 200 µm, the other one under a high magnification with the scale bar (white) of 20 µm, focusing on the specific surface structures.*

Optical microscopy images of solvent vapor-degraded P3HT:PCBM films are presented in figure 6.2a, 6.2b, 6.2c, and 6.2d under a low magnification. Behaving differently to the corresponding freshly prepared films as reported in literature [5], the degraded samples exhibit prominent surface structures in the micrometer scale. Moreover, tremendous variations in surface morphologies are observed amongst all films. In order to closely observe their distinct structures, zoomed images are shown in figure 6.2e, 6.2f, 6.2g, and 6.2h. The chlorobenzene-, toluene-, and xylene-related samples (figure 6.2e, 6.2f, and 6.2g) show specific structures with sharp edges and textured surfaces, which have been commonly observed for PCBM crystals [122–124]. The sample treated with dichlorobenzene vapor shows spherical structures, which are not typically associated with PCBM crystalline features. Therefore, they are ascribed to a surface morphology rather than big PCBM agglomerates. This estimation will be further evidenced by GIWAXS measurements, as discussed in section 6.4

In detail, figure 6.2a reveals large flower-shaped PCBM aggregates. This effect has been also observed by Paternó et al. [124], who determined these structures as PCBM crystalline aggregates via a micro-focused X-ray diffraction technique. For samples degraded in toluene and xylene vapors (figure 6.2b and 6.2c), more and smaller PCBM aggregates are formed. Additionally, in figure 6.2c, PCBM depletion regions indicated by a lighter yellow color are found close to PCBM aggregates. Similar observations have been discussed in literature [5].

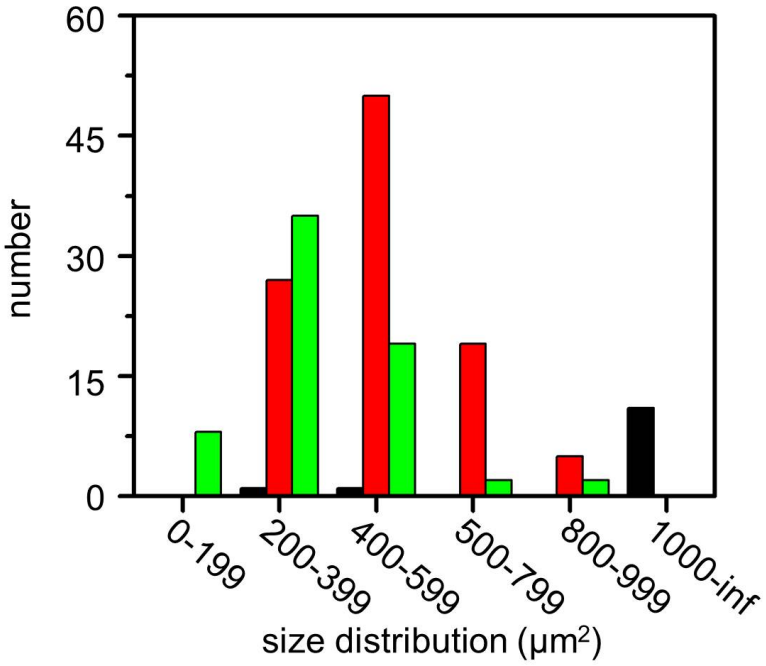

Figure 6.3: *Size distributions of PCBM aggregates in degraded P3HT:PCBM films post-treated with chlorobenzene vapor (black), toluene vapor (red), and xylene vapor (green). These values are extracted from optical microscopy images over a scan area of 1.02 × 0.82 mm². Reproduced from Ref. [109] with permission from the Royal Society of Chemistry.*

Furthermore, figure 6.3 illustrates size distributions of PCBM aggregates in these three samples, which are extracted from optical microscopy images under a scan area of 1.02 × 0.82 mm^2. For chlorobenzene-related sample, the size distribution of PCBM aggregates is mainly located in the range larger than 1000 μm^2, while toluene- and xylene-related samples show the presence of PCBM aggregates with smaller sizes which are mostly in the range from 200 μm^2 to 600 μm^2. The number of PCBM aggregates and their area fractions are extracted from the same optical microscopy images and summarized in table 6.2. The film degraded in toluene vapor shows 101 aggregates, while those post-treated

solvent	number of aggregates	area fraction (%)
chlorobenzene	12	4.9
toluene	101	3.8
xylene	65	1.8

Table 6.2: *Numbers and area fractions of PCBM aggregates in P3HT:PCBM films degraded in chlorobenzene, toluene, and xylene vapors. The values are extracted from optical microscopy images under a scan area of 1.02 × 0.82 mm^2.*

with chlorobenzene and xylene vapors only have 12 and 65 aggregates, respectively. In addition, the chlorobenzene-treated sample has the largest area fraction of PCBM aggregates (4.9%), in comparison to toluene- (3.8%) and xylene-related samples (1.8%).

The influence of different solvent vapors on the morphology is correlated to the fact that the P3HT:PCBM film absorbs solvent molecules during solvent vapor treatment, which enables the rearrangement of P3HT and PCBM components. Hence, the ability of P3HT and PCBM to uptake solvent molecules in various solvent vapors is significant. At first, the vapor pressure of the individual solvents is considered. Amongst all solvents, dichlorobenzene has the lowest vapor pressure of only 1.4 mmHg at 25 °C, while vapor pressures of chlorobenzene, toluene, and xylene are 12.0 mmHg, 28.4 mmHg, and 6.6 mmHg, as mentioned before. During 5 days of solvent vapor treatment, the total absorption of dichlorobenzene molecules could be hindered due to its lowest vapor pressure as compared to the other solvents. Accordingly, PCBM agglomeration is prevented in a saturated dichlorobenzene vapor, as revealed by figure 6.2d. Hu and coworkers studied the weight percentage increments of P3HT:PCBM films in different solvent vapors, and they found that the treatment with dichlorobenzene vapor induced the smallest weight gain in the film [125]. However, they also reported that the most pronounced weight increase in weight was observed in chlorobenzene-related sample rather than the sample post-treated with toluene vapor, although toluene has a higher vapor pressure than chlorobenzene. Hence, the difference in vapor pressure is only one important factor for the absorption of solvent molecules. Additionally, the solubilities of P3HT and PCBM in the individual solvent are taken into account. As found in literature, the solubilities of PCBM are 39.4 mg/ml for chlorobenzene, 16.3 mg/ml for toluene, 24.5 mg/ml for xylene, and 35.9 mg/ml for dichlorobenzene, while P3HT shows solubilities of 33.8 mg/ml, 1.4 mg/ml, 3.4 mg/ml, and 37.1 mg/ml for the corresponding solvents [125]. It is found that chlorobenzene shows a high solubility for both P3HT and PCBM. Therefore, the sample stored in a chlorobenzene vapor gets a much higher weight increase than other samples. The high absorption of solvent molecules explains why the film treated with

chlorobenzene vapor forms the biggest PCBM aggregates. In contrast, toluene and xylene show a low miscibility between P3HT and PCBM, which is correlated to the formation of more PCBM clusters with relatively smaller sizes. Thereby, for solvent vapor treatment, the vapor pressure, solubility of PCBM and P3HT, and the miscibility between these two components affect the PCBM aggregates growth.

AFM measurements are carried out to further characterize the morphology on the nanometer scale. The measurements are performed on homogeneous regions rather than the areas dominated by PCBM aggregates, because free charge carriers are mainly generated in P3HT:PCBM blends rather than PCBM-governed phases. The resulting topography images are shown in figure 6.4. In general, the surface morphologies of these samples are different from each other. As revealed in literatures [5, 26], pristine samples did not show remarkably different surface morphologies. Therefore, it is deduced that the varying surface topography of these samples is caused by different solvent vapor treatments.

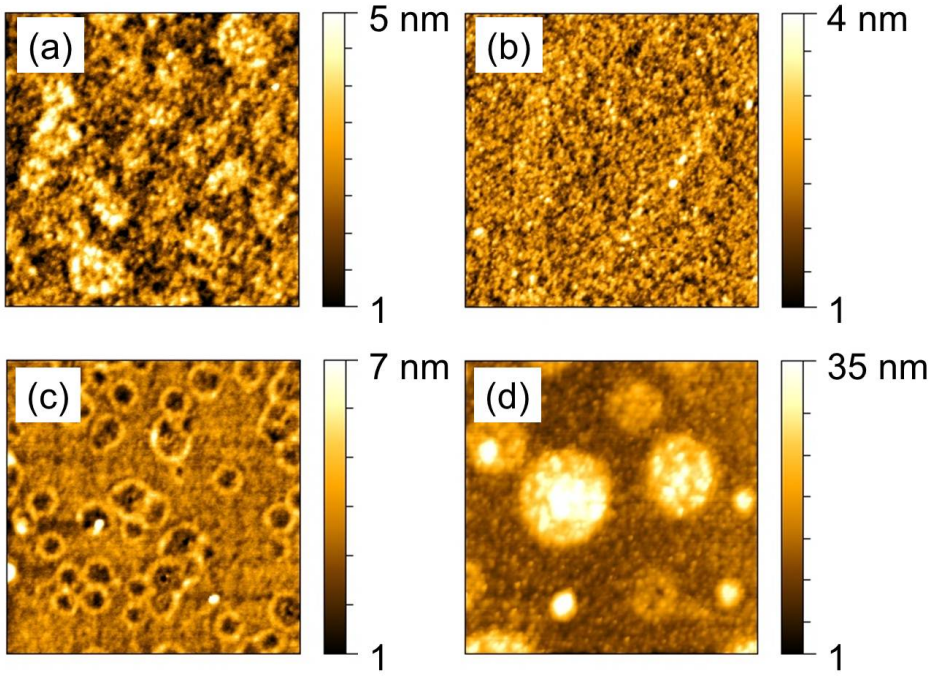

Figure 6.4: *AFM topographic images (8 × 8 μm^2) of P3HT:PCBM films degraded in (a) chlorobenzene vapor, (b) toluene vapor, (c) xylene vapor, and (d) dichlorobenzene vapor. The surface roughness, extracted from the AFM data, is 1 nm, 1 nm, 1 nm, and 6 nm, respectively.*

Chlorobenzene-, xylene-, and dichlorobenzene-related films (figure 6.4a, 6.4c, and 6.4d) exhibit pronounced grain structures. More specifically, donut-shaped and spherical nanostructures are observed in the samples post-treated with xylene and dichlorobenzene va-

pors, respectively. The sample treated with toluene vapor reveals a homogeneous morphology with fine nanostructures. Nevertheless, all degraded samples exhibit coarsened surface structures in comparison to their respective pristine samples. In addition, the surface rms-roughness is extracted from the AFM images. Only the sample post-treated with dichlorobenzene vapor shows a much larger surface roughness of around 6 nm. However, these information is restricted to surface topographies, strong changes of the inner film morphology might take place as well.

6.2.2 Inner morphology

As proved in previous work, the inner morphology of P3HT:PCBM film is usually different from its surface morphology [5, 26]. In order to obtain structural information with high statistics about the inner morphology of degraded P3HT:PCBM films, GISAXS measurements were performed. These measurements were carried out at the synchrotron beamline BW4 of the DORIS III storage ring at DESY, Hamburg, Germany. The wavelength was 0.138 nm. In order to enable the X-ray beam to penetrate the whole film, a constant incident angle of 0.4° was chosen. The sample-detector distance was set to 2088 mm for a reasonable q range. A MarCCD area detector was used, having 2043 × 2043 pixel with each pixel size of 79.1 × 79.1 μm^2.

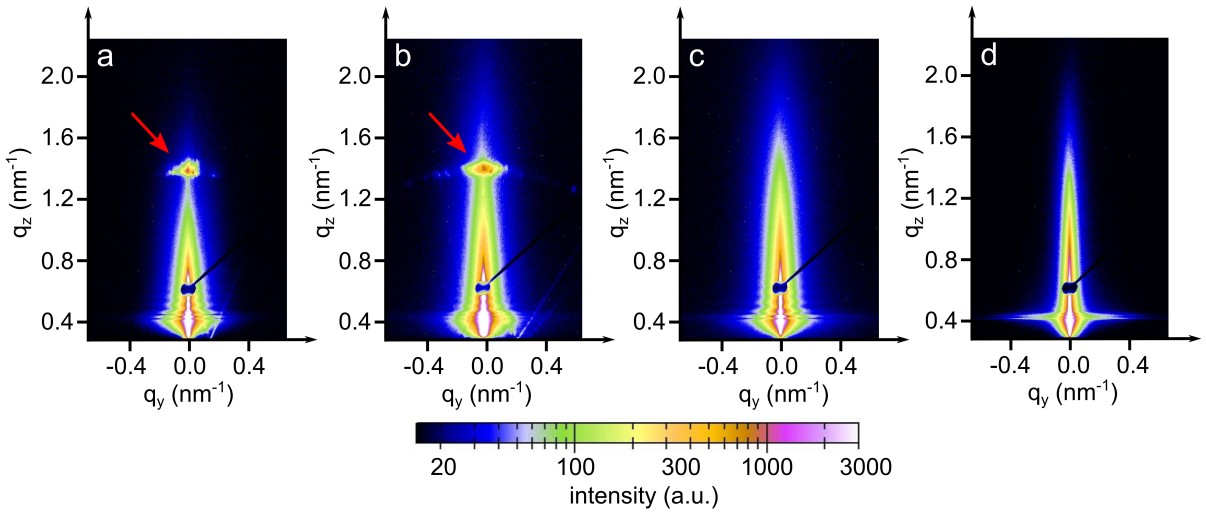

Figure 6.5: *2D GISAXS data of P3HT:PCBM films degraded in (a) chlorobenzene vapor, (b) toluene vapor, (c) xylene vapor, and (d) dichlorobenzene vapor. Bragg peaks observed in (a) and (b) are indicated by red arrows. Reproduced from Ref. [109] with permission from the Royal Society of Chemistry.*

In figure 6.5 the 2D GISAXS data of the degraded P3HT:PCBM films are displayed.

The specularly reflected beam (specular peak) is shielded by a beamstop to prevent the detector from oversaturation. For all images Yoneda peaks are well observed, which are located at the positions of the critical angles of the respective materials found in the films. Besides, intensity oscillations along the q_z direction near the region of the Yoneda peaks are seen in the 2D GISAXS data of the P3HT:PCBM films post-treated with chlorobenzene, toluene, and xylene vapors, as revealed in figure 6.5a, 6.5b, and 6.5c, respectively. On the other hand, the 2D GISAXS data of the sample treated with dichlorobenzene vapor does not show this phenomenon (figure 6.5d). The intensity oscillation is a signal for a partially correlated surface roughness, indicating that the P3HT:PCBM layers can partly follow the surface structure of the substrate. A detailed discussion about the correlated roughness of P3HT:PCBM layers has been published in previous work by Guo and coworkers [26]. For the dichlorobenzene-related sample, correlated roughness might damp out due to high surface roughness arising during solvent vapor treatment, as revealed by AFM measurements.

In addition, the scattering signal of 2D GISAXS data of the sample post-treated with dichlorobenzene vapor (figure 6.5d) extends further into a higher q_y region than all other samples, suggesting a smaller inner structure. Interestingly, prominent Bragg peaks are only found for the chlorobenzene- and toluene- related samples, as indicated by red arrows in figure 6.5a and 6.5b. These peaks are ascribed to the Bragg reflections of large PCBM crystals. So far, notable Bragg peaks corresponding to PCBM crystals are rarely reported. A more detailed discussion about the crystalline order will be presented in the following evaluation of GIWAXS measurements in section 6.4.

Vertical line cuts extracted from 2D GISAXS data are shown in figure 6.6a. The vertical structural information is obtained from these line cuts. Broadened specular peaks are found (at $\alpha_i + \alpha_f$ from 0.7° to 0.9°) for all samples, especially for the samples post-treated with chlorobenzene (black), toluene (blue), and xylene vapors (green). The broadening of the specular reflection is caused by big surface structures, as seen in the corresponding optical microscopy images (figure 6.2) [104]. Additionally, the positions of the Yoneda peaks of P3HT, PCBM, and silicon are indicated by red, black, and grey dotted lines, respectively. Since the positions of theses peaks are material sensitive, they do not change for different samples. The most pronounced features are the Bragg peaks located at $\alpha_i + \alpha_f \approx 1.7°$ for the chlorobenzene- and toluene- degraded P3HT:PCBM films, which indicates that large PCBM crystals are formed in these two samples.

Horizontal line cuts, as shown in figure 6.6b, are performed at the P3HT Yoneda peak position. These cuts comprise lateral structural information about the inner films. For a quantitative analysis, the horizontal line cuts are fitted using the model within the framework of the DWBA as represented by solid lines in figure 6.6b. The detailed fitting

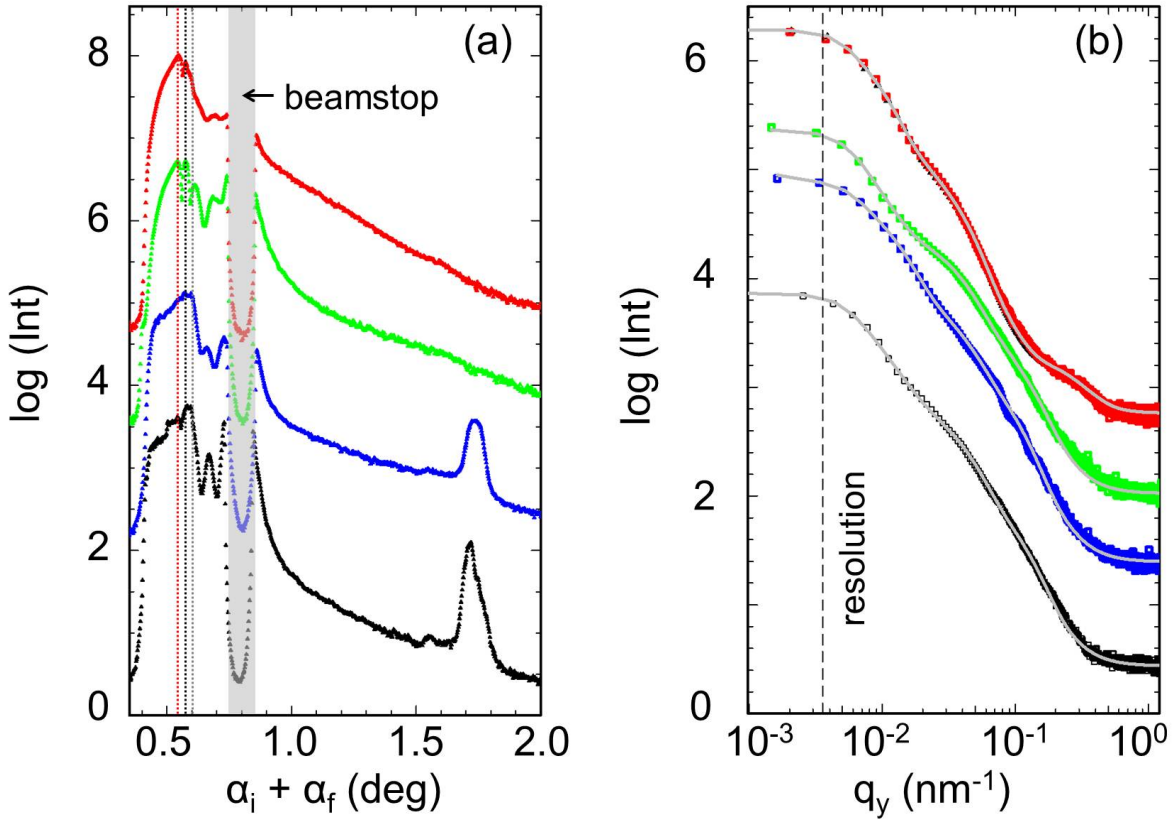

Figure 6.6: *(a) Vertical and (b) horizontal line cuts (symbols) extracted from 2D GISAXS data of P3HT:PCBM films degraded in chlorobenzene vapor (black), toluene vapor (blue), xylene vapor (green), and dichlorobenzene vapor (red). In (a), the positions of Yoneda peaks of P3HT, PCBM, and silicon are labeled by red, black, and grey dotted lines, respectively, and the beamstop is indicated by the grey bar. Fits of horizontal line cuts are illustrated by grey solid lines in (b). The curves are shifted along the intensity axis for clarity.*

procedure has been introduced in section 3.2.5. Three form and structure factors are used to obtain an optimized fitting result, suggesting that three substructures are resolved by GISAXS measurements for all samples. The presence of multiple substructures in P3HT:PCBM films has already been proposed in literature [41,126,127]. Generally, a well-established model for P3HT:PCBM BHJ films assumes the existence of intermixed phases between amorphous P3HT and PCBM, P3HT lamella dominated phases, and large PCBM aggregates [126, 128]. Nevertheless, the probed sizes of these substructures are usually different from sample to sample, as they are strongly influenced by the sample preparation method and also restricted by the accessible q range in scattering-based measurements. For example, Yin and coworkers investigated a thick P3HT:PCBM film via small angle neutron scattering (SANS) [129]. Focusing on a high q region, they found that below a certain threshold of PCBM loading, only one substructure existed in the film, whereas

additional large PCBM aggregates were observed when the amount of PCBM was above 50 vol%. Additionally, Huang et al. observed two substructures in a P3HT:PCBM film via GISAXS measurements [130]. They referred these structures to the amorphous P3HT matrix filled with PCBM and to large PCBM aggregates. Extending q range toward smaller values, three substructures were also observed in thin P3HT:PCBM films via GISAXS measurements [41, 131].

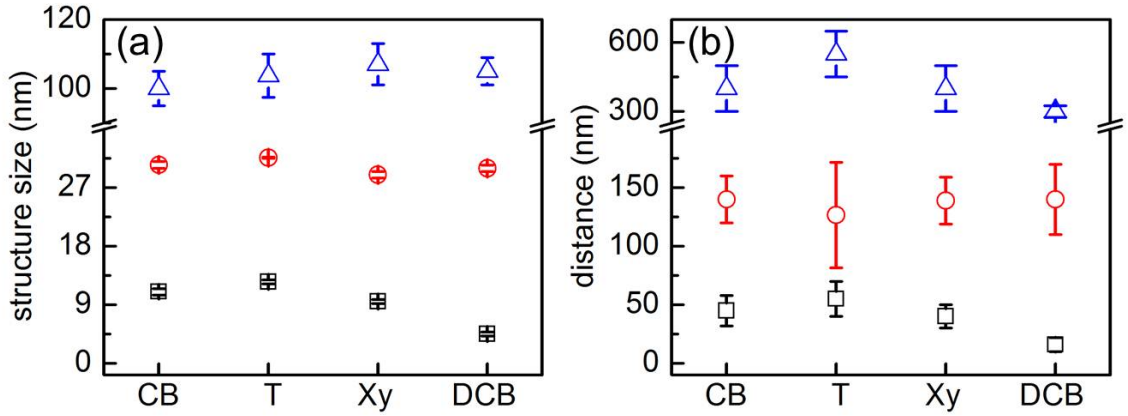

Figure 6.7: *(a) Quantitative information about structure sizes and (b) distances for P3HT:PCBM films degraded in chlorobenzene vapor, toluene vapor, xylene vapor, and dichlorobenzene vapor. These values are extracted from fitting results of horizontal line cuts of 2D GISAXS data. Three substructures are found, and their corresponding values are represented by black, red, and blue colors, respectively.*

The structure sizes and distances are extracted from the fitting results and summarized in figure 6.7. For all samples, three average structure sizes are found in the order of 10 nm, 30 nm, and 105 nm (radii of domains), respectively. Their corresponding distances are in the order of around 40 nm, 140 nm, and 400 nm (center to center distance). Following by the discussion about substructures in P3HT:PCBM films in previous paragraph, we ascribe the smallest substructure to an amorphous P3HT matrix with embedded PCBM. With a more complex analysis using the software ISGISAXS, Ruderer and coworkers reported similar structure sizes in P3HT:PCBM films from 3 nm to 10 nm [101]. By taking into account distinct scattering length densities of P3HT and PCBM, they evidenced that the matrix was amorphous P3HT and the filler was PCBM. The middle substructure is correlated to the phases predominated by P3HT crystals. Similar structure sizes of around 35 nm were found by Schaffer and coworkers in a P3HT:PCBM film [131]. They considered this substructure as pure P3HT phase and, based on this point, successfully found the correlation between morphological decay and device degradation. Finally, the

largest substructure is understood as the surface structures. It can be evidenced by the line cuts extracted from the AFM data as shown in figure 6.8, which reveals structure sizes similar to the biggest substructure. In addition, Swinnen et al. also observed large aggregates in a P3HT:PCBM film [132]. Via selected area electron diffraction analysis and transmission electron microscopy, they reported that the large phase separation was formed by PCBM aggregates and almost pure P3HT.

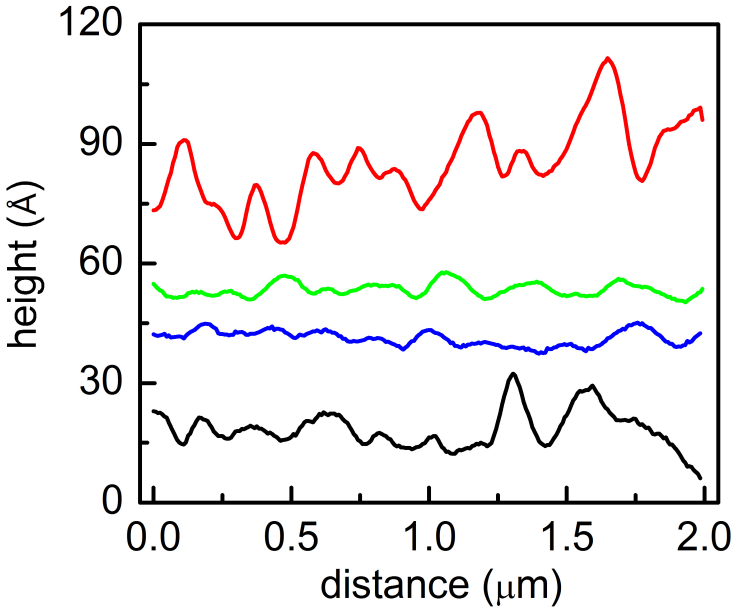

Figure 6.8: *Line cuts extracted from AFM data of P3HT:PCBM films degraded in chlorobenzene vapor (black), toluene vapor (blue), xylene vapor (green), and dichlorobenzene vapor (red). The scan area of the AFM measurements is 2 × 2 μm^2. Reproduced from Ref. [109] with permission from the Royal Society of Chemistry.*

Since the exciton diffusion length of P3HT was reported to be 10 to 20 nm, the smallest substructures, on the order of 10 nm, are expected to dominate the photovoltaic performance of the corresponding solar cells. In detail, the smallest structure size of 11 nm, 12.5 nm, 9.5 nm, and 4.5 nm are found in the chlorobenzene, toluene, xylene, and dichlorobenzene vapor degraded P3HT:PCBM films, respectively. The sample treated with dichlorobenzene vapor exhibits the smallest structures compared to the other samples. This relatively small structure size might correspond to a higher J_{SC} of its solar cell. However, for the other three samples, the smallest structure sizes are still in the range for an effective exciton dissociation. Therefore, the change in the inner structure of the active layer can not be the main reason for the complete failure of the solar cells degraded in chlorobenzene, toluene, and xylene vapors.

6.2.3 Results

Optical microscopy, AFM, and GISAXS are used to characterize the morphological degradation of P3HT:PCBM BHJ films post-treated under different solvent vapors. Optical microscopy images reveal that large PCBM aggregates form in chlorobenzene, toluene, and xylene-related samples, while no micro-sized PCBM clusters are observed in dichlorobenzene vapor post-treated sample. Moreover, the film degraded in chlorobenzene vapor has the largest sizes but least number of PCBM aggregates, which is correlated to a high vapor pressure and large solubility of PCBM in chlorobenzene. In addition, AFM measurements illustrate that all post-treated samples have coarsened surface structures as compared to the pristine films. Furthermore, for dichlorobenzene vapor post-treated film smaller domain sizes are found by GISAXS measurements, which could be a reason for the highest remaining J_{SC} of the corresponding solar cell. However, the sizes of the inner structures of all other samples are still in the range for an effective exciton dissociation. Hence, the inner structural evolution in different solvent vapors is not the main reason for the failure of solar cells in chlorobenzene, toluene, and xylene vapors. More investigations about the absorption and crystalline order of degraded P3HT:PCBM active layers are necessary to understand the degradation of the solar cell performance.

6.3 Absorption behavior

The UV/Vis absorption spectra of the P3HT:PCBM BHJ films post-treated via chlorobenzene, toluene, xylene, and dichlorobenzene vapors are normalized to the maximal value of the P3HT peak and displayed in figure 6.9a. The main peak position for P3HT at around 517 nm does not change for all samples, meaning the average conjugation length of P3HT chains does not degrade during solvent vapor annealing [32]. Furthermore, the shoulder-like features at around 550 nm and 600 nm are correlated to P3HT crystals [30]. The existence of these two absorption features suggests that the P3HT crystallites are preserved after the solvent vapor treatments.

In order to extract further information about the crystalline order of P3HT chains in these samples, the absorbance spectra are analyzed using the weakly coupled H-aggregate model (explained in section 2.3.2). Details on how to process the absorbance data is introduced in section 3.1.1. Briefly, the contributions of PCBM and amorphous P3HT are extracted from the absorbance spectra. Afterwards, each spectrum is fitted using five Gaussian peaks with equal width. By applying equation 2.20 to the (0-0) and (0-1) vibrionic peaks which are obtained from the fits, the values of free exciton bandwidth W are obtained for all samples and listed in figure 6.9b. In terms of P3HT:PCBM BHJ

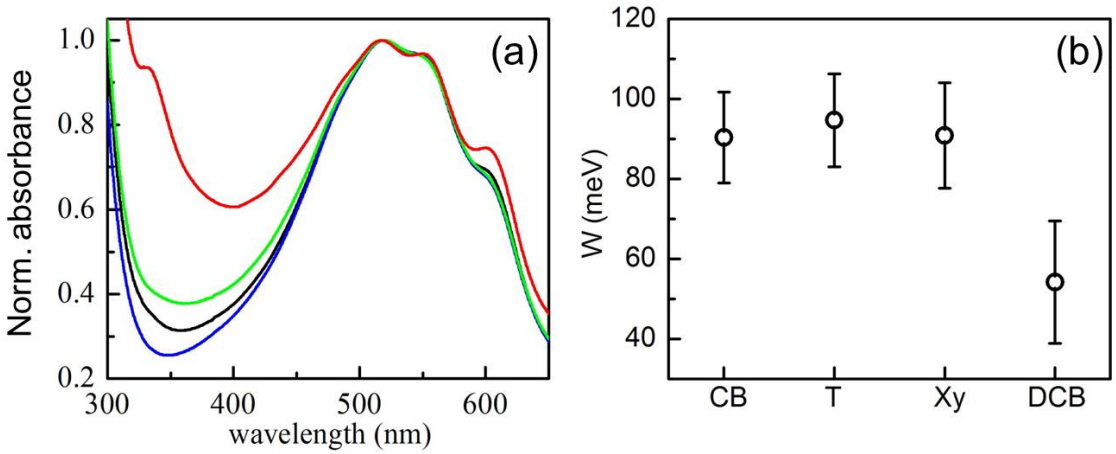

Figure 6.9: *(a) Normalized UV/vis absorption spectra of P3HT:PCBM films degraded in chlorobenzene vapor (black), toluene vapor (blue), xylene vapor (green), and dichlorobenzene vapor (red). (b) Free exciton bandwidth W of the corresponding samples, which are extracted from absorbance spectra and calculated using the weakly coupled aggregate model (equation 2.20). Reproduced from Ref. [109] with permission from the Royal Society of Chemistry.*

system, typical values of W have been reported to be (92 ± 10) meV, (76 ± 10) meV, and (140 ± 10) meV for well working devices [133]. The difference of these values is caused by thermal annealing or use of different solvents for sample preparations. For the present investigated P3HT:PCBM films, the values of W are in the range from (55 ± 15) meV to (95 ± 12) meV, suggesting that the resulting crystalline order of P3HT after long-term solvent vapor treatment is not responsible for the failure of the corresponding solar cells. In addition, a smaller W refers to a higher crystallinity of P3HT. Dichlorobenzene-related film shows the smallest W, indicating the highest P3HT crystallinity compared to the other samples. In general, for P3HT the crystalline regions afford significantly higher mobility of holes than its amorphous regions. Therefore, the highest crystallinity of P3HT in the film post-treated with dichlorobenzene corresponds to the highest J_{SC} of the solar cell. However, for chlorobenzene-, toluene-, and xylene-related samples, the sufficient crystalline order of P3HT hinted by W could not be the main reason for the failure of their resulting solar devices.

Besides information about the molecular ordering of P3HT, the absorption behavior of PCBM at around 335 nm is also revealed in figure 6.9a. Only the dichlorobenzene-related P3HT:PCBM film shows a weak PCBM absorption peak. The missing of the PCBM absorption peak for other samples is caused by the formation of large PCBM aggregates as illustrated in the optical microscopy images in figure 6.2. The large aggregates

can strongly scatter the light and subsequently lower the PCBM absorption. Liu and coworkers reported a similar absorption behavior of P3HT:PCBM film with large PCBM aggregates [134]. Moreover, the large PCBM aggregates result in much less PCBM being homogeneously distributed in the P3HT matrix, which significantly reduces the absorption of PCBM in the chlorobenzene, toluene, and xylene vapor post-treated samples.

Overall, the PCBM aggregates might impede P3HT crystallization, which is evidenced by the fact that the dichlorobenzene-related sample has the highest crystallinity. However, as compared to the evolution of P3HT crystallites, the formation of PCBM clusters, in chlorobenzene-, toluene-, and xylene-related samples seems to have much stronger influence on the degradation of their respective solar cells.

6.4 Crystalline order

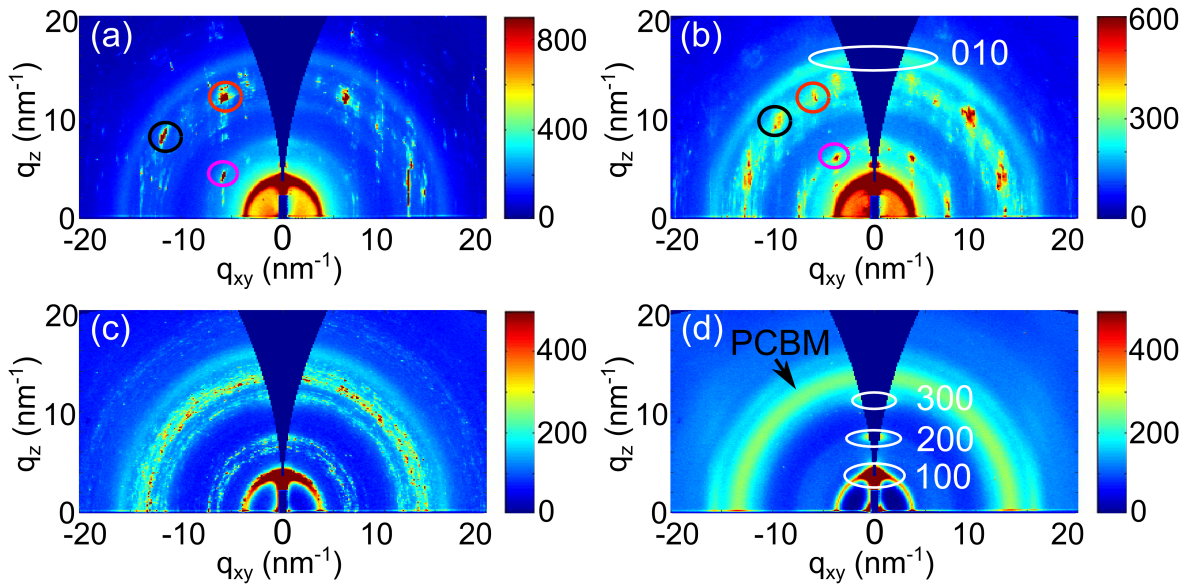

Figure 6.10: *2D GIWAXS data of P3HT:PCBM films degraded in (a) chlorobenzene vapor, (b) toluene vapor , (c) xylene vapor, and (d) dichlorobenzene vapor. Three prominent PCBM Bragg reflections are denoted by black, red, and magenta circles in (a) and (b). Bragg peaks of P3HT crystallites are labeled by white ellipses in (b) and (d). Reproduced from Ref. [109] with permission from the Royal Society of Chemistry.*

In order to probe the crystalline order, GIWAXS measurements on the degraded films are carried out. The 2D GIWAXS data are shown in figure 6.10. Obvious differences in the scattering patterns, dominated by the scattering signals from the PCBM component, are observed. Among the samples, only the dichlorobenzene-related P3HT:PCBM film

shows 2D GIWAXS data (figure 6.10d) similar to normal annealed P3HT:PCBM BHJ films [101].

More specifically, Bragg diffraction spots are clearly visible for the chlorobenzene and toluene vapor post-treated samples, as denoted by the red, black, and magenta round circles in figure 6.10a and 6.10b. These individual Bragg spots originate from large and well-ordered PCBM crystals. It is worthwhile to mention that the Bragg peaks observed in 2D GISAXS data (figure 6.5a and 6.5b) are not visible in the present 2D GIWAXS data because they are blocked by the beamstop. Nevertheless, the higher orders are accessible in the present 2D GIWAXS data. Similarly, Verploegen and coworkers found distinct Bragg diffraction spots in 2D GIWAXS data of a P3HT:PCBM BHJ film upon heating to 205 °C [117]. For a quantitative analysis, the coordinates of each Bragg spot, in terms of q_z, q_{xy}, and q, are taken from 2D GIWAXS data and summarized in table 6.3. The total q values of all three Bragg spots are similar for these two samples, suggesting that the same type of PCBM crystalline phase exists in P3HT:PCBM samples post-treated under chlorobenzene and toluene vapor. This observation is well consistent with the previous work done by Colle and coworkers [135], who also found that the same PCBM crystalline phase is formed in PCBM films prepared out of chlorobenzene and toluene, respectively. Moreover, an interesting feature is the flipped coordinates of q_{xy} and q_z of peak 1, referring to a reversed orientation of PCBM crystals in these two samples.

solvent	**peak 1 (nm^{-1})**			**peak 2 (nm^{-1})**			**peak 3 (nm^{-1})**		
	$\mathbf{q}_{xy}$	$\mathbf{q}_z$	**q**	$\mathbf{q}_{xy}$	$\mathbf{q}_z$	**q**	$\mathbf{q}_{xy}$	$\mathbf{q}_z$	**q**
chlorobenzene	5.98	3.95	7.17	11.92	7.95	14.33	5.67	11.77	13.06
toluene	3.9	5.95	7.17	9.80	9.03	13.33	5.70	11.73	13.04

Table 6.3: *Positions, in terms of q_{xy}, q_z, and q, of Bragg diffraction spots in the 2D GIWAXS data of P3HT:PCBM films degraded in chlorobenzene and toluene vapor. Peak 1, 2, and 3 refer to the Bragg spots denoted by magenta, black, and red round circles, labeled in figure 6.10a and 6.10b.*

The samples post-treated in xylene and dichlorobenzene vapor have no prominent Bragg diffraction spots, as revealed by figure 6.10c and 6.10d. For the sample post-treated with xylene vapor, a broad, patchy, half-ring-shaped feature appears in its 2D GIWAXS data (figure 6.10c). This scattering characteristic is correlated to a group of randomly distributed finer PCBM crystallites, as compared to the chlorobenzene- and toluene-related films. As already mentioned, the 2D GIWAXS data of the dichlorobenzene-treated film is very similar to normal annealed films. It shows a homogeneous, broad, half-ring-shaped feature originating from PCBM in the amorphous phase, as illustrated in figure 6.10d.

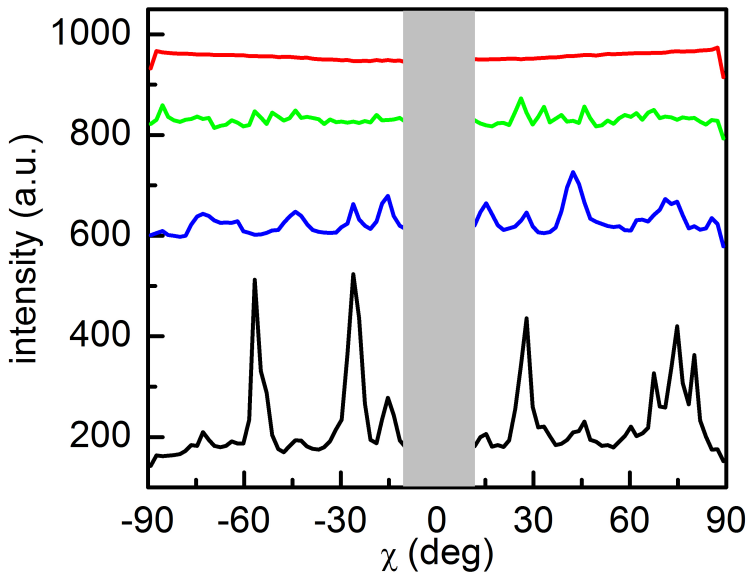

Figure 6.11: *Tube cuts along the main PCBM scattering signals from q = 12 nm^{-1} to q = 15.5 nm^{-1}. These cuts are extracted from 2D GIWAXS data of P3HT:PCBM films degraded in chlorobenzene vapor (black), toluene vapor (blue), xylene vapor (green), and dichlorobenzene vapor (red). The curves are shifted along intensity for clarity. Reproduced from Ref. [109] with permission from the Royal Society of Chemistry.*

In order to obtain information about the orientation of PCBM crystals, tube cuts along the main PCBM scattering signals are performed from q = 12 nm^{-1} to q = 15.5 nm^{-1} on the 2D GIWAXS data. The corresponding curves are shown in figure 6.11. First, the locations of the scattering peaks will be discussed. For P3HT:PCBM films post-treated with chlorobenzene and toluene vapor (black and blue curves in figure 6.11), the scattering peaks are located at almost similar positions of around ± 15°, ± 30°, ± 45°, ± 60°, and ± 75°, suggesting a certain, similar orientation in these two samples. For the xylene vapor post-treated film (green curve in figure 6.11), more peaks are visible, which show a random distribution. Accordingly, it is inferred that the PCBM crystals do not have any preferred orientation. Regarding the dichlorobenzene-related sample (red curve in figure 6.11), a relatively flat curve without apparent peaks is observed, implying no PCBM crystals are formed within this sample. These findings further verify the deduction made from optical microscopy measurements in section 6.2.1. For chlorobenzene-, toluene-, and xylene-related films, the aggregates are mainly ascribed to PCBM crystals, while for dichlorobenzene-related sample the surface morphology is only correlated to a surface structure rather than clusters of PCBM crystallites. Then, intensity and width of the corresponding peaks are compared for all samples. Generally, higher peak intensities and

sharper peaks are correlated to larger crystals. The tube cut for the chlorobenzene vapor post-treated sample has the highest and sharpest peaks, indicating the largest PCBM crystals in this sample.

Consequently, it is concluded that the type of the solvent vapor has a strong impact on the PCBM crystallization. By selecting the proper solvent vapor post-treatment, the crystalline order of PCBM can be tuned in terms of sizes and orientations. Most significantly, the degradation in photovoltaic performance of the chlorobenzene, toluene, and xylene vapor post-treated solar cells are mainly correlated to the formation of PCBM crystals. In principle, solvent vapor annealing is similar to commonly used thermal annealing. Both treatments enable P3HT and PCBM molecules to move and subsequently form a thermodynamically favorable morphology. As reported, thermal annealing is a non-monotonic impact in the photovoltaic performance [136]. Treat and coworkers have found that micrometer-scale PCBM crystals are formed in P3HT:PCBM BHJ films under long-term thermal annealing [136]. They ascribed the degradation in the corresponding solar cells to the formation of large PCBM crystals. Likewise, during long-term solvent vapor annealing using for instance chlorobenzene vapor, PCBM molecules tend to crystallize and have enough time to form numerous clusters. Accordingly, this long term solvent vapor treatment leads to extremely large domains of the PCBM phase in the micrometer scale, as illustrated by microscopy image in figure 6.2a.

In addition to gaining information about the molecular ordering of PCBM, the intermolecular structure of P3HT can also be resolved via 2D GIWAXS data. Clearly observed (100) and (010) Bragg peaks (figure 6.10), indicate the presence of P3HT crystals in the films. Moreover, for the samples post-treated with chlorobenzene, toluene, and xylene vapors, (010) Bragg reflections appear with higher intensity in the horizontal direction compared to the vertical direction, suggesting a face-on dominant orientation for P3HT crystals. For dichlorobenzene-related film, the (010) Bragg reflections show opposite features, denoting an edge-on dominated orientation for P3HT crystals in this sample.

For a further quantitative analysis, the vertical and horizontal sector integrals, extracted from 2D GIWAXS data, are shown in figure 6.12a and 6.12c, respectively. Due to extremely high intensities of the peaks at around 3.7 nm^{-1} in the vertical integrals, the q range above 5 nm^{-1} is shown in figure 6.12b for a better visualization. Sharp peaks with high intensities, as denoted by black arrows in figure 6.12, are generated by large PCBM crystals. These peaks might suppress the scattering features caused by P3HT crystals due to much higher intensities. For P3HT, the (100) peak with its higher orders of (200) peak and (300) peak as well as the (010) peak are visible in all vertical integrals in figure 6.12a and 6.12b. This illustrates that P3HT is already highly crystalline in all these samples.

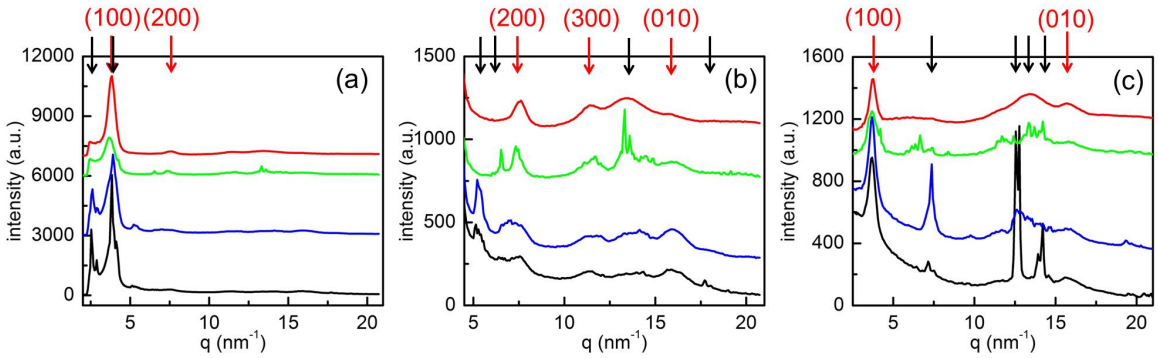

Figure 6.12: *(a) Vertical and (c) horizontal sector integrals of 2D GIWAXS data of P3HT:PCBM films degraded in chlorobenzene vapor (black), toluene vapor (blue), xylene vapor (green), and dichlorobenzene vapor (red). In order to clearly visualize the features at high q values in (a), the q range above 5 nm^{-1} is shown in (b). The Bragg peaks generated by P3HT and PCBM crystals are labeled by red and black arrows, respectively. The curves are shifted along intensity for clarity.*

From the peak positions, lattice constants of P3HT crystals are calculated and summarized in table 6.4. (100) and (010) Bragg peak lattice constants of 1.7 nm and 0.4 nm are the same for all samples, except for the (100) peak extracted from the vertical sector integrals. It seems that the distinct values of the (100) peaks extracted from the vertical sector integrals might be caused by the interference with strong scattering signals from PCBM crystals, as revealed by the almost overlapping peaks at around 3.7 nm^{-1} in figure 6.12a. The lattice constant values are in good agreement with literature [5]. In conclusion, the P3HT crystals are well preserved after long-term solvent vapor annealing. Moreover, the lattice constants of P3HT crystals are not influenced by solvent vapor annealing. Therefore, the evolution of P3HT crystalline ordering is not responsible for the degradation of the aged solar cells.

solvent	**lattice constant (nm)**			
	(100)h	**(010)h**	**(100)v**	**(010)v**
chlorobenzene	1.70	0.40	1.71	0.40
toluene	1.70	0.40	1.66	0.40
xylene	1.71	0.40	1.71	0.40
dichlorobenzene	1.70	0.40	1.64	0.40

Table 6.4: *Lattice constants of P3HT crystals extracted from vertical (v) and horizontal (h) sector integrals of 2D GIWAXS data of P3HT:PCBM films degraded in chlorobenzene, toluene, xylene, and dichlorobenzene vapors.*

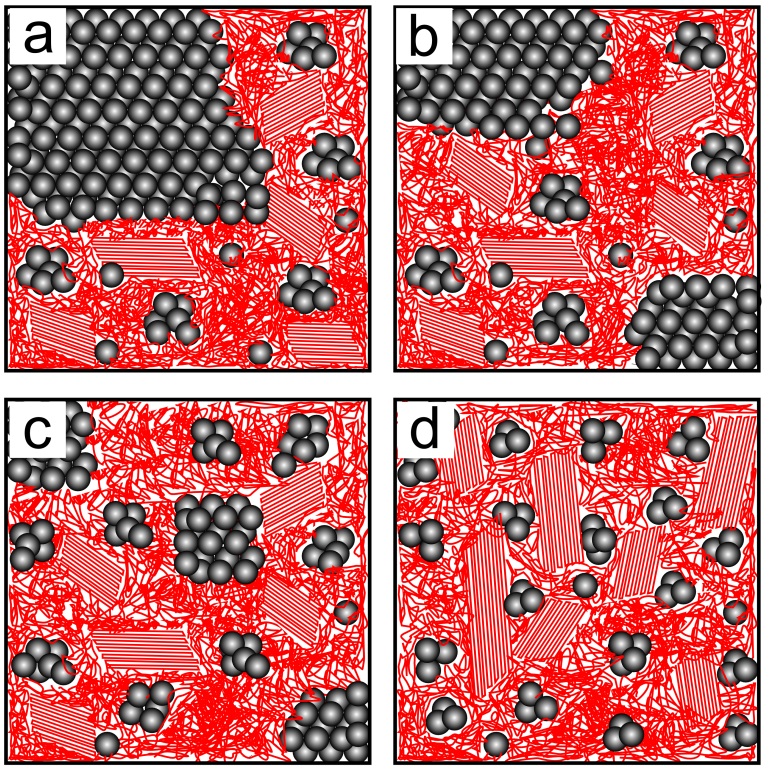

Figure 6.13: *Schematic illustrations at the microscale for P3HT:PCBM BHJ films degraded in (a) chlorobenzene vapor, (b) toluene vapor, (c) xylene vapor, and (d) dichlorobenzene vapor. Grey spheres and red lines correspond to PCBM and P3HT components, respectively. Parallel straight lines represent P3HT crystal phases and tangled lines denote P3HT amorphous phases.*

In figure 6.13, the results of morphology and crystalline order are summarized in schematic illustrations at the microscale for P3HT:PCBM BHJ films post-treated with different solvent vapors. Grey spheres and red lines represent PCBM and P3HT components, respectively. For molecular ordering, the sample annealed in dichlorobenzene vapor shows the highest P3HT crystallinity, with an edge-on dominated orientation (figure 6.13d). Whereas the other three samples have a relatively low P3HT crystallinity with a preferred face-on orientation. However, the P3HT crystallinity for these three samples still fulfills the requirement for a properly working solar cell. Therefore, the evolution in P3HT crystallinity under different solvent vapor annealing is not the main reason for the failure of the respective solar cells. With respect to the phase separation between P3HT and PCBM, the domain sizes are distinct, but they are still in the range for an efficient exciton dissociation for all samples. Hence, the development of nanomorphology under different solvent vapor treatments is not responsible for the failed devices, either. Finally, on the micrometer scale, significant differences between the dichlorobenzene-related

sample and the other three samples are found. In brief, only the sample with long-term dichlorobenzene vapor post-treatment does not form large PCBM crystals, while the chlorobenzene-, toluene-, and xylene-related samples have PCBM crystallized in large sizes. As a consequence, for our selected solvent vapors, PCBM molecules are more sensitive than P3HT chains, and accordingly the formation of PCBM crystallites are considered as the main reason for the complete failure of the resulting solar cells.

6.5 Summary

The solvent vapor, generated during the preparation of solar cells, has strong influence on the stability of these devices. We select chlorobenzene, toluene, xylene, and dichlorobenzene individually as the possible solvent for the solar cell preparation and subsequent vapor treatment. All solar cells seriously degrade after long-term saturated solvent vapor treatment. Only the dichlorobenzene-related device survives with the remaining PCE of (1.66 ± 0.07) %.

Via investigations on the morphology, absorption behavior, and crystalline order of the degraded P3HT:PCBM films, the reason for solar cell failure is ascribed to the formation of large scale PCBM crystals. In comparison, the evolution of phase separation and P3HT crystallinity are less strongly effected. It is concluded that among all investigated solvent vapors, dichlorobenzene is the best one due to PCBM keeping amorphous in the active layer. Hence, in terms of long term stability of solution processed P3HT:PCBM solar cells, dichlorobenzene or other solvents with a low vapor pressure are beneficial for the solar cell stability during fabrication and handling. Moreover, a proper solar cell encapsulation, which can selectively release the solvent residuals in the active layer, is of great importance.

7 Inverted solar cells based on a P3HT:PCBM system

Parts of this chapter have been published in the articles: Development of the Morphology during Functional Stack Build-up of P3HT:PCBM Bulk Heterojunction Solar Cells with Inverted Geometry [137] (W. Wang et al., ACS Appl. Mater. Interfaces, 7, 602-610, 2015, DOI: 10.1021/am5067749), and In operando morphology investigation of inverted bulk heterojunction organic solar cells by GISAXS [138] (W. Wang et al., J. Mater. Chem. A, 3, 8324-8331, 2015, DOI: 10.1039/c5ta01109d).

As described in chapter 5, many external conditions have been applied to increase the PCE value of the P3HT:PCBM BHJ solar cells, such as thermal annealing, solvent annealing, or use of processing solvent additives [86, 93]. Alternatively, new designs of solar cell architecture also dramatically improve the solar cell efficiency [139, 140]. The tandem structure is the state-of-the-art architecture, revealing a PCE to date over 11% in triple-junction polymer solar cells [141]. Additionally, recent studies have confirmed that the use of inverted geometry in solar cells can increase the PCE of single-junction polymer solar cells as well [142, 143].

So far, most research carried out on inverted polymer solar cells mainly pay close attention to raise solar cell efficiency, for example by modifying blocking layers [144–146]. Only a few studies focused on the morphology of the active layer and the relationship between the morphology and device performance. Moreover, these characterizations are limited to the active layer and do not consider the complex architecture of the whole solar devices. Therefore, understanding the morphology of the active layer in a real solar cell is significant. The technique GISAXS is a non-destructive method to reveal the inner morphology, especially for the active layer buried below the blocking layer and top electrode. For example, Guo and coworkers have successfully studied the morphological evolution during the preparation route towards functional stacks of the P3HT:PCBM BHJ solar cell with a standard geometry via GISAXS [26]. To complete the understanding, in

this chapter, GISAXS was employed as a main technique to track the inner morphological development of the P3HT:PCBM active layer during the functional stacks build-up with an inverted geometry.

Furthermore, it is also demonstrated that by adopting the inverted geometry the solar cells achieve a higher long-term stability [147, 148]. In order to explain why the inverted solar cell owns better stability as compared to the standard one, some general mechanisms have been proposed [149]. It is believed that the polymer degradation is prevented due to the UV absorption of the metal oxide layer (ZnO or TiO_2) underneath. In addition, in the inverted geometry the metal oxide layer directly contacts the ITO, avoiding the erosion of ITO electrodes by the conventional PEDOT:PSS layer in a standard geometry [150]. Moreover, with the inverted geometry the diffusion of water and oxygen molecules into solar cells are retarded since the active layer is sandwiched between two blocking layers. All the statements are based on the chemical reactions and only a few researches payed attention to the physical degradation such as morphological degradation. However, the stability of the morphology of the active layer also plays an important role for the solar cells' stability. As revealed by Schaffer et al., the morphological degradation of the active layer caused a reduction of the effective area for electrical power conversion and accordingly of the J_{SC} of the solar cells with a standard geometry [131].

In this chapter, we introduce a simple inverted geometry for P3HT:PCBM BHJ solar cells. The photovoltaic performance is significantly improved as compared to the standard P3HT:PCBM solar cells, as shown in section 7.1. We explore the relationship between the high solar cell efficiency and the morphology. The focus is put on the stepwise development of the P3HT:PCBM BHJ morphology during the functional stack build-up, probed mainly by GISAXS. In section 7.2, the stability of the inverted solar cells is presented. The direct correlation between the morphology of P3HT:PCBM active layer and the solar cell performance is investigated by in operando GISAXS and J-V measurements during the solar cell operation.

7.1 Morphological evolution of inverted P3HT:PCBM solar cell during assembling

The inverted P3HT:PCBM BHJ solar cells are prepared as described in section section 4.3. The photovoltaic performance is determined via J-V characteristic, as discussed in section 7.1.1. Afterwards, in section 7.1.2 the morphological evolution of P3HT:PCBM active layer is characterized by AFM and GISAXS measurements as a function of the multilayer

stack build-up. The findings from morphology measurements are linked to high efficiency of the inverted solar cells.

7.1.1 Solar cell performance

In figure 7.1a and 7.1b, the schemes of the final device layer structure of standard and inverted P3HT:PCBM BHJ solar cells are displayed. Contrary to the standard solar cells, in the inverted ones the holes are transported from P3HT to the top electrodes and the electrons transfer from PCBM to the bottom electrodes. In addition, instead of aluminum, gold is used in the inverted solar cells as the top electrodes to match the energy level of the materials in the whole device. ITO is replaced with FTO due to high temperature stability of FTO.

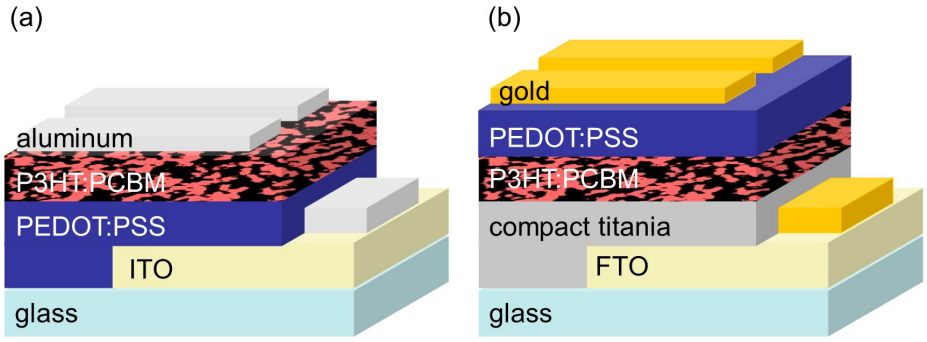

Figure 7.1: *Sketches of P3HT:PCBM BHJ organic solar cells with (a) standard and (b) inverted geometry, with their functional layers labeled.*

Figure 7.2 presents the J-V curves of the standard and inverted P3HT:PCBM solar cells under illumination. The corresponding photovoltaic performance is characterized by J_{SC}, V_{OC}, FF, and PCE, which are summarized in table 7.1. It is apparent that the J_{SC} is the most evidently increased parameter for inverted solar cells, showing the value of (13.1 ± 0.3) mA/cm^2 as compared to (8.9 ± 0.2) mA/cm^2 with a standard geometry. Whereas the V_{OC} of these two types of solar cells stays in the similar range (0.62 ± 0.01) V for standard solar cells and (0.58 ± 0.01) V for inverted solar cells). It is due to the fact that the same donor and accepter materials are used in these two types of solar cells, which mainly determine the V_{OC} of the P3HT:PCBM solar cells [151]. Additionally, the FF of (55.9 ± 0.7) % in inverted solar cells maintains similarly to that of (57.4 ± 1.3) % in the standard solar cells. In order to obtain further information beyond these photovoltaic parameters as shown above, the values of R_s and R_{sh} are extracted and listed in table 7.1, too. The relatively smaller R_s in inverted solar cells contributes to the higher J_{SC}, while

geometry	J_{SC} **(mA/cm^2)**	V_{OC} **(V)**	FF **(%)**	PCE **(%)**	R_s **(Ω·cm^2)**	R_{sh} **(Ω·cm^2)**
standard	8.9 ± 0.2	0.62 ± 0.01	57.4 ± 1.3	3.1 ± 0.1	12 ± 2	470 ± 42
inverted	13.1 ± 0.1	0.58 ± 0.01	55.9 ± 0.7	4.2 ± 0.2	7 ± 1	340 ± 45

Table 7.1: *Comparisons of photovoltaic parameters of the standard and inverted P3HT:PCBM BHJ organic solar cells.*

the relatively smaller R_{sh} results in the lower V_{OC} and FF as compared to standard solar cells. In total, the PCE of the inverted solar cells are raised to (4.2 ± 0.2) % in comparison to (3.1 ± 0.1) % in standard solar cells, which is mainly ascribed to the increased J_{SC}. The maximum PCE of inverted solar cells reaches 4.4%, which is among the highest reported values for P3HT:PCBM BHJ solar cells [152].

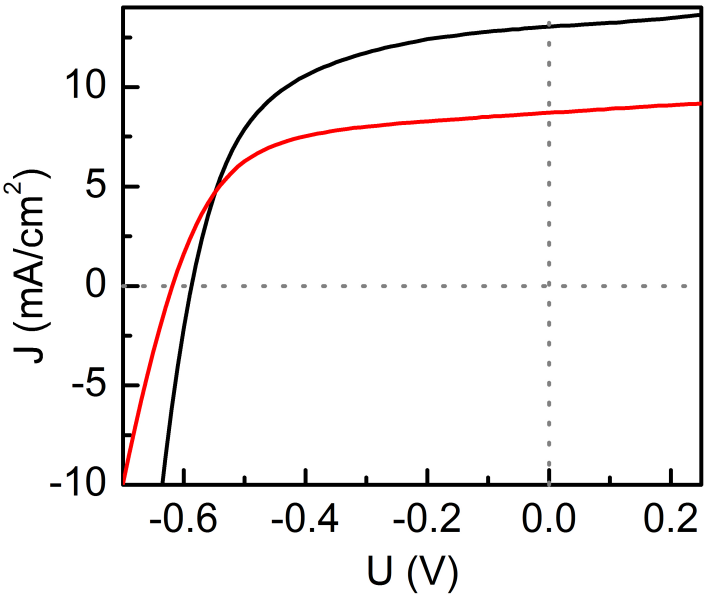

Figure 7.2: *J-V curves of the P3HT:PCBM BHJ organic solar cells under AM 1.5 solar illumination with standard (red color) and inverted (black color) geometries.*

Furthermore, the EQE measurements are carried out on both types of solar cells, as shown in figure 7.3a. It is noteworthy that except for the small range from 300 nm to 345 nm, the overall EQE of the inverted solar cell is much higher than that of standard solar cell. The tendency of the EQE between these two solar cell is consistent with that of the J_{SC} extracted from J-V measurements. In order to understand the relative loss of EQE in the range from 300 nm to 345 nm in the inverted solar cell, the transmittance of

TiO_2 and PEDOT:PSS films are probed and shown in figure 7.3b. The TiO_2 layer shows much lower transmittance in the range below 345 nm than that of the PEDOT:PSS layer, showing that less light reaches the active layer in this wavelength range for an inverted solar cell. Accordingly, a lower EQE intensity is detected below the wavelength of 345 nm in an inverted solar cell.

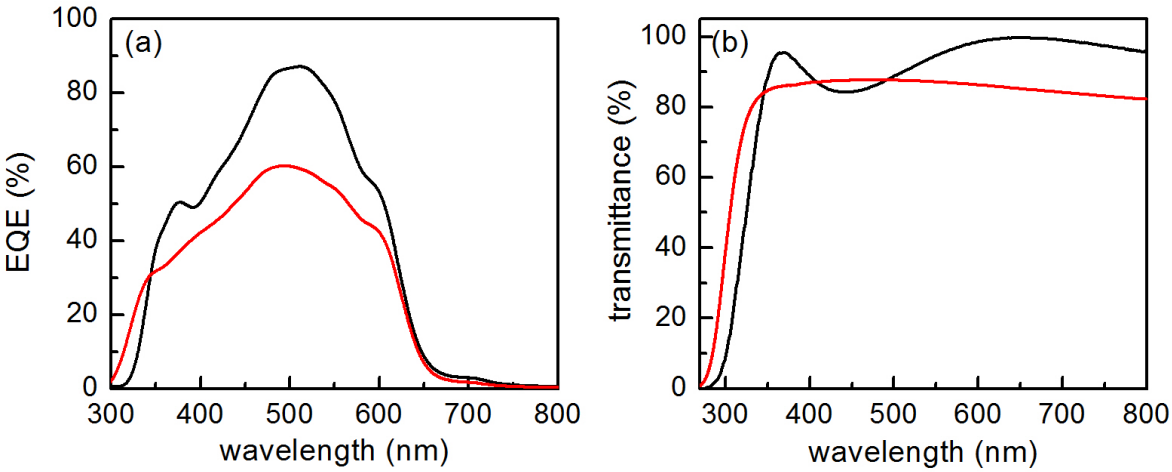

Figure 7.3: *(a) EQE of the P3HT:PCBM BHJ organic solar cells with standard (red color) and inverted (black color) geometry. (b) Transmittance of PEDOT:PSS (red color) and TiO_2 layers (black color) on glass substrates.*

7.1.2 Morphology

As reported in section 7.1.1 the high efficiencies of P3HT:PCBM BHJ solar cells have been obtained by utilizing the inverted geometry. Thus, the fundamental understanding of the relationship between morphology and performance is of great interest. It is well known that the morphologies of the active layer play the most important role for solar cell performance [153, 154].

Gradual functional stack build-up of a P3HT:PCBM inverted solar cell is revealed step-by-step as shown in figure 7.4. The pre-cleaned FTO substrate is partly etched away (named as S1). The compact TiO_2 layer is deposited from a sol-gel solution and then treated with calcination (denoted as S2). Afterwards, a finer layer of TiO_2 (denoted as S3) is formed by a $TiCl_4$ bath treatment. Sample S4 is resulted from P3HT:PCBM film deposition via spin coating. Then, the electron blocking layer PEDOT:PSS is formed by spray coating (denoted as S5). Thereafter, the gold contacts are deposited on top of PEDOT:PSS layer (denoted as S6). Finally thermal annealing in N_2 flow is applied on the whole device (denoted as S7).

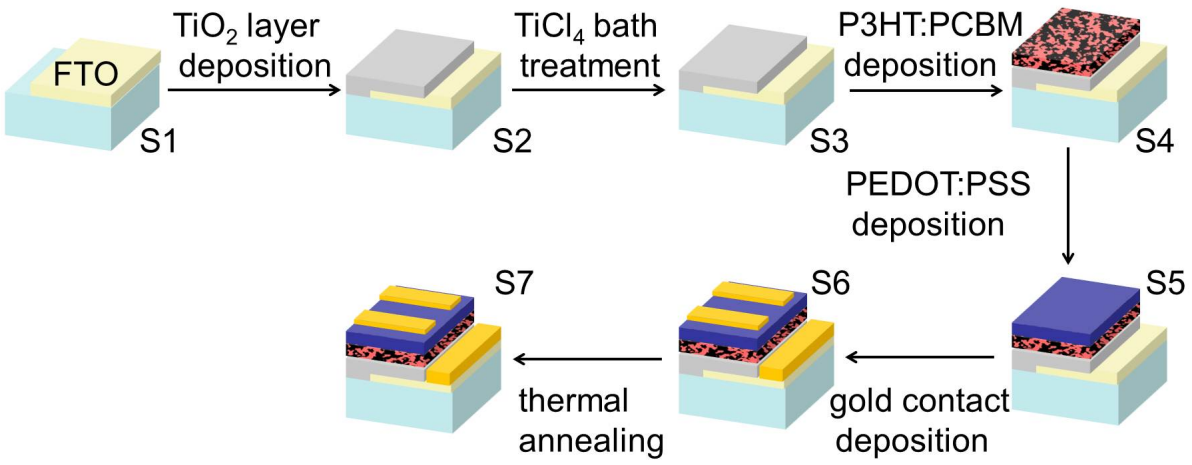

Figure 7.4: *Scheme of the functional stack build-up of inverted P3HT:PCBM BHJ solar cell.*

In addition, a SEM cross sectional image is shown in figure 7.5. The FTO layer located at the bottom of the image (bright color) shows a thickness of around 700 nm. Above FTO, a TiO_2 layer is observed with a film thickness of around 200 nm. The black layer on top of TiO_2 are the P3HT:PCBM and PEDOT:PSS layers. Due to the low contrast between these two films, individual P3HT:PCBM or PEDOT:PSS layer can not be distinguished in the SEM image. On top of the image, a thin layer of gold is observed. Besides for the stack information obtained from the SEM image, good contacts between each of two neighboring functional layers are also evidenced, which ensures the good photovoltaic performance of the investigated solar cells.

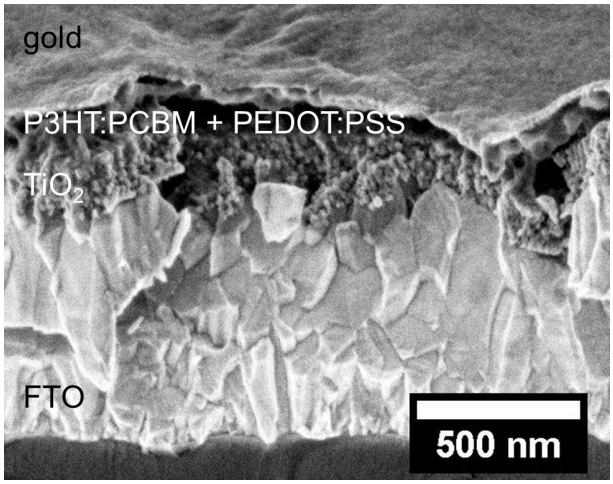

Figure 7.5: *Cross sectional SEM image of an inverted P3HT:PCBM BHJ solar cell.*

Surface morphology

In figure 7.6 AFM topography images demonstrate the development of the surface morphology of P3HT:PCBM inverted solar cells during functional stack build-up. The surface structure of bare FTO substrate (S1) shows large and pyramidal-shaped grains (figure 7.6a), with a high surface roughness. After TiO_2 deposition (S2), the dot-like structures are observed. The dot-shaped grains become denser after the $TiCl_4$ bath treatment (S3), which is beneficial for the electron transport at the interface between the TiO_2 layer and the active layer. After P3HT:PCBM spin coating (S4), the inter-connected structures are observed. However the dot-shaped grains are still visible, because P3HT:PCBM duplicates the morphology of the TiO_2 layer underneath. With further addition of PEDOT:PSS layer (S5), the similar features to P3HT:PCBM layer are formed with slightly coarsened structures. With the gold contacts (S6 and S7), different morphologies are formed. The grains are attributed to the aggregation of small gold nanoparticles.

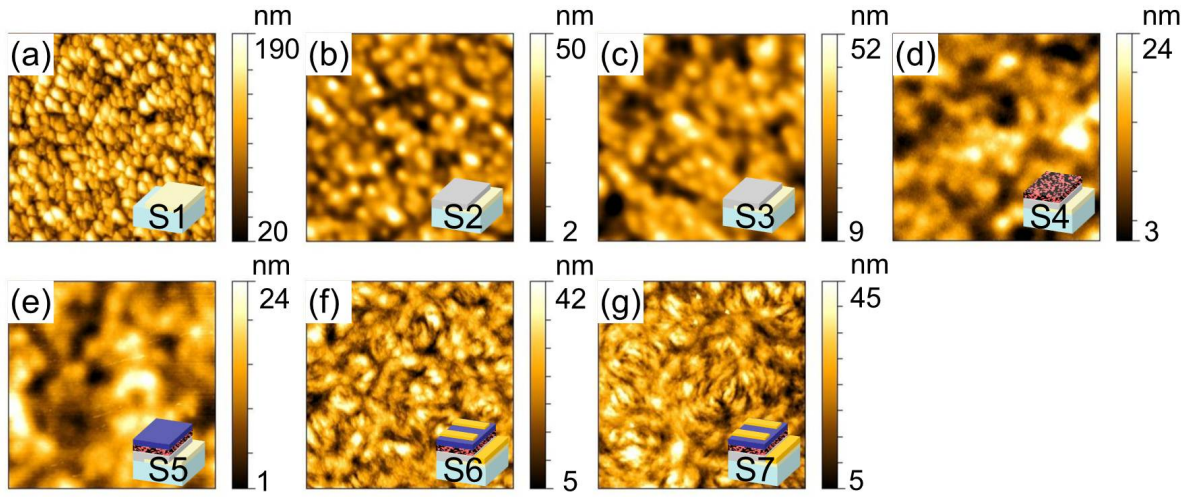

Figure 7.6: *AFM topography images of individual steps from the stack build-up in inverted P3HT:PCBM solar cell, from S1 to S7 denoted as (a) to (g). The scan size is* $4 \times 4\ \mu m^2$.

Furthermore, the surface roughness is calculated from the AFM measurements and plotted in figure 7.7. The roughness is found to be around 30 nm for the bare FTO substrate, which is much larger in comparison to the ITO substrate used in standard solar cells. The high surface roughness of FTO may lead to strong internal light scattering inside the solar cells, therefore light harvesting of the active layer is promoted. Accordingly, a higher current density is expected for inverted solar cells than standard ones because of the greater light harvest induced by rough FTO substrates. Similarly, Kim and coworkers reported that the device constructed on the substrate with surface structures like winkles showed substantial improvements in light harvesting efficiency [155]. With the TiO_2 layer

(S2) deposited on top of FTO, the roughness of the stack is strongly reduced to below 10 nm and further to around 6 nm after $TiCl_4$ bath treatment (S3). After spin coating of P3HT:PCBM, the sample S4 still has the roughness of around 5 nm. As reported, the roughness for P3HT:PCBM films is around 1 nm if deposited on flat substrates in a similar way [5]. The higher surface roughness is attributed to the large roughness of the FTO substrate. The rougher surface of the P3HT:PCBM layer is beneficial for reducing the light reflection at the interface and accordingly improves the light absorption, indicated by an increased current density. The stack with PEDOT:PSS layer, S5, keeps similar surface roughness to sample S4. Finally, with addition of gold contact (S6 and S7), the surface roughness of the device is slightly increasing again, which is due to the growth mechanism of the gold particles on the polymer layer [156].

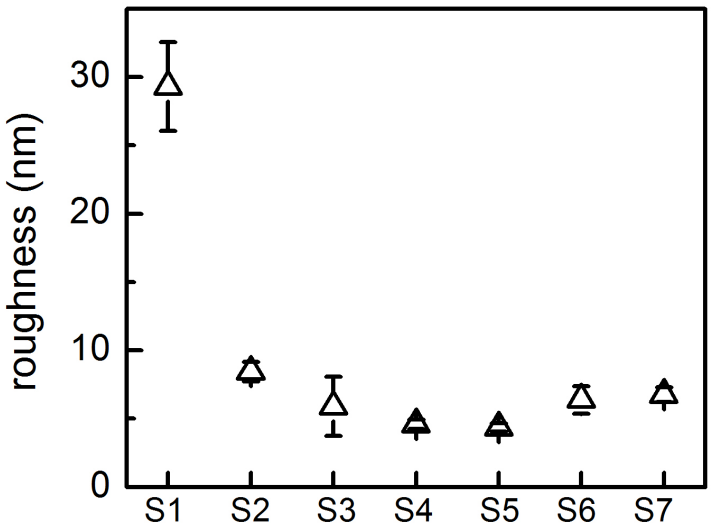

Figure 7.7: *The surface roughness of each functional stack, extracted from AFM topography data. Reproduced with permission from Ref. [137] copyright 2015 American Chemical Society.*

In order to closely observe the small gold nanoparticles, additional SEM measurements are carried out on the samples S6 and S7. The resulting images are shown in figure 7.8. For the sample S6, directly after gold layer deposition, small dot-shape structures with a diameter of around 15 nm are visible in figure 7.8a. These dot-shaped grains are isolated from each other. For the sample S7, after thermal annealing, aggregates of gold nanoparticles are formed, showing much larger grains and coarsened structures, as shown in figure 7.8b.

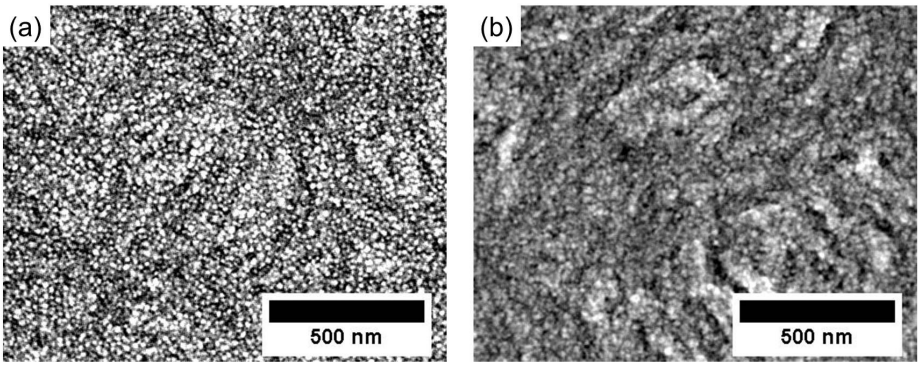

Figure 7.8: *SEM images of the functional stack with gold layer (a) before (S6) and (b) after thermal annealing (S7).*

Inner morphology

The AFM images reveal the development of surface structures during the solar cell assembling. However, the obtained structural information is local. The scan size is limited to the length within several micrometers. Moreover, the structures probed by AFM are restricted to the surface structure. As reported, the surface morphology of the thin film may differ from the inner morphology [5]. Therefore, GISAXS measurements are employed to resolve the evolution of the inner morphology during the functional stack build-up. The obtained structural information exhibits high statistics, with the probed region extending to several millimeters. The GISAXS measurements were done at the P03/MiNaXS beamline of the PETRA III storage ring at DESY, Hamburg, Germany. The X-ray wavelength was 0.0957 nm and the sample detector distance was selected to be 3180 mm for a reasonable q range. In order to probe the inner film structures, an incident angle of 0.45° was selected, which is above the critical angles of all the materials involved in the solar cells. The corresponding critical angles of each material are listed in table 7.2.

In figure 7.9, the 2D GISAXS data of each stack S1 to S7 are shown. The specular peak is shielded by a beamstop to protect the detector from over-saturation, showing a black dot in the middle of each image. Below the specular peak, the maximum intensity is in the Yoneda peak regions. Generally, the Yoneda peak is material-sensitive and located at

material	**FTO**	**TiO_2**	**P3HT**	**PCBM**	**PEDOT**	**PSS**	**gold**
critical angle (deg)	0.223	0.173	0.099	0.111	0.092	0.092	0.343

Table 7.2: *Yoneda peak of all investigated materials at $\lambda = 0.0957$ nm.*

the position of the critical angle of this material. The sample S1 (FTO substrate), shows a wing-like scattering feature, suggesting well-defined structures with sizes in the ranges of several nanometers. With the TiO_2 layer (S2 and S3) deposited on top of the FTO, the 2D GISAXS data changes from that of the FTO substrate. The overall intensity is strongly increased because the TiO_2 layer flatten the sample surface, which is in good agreement with the surface roughness investigation from AFM measurements. Continuing with the P3HT:PCBM layer (S4) and with the PEDOT:PSS layer (S5) deposition, different 2D GISAXS patterns show up due to the new materials probed. However, the 2D GISAXS data between these two stacks of S4 and S5 are quite similar due to the low contrast between these polymers. For the final device with gold contact on top (S6 and S7), the 2D GISAXS data is completely different from that of the previous stacks, because gold has much stronger scattering as compared to other materials buried underneath.

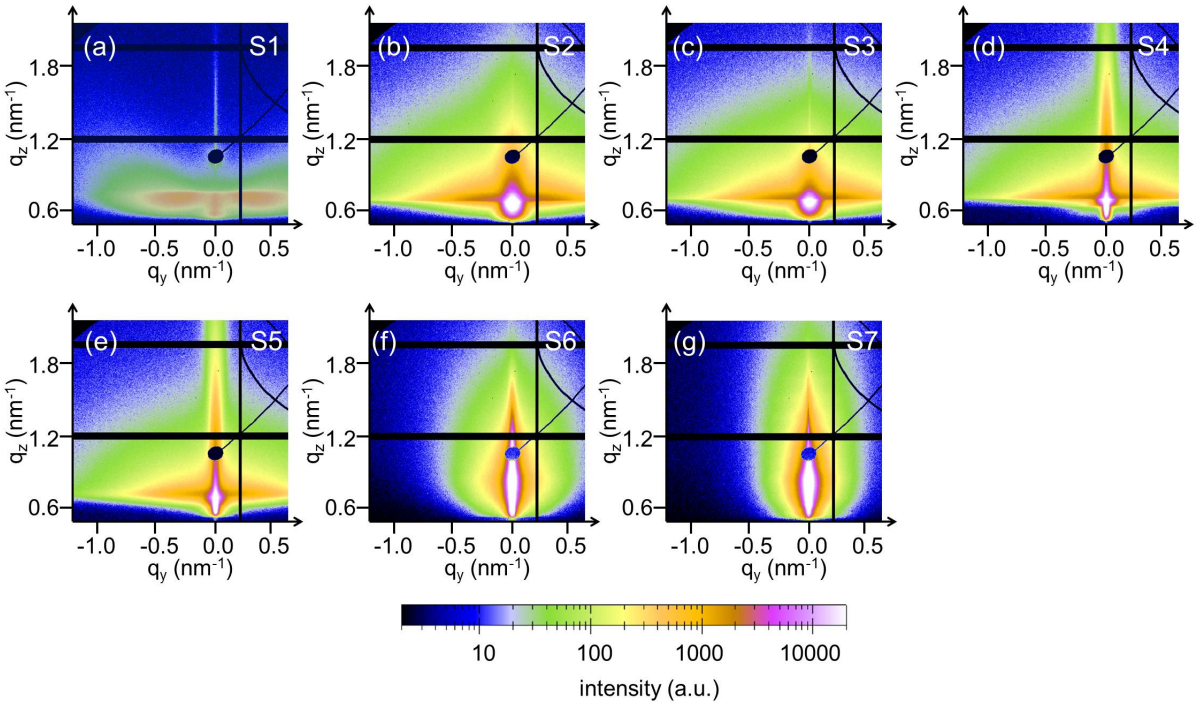

Figure 7.9: *2D GISAXS data measured at the individual samples of the functional stack build-up in the inverted P3HT:PCBM solar cell, from S1 to S7 denoted as (a) to (g). The scale bar of intensity is identical for all the 2D GISAXS data to illustrate the variation in scattering density.*

In order to obtain the structural information in the direction normal to the sample surface, the vertical line cuts are performed for all 2D GISAXS data and plotted in figure 7.10a. The beamstop shielded part is denoted by a grey box in figure 7.10a. Generally, all the vertical line cuts are dominated by the Yoneda region which is determined by the

materials of the probed sample. For example, the Yoneda peak of FTO (S1), locating at q_z equal to 0.75 nm^{-1}, is highlight with a dashed line in the graph. However, for the samples with other layer on top of FTO, the signal of the Yoneda peak of FTO is significantly weaker in comparison to the bare FTO substrate. This is due to the fact that the new Yoneda peaks corresponding to TiO_2 or other materials on the top layer appear and superimpose to the Yoneda peak of FTO. Throughout all the vertical line cuts, the Yoneda peak of each material is visible, suggesting no changes of the materials during the functional stack build-up.

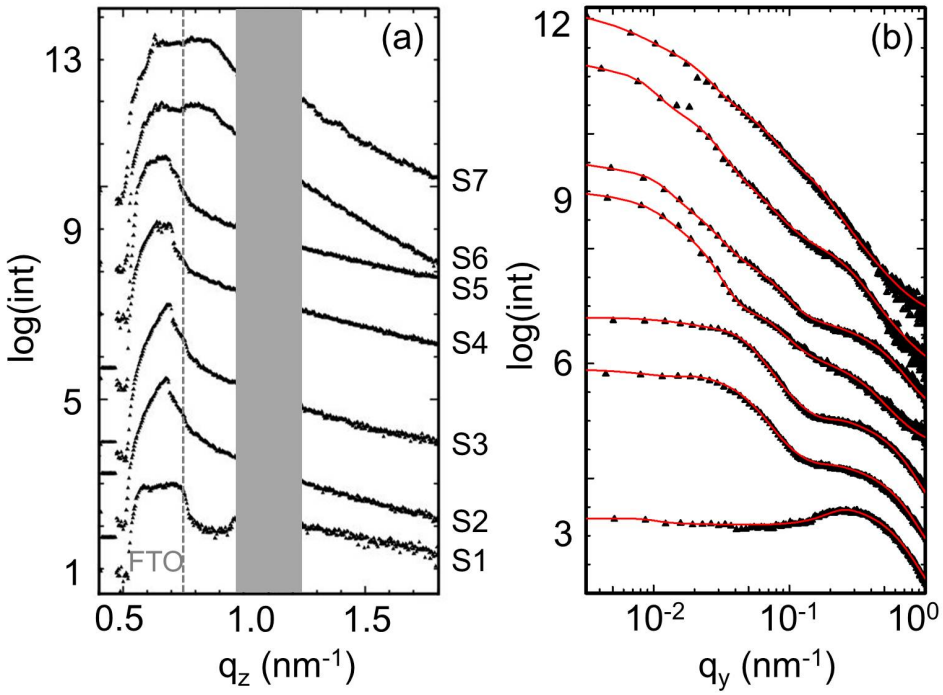

Figure 7.10: *(a) Vertical line cuts extracted from the 2D GISAXS data of the functional stacks. The area shielded by the beamstop is indicated by a grey rectangle. (b) Horizontal line cuts (black triangles) together with their best fits (red lines). The curves are shifted along the intensity axis for clarity. The curve from the bottom to the top indicate the sample in the sequence from S1 to S7.*

Horizontal line cuts of the 2D GISAXS data are shown in figure 7.10b. These line cuts include the information about lateral structures inside the samples. Since the most pronounced scattering intensity is located at the Yoneda peak region of the respective material, the horizontal line cuts are performed at the Yoneda peak of the concerned material [48]. For functional stacks without P3HT:PCBM layer (from S1 to S3), the horizontal line cuts are always performed at the Yoneda peak of the newly deposited material. For example, the horizontal line cut is performed at the Yoneda peak position of

FTO for S1 and of TiO_2 for S2 and S3. While for the functional stacks with P3HT:PCBM layer, the horizontal line cuts are performed at the Yoneda peak position of P3HT since the inner morphology of the active layer plays the most important role for the solar cell performance.

In order to obtain further quantitative information, a model in the framework of the DWBA is used to fit the horizontal line cuts. This model includes the contributions from the form factor of individual scattering centers and the corresponding distance between the neighbor scattering centers (structure factor). In order to achieve the best fits, three cylindrical form factors are used, denoted as the average structure sizes. The corresponding structure factor is assigned to each form factor, named as distance in this section. The best obtained fits (red lines) are shown together with the corresponding horizontal line cuts in figure 7.10b. For the FTO substrate, a pronounced peak is observed in figure 7.10b, suggesting a well-defined lateral FTO structure. With the TiO_2 layer deposition, the peak related to the FTO structure is still visible, however a new peak appears at the position of a smaller q_y value. After the $TiCl_4$ bath treatment and calcination, the horizontal line cut stays similar. Continuing with P3HT:PCBM spin coating, the horizontal line cut appears changed. A new peak located at a smaller q_y value suggests large structures exist in the P3HT:PCBM layer. Moreover, the structure originating from the FTO substrate is still visible but much less prominent. For the functional stack with the PEDOT:PSS layer, the horizontal line cut does not change obviously due to the low temperature process which normally does not alter the inner morphology of the active layer. Directly after the process of gold evaporation, the peak shifts to a smaller q_y value, suggesting an increased structure size in the active layer. Later on, the structure sizes continuously increase due to final thermal annealing.

The structure sizes and distances obtained from the horizontal line cuts are summarized as a function of multilayer stack assembling and illustrated in figure 7.11. According to the position where the horizontal line cut is performed, the structural information is assigned to the structure of FTO for sample S1, TiO_2 for sample S2 and S3, and P3HT for the other samples with P3HT:PCBM layer (from S4 to S7). The FTO layer possesses two characteristic structure sizes of $(2.7 \pm^{0.2}_{0.1})$ nm and $(36.5 \pm^{16.5}_{13.5})$ nm, with corresponding distances of $(17 \pm^{2}_{1})$ nm and $(75.5 \pm^{24.5}_{15.5})$ nm. With addition of TiO_2 layer, the small structure size of around 2.7 nm is replicated by TiO_2. However a new structure size of $(26.5 \pm^{1.0}_{1.5})$ nm with a distance of $(135 \pm^{15}_{10})$ nm appears, attributed to TiO_2 nanoparticles. After the $TiCl_4$ bath treatment and calcination, the structure size of around 26.5 nm does not change but reveals a much smaller distance of $(75 \pm^{15}_{10})$ nm. The decreased distance between TiO_2 nanoparticles is explained by the fact that the gaps are filled by the TiO_2 nanoparticles formed during the $TiCl_4$ bath treatment. It indicates that the finer layer

of TiO_2 is arisen, which is consistent with the features observed in AFM images that a denser layer is formed after $TiCl_4$ bath treatment.

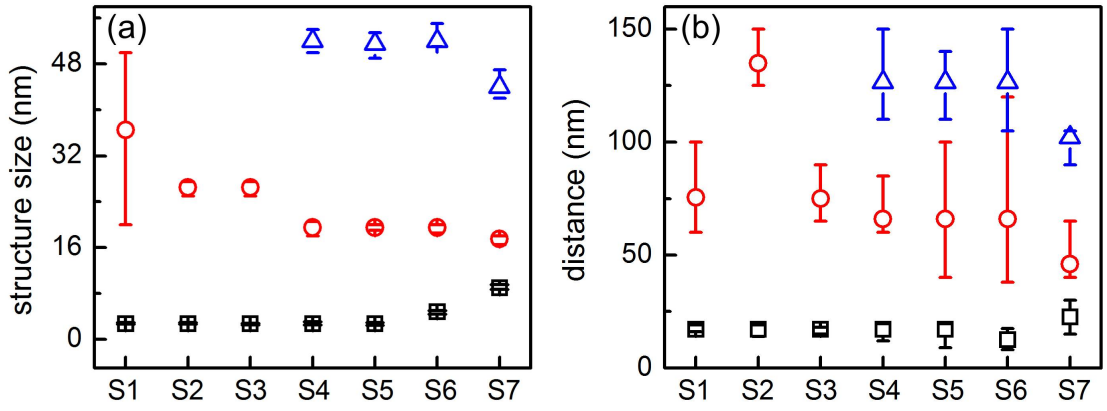

Figure 7.11: *(a) Structure sizes and (b) corresponding distances of each functional stack of inverted P3HT:PCBM solar cells, extracted from the fits of horizontal line cuts. Two structures are used to obtain the best fits for the samples S1, S2, and S3, whereas three structures are used for the other samples. The black, red, and blue colors indicate the small, medium, and large structures, respectively. Reproduced with permission from Ref. [137] copyright 2015 American Chemical Society.*

With P3HT:PCBM spin coating, the small structure of around 2.7 nm originated from FTO substrate is further replicated by P3HT. However, two new structures are formed by P3HT itself, with structure sizes of $(19.5 \pm^{1.0}_{1.5})$ nm and $(52 \pm^{2}_{2})$ nm, and corresponding distances of $(66 \pm^{19}_{6})$ nm and $(126.5 \pm^{23.5}_{16.5})$ nm. Afterwards, the PEDOT:PSS is deposited on top of P3HT:PCBM layer by spray coating. During this process, the inner morphology of the active layer does not change. The active layer still has three structures, with the same structure sizes and distances, suggesting the active layer can be successfully preserved after spray coating a PEDOT:PSS layer on top. After gold evaporation, the smallest structure size of P3HT increases from around 2.7 nm to $(4.8 \pm^{0.2}_{0.4})$ nm, while the other two structures remain unchanged. The increase of the smallest structure size of P3HT may be caused by the thermal load during the gold evaporation. Similarly, Guo et al. also found the structure size of P3HT increases after the aluminum evaporation in a standard P3HT:PCBM solar cell [26]. Afterwards, thermal annealing was carried out in a controlled environment with constant nitrogen flow. It clearly shows that the smallest structure size of P3HT further increases from around 4.8 nm to $(9 \pm^{0.5}_{0.3})$ nm, which partially originating from the thermal load. Such structure coarsening behavior of P3HT:PCBM film after thermal treatment has been already observed [157]. The struc-

ture size of around 9 nm is in the range of the exciton diffusion length of 10 nm in P3HT, suggesting an efficient exciton dissociation [115]. This enlarged structure size of P3HT indicates less interface between P3HT and PCBM, which lowers the recombination probability of the holes and electrons. Instead, the other two structure sizes of P3HT decrease after thermal annealing (from around 19.5 nm to ($26.5 \pm^{0.5}_{1.0}$) nm, and from around 52 nm to ($44 \pm \frac{3}{2}$) nm), suggesting the exciton dissociation is more efficient since in smaller P3HT domains more exciton can reach the interface. In a standard P3HT:PCBM solar cell, the large structure size of P3HT is reported to be 65 nm, which is much larger than it in inverted solar cells [26]. Therefore, the higher J_{SC} and PCE of inverted P3HT:PCBM solar cell as compared to a standard one can be explained by the smaller structure sizes of P3HT in the active layer.

7.1.3 Results

It is demonstrated from this work that a highly efficient polymer solar cell can be obtained by utilizing an inverted geometry. Different from the standard geometry, in an inverted solar cells charge carriers are transported in an opposite way, where the holes are collected at the top electrodes of gold and the electrons are collected at the bottom electrodes of FTO. As a standard system, P3HT:PCBM BHJ solar cells are investigated in this work. The PCE of the inverted solar cell achieves (4.2 ± 0.2) %, with a maximum value of around 4.4%, whereas the PCE of the standard solar cells is only (3.1 ± 0.1) %. This PCE value we obtained is among the highest values of P3HT:PCBM systems. Taking all the photovoltaic parameters into account, the J_{SC} of (13.1 ± 0.3) mA/cm^2 is much higher as compared to the standard solar cell and therefore it is the main reason for the PCE improvement.

In order to understand the reason lying behind the high efficiency of inverted solar cells, the morphological evolution is probed. AFM and GISAXS measurements are carried out on each step of the functional stack build-up in sequence of the solar cell assembling. With AFM measurements, it is observed that FTO substrates exhibit a very high roughness of around 30 nm, which is beneficial for the internal light scattering and therefore elevates the light harvesting of the active layer. Furthermore, GISAXS measurements reveal that newly deposited P3HT:PCBM layer has three structure sizes of around 2.7 nm, 19.2 nm, and 52 nm, where the structure of around 2.7 nm is originated from duplicating the structure of the FTO layer. After final thermal treatment, the structure sizes of the active layer are around 9 nm, 17.5 nm, and 44 nm. In comparison to standard solar cells, the structure sizes of the active layer are much closer to the exciton diffusion length in P3HT. Therefore, exciton dissociation is more efficient and accordingly the J_{SC} is much

higher in inverted solar cells. In summary, both high roughness of the FTO substrate and small structure sizes of active layer in the final device contribute to the high performance of the inverted P3HT:PCBM solar cells. Furthermore, it is inferred that proper surface modification of the bottom substrates can be beneficial for achieving high efficiency.

7.2 Stability

In the previous section, the improvement in photovoltaic performance resulted from using an inverted geometry has been discussed. In the following section, the stability of inverted P3HT:PCBM BHJ solar cells will be investigated. At first, in section 7.2.1, the device stability during 4 hours continuous operation under illumination is studied. Then, in section 7.2.2, a long-term stability of the solar devices, without encapsulation, stored under dark ambient condition, is probed periodically for more than 150 days.

7.2.1 In operando morphology and photovoltaic performance investigation

As reported, the degradation in photovoltaic performance of a standard P3HT:PCBM solar cell is correlated to a morphological degradation in the active layer [131]. In the following, during an inverted solar cell operation under illumination, the morphological evolution of the active layer is investigated via GISAXS measurements. The relationship of morphology and solar cell performance is studied.

In operando morphology investigation

In order to probe the inner morphology evolution of the active layer in an inverted P3HT:PCBM solar cell during operation under illumination, in operando GISAXS measurements were carried out at the Austrian SAXS beamline of the Elettra synchrotron source in Trieste, Italy. The X-ray wavelength was 0.154 nm and the SDD was set to 1776 mm. In order to enable the X-ray fully penetrate the sample, an incident angle of 0.53° was selected. A pocket solar was employed to mount the solar cell for in operando measurements, which enables the simultaneous J-V curve recording and GISAXS characterization. In addition, the pocket solar can be evacuated to minimize the degradation from moisture and oxygen. In order to compare to our previous investigation on the standard solar cell, the same pocket solar was used for the inverted solar cell. The detailed description of the pocket solar has been published in [131]. Since the impact of

moisture and oxygen on inverted and standard geometries were ruled out under vacuum, the observation was focused on the difference in morphological evolutions. The GISAXS measurements were taken before illumination (denoted as 0 min), and after operation for 3, 10, 15, 30, 60, 120, 180, and 240 min under illumination, respectively. Instead of directly probing at the gold electrode, three different positions near the gold electrodes were selected to prevent the strong scattering signal of the gold electrodes suppressing the signal from the active layer.

All these 2D GISAXS data are identical. The initial data is shown in figure 7.12a as an example, with the zoom of the featured pattern illustrated in figure 7.12b. The half-circle-shaped scattering is attributed to the TiO_2 layer and FTO substrate, as described in section 7.1.2. The Yoneda region is denoted by the red arrow with letter Y in figure 7.12a, locating at the bottom of the 2D GISAXS data. Additionally, the Bragg reflection is shown at the top of the image labeled by letter B, which is correlated to the P3HT (100) peak.

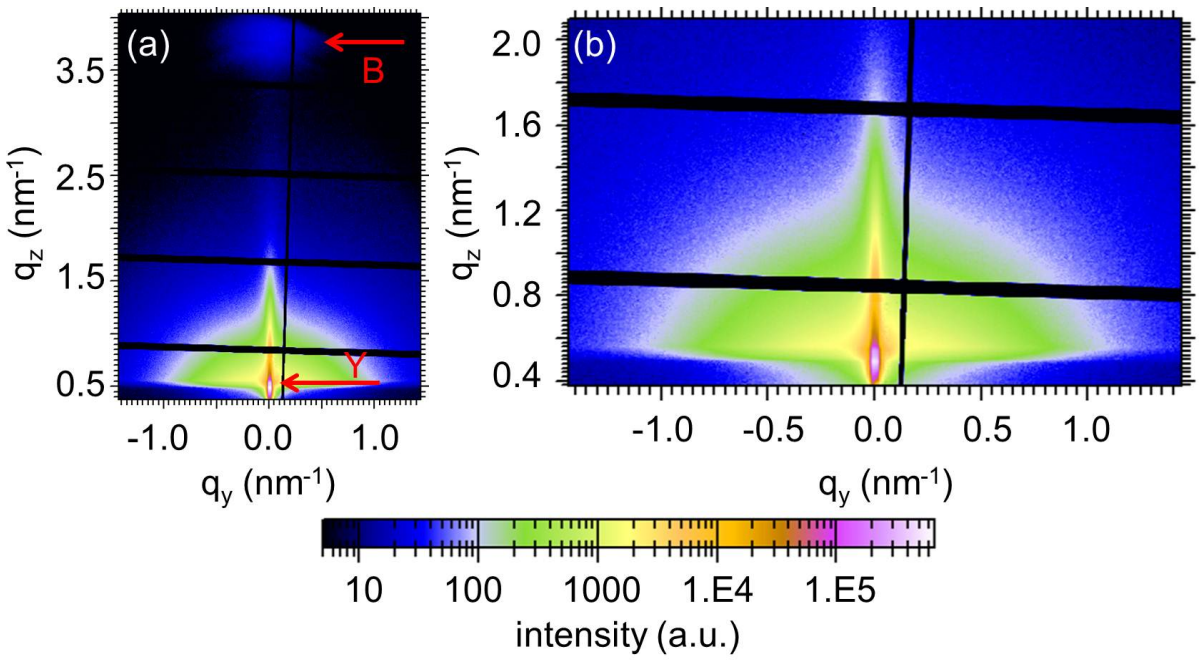

Figure 7.12: *(a) Initial (0 min) 2D GISAXS data of the inverted P3HT:PCBM BHJ solar cell. The P3HT (100) Bragg reflection (B) and Yoneda region (Y) are pointed by the red arrows, respectively. (b) Zoom-in of figure (a).*

The vertical line cuts are firstly extracted from all the 2D GISAXS data at the position of $q_y = 0$. In order to visualize the morphological evolution, all the cuts are plotted on top of each other in figure 7.13a. No visible difference is observed. For clearly illustrating the Yoneda region, a zoom-in is shown as the inset in figure 7.13a. It shows that the position of P3HT Yoneda peak, locating at 0.48 nm^{-1}, indicated by the black arrow, does not

alter with time. Therefore it is inferred that the composition of the active layer is stable, and no molecular diffusion occurs during the solar cell operation under solar illumination for 240 min. In addition, the P3HT (100) Bragg peak is located at $q_z = 3.75$ nm^{-1} with its FWHM of (0.63 ± 0.05) nm^{-1}, correlated to the spacing distance of 1.68 nm and the correlation length of (10.0 ± 0.8) nm along (100) direction. This peak is also stable with time, suggesting no degradation occurs on the level of molecular packing.

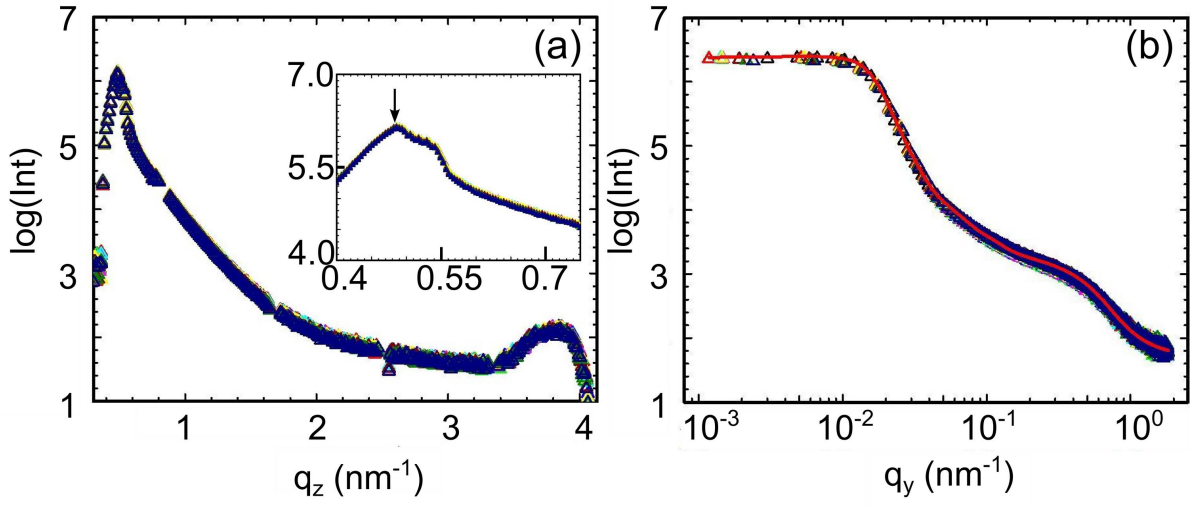

Figure 7.13: *(a) Vertical line cuts and (b) horizontal line cuts (symbols) with their fit (red line) extracted from the 2D GISAXS data of the inverted P3HT:PCBM solar cell illuminated for 0, 3, 10, 15, 30, 60, 120, 180, and 240 min. The zoom-in of the Yoneda region is shown as the inset in (a). In order to clearly illustrate the morphological evolution, the curves are plotted on top of each other in each image. Different colors represent different illumination times. Reproduced from Ref. [138] with permission from the Royal Society of Chemistry.*

The horizontal line cuts of the 2D GISAXS data reveal the evolution of the lateral structures in the active layer. As discussed in section 7.1.2, the horizontal line cuts are applied at the position of the P3HT Yoneda peak. All horizontal line cuts are plotted on top of each other in figure 7.13b to visualize the difference. All curves fully overlap, suggesting no nanostructure variation takes place. Therefore, the morphological degradation in the active layer does not happen. This observation is opposite to that of the standard P3HT:PCBM solar cell as reported by Schaffer et al. [131]. They found that the nanomorphology of the P3HT:PCBM layer degraded in standard solar cells during the operation under illumination. The small domains vanished and the large domains grew with time, which resulted in a reduction of the effective area of interface between P3HT and PCBM phases. As a consequence, the J_{SC} of the solar cell decayed, which was the main reason for the solar cell degradation. As compared to the standard solar cell, the

stability of the nanomorphology of the active layer in inverted solar cells is significantly improved, which can be explained in terms of two factors. Firstly, the TiO_2 layer underneath P3HT:PCBM film can absorb the UV light, which protects the P3HT chain from scission under the UV illumination. Accordingly, the polymer chains remain their high molecular weight. The mobility of the chains is restricted and the relaxation of polymer chains are prevented. Secondly, the interactions between the TiO_2 and P3HT:PCBM layers are different from that between PEDOT:PSS and P3HT:PCBM, which also influence the morphology of the P3HT:PCBM layer. Previous work from Zhao et al. revealed that the P3HT films exhibited different morphologies and stabilities when they were deposited on conductive substrates or on glass [158].

Since all the horizontal line cuts are identical, one single fit is shown as an example in figure 7.12b as the red line. Corresponding P3HT structure sizes of (2.5 ± 0.2) nm, (19 ± 1) nm, and (82 ± 4) nm are extracted, with their corresponding distances of (45 ± 5) nm, (180 ± 30) nm, and (420 ± 100) nm. In summary, the morphology of P3HT:PCBM active layer in an inverted solar cell is fully stabilized, which is strongly improved as compared to a standard solar cell. The stability of the active layer is attributed to the TiO_2 blocking layer underneath.

J-V sweep

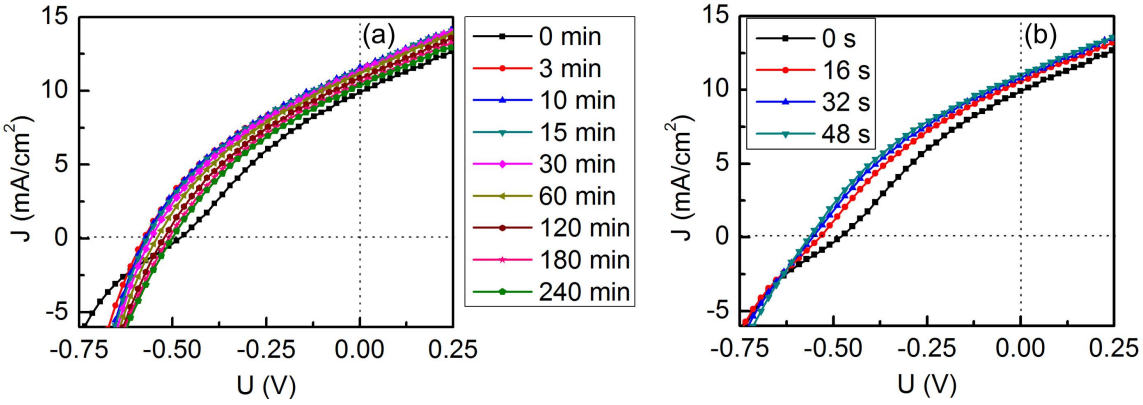

Figure 7.14: *J-V curves of inverted P3HT:PCBM solar cells illuminated for (a) 0, 3, 10, 15, 30, 60, 120, 180, and 240 min, and (b) 0, 16, 32, and 48 seconds.*

It has been shown that the inner morphology of the active layer is stable in inverted solar cells. Therefore, the evolution of the photovoltaic performance is of great interest during this period. The J-V sweeps with an interval of 16 seconds are recorded simultaneously with the GISAXS measurements. In order to correlate with the GISAXS measurements,

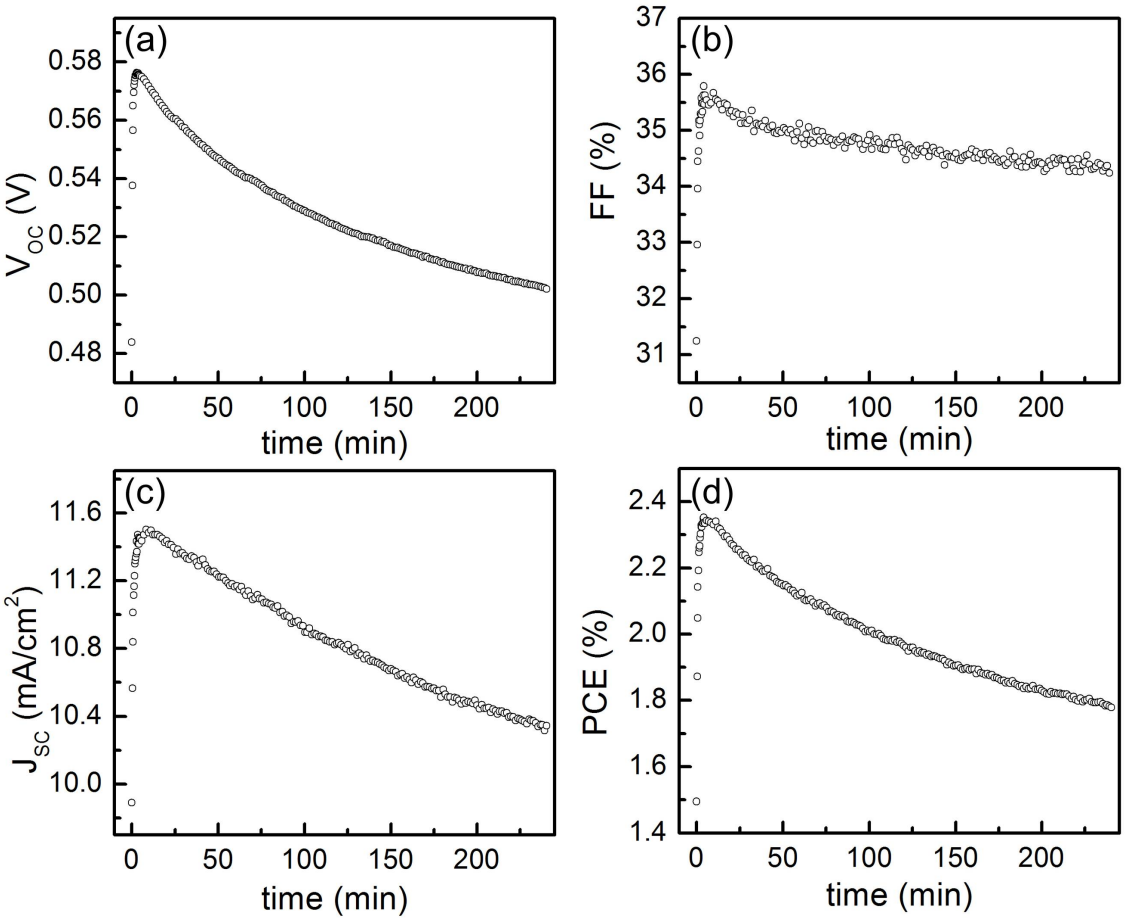

Figure 7.15: *Evolution of all the photovoltaic parameters (a) V_{OC}, (b) FF, (c) J_{SC}, and (d) PCE. In order to achieve higher statistic, every five points are averaged. Reproduced from Ref. [138] with permission from the Royal Society of Chemistry.*

the J-V curves recorded with illumination for 0 (the beginning of illumination), 3, 10, 15, 30, 60, 120, 180, and 240 min are selected and shown in figure 7.14a. The initial J-V curve (at 0 min) shows an S-shape, with the smallest J_{SC} and V_{OC}. However, with running the J-V measurements, the shape of J-V curve transits toward similar to rectangle. In order to look closely into the transition within the initial period, the first four J-V curves with illumination for 0, 16, 32, and 48 seconds are shown in figure 7.14b. It is found that the transition is a fast process, with the most pronounced change from 0 to 16 seconds. It indicates that the self-healing process occurs in the inverted solar cells during operation for the first seconds. Similar behavior has been also observed in the inverted solar cell by Lloyd et al. [159]. They attributed the self-healing process to the evolution of the interface between the electron blocking layer and the top electrodes. From 3 min till around 10 min,

the J-V curves are quite similar, suggesting a stable photovoltaic performance. However, afterwards the J-V curves decays slowly with time, showing decreasing J_{SC} and V_{OC}.

Photovoltaic parameters including J_{SC}, V_{OC}, FF, and PCE are extracted from each J-V curve and displayed as the function of illumination time in figure 7.15. Generally, all these parameters evolve in a similar way. Within the first minutes, all parameters are dramatically improved, which is caused by self-healing as discussed in previous paragraph. Afterwards, a relatively stable period exists till around 10 min. Then, all the parameters continuously decay with time. The decay of J_{SC}, V_{OC}, and FF contributes to the degradation of the PCE.

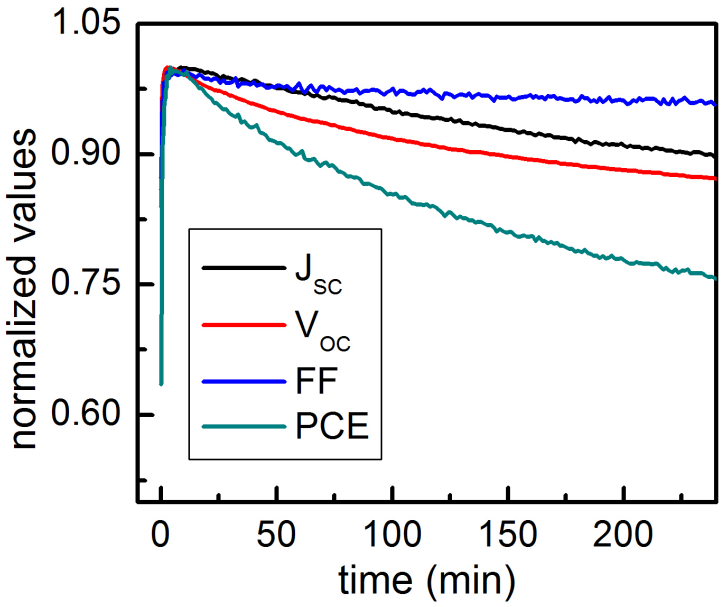

Figure 7.16: *Evolution of all the photovoltaic parameters V_{OC}, FF, J_{SC}, and PCE, normalized to their corresponding maximum values. In order to achieve higher statistic, every five points are averaged. Reproduced from Ref. [138] with permission from the Royal Society of Chemistry.*

In order to compare the decay behavior of the inverted solar cell to our previous work (standard solar cell), all the photovoltaic parameters are normalized to their respective maximum values and depicted in figure 7.16. Generally, the stability of J_{SC} and PCE of the inverted solar cell is substantially improved in comparison to the standard solar cell, while its V_{OC} and FF show a similar decay level to the standard solar cell. In details, V_{OC} sustains 90% to its maximum values. The reason for this decay might be the temperature increase by 10 °C during the measurements. It has been reported that V_{OC} drops with increasing temperature due to the photochemical reaction in the polymers [160]. The

FF is the most stable parameter, which still maintains 96% of its maximum. The most remarkable results are the evolution of J_{SC} and PCE. With the inverted geometry, they are preserved around 90% and 75% of their corresponding maximum values, while they only keep around 80% and 65% in the standard solar cell. According to the decay behavior of all parameters, it can be concluded that the improvement of the PCE stability is mainly ascribed to a more stable J_{SC}.

Correlated to the observation from in operando GISAXS measurements, it is inferred that the improvement of the stability of J_{SC} is caused by a stable morphology of the active layer in an inverted solar cell. Similarly, Schaffer et al. found that the decay of J_{SC} in a standard solar cell completely follows the morphological degradation of the active layer [131]. As a result, the stabilized P3HT:PCBM active layer contributes to the highly improved stability of J_{SC} and PCE, while it has a weak influence on the V_{OC} and FF.

7.2.2 Long-term stability

Although the inverted P3HT:PCBM solar cell shows a high stability during continuous operation under illumination for 240 min, the investigation of long term stability is also significant. Thus, in a second experiment the inverted solar cells were kept in a dark ambient condition and measured periodically up to more than 150 days. The photovoltaic parameters (J_{SC}, V_{OC}, FF, and PCE) are extracted from J-V measurements and illustrated as a function of storage time, in figure 7.17. In order to show the trend, red dashed lines are plotted as guide to the eye in figure 7.17. J_{SC} maintains similar during the first 21 days and then suddenly decreases. After 37 days a much slower decrease follows until the last measurement, corresponding to a loss less than 15% of the maximum value of J_{SC}. However, V_{OC} and FF strongly improved during the first 21 days. After that, no significant changes are observed. In general, standard P3HT:PCBM solar cells degrade quickly in ambient conditions [161]. It is notable that the PCE of the inverted solar cell remains around 88% compared to its maximum value after more than 150 days storage. The evolution of the PCE can be divided into two regions. The first pronounced growth is attributed to the increase of V_{OC} and FF in the first 21 days, while the degradation occurs due to the decay of all the photovoltaic parameters after 21 days. In summary, a significant improvement in the long-term stability of the inverted P3HT:PCBM solar cell is achieved, also when stored in ambient conditions.

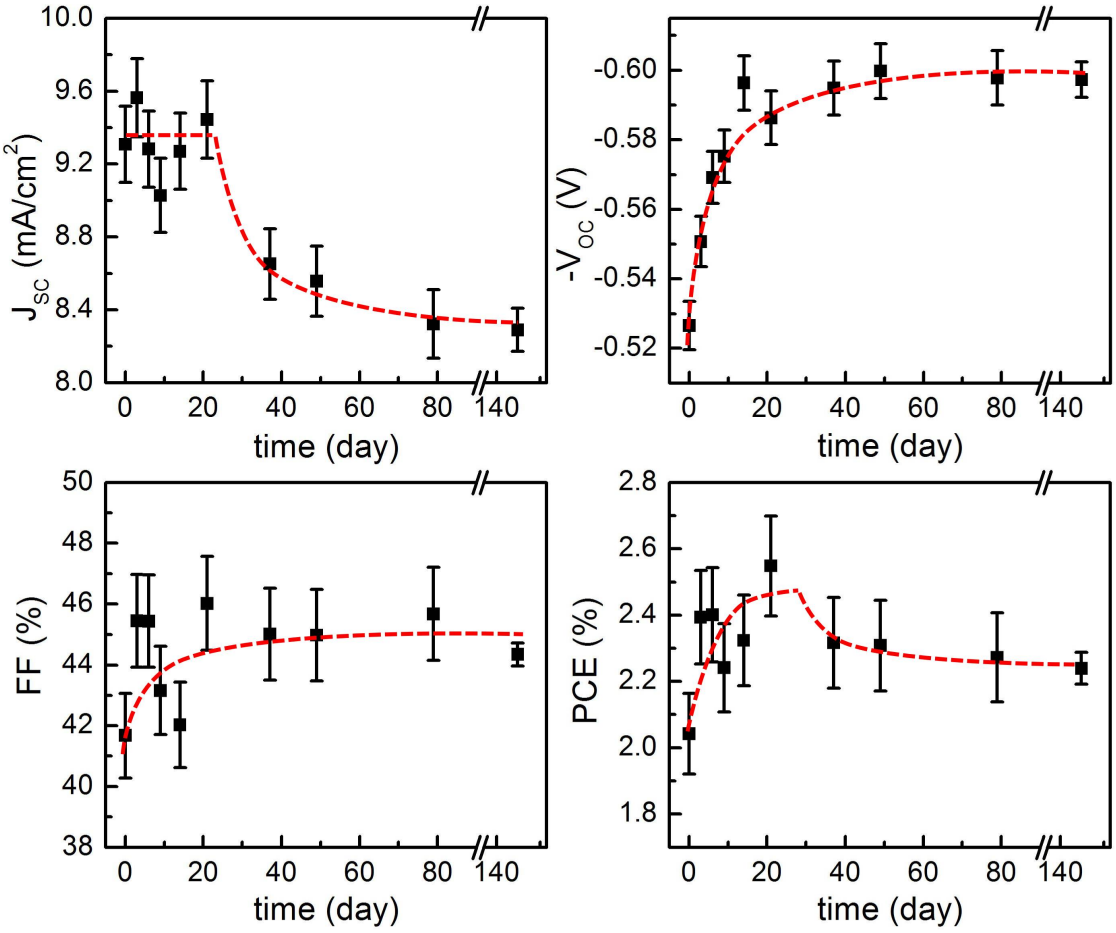

Figure 7.17: *Long-Term evolution of all the photovoltaic parameters of V_{OC}, FF, J_{SC}, and PCE. The red dashed lines are used as a guide to the eye.*

7.2.3 Results

In this work it is demonstrated that the inverted P3HT:PCBM BHJ solar cells show highly stable performance during operation, which is a dramatic improvement as compared to the standard solar cell geometry. In order to explore the correlation between the morphology and the solar cell performance, in operando GISAXS measurements are carried out under illumination for 240 min. Simultaneously, J-V sweeps are recorded. The PCE of the inverted solar cell is preserved to 75% as compared to its maximum value after 240 min continuous operation. By taking all the photovoltaic parameters into account, it is found that the V_{OC} and FF show quite similar decay behavior as in the standard solar cell, whereas the J_{SC} shows much higher stability. Therefore, the higher stable J_{SC} is the main factor for the higher stability of the PCE. The in operando GISAXS measurements reveal that the morphology of the P3HT:PCBM active layer in an inverted solar cell re-

mains stable and does not alter during the device operation. The unchanged morphology is mainly attributed to the TiO_2 layer underneath, which absorbs UV light and accordingly protects the P3HT from UV degradation and molecular relaxation. However, in a standard solar cell the P3HT:PCBM layer undergoes degradation with time which is fully responsible for the efficiency degradation. Therefore, the morphology stabilization of the active layer in the inverted solar cells is directly correlated to the improved stability of the J_{SC} and PCE for the first time.

Furthermore, the inverted devices show long-term stable, even when they are stored in air. The photovoltaic properties are examined periodically and it is found that the PCE of the inverted solar cell remains 88% after more than 150 days. Therefore, it is concluded that the morphological stability of the active layer, such as utilizing the inverted geometry for solar cells, can lead to highly stable polymer solar cells.

7.3 Summary

By utilizing inverted geometry in P3HT:PCBM BHJ polymer solar cells, a significant increase of PCE compared to the standard geometry is obtained. The improved PCE is mainly ascribed to the high J_{SC}. It is proposed that the inverted geometry induces higher internal light harvesting and smaller structure sizes of the P3HT:PCBM active layer, which are revealed by AFM and GISAXS measurements on each functional stack. Hence, more exciton are generated in the active layer and dissociated at the interface. Accordingly a higher J_{SC} is obtained. Furthermore, from this study it is inferred that proper structuring the surface of substrate can be beneficial for the high efficiency. Additionally, it is found that the inverted P3HT:PCBM solar cells show quite stable photovoltaic performance due to its stable morphology of the active layer. The PCE is preserved for 75% compared to its maximum value after 240 min of continuous operation under illumination, which is mainly attributed to a highly stable J_{SC}. A fully stabilized P3HT:PCBM active layer is considered as the direct reason for the stable J_{SC}, indicated by the in operando GISAXS measurements. Furthermore, the inverted solar cell has a long-term stability, when it is stored under dark ambient condition. Through periodically J-V measurements, it shows that the device remains 88% of its maximum PCE after more than 150 days storage.

In conclusion, the inverted geometry is a constructive strategy towards highly efficient and stable polymer solar cells. Furthermore, in order to optimize the solar cell performance in efficiency and stability, one should not only consider the morphology of active layer, but also pay attention to the influence of the device architecture of the solar cells.

8 Low temperature route to flexible nanostructured P3HT/TiO_2 hybrid films

Besides organic solar cells, hybrid solar cells are another widely investigated system in the field of photovoltaics. They comprise an inorganic semiconductor as electron conducting material and a conjugated semiconducting polymer as donor material. As one of the broadly used inorganic semiconductors, TiO_2 shows its distinct advantages such as cheap, stable, non-toxic, and abundantly availability. Moreover, nanostructured TiO_2 can be easily fabricated using a sol-gel process with the help of a structure directing polymer template. This routine enables the demand for a large interface between TiO_2 and the donor material where the charge separation takes place [24, 162]. Following film deposition a calcination process above 400 °C is required to obtain crystalline titania as well as burning away the structure directing polymer templates [163]. However, this high temperature step is not feasible for the deposition of TiO_2 on flexible organic substrates such as poly(ethylene terephthalate) (PET) and polyethylene naphthalate (PEN) which cannot withstand temperatures above 150 °C [23]. Therefore, low processing temperatures are causing less-energy consumption and essential for flexible substrates [164]. Furthermore, TiO_2 is a brittle material with low flexural strength that may fail in bending applications [60]. Therefore, the mechanical investigation on the TiO_2-based active layer is important for flexible hybrid solar cells.

Our previous work has already demonstrated a novel synthesis for rutile phase TiO_2 nanostructures at low temperatures [23, 165]. In this chapter, the amphiphilic diblock copolymer PS-b-PEO is used as the structure directing template. Various methods for template extraction are compared, as shown in section 8.1. In order to finalize the active layer preparation the porous TiO_2 film is backfilled with the donor material P3HT, which is discussed in detail in section 8.2. In section 8.3 and section 8.4, the mechanical properties of the TiO_2 based films are firstly characterized and then evaluated by appropriate models. These parts are based on the master's thesis of Widmann [25].

We have submitted a manuscript based on the results of this chapter.

8.1 Polymer template extraction

The nanostructured TiO_2 thin films are prepared by diblock copolymer template assisted sol-gel synthesis. Thereafter, the polymer template needs to be completely removed at low temperature, without destroying the TiO_2 network. Towards this goal, different extraction methods are applied. One PS-b-PEO/TiO_2 hybrid film without template extraction is prepared as the pristine sample. Another sample is prepared as a reference sample after conventional high temperature calcination. Detailed information about different extraction methods are summarized in table 8.1. First of all, the film thickness is probed with white light interferometry. The as-prepared sample shows a thickness of (204 $\pm$ 1) nm, which is in good agreement with the need for the active layer of hybrid solar cells. After polymer template removal, all the samples show a shrinkage of the film thickness. The samples with calcination and UV irradiation treatment provide the thinnest films, with 62% and 47% reduction of film thickness, respectively, while the other two samples show a reduction of around 15%.

The morphology of the resulting TiO_2 films is of high significance for hybrid solar cell applications. Therefore, the real-space and reciprocal-space analyses are discussed in section 8.1.1 and section 8.1.2, respectively. Furthermore, the corresponding porosity is calculated, as represented in section 8.1.3.

8.1.1 Real-space analysis

As shown in figure 8.1, the surface morphologies of the as-prepared PS-b-PEO/TiO_2 film and the resulting porous TiO_2 films with different polymer extraction methods are probed with SEM measurements. The sample with polymer template (figure 8.1a) shows a wavy surface morphology, which is common for non-conducting polymers. Although its surface morphology is blurry, the TiO_2 network is visible, indicating a successful structure formation by the polymer template PS-b-PEO. After template extraction, all the samples show a porous network-like structure with slightly different morphologies. It infers that the polymer template is removed successfully from the top surface. In general, the low temperature routes give rise to a uniform surface morphology as shown in figure 8.1b, 8.1c, and 8.1d, whereas the film with high temperature calcination shows strong collapse and local dense structure (figure 8.1e). The film collapse might be the reason that the calcined film shows the most significant shrinkage in film thickness. In the case of the TiO_2 film

sample	extraction method	time	temperature (°C)	film thickness (nm)
I	none	/	/	204 ± 1
II	DMF and CB baths	10 min and 1 h	RT	178 ± 2
III	UV irradiation	20 h	90	108 ± 6
IV	O_2 plasma	30 min	RT	178 ± 3
V	calcination	4 h	400	77 ± 3

Table 8.1: *Sample list with different extraction methods, treatment duration, the temperature, and the final film thickness. The film thickness is obtained by white light interferometry measurements.*

where the PS-b-PEO is extracted using organic solvent treatment (figure 8.1b), thicker walls of the network are observed compared to the UV irradiation and the O_2 plasma treatment (figure 8.1c and 8.1d). It appears that the UV and the O_2 plasma interact more aggressively with the TiO_2, which results in a thinner wall of the network and a stronger shrinkage of the film thickness than the sample using organic solvent extraction. In conclusion, the low temperature extraction (room temperature) is milder than high temperature calcination, which achieves better interconnected TiO_2 networks.

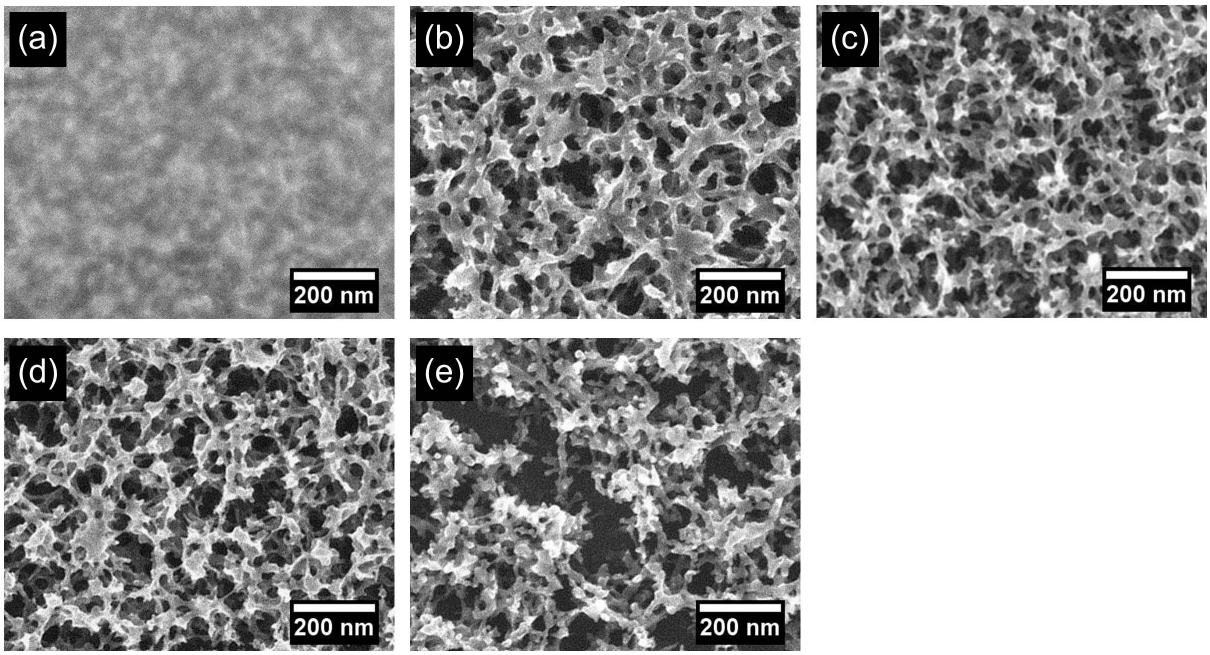

Figure 8.1: *SEM images of the as-prepared PS-b-PEO/TiO_2 film and the resulting porous TiO_2 films with different polymer extraction methods listed in table 8.1. Image from (a) to (e) represents the sample from I to V, respectively.*

Furthermore, in order to confirm a complete extraction, cross-section SEM measurements are performed. All images are shown in figure 8.2. In general, the top region of the images shows the surface morphology. The edge, located in the center of the image, represents the cross-section of the TiO_2 film. The bottom area shows the silicon substrate. For the sample without polymer extraction (figure 8.2a), a compact layer of PS-b-PEO/TiO_2 is observed with a relatively flat top surface. After the PS-b-PEO removal, all the samples show porous structures, with a rough surface. Interconnected TiO_2 networks are also observed in vertical direction. For the samples with solvent treatment and UV irradiation (figure 8.2b and 8.2c), the porous structure can be observed at the bottom of the film, indicating a complete removal of the polymer template. However, the PS-b-PEO is only partially removed from the sample which is treated with an O_2 plasma, since a dense layer still exists at the bottom of the film (figure 8.2d). The cross sectional image of the calcined sample, shown in figure 8.2e, confirms the strong collapse of the TiO_2 film which yields a large surface roughness. The pores are small and rare, which could cause a serious challenge for the P3HT backfilling. Therefore, it is summarized that among all investigated extraction methods the solvent treatment and UV irradiation are equally good for the polymer template extraction.

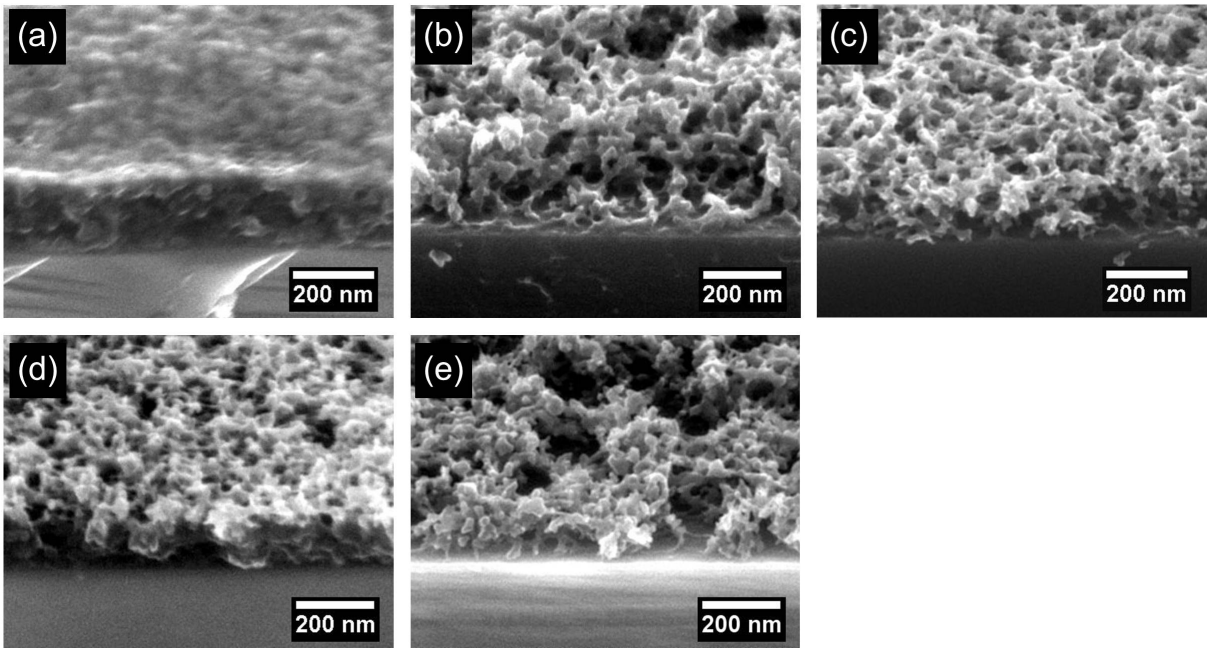

Figure 8.2: *Cross-section SEM images of the as-prepared PS-b-PEO/TiO_2 film and the resulting porous TiO_2 films with different polymer extraction methods listed in table 8.1. Image from (a) to (e) represents the sample from I to V, respectively.*

8.1.2 Reciprocal-space investigation

In order to get an insight into the inner morphology of different samples, GISAXS measurements are performed. Compared to SEM measurements, GISAXS probes a macroscopic area, providing better statistics. The GISAXS measurements were performed at 1W2A beamline at the Beijing Synchrotron Radiation Facility (BSRF), Beijing, China. The wavelength was 0.154 nm. The incident angle was set to 0.52° and the sample-detector distance was selected as 2994 mm. A Pilatus detector was used, providing 981 × 1043 pixel with pixel size of 172 × 172 μm^2.

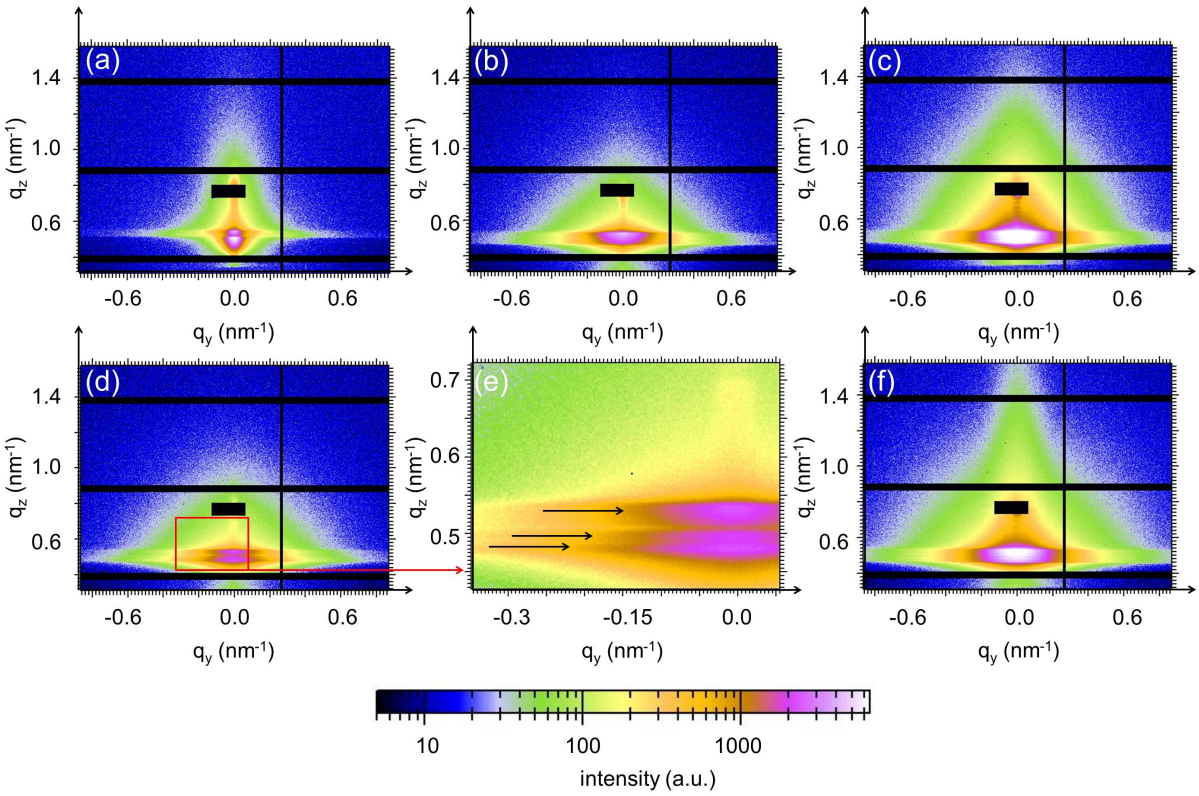

Figure 8.3: *2D GISAXS data of the PS-b-PEO/TiO_2 film and the porous TiO_2 films with different polymer extraction methods shown in table 8.1. Images from (a) to (d) represents the sample from I to IV, respectively, and (f) for the sample V. (e) provides a zoom-in near the Yoneda region of the sample extracted with an O_2 plasma, which is denoted by a red rectangle in (d). The black arrows in (e) point out three Yoneda regions.*

The 2D GISAXS data of all investigated samples are presented in figure 8.3. The specular reflected beam is shielded by a rectangular beamstop. In general, the material sensitive Yoneda peaks are pronounced for all samples. For the sample without template extraction (figure 8.3a), two distinct Yoneda peaks are visible, which are assigned to silicon and TiO_2 with PS-b-PEO. In addition, the diffuse scattering along the Yoneda peaks are

weaker than for all the other samples. This is caused by the smaller X-ray contrast between TiO_2 and PS-b-PEO than that between TiO_2 and air. Similarly, Rawolle et al. observed that the scattering intensity of the porous TiO_2 film is stronger than that of the P3HT-backfilled sample [69]. After PS-b-PEO removal, except for the O_2 plasma-treated sample, all the samples show a single Yoneda peak. Only the TiO_2 film processed via the O_2 plasma still has distinct Yoneda peaks, as seen in figure 8.3d, indicating incomplete extraction. Furthermore, three Yoneda peaks are observed, indicated by three black arrows in figure 8.3e. They are assigned to the Yoneda peaks of silicon, porous TiO_2, and the TiO_2 with PS-b-PEO, respectively.

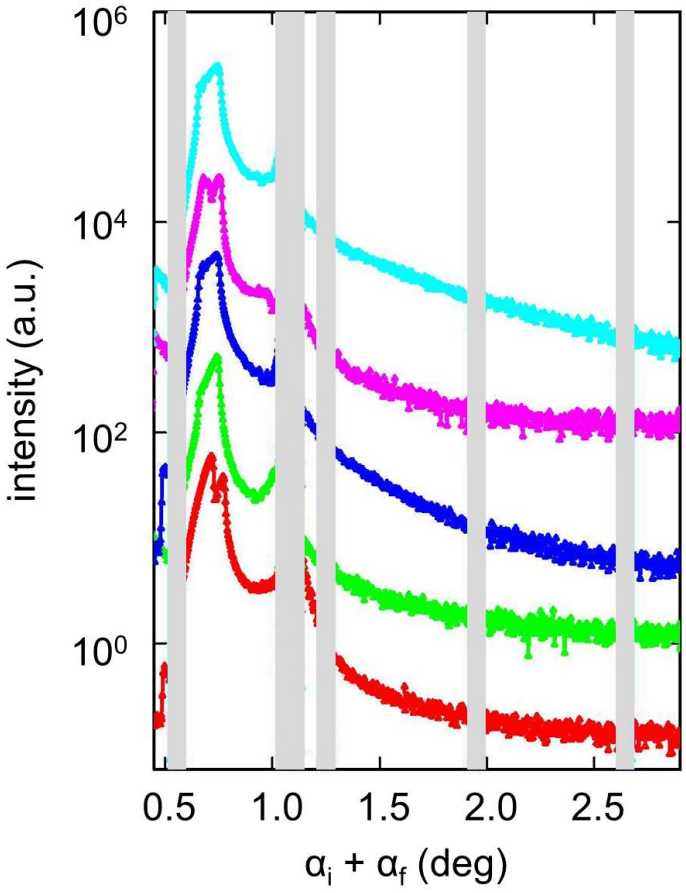

Figure 8.4: *Vertical line cuts extracted from the 2D GISAXS data of the as-prepared PS-b-PEO/TiO_2 film and the resulting porous TiO_2 films with different polymer extraction methods. From bottom to top the curves are correlated to the sample I to V as shown in table 8.1. The grey bars indicate the detector dead areas and the beamstop. The cuts are shifted along the intensity axis for clarity.*

In order to obtain more information about the vertical film composition, vertical line cuts are extracted from the 2D GISAXS data at the position of $q_y = 0$. The image is

shown in figure 8.4. The beamstop and the dead areas on the detector are shown as grey bars in figure 8.4. In general, the peaks located at the region from 0.5° to 0.8° are Yoneda peaks. The one on the left side is related to the investigated materials' specific Yoneda peak, and the right one is attributed to the silicon substrate. For the TiO_2 film without polymer template extraction (red curve in figure 8.4), the left Yoneda peak is at around 0.7°, which is attributed to the PS-b-PEO/TiO_2 composite. The sample with its template extracted by O_2 plasma, the magenta curve in figure 8.4, also shows distinct Yoneda peaks due to an incomplete polymer template extraction. In addition, a small shoulder is observed at around 0.9°, which might be arisen by an enrichment layer in the sample. This enrichment layer is ascribed to a top layer where the PS-b-PEO is completely removed. Combined with the SEM characterization, it infers that this sample has two layers, which are a porous TiO_2 layer on top and a compact layer of PS-b-PEO/TiO_2 at the bottom of the film. For the other three samples, a broad Yoneda peak with the maximum at the silicon Yoneda peak is observed. This position is assigned to porous TiO_2, and shifts towards smaller angle as compared to the one of the un-extracted film. This is caused by the fact that the critical angle of the porous TiO_2 film is smaller than that of the PS-b-PEO/TiO_2 film due to its lower density.

To reveal the inner structures parallel to the substrate, horizontal line cuts are collected at the Yoneda peak position of the TiO_2 related-material and plotted in figure 8.5a. For example, the Yoneda peak of PS-b-PEO/TiO_2 composite is taken for the sample without polymer template extraction, while the Yoneda peak of porous TiO_2 is chosen for the sample after PS-b-PEO removal. All the cuts show a broad shoulder without any pronounced peaks, suggesting a broad structure size distribution in the films.

To get quantitative information about the inner structure, horizontal line cuts are fitted in the way as described in section 3.2.5 and also plotted in figure 8.5a. Three cylinder from factors with the corresponding structure factors are used to obtain the best fitting. The radius of the cylinder is named as structure size and the distance refers to center to center distance between the cylinders (figure 8.5b and 8.5c). The smallest structures with a structure size of around 4.5 nm and a distance of around 29 nm are observed for all samples, which are assigned to TiO_2 granules. These structures are quite stable, despite the different extraction processes used. The intermediate structure is related to the TiO_2 network. In general, the structure size is reduced while the distance stays after PS-b-PEO removal. The decrease in structure size might be caused by the pattern collapse due to removal of the polymer scaffold [24]. In addition, the samples processed via UV irradiation, O_2 plasma, and calcination show quite similar structure sizes, which are smaller than the sample with its template removed by solvent. This is consistent with the observation from the SEM images in figure 8.1 that these three samples show thinner

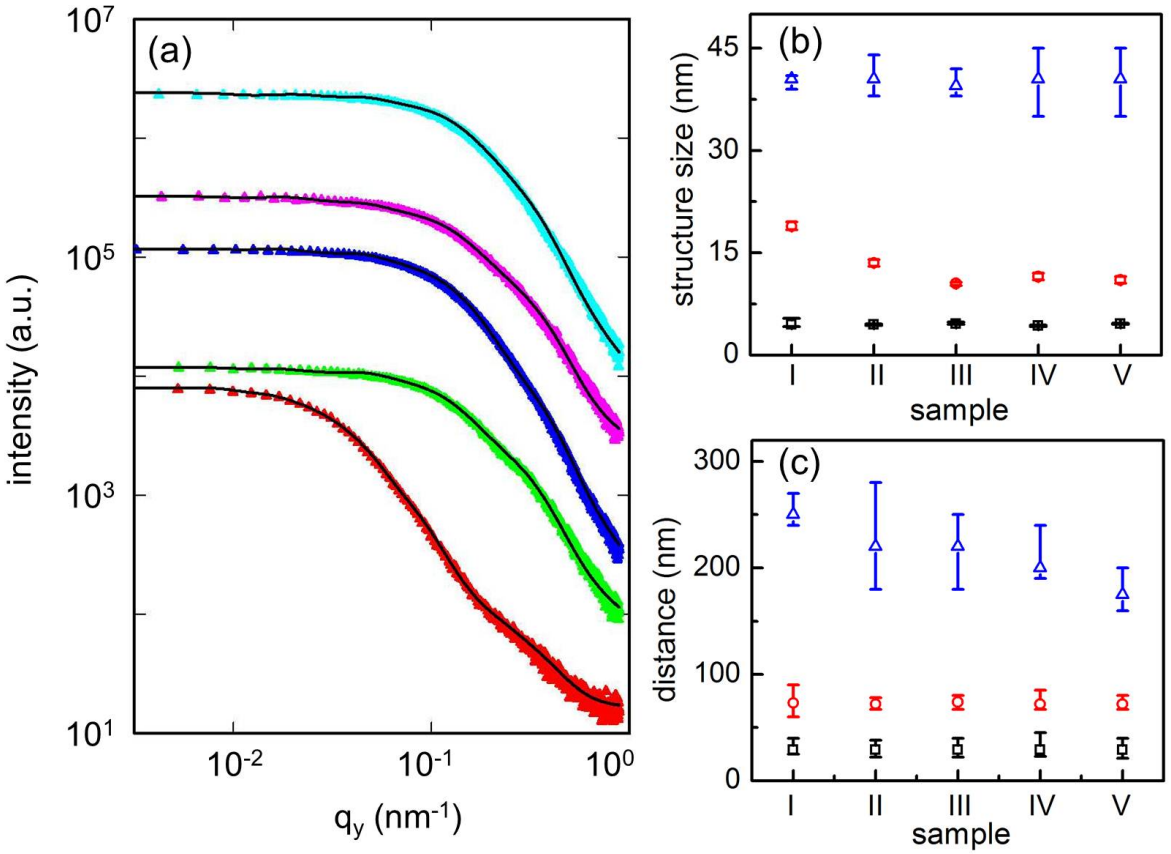

Figure 8.5: *(a) Horizontal line cuts extracted from the 2D GISAXS data of the as-prepared PS-b-PEO/TiO_2 film and the resulting porous TiO_2 films with different polymer extraction methods. From bottom to top the curves are correlated to the sample from I to V as shown in table 8.1. The cuts are shifted along the intensity axis for clarity. (b) Structure sizes and (c) distances obtained from the GISAXS fits for the samples from I to V. Three cylindrical form factors are used to attain the optimized fits, denoted by black, red, and blue colors, respectively.*

walls of the TiO_2 network as compared to the one with solvent extraction. The reason for the smaller structure sizes can be due to the stronger energetic interaction of the UV, O_2 plasma, or high temperature with the samples, which is verified by the stronger decrease of film thickness as discussed in table 8.1. The largest structure, which is attributed to long distance features, originates from the aggregation in the sol-gel process. Generally, all the samples show similar structure sizes but different distances. It seems the various distances are related to the polymer removal methods. If the extraction process is aggressive, the aggregates tend to collapse and therefore shorten the distance. The extreme case is shown in the sample with calcination. Therefore, it is concluded that the solvent treatment is

the most gentle way to remove the PS-b-PEO and keep the TiO_2 structure close to the as-prepared film.

8.1.3 Porosity

The porosity of the TiO_2 films is obtained from white light interferometry measurements, as explained in section 3.2.4. By fitting the value of the effective refractive index of the porous TiO_2 film and comparison with the theoretical value of bulk TiO_2 ($n_{TiO_2} = 2.49$) and air ($n_{air} = 1$), the porosity of the investigated TiO_2 films are calculated by the Bruggeman effective medium approximation (equation 3.3) and shown in table 8.2. The porous TiO_2 films obtained by solvent treatment and UV irradiation treatment show the highest porosity of around 76%. The porosity of the O_2 plasma-treated sample is (62 ± 6) %, which is related to an incomplete extraction of the polymer template. However, the value is not fully accurate for this sample, since the contribution of the polymer PS-b-PEO with $n \approx 1.5$ is neglected. For the calcined sample, the porosity is (68 ± 3) %. Thus, its porosity is smaller than the porosity of the sample with its template extracted by solvent treatment and UV irradiation method. This is related to the collapse of the TiO_2 network during calcination, as discussed before. In general, a high porosity of the TiO_2 film provides a high surface area to volume ratio, which is beneficial for dye loading in a dye-sensitized solar cell or efficient backfilling with a electron donor material in hybrid solar cell due to presence of a large interface.

sample	extraction method	refractive index	porosity (%)
II	DMF and CB baths	1.28 ± 0.05	76 ± 3
III	UV irradiation	1.28 ± 0.1	76 ± 4
IV	O_2 plasma	1.5 ± 0.1	62 ± 6
V	calcination	1.42 ± 0.1	68 ± 3

Table 8.2: *Sample lists with different extraction methods, refractive index, and porosity. The refractive index and porosity are derived from white light interferometry measurements.*

8.1.4 Results

A low temperature routine towards porous TiO_2 films is thoroughly studied. A TiO_2 sol-gel synthesis using the structure directing diblock copolymer PS-b-PEO is used to fabricate nanostructured TiO_2 films. Different methods for PS-b-PEO removal at low temperature are investigated and compared, namely solvent (DMF and chlorobenzene)

treatment, UV irradiation, and O_2 plasma. Additionally, a reference sample is prepared using calcination treatment for polymer extraction, which is the most commonly used fabrication route for nanostructured TiO_2. It was found in the SEM measurements that all the samples have a porous nanostructure. However, the cross-section images show that the solvent treatment and UV irradiation are the most effective methods while the O_2 plasma removes the PS-b-PEO only from the top layer. Furthermore, GISAXS measurements confirmed that the O_2 plasma does not completely remove PS-b-PEO from the sample. Also, the solvent treatment enables the resulting sample to keep the TiO_2 structure most close to the as-prepared PS-b-PEO/TiO_2 film. Whereas all the other methods induce the reduction of TiO_2 domain sizes, which might be caused by the strong interaction of the UV light or the O_2 plasma. Finally, the porosity of the corresponding films are investigated by white light interferometry. It is found that both the samples with solvent treatment as well as the ones with UV irradiation show a higher porosity of around 76% as compared to the calcined sample (68%). In conclusion, the solvent treatment and UV irradiation are considered as the most effective way for low temperature route towards the porous TiO_2 film.

8.2 Backfilling with electron donor P3HT

In order to finalize the active layer which could be used in a hybrid solar cell, a complete backfilling with donor material into porous TiO_2 network is essential. In this thesis, the conjugated polymer P3HT is selected as the donor material. As discussed in section 8.1, solvent treatment and UV irradiation are appropriate methods for template removal at low temperature, therefore, only these two different extraction methods are selected to prepare the porous TiO_2 film for investigating the P3HT backfilling step. The detailed process of backfilling with P3HT is thoroughly described in section 4.2.3. It is of great interest to understand the influence of the extraction method on the morphology of the backfilled sample P3HT/TiO_2. In order to distinguish both samples in following sections, the P3HT/TiO_2 film with its porous TiO_2 structure obtained from solvent treatment is shorten as P3HT/$TiO_{2solvent}$, while the other sample is named as P3HT/TiO_{2UV}.

Real-space analysis

The cross sectional SEM measurements are performed on both P3HT/TiO_2 samples, as shown in figure 8.6. Firstly, the film thickness is extracted from the SEM images, which is (211 ± 13) nm for the P3HT/$TiO_{2solvent}$ film and (146 ± 10) nm for the P3HT/TiO_{2UV} film. As compared to the corresponding porous TiO_2 film before backfilling, the film

thickness increases by around 35 nm for both samples. Thus, formation of a P3HT overlayer on top of the hybrid film is suggested. This is beneficial for a hybrid solar cell, since the overlayer improves the charge carrier transport towards the correct electrode and diminish the recombination at the electrode interface. Moreover, it is found that the P3HT/$TiO_{2solvent}$ film (figure 8.6a) has a rough surface as compared to the P3HT/TiO_{2UV} film which is shown in figure 8.6b. It might originate from the rougher surface of the porous TiO_2 obtained from solvent treatment. Finally, it is worthwhile to mention that both samples show successful P3HT backfilling, since most of the pores are not visible anymore. However, taking a closer look, several little open pores still exist in the P3HT/TiO_{2UV} film, suggesting a relatively less efficient backfilling of the P3HT/TiO_{2UV} films compared to the P3HT/$TiO_{2solvent}$ films.

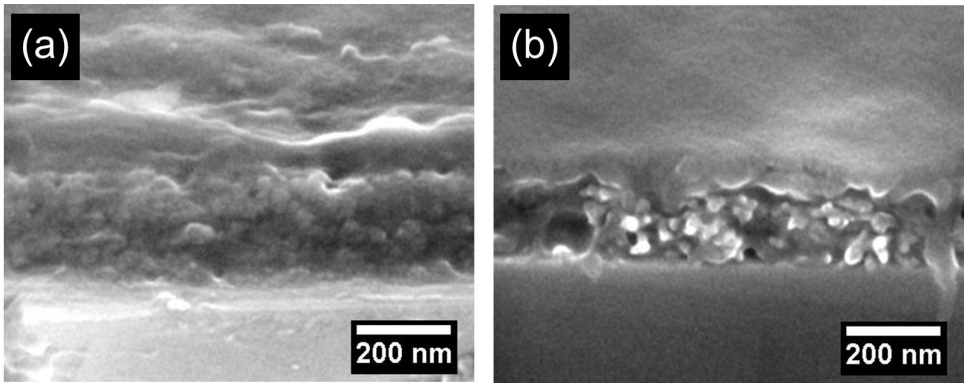

Figure 8.6: *Cross-section SEM images of (a) the P3HT/$TiO_{2solvent}$ and (b) the P3HT/TiO_{2UV} films.*

Reciprocal-space investigation

Since SEM measurements only probe the surface morphology of a local area, GISAXS measurements are carried out on both samples to reveal the inner structure with high statistical relevance. The GISAXS measurements were performed under the same conditions as described in section 8.1. The 2D GISAXS data is shown in figure 8.7. Generally, the patterns are quite similar compared to that of the PS-b-PEO/TiO_2 film as shown in figure 8.3a, indicating a successful backfilling with P3HT. However, the scattering along the q_z direction extends to high q values, which is due to the different scattering properties of P3HT as compared with PS-b-PEO [121].

Vertical line cuts are extracted from the 2D GISAXS data at the position of $q_y = 0$ for the P3HT/$TiO_{2solvent}$ film, while for the P3HT/TiO_{2UV} film the vertical line cut is collected at $q_y \approx 0.03$ nm^{-1} due to in-plane asymmetric scattering at $q_y = 0$ which is probably caused by the rough silicon edge of this sample. Both vertical line cuts are

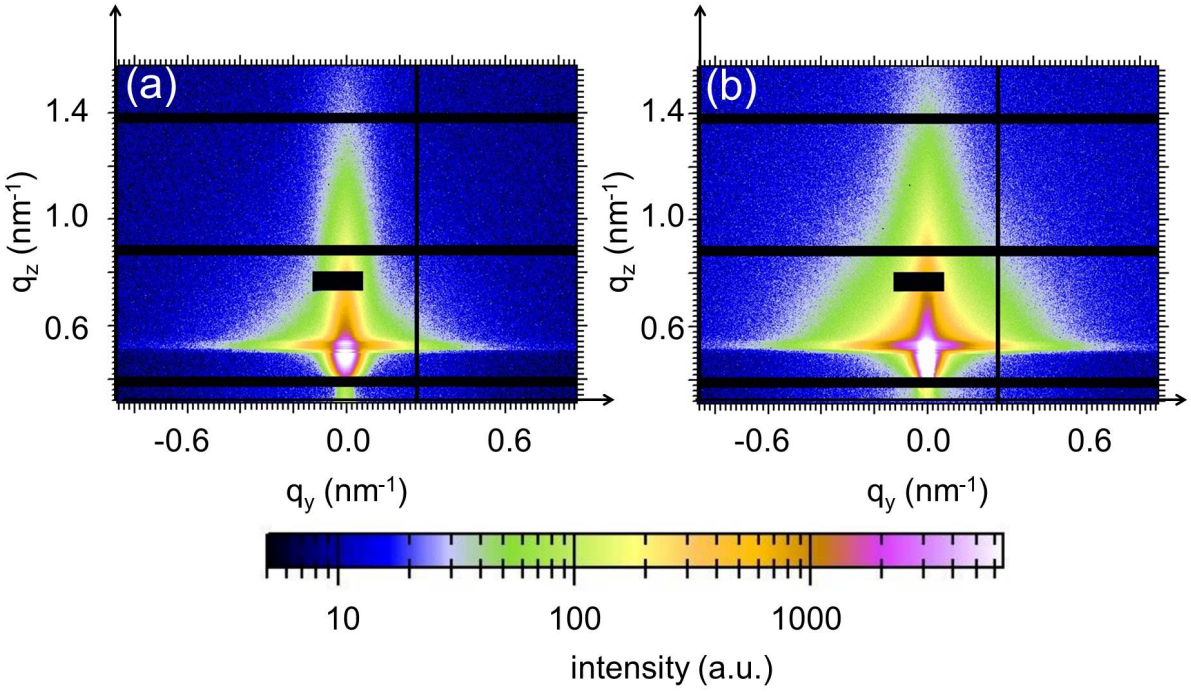

Figure 8.7: *2D GISAXS data of (a) the P3HT/TiO$_{2solvent}$ and (b) the P3HT/TiO$_{2UV}$ films.*

plotted in figure 8.8a. Generally, three Yoneda peaks are observed. They are located at similar angles in both vertical line cuts, indicating the same film composition for both P3HT/TiO$_{2solvent}$ and P3HT/TiO$_{2UV}$ films. In figure 8.8a the Yoneda peak on the right side is identified as silicon peak and the one in the middle is correlated to P3HT/TiO$_2$. Additionally, the P3HT Yoneda peak is visible at the left side, which is assigned to the P3HT enrichment layer as observed in SEM cross-section images (figure 8.6).

sample	**structure 1**		**structure 2**		**structure 3**	
	FF1 (nm)	**SF1 (nm)**	**FF2 (nm)**	**SF2 (nm)**	**FF3 (nm)**	**SF3 (nm)**
P3HT/TiO$_{2solvent}$	$4.6^{+0.1}_{-0.2}$	29^{+3}_{-9}	$12^{+0.5}_{-0.5}$	76^{+24}_{-6}	$42^{+0.5}_{-0.5}$	220^{+20}_{-5}
P3HT/TiO$_{2UV}$	$4.6^{+0.1}_{-0.1}$	29^{+16}_{-10}	$10.5^{+0.5}_{-0.5}$	77^{+13}_{-7}	47^{+1}_{-1}	250^{+20}_{-20}

Table 8.3: *Fitting results obtained from the horizontal line cuts of the 2D GISAXS data of the P3HT/TiO$_{2solvent}$ and the P3HT/TiO$_{2UV}$ films. Three structures are used to obtain the best fits, named as structure 1, 2 and 3. FF and SF are abbreviations for the form factor and the structure factor, respectively.*

In order to examine the inner structures in lateral direction, horizontal line cuts are taken at the Yoneda peak position of the P3HT/TiO$_2$. They are plotted in figure 8.8b.

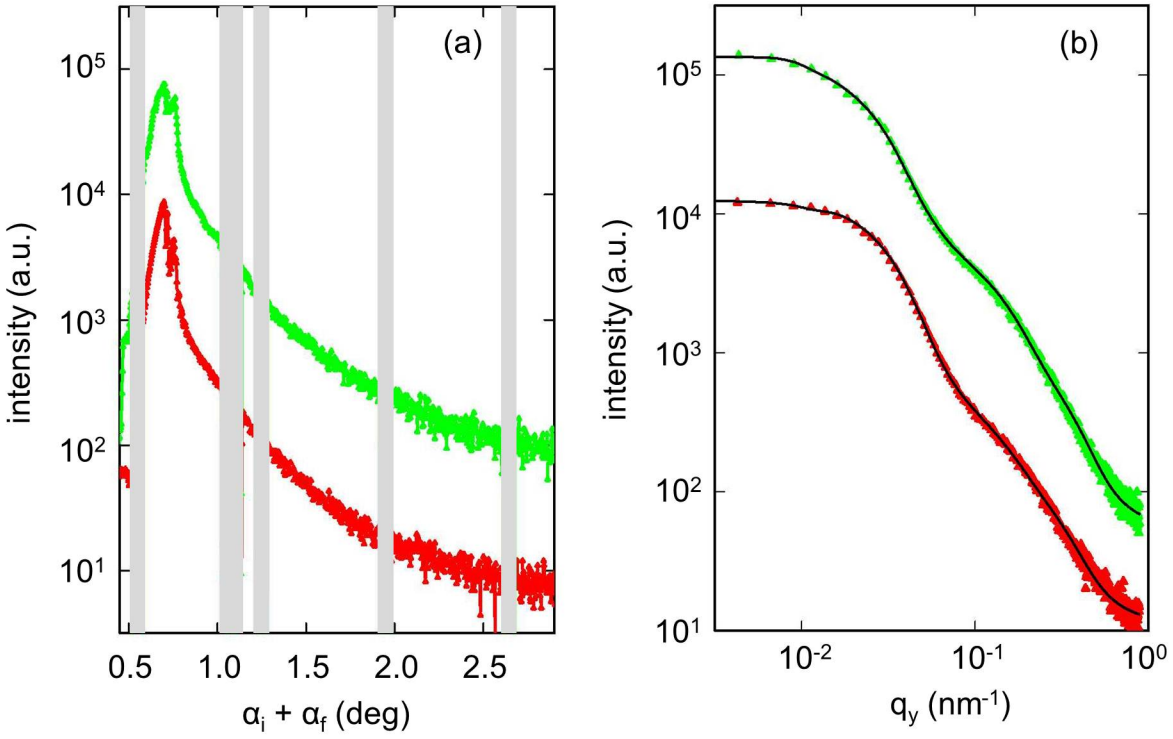

Figure 8.8: *(a) Vertical line cuts extracted from the 2D GISAXS data of the P3HT/$TiO_{2solvent}$ (red) and P3HT/TiO_{2UV} (green) films. (b) Horizontal line cuts (symbols) with their fittings (lines). The cuts are shifted along the intensity axis for clarity.*

The model as discussed in section 3.2.5 is used to fit the horizontal line cuts. Generally, three cylinder-shaped form factors are used in one horizontal line cut to achieve the best fitting. Resulting fitting parameters are listed in table 8.3. The smallest structures with a radius of around 4.6 nm and a center to center distance of about 29 nm are observed in both samples. They are the same as the smallest structure in the porous TiO_2 film before P3HT backfilling and therefore, these structure are assigned to TiO_2 granules. The intermediate and the large structures are also comparable to the porous TiO_2 film but with slightly coarsened sizes, which is probably due to the influence of the backfilling process.

In conclusion, the backfilling of P3HT into the porous TiO_2 film is successfully performed for both extraction methods, namely solvent treatment and UV irradiation. Moreover, the TiO_2 network is preserved after P3HT backfilling, which ensures a large interfacial area between TiO_2 and P3HT and accordingly a pronounced performance of P3HT/TiO_2 active layer.

8.3 Mechanical properties of the TiO_2-based films

Fabrication of the TiO_2-based films at low temperature ensures the use of flexible and temperature sensitive substrates like PET. Thus, understanding of the mechanical properties of the TiO_2-based films is of great interest for flexible applications. Therefore, the TiO_2-based films are prepared on PET substrates and then subjected to a two-point bending test to investigate the material fatigue and the final failure. With this bending setup, the samples are repeatedly bent up to 5000 times. Afterwards, the resulting cracks in the sample are examined by SEM measurements.

In order to fully understand the influence of backfilling on the mechanical properties of the TiO_2-based films, a series of samples is prepared. The TiO_2 films with their templates extracted by UV irradiation and solvent treatment are abbreviated as fully-extracted TiO_{2UV} and fully-extracted $TiO_{2solvent}$, respectively. Their mechanical properties are firstly investigated in section 8.3.1 and section 8.3.2 in sequence. Then the so-called partially-extracted TiO_2 film, obtained by the O_2 plasma, is studied in section 8.3.3. Thereafter, the named P3HT backfilled TiO_2 is examined (section 8.3.4). Finally, the comparison among all the investigated samples are summarized in section 8.3.5.

8.3.1 Fully-extracted TiO_{2UV} films

As revealed in section 8.1 and section 8.2, UV irradiation and solvent treatment are effective methods to remove the PS-b-PEO template. Therefore, the porous TiO_2 films obtained from UV irradiation are subjected to the bending tests. However, it is found that after the UV irradiation the PET foil becomes brittle and consequently starts to break in prior to the failure of the porous TiO_2 film even under a very small strain. In order to ensure the failure is mainly induced by PET foil rather than the TiO_2 film, the bare PET substrates are stored in the UV chamber for 20 h. It is found that the color of the PET foil changes from transparent to yellowish, indicating the degradation of the PET. Afterwards, the degraded PET foil is subjected to a bending test and broke at a very small strain. Therefore, the extraction by UV irradiation is not suitable for flexible polymer substrate applications.

8.3.2 Fully-extracted $TiO_{2solvent}$ films

Alternatively, five identical porous TiO_2 films obtained by solvent extraction are investigated. They are bent for 10, 100, 500, 1000, and 5000 times, respectively. As introduced in section 2.5.1, the maximal strain is calculated to (2.7 $\pm$ 0.2) %. All the samples are

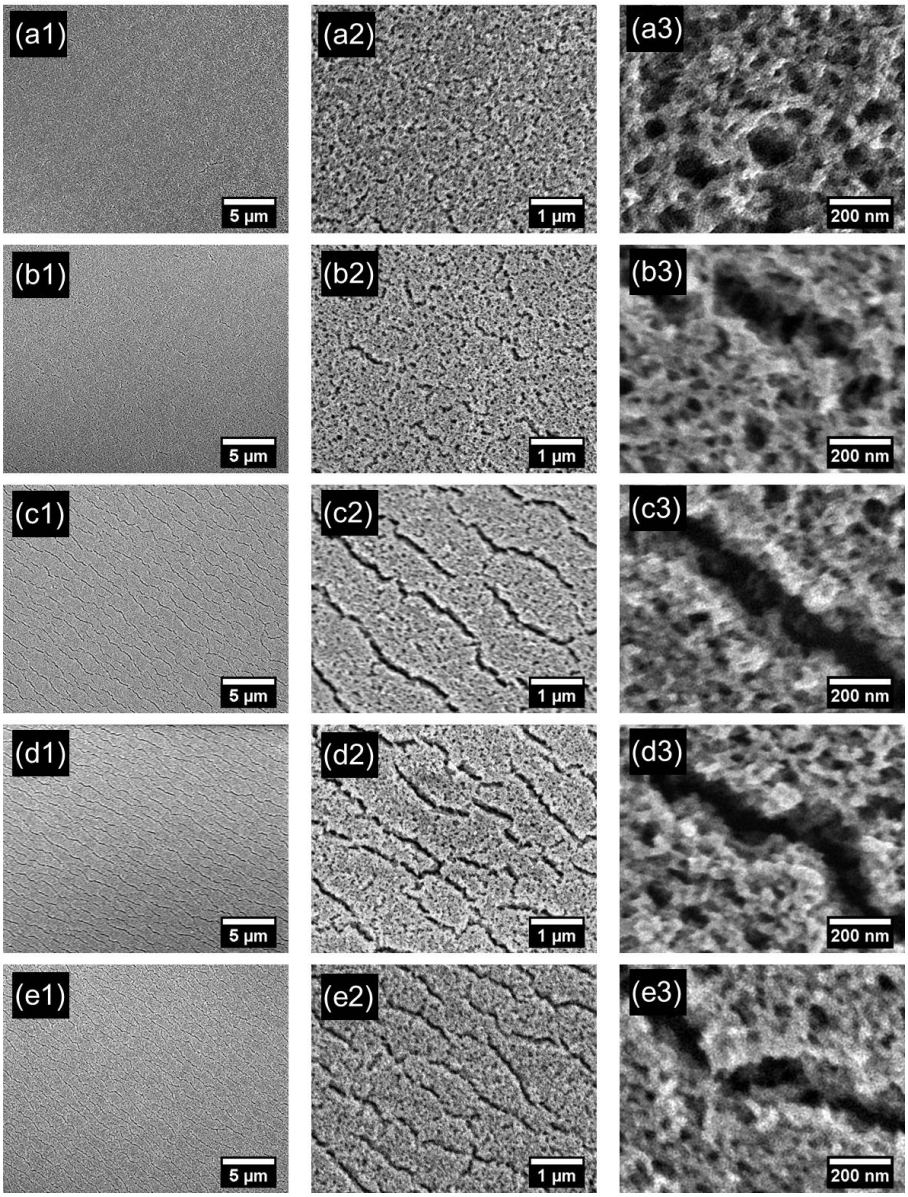

Figure 8.9: *SEM images of the $TiO_{2solvent}$ films at different numbers of bending cycles of (a) 10, (b) 100, (c) 500, (d) 1000, and (e) 5000. Three different magnifications are taken for SEM measurements of each sample, denoted as 1, 2, and 3 in this figure.*

then examined by SEM measurements with three different magnifications, as shown in figure 8.9. The sample bent for 10 times does not show any cracks on different magnifications as revealed by figure 8.9a1, 8.9a2, and 8.9a3. After bending for 100 times, the cracks appear as depicted in figure 8.9b3. These cracks are rare and small (figure 8.9b1 and 8.9b2). After bending for 500 times, the cracks are strongly propagated. These cracks are long and occupy the whole probed area (figure 8.9c1 and 8.9c2). Moreover, all the cracks are orientated perpendicularly to the bending direction. Further bending for

1000 (figure 8.9d) and 5000 times (figure 8.9e) show no prominent difference but a steady increase in the number of cracks.

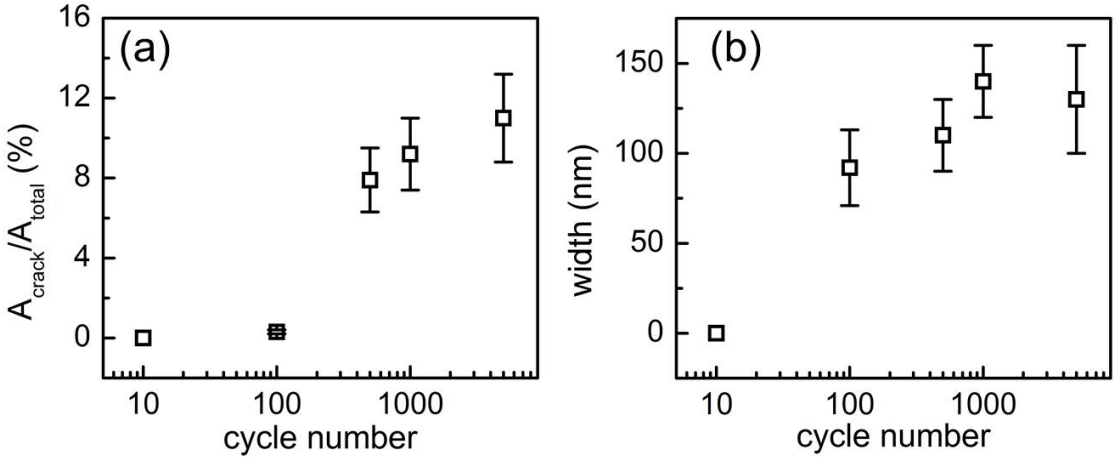

Figure 8.10: *(a) Surface area fractions and (b) widths of cracks on the fully-extracted TiO_2solvent films as a function of bending cycle numbers. All values are extracted from the corresponding SEM images.*

In order to reveal the crack propagation quantitatively, the surface area fractions and widths of cracks are extracted from the SEM images as a function of bending cycles. In figure 8.10a, the surface area fractions of cracks are summarized. It is found that the area fraction of cracks is nearly zero in the sample bent for 10 and 100 times, without prominent cracks occurring. However, for the sample with 500 bending cycles, film failure is detected, with around 8% area fraction of cracks. After bending 1000 and 5000 times, the area fraction of cracks increases to around 9.5% and 11%, respectively. Therefore, a bending cycle between 100 and 500 is considered as a critical point for the failure of the $TiO_{2solvent}$ films. Furthermore, the widths of cracks as a function of bending cycles are reported in figure 8.10b. Since no cracks are observed for the sample with 10 bending cycles, the width is set to zero. After 100 times bending, the average width of cracks is around 90 nm. Then, with more bending cycles, the width increases slowly. However, for the sample with 5000 bending cycles, the average width of the cracks stays similar to that with 1000 bending cycles, while the area fraction of cracks is clearly larger. It seems that the increase in surface area fraction of cracks is mainly caused by the growth of number of cracks. Therefore, it is inferred that for the sample with more than 1000 bending cycles, the surface strain is mainly released by the formation of cracks rather than broadening the cracks. The lengths of cracks are also of importance for evaluating the crack propagation. However, it cannot be obtained for these samples since many cracks do not show clear start and end points.

8.3.3 Partially-extracted TiO_2 films

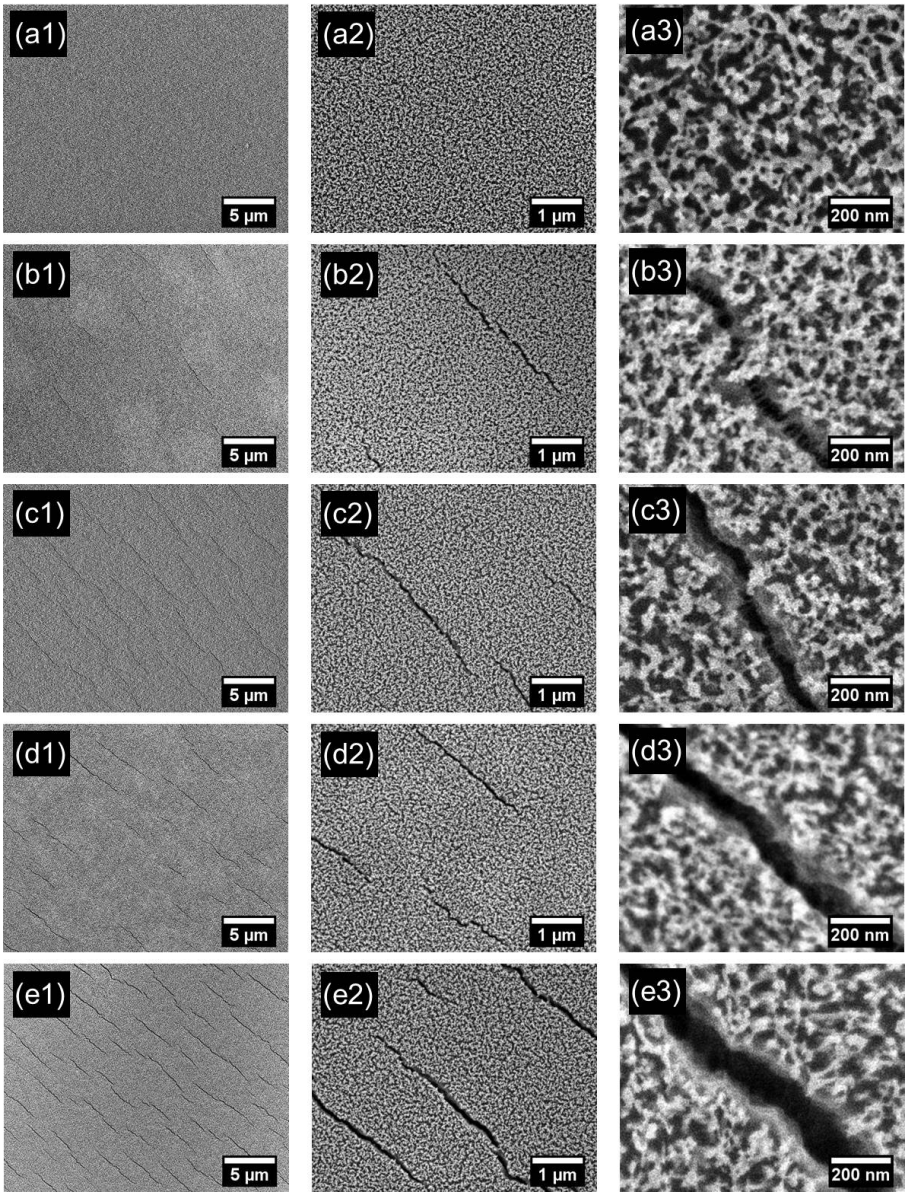

Figure 8.11: *SEM images of the partially-extracted TiO_2 films via the O_2 plasma method with bending cycles of (a) 10, (b) 100, (c) 500, (d) 1000, and (e) 5000, respectively. Three different magnifications are taken for SEM measurements of each sample, denoted as 1, 2, and 3 in this figure.*

The mechanical properties of the partially-extracted TiO_2 films are also investigated via bending tests to estimate whether the remaining polymer enhances the flexibility of the TiO_2 films. The maximal strain is calculated to (2.9 ± 0.2) %. In the same way as before five identical samples, treated with an O_2 plasma for 30 min, are prepared. Thereafter, they are bended for 10, 100, 500, 1000, and 5000 times, respectively. The

SEM measurements are carried out on these resulting samples and shown in figure 8.11. As discussed in section 8.1, structured porous TiO_2 is observed at the surface while the bottom layer still contains the PS-b-PEO residues.

After 10 times bending, no failure is observed as revealed in figure 8.11a. For the sample with 100 bending cycles, a few cracks appear at the film surfaces (figure 8.11b1). Most significantly, some fiber-like structures are visible in the deeper region of the crack in figure 8.11b3, bridging the two sides of this crack. These fiber-like structures are considered as PS-b-PEO, which could cause plastic deformation under strain. Senses et al. have also represented fiber-like structure of PS under strain [166]. After 500 bending cycles the cracks get broader and their number increases as shown in figure 8.11c. Finally, for the samples with 1000 and 5000 bending cycles the cracks are further propagated.

The quantitative analysis of cracks in dependence on bending cycle is obtained from SEM images and displayed in figure 8.12. First of all, the surface area fraction is summarized in figure 8.12a. It is found that with increasing bending cycles, the area of cracks steadily grows. The average width and length of cracks are depicted in figure 8.12b and 8.12c, respectively. Up to 500 bending cycles an increment in both width and length is observed. Afterwards, the lengths of cracks stay similar even with 5000 bending cycles, while a steady but slowly broadening in width to around 120 nm is found after 5000 bending cycles. Therefore, it is inferred that the cracks grow mainly in number rather than in length. As compared to the fully-extracted $TiO_{2solvent}$ films, the average lengths of cracks are much smaller in the partially-extracted TiO_2 films. It might be related to the remaining PS-b-PEO, which strongly restrains the crack lengths.

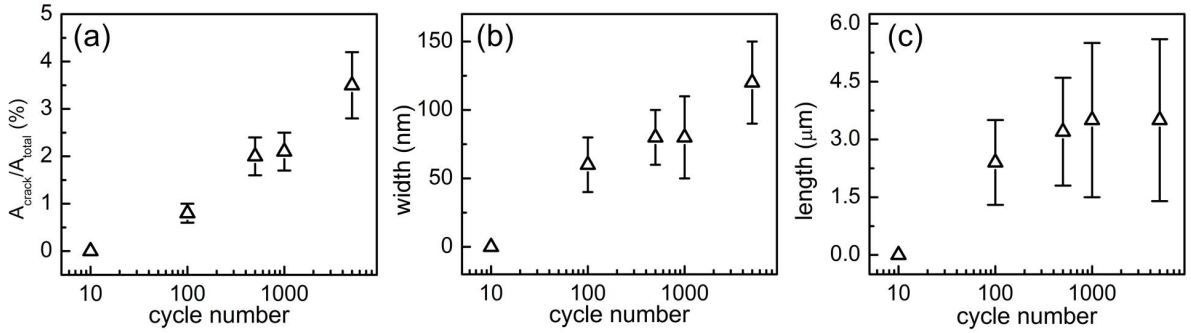

Figure 8.12: *(a) Surface area fractions, (b) widths, and (c) lengths of cracks on the partially-extracted TiO_2 films treated with the O_2 plasma as a function of bending cycles. All the values are extracted from the corresponding SEM images.*

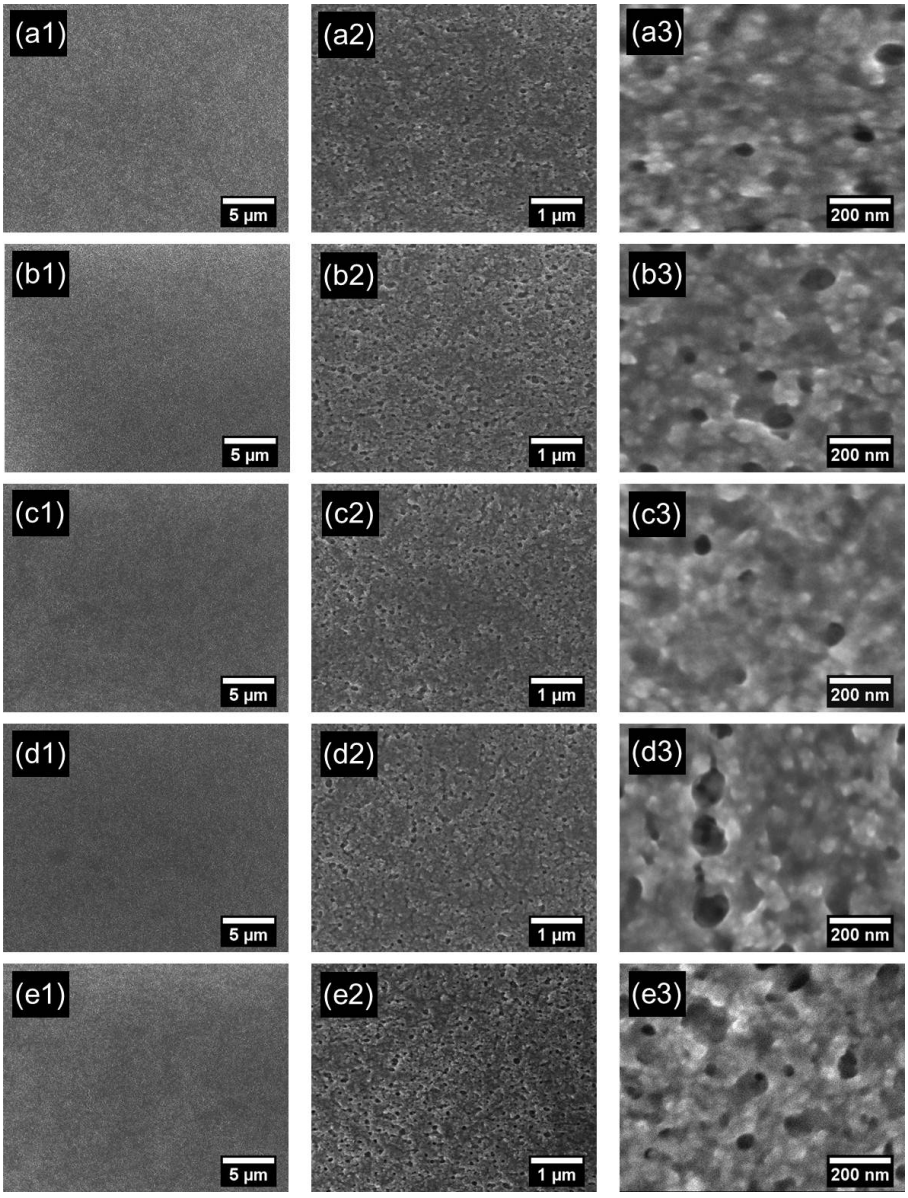

Figure 8.13: *SEM images of P3HT/$TiO_{2solvent}$ at different numbers of bending cycles of (a) 10, (b) 100, (c) 500, (d) 1000, and (e) 5000, respectively. Three different magnifications are taken for SEM measurements of each sample, denoted as 1, 2, and 3 in this figure.*

8.3.4 P3HT backfilled TiO_2 films

Finally the P3HT/TiO_2 hybrid films are prepared on PET, which are of great interests due to the potential application for the photoactive layer of flexible hybrid solar cells. As discussed, the UV irradiation degrades the PET and therefore, the porous TiO_2 films are prepared using the solvent treatment. Afterwards, they are backfilled with P3HT. As before, five samples are prepared and bent for 10, 100, 500, 1000, and 5000 times, respectively. The maximal strain on the surface is calculated to (2.8 ± 0.2) %. Then the

samples are probed by SEM, and the resulting images with different magnifications are presented in figure 8.13.

It is noticed that the surface morphology of P3HT/$TiO_{2solvent}$ on PET is slightly different from the same film deposited on silicon substrates. Taking the figure 8.13a2 as an example, it seems there is no P3HT enrichment layer on top of the sample. Besides, the outlines of TiO_2 structures are also roughly observed. However, the same sample prepared on silicon substrate has a wavy surface, which is typical for polymer films. Therefore, it is inferred that the substrate influences the backfilling into the porous TiO_2 films. Anyway, although some pores still exist on the surface, they are rare and the overall backfilling process is still successful as demonstrated in the SEM image with higher magnification (figure 8.13a3).

In agreement with all the above discussed results, the sample with 10 bending cycles does not show any cracks on the surface as illustrated in figure 8.13a. However, it is noted that none of the samples fail, even not the sample with 5000 bending cycles. No cracks are observed at the sample surface, as represented in figure 8.13b, 8.13c, 8.13d, and 8.13e. Therefore, it is preliminarily concluded that with P3HT backfilled hybrid films are more flexible.

Although no cracks are formed on top of the P3HT/TiO_2 hybrid films, the cracks are still possibly hidden under the polymer and exist in the TiO_2 structure. Hence, all these samples are immersed in a chlorobenzene bath for 3 hours to completely remove the P3HT after bending tests. Thereafter, SEM measurements are performed again and the corresponding images are shown in figure 8.14. First of all, all the samples show porous structures, which are similar to the porous TiO_2 films extracted by solvent treatment as illustrated in figure 8.9a. However, in these samples some fissures are observed in the SEM images, such as in figure 8.14d1. Nevertheless, these fissures are very shallow and do not extend to a deeper position inside the films, as illustrated in figure 8.14c2. Additionally, they do not have any preferred orientation and propagations with bending cycles, suggesting that these fissures are assigned to a surface structure probably caused by the repeated solvent treatments rather than the cracks induced by the cyclic bending. Therefore, it is finally confirmed that the P3HT/TiO_2 hybrid films are fully flexible. In comparison to the fully-extracted and the partially-extracted TiO_2 films, the P3HT backfilled TiO_2 films have an improved mechanical stability under thousands of bending cycles.

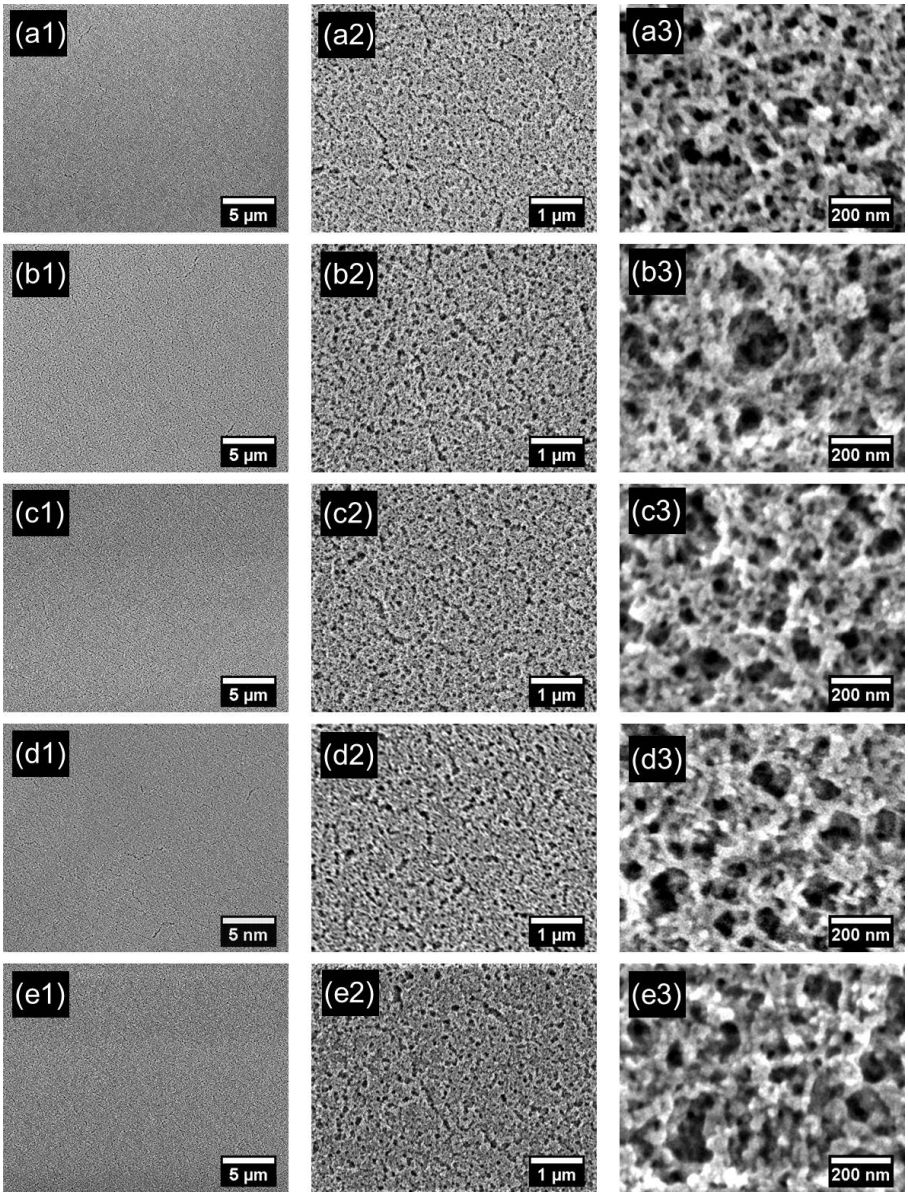

Figure 8.14: *SEM images of P3HT/$TiO_{2solvent}$ with P3HT extracted by chlorobenzene treatment at different bending cycles of (a) 10, (b) 100, (c) 500, (d) 1000, and (e) 5000. Three different magnifications are taken for SEM measurements of each sample, denoted as 1, 2, and 3 in this figure.*

8.3.5 Comparisons

The crack propagation in dependence on the bending cycle numbers is compared among the fully-extracted TiO_2, partially-extracted TiO_2, and P3HT backfilled TiO_2 films. The surface area fractions and widths of cracks of all the samples are summarized in figure 8.15a and 8.15b, respectively. Since no cracks are observed on the P3HT/TiO_2 films, the surface area fractions and widths of cracks are set to zero. In general, all the samples

do not show cracks after 10 bending cycles, indicating a flexible property. All of them could be possibly used on a curved surface under a certain strain. In addition, it is revealed that the propagation of cracks on the porous TiO_2 films is the fastest. A significant increase of area fraction is observed between 100 and 500 bending cycles, while when the PS-b-PEO is only extracted from the top surface of the sample, the area fraction of cracks are prominently suppressed, as illustrated in figure 8.15a. If the fully-extracted TiO_2 film is backfilled with P3HT, the resulting sample is fully flexible, without showing any cracks even after 5000 bending cycles. Besides, figure 8.15b reveals that the average width of cracks is steadily expanded with increasing bending cycles for both the fully-extracted and the partially-extracted TiO_2 films, but the fully-extracted TiO_2 films show slightly wider cracks. Finally, the fully-extracted TiO_2 films have much bigger cracks than the partially-extracted sample. In general, addition of polymer in the porous TiO_2 film can strongly increase the flexibility of the resulting samples.

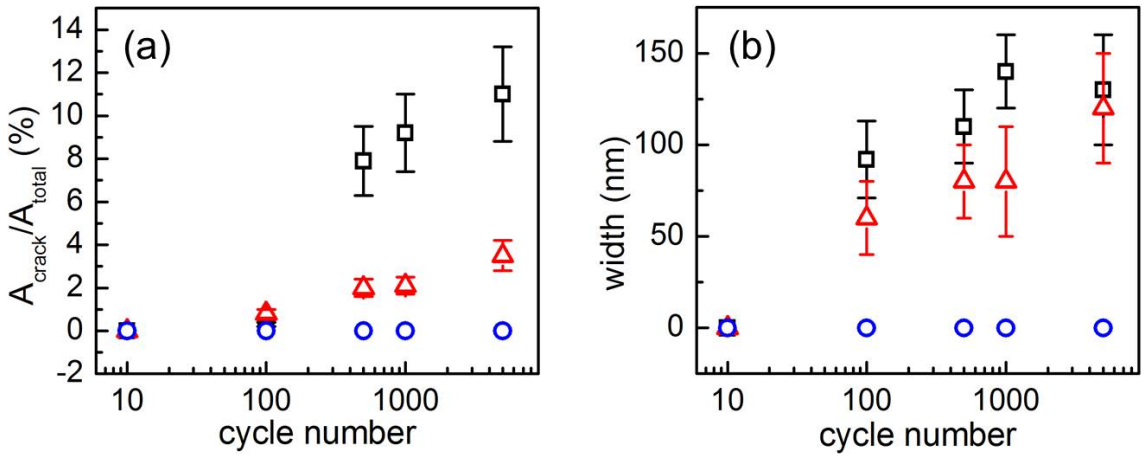

Figure 8.15: *Comparisons among the fully-extracted TiO_2 (black color), the partially-extracted TiO_2 (red color), and the P3HT backfilled TiO_2 (blue) films. (a) The surface area fractions and (b) the widths of cracks are shown as a function of bending cycles. All values are extracted from the SEM images.*

8.3.6 Results

The mechanical properties of the corresponding TiO_2-related samples, including the fully-extracted TiO_2 films by UV irradiation and solvent treatment, the partially-extracted TiO_2 films treated with the O_2 plasma, and the P3HT backfilled TiO_2 films, are examined by a custom made two-point bending machine [25]. All samples are probed under

tests with 10, 100, 500, 1000, and 5000 times of continuous bends, respectively. The fully-extracted TiO_{2UV} films completely lose their flexibility due to the strong degradation of PET foils under UV irradiation. In case of the fully-extracted $TiO_{2solvent}$ films, cracks are seen after 100 times of bends, and the cracks develop fast. For the partially-extracted TiO_2 films treated with the O_2 plasma, some cracks are still formed, but the failure is substantially suppressed with increasing bending cycle numbers. Finally, it is found that the flexibility of the P3HT backfilled TiO_2 films are significantly improved. No cracks are observed even after 5000 bending cycles. In conclusion, backfilling the porous TiO_2 films with P3HT can effectively improve the flexibility of the resulting samples and shows a great potential application in flexible hybrid solar cells.

8.4 Models for the TiO_2-based samples and crack propagations

Elastic modulus estimation

In order to understand why addition polymer in porous TiO_2 structures elevates the flexibility of the resulting samples, the concept of elastic modulus is adopted. In brief, the smaller elastic modulus, the larger deformation can sustain before failure. Three different models are applied to these samples, which have been discussed in detailed in section 2.5.2. First of all, the fully-extracted $TiO_{2solvent}$ films can be depicted by an open-cell foam model, with its sketch of a unit cell shown in figure 2.26b. The elastic modulus for porous TiO_2 is calculated by:

$$E = E_{TiO_2}(1 - \Phi)^2 \tag{8.1}$$

with a porosity $\Phi = 0.76$ as derived from white light interferometry. Accordingly, the effective elastic modulus of the fully-extracted TiO_2 film is calculated to be $0.0576 \cdot E_{TiO_2}$, which is strongly decreased as compared to bulk TiO_2. It indicates that the porous material is generally much more flexible than its bulk form. Moreover, with increasing porosity, the flexibility is boosted as well. However, this calculation is just a rough estimation for foam materials. More accurate modeling can be provided by specialized methods, such as the finite element method.

The partially-extracted TiO_2 film via O_2 plasma treatment can be considered as a bi-layer structure which constitutes a PS-b-PEO/TiO_2 hybrid layer and a porous TiO_2 layer. Firstly, the PS-b-PEO/TiO_2 hybrid film can be described by a composite model. In this case, PS-b-PEO is regarded as the matrix material and TiO_2 as the filler. Furthermore, the TiO_2 structures are modeled by randomly distributed short fibers. The rough sketch of the composite model is shown in figure 2.27b. With the semi-empirical Halpin-Tsai model, the effective elastic modulus of the PS-b-PEO/TiO_2 hybrid film can be calculated by:

$$E = E_{PS-b-PEO}\frac{1+\xi\eta V_{TiO_2}}{1-\eta V_{TiO_2}} \tag{8.2}$$

where,

$$\eta = \frac{E_{TiO_2} - E_{PS-b-PEO}}{E_{TiO_2} + \xi E_{PS-b-PEO}} \tag{8.3}$$

with ξ is calculated by 2(l/d). From GISAXS measurements the diameter of TiO_2 cylinders is known to be $d = 38$ nm and the corresponding center to center distance is 73 nm. The SEM images of porous TiO_2 (figure 2.26a), prove the roughly spherical pore shape. Therefore, the length of the TiO_2 cylinders is estimated to be the same with the pore size, which equals to 35 nm. Then ξ is equivalent to 1.84. The $E_{PS-b-PEO}$ is set to be kE_{TiO_2}. The effective elastic modulus of the PS-b-PEO/TiO_2 hybrid film can be simplified as:

$$E = kE_{TiO_2}\frac{1.44+1.4k}{0.76+2.08k} \tag{8.4}$$

It is easily found that when k is smaller than 1, meaning the polymer has a smaller elastic modulus than TiO_2, the effective elastic modulus of the hybrid film would be smaller than that of TiO_2 bulk material. Conversely, if the polymer has larger elastic modulus than TiO_2, an increment in effective elastic modulus of the hybrid film exists. Thereafter, the upper layer of porous TiO_2 is taken into account. The elastic modulus of porous TiO_2 of $0.0576 \cdot E_{TiO_2}$ is substituted into the formula:

$$E = \frac{d_T E_T + d_H E_H}{d_T + d_H} \tag{8.5}$$

where d represents the film thickness. The subscripts T denotes the porous TiO_2 and H denotes the PS-b-PEO/TiO_2 hybrid film. From the SEM cross-section image it can be deduced that the O_2 plasma can only remove roughly 50 nm thick PS-b-PEO from the as-prepared sample. Therefore, the film thickness of the PS-b-PEO/TiO_2 hybrid film and porous TiO_2 is estimated to be around $d_H = 130$ nm and $d_T = 50$ nm, respectively. Thus, the effective elastic modulus of the partially-extracted TiO_2 film is calculated to be:

$$E = E_{TiO_2}\left(0.016 + \frac{0.72k(1.44 + 1.4k)}{0.76 + 2.08k}\right) \tag{8.6}$$

In the following, the backfilled TiO_2 film is discussed. Considering an incomplete backfilling by P3HT as reported in our previous work, a backfilling degree of around 85% is achieved [91]. This means 85% pores are filled by P3HT. The same model as discussed for the PS-b-PEO/TiO_2 hybrid film is also applicable to the P3HT/TiO_2 hybrid film, further taken into account the backfilling degree (85%) and porosity of the porous TiO_2 films (76%). Therefore, the volume fraction of P3HT would be 65%, and the porosity of this hybrid film is 11%. With the developed Halpin-Tsai model, the effective elastic modulus of the P3HT/TiO_2 hybrid film can be calculated by:

$$E = E_m \frac{1 + \xi\eta V_f}{1 - \eta V_f}\left(1 - \frac{\rho}{1 - V_f}\right)^{K_0(1-V_f)} \tag{8.7}$$

With all values inserting into the formula reference, the effective elastic modulus of the P3HT/TiO_2 hybrid film is simplified to be:

$$E = 0.79kE_{TiO_2}\frac{1.44 + 1.4k}{0.76 + 2.08k} \tag{8.8}$$

Till now, the effective elastic moduli of these samples are all described by the elastic modulus of TiO_2 bulk material E_{TiO_2} and the ratio k of elastic modulus between the used polymer and TiO_2 bulk. Since the comparison is not straightforward merely from the formulas, all equations are plotted in figure 8.16a with its zoom-in shown in 8.16b. It is necessary to mention that the variable k is not the same between different samples. More specifically, for partially-extracted TiO_2 (magenta symbols), k equals to the ratio between $E_{PS-b-PEO}$ and E_{TiO_2}, while for the P3HT/TiO_2 hybrid film k is the ratio between E_{P3HT} and E_{TiO_2}. Moreover, because the porous TiO_2 film does not correlate to any polymer, the ratio between $E_{effective}$ and E_{TiO_2} is set to a constant value of 0.0576, as having been calculated in the beginning of this section.

On the one hand, the porous TiO_2 film decreases its $E_{effective}$ significantly, as compared to bulk TiO_2. On the other hand, figure 8.16b reveals that below critical values of k, both

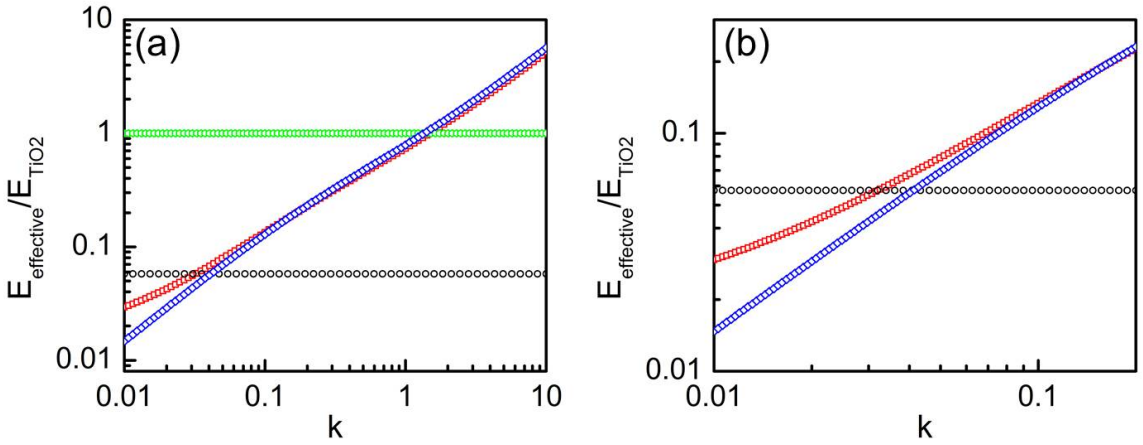

Figure 8.16: *(a) The comparison of $E_{effective}/E_{TiO_2}$ as a function of k (the ratio of elastic modulus between used polymer and TiO_2 bulk). The fully-extracted TiO_2, partially-extracted TiO_2, and P3HT backfilled TiO_2 films are indicated by black, red, and blue colors. The TiO_2 bulk serves as a reference, using green color. A zoom-in region is shown in (b).*

partially-extracted and polymer filled TiO_2 films can lower their resulting elastic moduli further, even with comparison to the porous TiO_2 film. In order to give an estimation, the values of elastic modulus of TiO_2 bulk and P3HT bare polymer are taken from literature, which are around 250 Gpa and 1 Gpa, respectively [167–169]. The elastic modulus of PS-b-PEO is approximated the same as PS, with a value of around 3.2 Gpa, since the PS block contributes $72\%_{Wt\%}$ to the whole diblock copolymer [170,171]. With all these values from literatures, the elastic modulus of fully-extracted, partially-extracted, and backfilled TiO_2 films are approximated to be 14.4 Gpa, 8.27 Gpa, and 1.49 Gpa, respectively. Although the models are based on rough estimations, the trend of the effective elastic modules obtained from the open-cell foam model and the Halpin-Tsai model is well evidenced by the experimental results. Moreover, by proper selecting the value k (as shown in figure 8.16), the flexibility of the samples can be designed for tuning purpose.

Load sharing

Elastic modulus has been considered as one important aspect for evaluating the flexibility of the thin films. While the load sharing is another perspective to understand crack propagation. A simplified TiO_2 lattice model is sketched in figure 8.17a. When the bending stress is applied on the sample, some area could experience higher stress. If these lattices are overloaded, they would start to break in prior to the rest lattices as shown in figure 8.17b. Then the stress carried by these struts is transferred to the next unbroken neighbors, as denoted by the red line in figure 8.17b. If the stress is higher than the

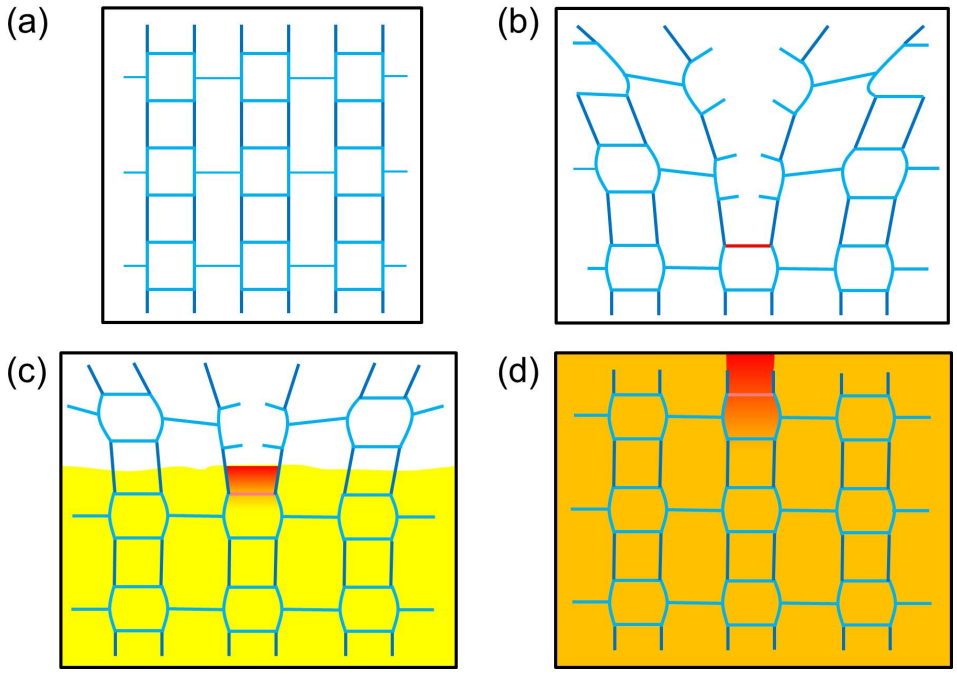

Figure 8.17: *Sketches of the 2D projection of (a) the porous TiO_2 film without bending, (b) the failed fully-extracted TiO_2 film, (c) the failed partially-extracted TiO_2 film, and (d) the P3HT backfilled TiO_2 film after bending tests. The red color denotes high stress. The yellow layer describes the PS-b-PEO and the orange layer represents the P3HT.*

mechanical strength of the strut, the crack propagates, otherwise the fracture reaches equilibrium and the crack propagation stops. The partially-extracted and backfilled TiO_2 samples can be considered as a composite, which constitutes polymer matrix and TiO_2 fillers. The local load sharing predicts that the load is partially carried by the local neighbors. In case of the partially-extracted TiO_2 samples, the top porous TiO_2 undergoes a similar fracture behavior to the fully-extracted sample. However, when the stress transfers to the bottom layer of PS-b-PEO/TiO_2, a local load sharing is carried out and therefore, the load on the TiO_2 strut is reduced as displayed in figure 8.17c. It explains why the crack propagation in the partially-extracted TiO_2 samples (figure 8.17a) is much slower than in the fully-extracted TiO_2 samples. Finally, in terms of the P3HT/TiO_2 hybrid films (figure 8.17d), P3HT shares part of the load and the stress distributed on the TiO_2 strut is supposed to be smaller than its mechanical strength. Hence, the fracture is hindered.

8.5 Summary

In summary, the sol-gel process assisted with use of a structure directing diblock copolymer PS-b-PEO allows the fabrication of nanostructured TiO_2 films at low temperatures. Solvent treatment, UV irradiation, and O_2 plasma are used to remove the PS-b-PEO template. SEM measurements show that the porous TiO_2 structure is preserved after these treatments. However, only solvent treatment and UV irradiation can fully remove the PS-b-PEO, while O_2 plasma only extracts the PS-b-PEO from the top surface. Furthermore, with GISAXS the inner morphology is examined. It is found that after a solvent treatment, the structure size of TiO_2 is most close to that of the as-prepared sample (the PS-b-PEO/TiO_2 hybrid film), while the samples treated by the other methods show reduced structure sizes of TiO_2. Moreover, the porosity is investigated by white light interferometry. It reveals that the samples using solvent treatment and UV irradiation have similar porosity of around 76%, which is much higher than the sample obtained from calcination. To sum up, both solvent treatment and UV irradiation can effectively remove the polymer template. Nevertheless, the solvent treatment is a mild method which mostly preserves the original TiO_2 nanostructure, but the UV irradiation has strong interaction with TiO_2 nanostructure and reduces its structure sizes.

When porous TiO_2 films are obtained, P3HT backfilling is studied afterwards. Both methods of solvent treatment and UV irradiation are used to prepare porous TiO_2 films. It is found that there is no significant difference in the resulting backfilled samples. In general, the backfilling process is successful. GISAXS measurements confirms that the inner structure of TiO_2 is preserved following the backfilling process.

Finally, the flexibility of the corresponding samples treated by solvent treatment, UV irradiation, O_2 plasma, and P3HT backfilling are studied. A custom made two-point bending machine is used to apply the continuous cyclic bends for 10, 100, 500, 1000, and 5000 times, respectively. SEM measurements are employed to examine the crack formation and propagation. It is worthwhile to mention that UV irradiation is not suitable for producing flexible devices, since the PET foil can not survive under long-term UV illumination. It failed much earlier than the investigated films. For other samples, no side effect is observed on the PET substrates. It is found that the fully-extracted and partially-extracted TiO_2 films start to form cracks after 100 bends. However, by calculating the area fraction and width of the cracks, it is shown that the crack propagation in the partially-extracted films is significantly suppressed. The most promising samples are the P3HT backfilled films, which do not have any cracks even after 5000 bends. Hence, the P3HT/TiO_2 films are considered as the most flexible sample, which show great potential for further application in highly flexible or bendable hybrid solar cells.

In order to understand the origin of different mechanical behaviours of these samples, two main types of micromechanical models are applied to effectively estimate the elastic modulus of the corresponding films. With the open-cell foam model, the porous TiO_2 films are supposed to have an effective elastic modulus of around 14.4 Gpa, while the hybrid films are considered as a composite, which constitutes the polymer matrix and TiO_2 fillers. With applying the semi-empirical Halpin-Tsai model, the effective elastic modulus of the partially-extracted and P3HT backfilled TiO_2 films are approximated to be 8.27 Gpa and 1.49 Gpa, respectively. Although the models are based on rough estimations, the trend of the flexibility of all the samples can still be well explained. Moreover, load sharing is proposed to explain the crack propagation. In brief, with the polymer matrix the load is partially carried by the local neighbors of TiO_2 struts, therefore the load on one specific TiO_2 strut is reduced.

In conclusion, porous TiO_2 films can be prepared at low temperature. Among all different polymer template removal methods, solvent treatment is regarded as the most promising method to fully remove the polymer template and obtain a high porosity. Furthermore, the successful backfilling of P3HT (a standard electron donor material) into the nanostructured TiO_2 network is evidenced by SEM and GISAXS measurements. The most promising property is the high flexibility of the P3HT/TiO_2 hybrid films, which do not fail even after 5000 times of bends due to the low effective elastic modulus. Consequently, the P3HT/TiO_2 hybrid films show a great potential for future application as the active layer of highly flexible or bendable hybrid solar cells.

9 Conclusion and outlook

In the present thesis, the main focus is on the nanostructure-performance correlation of polymer-based solar cells. Two main types of active layers, P3HT:PCBM BHJ films and P3HT/TiO_2 hybrid films are investigated for the application of polymer:fullerene solar cells and potentially for hybrid solar cells, respectively. For P3HT:PCBM solar cells, the morphology of the active layer is affected by processing solvent additives, exposing to solvent vapor atmosphere, and adapting of different configurations. Accordingly, the efficiency and stability of the corresponding solar cells can be optimized by adjusting these parameters. For P3HT/TiO_2 hybrid films, a straightforward preparation method at low temperatures is established. The flexibility of TiO_2-based samples are studied on basis of various extraction methods and film constituents.

Different volume concentrations of the solvent additive ODT are used in the preparation of P3HT:PCBM BHJ active layers. The morphology, crystallinity, and molecular dispersity of PCBM in P3HT are thoroughly investigated. It is found that with the aid of ODT the inner structures of the active layers shrink, the crystallinity of P3HT is significantly increased, and more PCBM is incorporated into the P3HT matrix. All these features lead to an improvement in efficiency of the resulting solar cells among which the device with 9 vol% of ODT exhibits the highest PCE.

The influence of different solvent atmospheres on the long-term stability of P3HT:PCBM BHJ solar cells is studied. Among all investigated solvent vapors, dichlorobenzene has the smallest impact on the long-term stability of the P3HT:PCBM solar cells. The absorption behavior, crystalline order, and inner morphology of the resulting P3HT:PCBM films are not strongly degraded by the treatments with different solvent vapors. However, large PCBM crystals are found in the P3HT:PCBM films after exposure to these solvent vapors except for dichlorobenzene. Therefore, the absence of large PCBM crystals is ascribed to be the main reason for the relatively high stability of solar cells stored in dichlorobenzene vapor.

An inverted geometry is adapted for P3HT:PCBM solar cells. It is demonstrated that the inverted geometry significantly improves the device efficiency compared to the standard geometry. The obtained maximal efficiency is among the highest reported values for

P3HT:PCBM BHJ systems so far. The improvement of device performance is attributed to the improved internal light harvesting and smaller structure sizes of P3HT:PCBM active layers. Moreover, it is found that the inverted P3HT:PCBM solar cells exhibit stable photovoltaic performance during continuous operation under illumination and after a long-term storage in dark without encapsulation. This high stability is ascribed to the fact that the inverted geometry can fully overcome the morphological degradation in the active layers.

Flexible P3HT/TiO_2 hybrid films are fabricated at low temperatures by use of the titania precursor EGMT and different template polymer extraction methods. Among all extraction methods, solvent treatment is considered to be the best one to most efficiently remove the template polymer and preserve the original TiO_2 nanostructures from the sol-gel process. After a successful P3HT backfilling into nanostructured TiO_2 films, the resulting P3HT/TiO_2 hybrid films are found to be highly flexible, not showing any cracks after extensive bending tests. A strong improvement in flexibility is achieved compared to pure porous TiO_2 films. The origin of the increased stability is further explained by the semi-empirical Halpin-Tsai model. The produced P3HT/TiO_2 hybrid films show a great potential for highly flexible and bendable hybrid solar cells.

In conclusion, the present thesis reveals the correlation between the morphology of the active layer and the device performance. Basically, P3HT:PCBM BHJ solar cells exhibit the best photovoltaic performance if the nanostructure size of their active layers is close to the exciton diffusion length. A high crystallinity of P3HT is also desired for high efficiency. Furthermore, a stable morphology of the active layers over time is quite beneficial for prolonging the lifetime of the corresponding solar cells. For hybrid P3HT/titania films, infiltration of low elastic modulus material like P3HT into porous titania films can strongly improve the flexibility of the hybrid films, which provides promising applications for flexible and bendable hybrid devices.

In future, projects about polymer:fullerene solar cells should address further lifetime extension. In particular, in the case of novel low-bandgap semiconducting polymers which give rise to great photovoltaic performance, strong degradation in moisture and oxygen most probably results in a poor stability. Adapting an inverted geometry has been proved to stabilize the morphology of the active layer. However, the use of PEDOT:PSS, an aqueous suspension, as the electron blocking layer on top of the active layer will result in a strong degradation of the solar cells by contact with water. Therefore, a replacement for PEDOT:PSS is needed. In addition, chemical modifications on the surface of the hole blocking layer are of great interest to tune the vertical material composition of the active layer, which will probably change an energetically unfavorable morphology to an energetically more favorable morphology. Accordingly, the stability would be improved.

Another possibility to prolong the lifetime will be a technology to build multijunction solar cells with the most sensitive junction sandwiched in the middle. For accomplishing flexible hybrid solar cells, fabrication of the flexible electrodes and blocking layers at low temperature will be the next step. Materials like graphene and silver nanowires can be used as the flexible electrodes. However, preparation of a flexible compact metal oxide layer at low temperatures as blocking layer might be a challenge. The final goal will be the production of working flexible hybrid solar cells.

Bibliography

[1] "Bp statistical review of world energy june 2016," tech. rep., BP, London, 2016.

[2] M. A. Green, K. Emery, Y. Hishikawa, W. Warta, and E. D. Dunlop, "Solar cell efficiency tables (version 48)," *Prog. Photovolt: Res. Appl.*, vol. 24, pp. 905–913, 2016.

[3] C. Deibel and V. Dyakonov, "Polymer–fullerene bulk heterojunction solar cells," *Rep. Prog. Phys.*, vol. 73, p. 096401, 2010.

[4] F. Padinger, R. Rittberger, and N. Sariciftci, "Effects of postproduction treatment on plastic solar cells," *Adv. Funct. Mater.*, vol. 13, pp. 85–88, 2003.

[5] M. A. Ruderer, S. Guo, R. Meier, H.-Y. Chiang, V. Körstgens, J. Wiedersich, J. Perlich, S. V. Roth, and P. Müller-Buschbaum, "Solvent-induced morphology in polymer-based systems for organic photovoltaics," *Adv. Funct. Mater.*, vol. 21, pp. 3382–3391, 2011.

[6] C. K. Chiang, C. R. Fincher, Y. W. Park, A. J. Heeger, H. Shirakawa, E. J. Louis, S. C. Gau, and A. G. MacDiarmid, "Electrical conductivity in doped polyacetylene," *Phys. Rev. Lett.*, vol. 39, pp. 1098–1101, 1977.

[7] M. Pope and C. E. Swenberg, *Electronic processes in organic crystals and polymers.* Oxford University Press, 2nd edition ed., 1999.

[8] V. Shrotriya, J. Ouyang, R. J. Tseng, G. Li, and Y. Yang, "Absorption spectra modification in poly(3-hexylthiophene):methanofullerene blend thin films," *Chem. Phys. Lett.*, vol. 411, pp. 138–143, 2005.

[9] F. Bencheikh, D. Duché, C. M. Ruiz, J.-J. Simon, and L. Escoubas, "Study of optical properties and molecular aggregation of conjugated low band gap copolymers: PTB7 and PTB7-Th," *J. Phys. Chem. C*, vol. 119, pp. 24643–24648, 2015.

[10] H. Koizumi, H. Dougauchi, and T. Ichikawa, "Mechanism of dedoping processes of conducting poly(3-alkylthiophenes)," *J. Phys. Chem. B*, vol. 109, pp. 15288–15290, 2005.

[11] M. Neumann, *Time-resolved imaging of the micro-mechanical behavior of elastomeric polypropylene*. PhD thesis, Technische Universität Chemnitz, Chemnitz, Germany, 2015.

[12] G. Strobl, "From the melt via mesomorphic and granular crystalline layers to lamellar crystallites: A major route followed in polymer crystallization?," *Eur. Phys. J. E*, vol. 3, pp. 165–183, 2000.

[13] G. Strobl, "Crystallization and melting of bulk polymers: New observations, conclusions and a thermodynamic scheme," *Prog. Polym. Sci.*, vol. 31, pp. 398–442, 2006.

[14] K. Tashiro, S. Sasaki, N. Gose, and M. Kobayashi, "Microscopically-viewed structural change of polyethylene during isothermal crystallization from the melt I. time-resolved FT-IR spectral measurements," *Polym. J.*, vol. 30, pp. 485–491, 1998.

[15] A. Fromhold, "Stress in dielectric contact layers on metals," *Surf. Sci.*, vol. 29, pp. 396–410, 1972.

[16] F. S. Bates and G. H. Fredrickson, "Block copolymer thermodynamics: Theory and experiment," *Annu. Rev. Phys. Chem.*, vol. 41, pp. 525–557, 1990.

[17] J. N. Albert and T. H. Epps, "Self-assembly of block copolymer thin films," *Mater. Today*, vol. 13, pp. 24–33, 2010.

[18] M. A. Niedermeier, *Novel structuring routines of titania films for application in photovoltaics*. PhD thesis, Technische Universität München, Munich, Germany, 2013.

[19] U. Diebold, "The surface science of titanium dioxide," *Surf. Sci. Rep.*, vol. 48, pp. 53–229, 2003.

[20] L. Kavan, M. Grätzel, S. E. Gilbert, C. Klemenz, and H. J. Scheel, "Electrochemical and photoelectrochemical investigation of single-crystal anatase," *J. Am. Chem. Soc.*, vol. 118, pp. 6716–6723, 1996.

[21] D. Reyes-Coronado, G. Rodríguez-Gattorno, M. E. Espinosa-Pesqueira, C. Cab, R. de Coss, and G. Oskam, "Phase-pure TiO_2 nanoparticles: anatase, brookite and rutile," *Nanotechnology*, vol. 19, p. 145605, 2008.

[22] A. D. Paola, M. Bellardita, and L. Palmisano, "Brookite, the least known TiO_2 photocatalyst," *Catalysts*, vol. 3, pp. 36–73, 2013.

[23] M. Rawolle, E. V. Braden, M. A. Niedermeier, D. Magerl, K. Sarkar, T. Fröschl, N. Hüsing, J. Perlich, and P. Müller-Buschbaum, "Low-temperature route to crystalline titania network structures in thin films," *ChemPhysChem*, vol. 13, pp. 2412–2417, 2012.

[24] Y.-J. Cheng and J. S. Gutmann, "Morphology phase diagram of ultrathin anatase TiO_2 films templated by a single PS-b-PEO block copolymer," *J. Am. Chem. Soc.*, vol. 128, pp. 4658–4674, 2006.

[25] T. Widmann, "Fabrication and characterization of active layers for flexible hybrid solar cells," Master's thesis, Technische Universität München, Munich, Germany, 2015.

[26] S. Guo, M. A. Ruderer, M. Rawolle, V. Körstgens, C. Birkenstock, J. Perlich, and P. Müller-Buschbaum, "Evolution of lateral structures during the functional stack build-up of P3HT:PCBM-based bulk heterojunction solar cells," *ACS Appl. Mater. Interfaces*, vol. 5, pp. 8581–8590, 2013.

[27] E. Moore, B. Gherman, and D. Yaron, "Coulomb screening and exciton binding energies in conjugated polymers," *J. Chem. Phys.*, vol. 106, p. 4216, 1997.

[28] S. Barth and H. Bässler, "Intrinsic photoconduction in PPV-type conjugated polymers," *Phys. Rev. Lett.*, vol. 79, pp. 4445–4448, 1997.

[29] J. Cornil, D. Beljonne, Z. Shuia, T. Hagler, I. Campbell, D. Bradley, J. Brédas, C. Spangler, and K. Müllen, "Vibronic structure in the optical absorption spectra of phenylene vinylene oligomers: a joint experimental and theoretical study," *Chem. Phys. Lett.*, vol. 247, pp. 425–432, 1995.

[30] P. J. Brown, D. S. Thomas, A. Köhler, J. S. Wilson, J.-S. Kim, C. M. Ramsdale, H. Sirringhaus, and R. H. Friend, "Effect of interchain interactions on the absorption and emission of poly(3-hexylthiophene)," *Phys. Rev. B*, vol. 67, p. 064203, 2003.

[31] F. C. Spano, "The spectral signatures of frenkel polarons in H- and J-aggregates," *Acc. Chem. Res.*, vol. 43, pp. 429–439, 2010.

[32] Y. Gao, T. P. Martin, E. T. Niles, A. J. Wise, A. K. Thomas, and J. K. Grey, "Understanding morphology-dependent polymer aggregation properties and photocurrent generation in polythiophene/fullerene solar cells of variable compositions," *J. Phys. Chem. C*, vol. 114, pp. 15121–15128, 2010.

[33] L. Lüer, "Oxygen-induced quenching of photoexcited states in polythiophene films," *Org. Electron.*, vol. 5, pp. 83–89, 2004.

[34] T. Stübinger and W. Brütting, "Exciton diffusion and optical interference in organic donor–acceptor photovoltaic cells," *J. Appl. Phys.*, vol. 90, p. 3632, 2001.

[35] P. Peumans, A. Yakimov, and S. R. Forrest, "Small molecular weight organic thin-film photodetectors and solar cells," *J. Appl. Phys.*, vol. 93, p. 3693, 2003.

[36] N. S. Sariciftci, L. Smilowitz, A. J. Heeger, and F. Wudl, "Photoinduced electron transfer from a conducting polymer to buckminsterfullerene," *Science*, vol. 258, pp. 1474–1476, 1992.

[37] L. Onsager, "Initial recombination of ions," *Phys. Rev.*, vol. 54, pp. 554–557, 1938.

[38] C. L. Braun, "Electric field assisted dissociation of charge transfer states as a mechanism of photocarrier production," *J. Chem. Phys.*, vol. 80, p. 4157, 1984.

[39] D. Alberga, A. Perrier, I. Ciofini, G. F. Mangiatordi, G. Lattanzi, and C. Adamo, "Morphological and charge transport properties of amorphous and crystalline P3HT and PBTTT: insights from theory," *Phys. Chem. Chem. Phys.*, vol. 17, pp. 18742–18750, 2015.

[40] P. E. Shaw, A. Ruseckas, and I. D. W. Samuel, "Exciton diffusion measurements in poly(3-hexylthiophene)," *Adv. Mater.*, vol. 20, pp. 3516–3520, 2008.

[41] D. Moseguí González, V. Körstgens, Y. Yao, L. Song, G. Santoro, S. V. Roth, and P. Müller-Buschbaum, "Improved power conversion efficiency of P3HT:PCBM organic solar cells by strong spin-orbit coupling-induced delayed fluorescence," *Adv. Energy Mater.*, vol. 5, p. 1401770, 2015.

[42] J.-H. Lee, M. Takafuji, T. Sagawa, and H. Ihara, "Reappraising the validity of poly(3-hexylthiophene) nanostructures in interdigitated bilayer organic solar cells," *Sol. Energy Mater. Sol. Cells*, vol. 147, pp. 68–74, 2016.

[43] M. Tolan, *X-Ray Scattering from Soft-Matter Thin Films.* Springer Berlin Heidelberg, 1999.

[44] Y. Yoneda, "Anomalous surface reflection of x rays," *Phys. Rev.*, vol. 131, pp. 2010–2013, 1963.

[45] H. Dosch, B. W. Batterman, and D. C. Wack, "Depth-controlled grazing-incidence diffraction of synchrotron x radiation," *Phys. Rev. Lett.*, vol. 56, pp. 1144–1147, 1986.

[46] P. Müller-Buschbaum, *Polymer Surfaces and Interfaces: Characterization, Modification and Applications.* Springer-Verlag Berlin Heidelberg, 2008.

[47] A. Naudon, D. Babonneau, D. Thiaudière, and S. Lequien, "Grazing-incidence small-angle X-ray scattering applied to the characterization of aggregates in surface regions," *Physica B*, vol. 283, pp. 69–74, 2000.

[48] P. Müller-Buschbaum, "Grazing incidence small-angle X-ray scattering: An advanced scattering technique for the investigation of nanostructured polymer films," *Anal. Bioanal.Chem.*, vol. 376, pp. 3–10, 2003.

[49] G. Renaud, R. Lazzari, and F. Leroy, "Probing surface and interface morphology with grazing incidence small angle X-ray scattering," *Surf. Sci. Rep.*, vol. 64, pp. 255–380, 2009.

[50] J. Rivnay, S. C. B. Mannsfeld, C. E. Miller, A. Salleo, and M. F. Toney, "Quantitative determination of organic semiconductor microstructure from the molecular to device scale," *Chem. Rev.*, vol. 112, pp. 5488–5519, 2012.

[51] L. Oesinghaus, "The morphology of perovskite solar cells studied by GIWAXS," Master's thesis, Technische Universität München, Munich, Germany, 2016.

[52] P. Müller-Buschbaum, "The active layer morphology of organic solar cells probed with grazing incidence scattering techniques," *Adv. Mater.*, vol. 26, pp. 7692–7709, 2014.

[53] Z. Jiang, "GIXSGUI : a MATLAB toolbox for grazing-incidence X-ray scattering data visualization and reduction, and indexing of buried three-dimensional periodic nanostructured films," *J. Appl. Cryst.*, vol. 48, pp. 917–926, 2015.

[54] Z. Jiang, *GIXSGUI [Online]. Available: https://www1.aps.anl.gov/science/scientific-software/gixsgui.*

[55] J. L. Baker, L. H. Jimison, S. Mannsfeld, S. Volkman, S. Yin, V. Subramanian, A. Salleo, A. P. Alivisatos, and M. F. Toney, "Quantification of thin film crystallographic orientation using X-ray diffraction with an area detector," *Langmuir*, vol. 26, pp. 9146–9151, 2010.

[56] A. Kirubanandham and S. Basu, *On Characterization of Mechanical Deformation in Flexible Electronic Structures, Application note.* Agilent Technologies.

[57] M. J. Matthewson, C. R. Kurkjian, and S. T. Gulati, "Strength measurement of optical fibers by bending," *J. Am. Ceram. Soc.*, vol. 69, pp. 815–821, 1986.

[58] S. T. Gulati, J. T. Westbrook, K. H. Vepakomma, T. Ono, and J. S. Kim, "Overview of strength tests for LCD substrates and panels," in *18th International Display Workshops 2011*, no. 94107, 2011.

[59] J. A. Rogers, T. Someya, and Y. Huang, "Materials and mechanics for stretchable electronics," *Science*, vol. 327, pp. 1603–1607, 2010.

[60] S.-I. Park, J.-H. Ahn, X. Feng, S. Wang, Y. Huang, and J. A. Rogers, "Theoretical and experimental studies of bending of inorganic electronic materials on plastic substrates," *Adv. Funct. Mater.*, vol. 18, pp. 2673–2684, 2008.

[61] W. Kim and C. Laird, "Crack nucleation and stage I propagation in high strain fatigue—I. microscopic and interferometric observations," *Acta Mater.*, vol. 26, pp. 777–787, 1978.

[62] W. Kim and C. Laird, "Crack nucleation and stage I propagation in high strain fatigue— II. mechanism," *Acta Mater.*, vol. 26, pp. 789–799, 1978.

[63] M. Ashby, "The properties of foams and lattices," *Phil. Trans. R. Soc. A*, vol. 364, pp. 15–30, 2006.

[64] V. Deshpande, M. Ashby, and N. Fleck, "Foam topology: bending versus stretching dominated architectures," *Acta Mater.*, vol. 49, pp. 1035–1040, 2001.

[65] T. Hanemann and D. V. Szabó, "Polymer-nanoparticle composites: From synthesis to modern applications," *Materials*, vol. 3, pp. 3468–3517, 2010.

[66] A. Coldea, *Suitability of Polymer-Infiltrated-Ceramic-Networks for CAD/CAM based dental restorative materials.* PhD thesis, University of Otago, Dunedin, New Zealand, 2014.

[67] M. A. Meyers, P.-Y. Chen, A. Y.-M. Lin, and Y. Seki, "Biological materials: Structure and mechanical properties," *Prog. Mater Sci.*, vol. 53, pp. 1–206, 2008.

[68] J. C. Halpin and J. L. Kardos, "The halpin-tsai equations: A review," *Polym. Eng. Sci.*, vol. 16, pp. 344–352, 1976.

[69] M. Rawolle, K. Sarkar, M. A. Niedermeier, M. Schindler, P. Lellig, J. S. Gutmann, J.-F. Moulin, M. Haese-Seiller, A. S. Wochnik, C. Scheu, and P. Müller-Buschbaum, "Infiltration of polymer hole-conductor into mesoporous titania structures for solid-state dye-sensitized solar cells," *ACS Appl. Mater. Interfaces*, vol. 5, pp. 719–729, 2013.

[70] C. W. Bert, "Prediction of elastic moduli of solids with oriented porosity," *J. Mater. Sci.*, vol. 20, pp. 2220–2224, 1985.

[71] P. Alam, *Porous Particle-Polymer Composites, Advances in Composite Materials - Analysis of Natural and Man-Made Materials.* InTech, 2011.

[72] N. Banerji, S. Cowan, E. Vauthey, and A. J. Heeger, "Ultrafast relaxation of the poly(3-hexylthiophene) emission spectrum," *J. Phys. Chem. C*, vol. 115, pp. 9726–9739, 2011.

[73] S. J. Lou, J. M. Szarko, T. Xu, L. Yu, T. J. Marks, and L. X. Chen, "Effects of additives on the morphology of solution phase aggregates formed by active layer components of high-efficiency organic solar cells," *J. Am. Chem. Soc.*, vol. 133, pp. 20661–20663, 2011.

[74] M. K. Siddiki, J. Li, D. Galipeau, and Q. Qiao, "A review of polymer multijunction solar cells," *Energy Environ. Sci.*, vol. 3, p. 867, 2010.

[75] S. Guldin, *Inorganic nanoarchitectures by organic self-assembly.* PhD thesis, University of Cambridge, Cambridge, UK, 2012.

[76] R. Hosemann, W. Vogel, D. Weick, and F. J. Baltá-Calleja, "Novel aspects of the real paracrystal," *Acta Crystallogr. Sect. A*, vol. 37, pp. 85–91, 1981.

[77] R. Kampmann, M. Haese-Seiller, V. Kudryashov, V. Deriglazov, M. Tristl, C. Daniel, B. Toperverg, A. Schreyer, and E. Sackmann, "The potential of the horizontal reflectometer REFSANS/FRM-II for measuring low reflectivity and diffuse surface scattering," *Physica B*, vol. 350, pp. E763–E766, 2004.

[78] R. Kampmann, M. Haese-Seiller, V. Kudryashov, B. Nickel, C. Daniel, W. Fenzl, A. Schreyer, E. Sackmann, and J. Rädler, "Horizontal TOF-neutron reflectometer REFSANS at FRM-II munich/Germany: First tests and status," *Physica B*, vol. 385-386, pp. 1161–1163, 2006.

[79] P. Müller-Buschbaum, G. Kaune, M. Haese-Seiller, and J.-F. Moulin, "Morphology determination of defect-rich diblock copolymer films with time-of-flight grazing-incidence small-angle neutron scattering," *J. Appl. Cryst.*, vol. 47, pp. 1228–1237, 2014.

[80] Y. Yao, E. Metwalli, J.-F. Moulin, B. Su, M. Opel, and P. Müller-Buschbaum, "Self-assembly of diblock copolymer–maghemite nanoparticle hybrid thin films," *ACS Appl. Mater. Interfaces*, vol. 6, pp. 18152–18162, 2014.

[81] I. Burgués-Ceballos, M. Stella, P. Lacharmoise, and E. Martínez-Ferrero, "Towards industrialization of polymer solar cells: material processing for upscaling," *J. Mater. Chem. A*, vol. 2, pp. 17711–17722, 2014.

[82] S. D. Dimitrov and J. R. Durrant, "Materials design considerations for charge generation in organic solar cells," *Chem. Mater.*, vol. 26, pp. 616–630, 2014.

[83] M. T. Dang, L. Hirsch, G. Wantz, and J. D. Wuest, "Controlling the morphology and performance of bulk heterojunctions in solar cells. Lessons learned from the benchmark poly(3-hexylthiophene):[6,6]-phenyl-C_{61}-butyric acid methyl ester system," *Chem. Rev.*, vol. 113, pp. 3734–3765, 2013.

[84] R. Kroon, M. Lenes, J. C. Hummelen, P. W. M. Blom, and B. de Boer, "Small bandgap polymers for organic solar cells (polymer material development in the last 5 years)," *Polym. Rev.*, vol. 48, pp. 531–582, 2008.

[85] W. Chen, M. P. Nikiforov, and S. B. Darling, "Morphology characterization in organic and hybrid solar cells," *Energy Environ. Sci.*, vol. 5, p. 8045, 2012.

[86] S. Cho, S.-H. Nho, M. Eo, and M. H. Lee, "Effects of processing additive on bipolar field-effect transistors based on blends of poly(3-hexylthiophene) and fullerene bearing long alkyl tails," *Org. Electron.*, vol. 15, pp. 1002–1011, 2014.

[87] J. Razzell-Hollis, W. C. Tsoi, and J.-S. Kim, "Directly probing the molecular order of conjugated polymer in OPV blends induced by different film thicknesses, substrates and additives," *J. Mater. Chem. C*, vol. 1, p. 6235, 2013.

[88] R. Rossmanith, C. K. Weiss, J. Geserick, N. Hüsing, U. Hörmann, U. Kaiser, and K. Landfester, "Porous anatase nanoparticles with high specific surface area prepared by miniemulsion technique," *Chem. Mater.*, vol. 20, pp. 5768–5780, 2008.

[89] Y. Denkwitz, M. Makosch, J. Geserick, U. Hörmann, S. Selve, U. Kaiser, N. Hüsing, and R. Behm, "Influence of the crystalline phase and surface area of the TiO_2 support on the CO oxidation activity of mesoporous au/TiO_2 catalysts," *Appl. Catal., B*, vol. 91, pp. 470–480, 2009.

[90] D. W. Schubert and T. Dunkel, "Spin coating from a molecular point of view: its concentration regimes, influence of molar mass and distribution," *Mater. Res. Innovations*, vol. 7, pp. 314–321, 2003.

[91] M. Rawolle, *Structuring and filling of titania films for applications in photovoltaics*. PhD thesis, Technische Universität München, Munich, Germany, 2013.

[92] H. Yu, S. Zhang, H. Zhao, G. Will, and P. Liu, "An efficient and low-cost TiO_2 compact layer for performance improvement of dye-sensitized solar cells," *Electrochim. Acta*, vol. 54, pp. 1319–1324, 2009.

[93] B. Gholamkhass, T. J. Peckham, and S. Holdcroft, "Poly(3-hexylthiophene) bearing pendant fullerenes: aggregation vs. self-organization," *Polym. Chem.*, vol. 1, p. 708, 2010.

[94] H.-Y. Chen, H. Yang, G. Yang, S. Sista, R. Zadoyan, G. Li, and Y. Yang, "Fast-grown interpenetrating network in poly(3-hexylthiophene): Methanofullerenes solar cells processed with additive," *J. Phys. Chem. C*, vol. 113, pp. 7946–7953, 2009.

[95] Y. Yao, J. Hou, Z. Xu, G. Li, and Y. Yang, "Effects of solvent mixtures on the nanoscale phase separation in polymer solar cells," *Adv. Funct. Mater.*, vol. 18, pp. 1783–1789, 2008.

[96] G. Li, V. Shrotriya, J. Huang, Y. Yao, T. Moriarty, K. Emery, and Y. Yang, "High-efficiency solution processable polymer photovoltaic cells by self-organization of polymer blends," *Nat. Mater.*, vol. 4, pp. 864–868, 2005.

[97] N. Shin, L. J. Richter, A. A. Herzing, R. J. Kline, and D. M. DeLongchamp, "Effect of processing additives on the solidification of blade-coated polymer/fullerene blend films via in-situ structure measurements," *Adv. Energy Mater.*, vol. 3, pp. 938–948, 2013.

[98] X. Liu, S. Huettner, Z. Rong, M. Sommer, and R. H. Friend, "Solvent additive control of morphology and crystallization in semiconducting polymer blends," *Adv. Mater.*, vol. 24, pp. 669–674, 2011.

[99] Z. Jin and J. Wang, "PIN architecture for ultrasensitive organic thin film photoconductors," *Sci. Rep.*, vol. 4, p. 5331, 2014.

[100] D. E. Motaung, G. F. Malgas, S. S. Nkosi, G. H. Mhlongo, B. W. Mwakikunga, T. Malwela, C. J. Arendse, T. F. G. Muller, and F. R. Cummings, "Comparative study: the effect of annealing conditions on the properties of P3HT:PCBM blends," *J. Mater. Sci.*, vol. 48, pp. 1763–1778, 2012.

[101] M. A. Ruderer, R. Meier, L. Porcar, R. Cubitt, and P. Müller-Buschbaum, "Phase separation and molecular intermixing in polymer–fullerene bulk heterojunction thin films," *J. Phys. Chem. Lett.*, vol. 3, pp. 683–688, 2012.

[102] C.-H. Liu, W.-H. Tseng, C.-Y. Cheng, C.-I. Wu, P.-T. Chou, and S.-H. Tung, "Effects of amorphous poly(3-hexylthiophene) on active-layer structure and solar cells performance," *J. Polym. Sci., Part B: Polym. Phys.*, vol. 54, pp. 975–985, 2016.

[103] L. Chang, I. E. Jacobs, M. P. Augustine, and A. J. Moulé, "Correlating dilute solvent interactions to morphology and OPV device performance," *Org. Electron.*, vol. 14, pp. 2431–2443, 2013.

[104] M. A. Ruderer, *Morphology of polymer-based films for organic photovoltaics.* PhD thesis, Technische Universität München, Munich, Germany, 2012.

[105] P. E. Hopkinson, P. A. Staniec, A. J. Pearson, A. D. F. Dunbar, T. Wang, A. J. Ryan, R. A. L. Jones, D. G. Lidzey, and A. M. Donald, "A phase diagram of the P3HT:PCBM organic photovoltaic system: Implications for device processing and performance," *Macromolecules*, vol. 44, pp. 2908–2917, 2011.

[106] G. Kalita, M. Masahiro, W. Koichi, and M. Umeno, "Nanostructured morphology of P3HT:PCBM bulk heterojunction solar cells," *Solid State Electron.*, vol. 54, pp. 447–451, 2010.

[107] J. Y. Na, B. Kang, D. H. Sin, K. Cho, and Y. D. Park, "Understanding solidification of polythiophene thin films during spin-coating: Effects of spin-coating time and processing additives," *Sci. Rep.*, vol. 5, p. 13288, 2015.

[108] A. J. Parnell, A. D. F. Dunbar, A. J. Pearson, P. A. Staniec, A. J. C. Dennison, H. Hamamatsu, M. W. A. Skoda, D. G. Lidzey, and R. A. L. Jones, "Depletion of PCBM at the cathode interface in P3HT/PCBM thin films as quantified via neutron reflectivity measurements," *Adv. Mater.*, vol. 22, pp. 2444–2447, 2010.

[109] W. Wang, S. Guo, E. M. Herzig, K. Sarkar, M. Schindler, D. Magerl, M. Philipp, J. Perlich, and P. Müller-Buschbaum, "Investigation of morphological degradation of P3HT:PCBM bulk heterojunction films exposed to long-term host solvent vapor," *J. Mater. Chem. A*, vol. 4, pp. 3743–3753, 2016.

[110] R. Søndergaard, M. Hösel, D. Angmo, T. T. Larsen-Olsen, and F. C. Krebs, "Roll-to-roll fabrication of polymer solar cells," *Mater. Today*, vol. 15, pp. 36–49, 2012.

[111] M. Kaltenbrunner, M. S. White, E. D. Głowacki, T. Sekitani, T. Someya, N. S. Sariciftci, and S. Bauer, "Ultrathin and lightweight organic solar cells with high flexibility," *Nat. Commun.*, vol. 3, p. 770, 2012.

[112] D. J. Burke and D. J. Lipomi, "Green chemistry for organic solar cells," *Energy Environ. Sci.*, vol. 6, p. 2053, 2013.

[113] Z. He, C. Zhong, S. Su, M. Xu, H. Wu, and Y. Cao, "Enhanced power-conversion efficiency in polymer solar cells using an inverted device structure," *Nat. Photon.*, vol. 6, pp. 593–597, 2012.

[114] Z. He, B. Xiao, F. Liu, H. Wu, Y. Yang, S. Xiao, C. Wang, T. P. Russell, and Y. Cao, "Single-junction polymer solar cells with high efficiency and photovoltage," *Nat. Photon.*, vol. 9, pp. 174–179, 2015.

[115] P. Kohn, Z. Rong, K. H. Scherer, A. Sepe, M. Sommer, P. Müller-Buschbaum, R. H. Friend, U. Steiner, and S. Hüttner, "Crystallization-induced 10-nm structure formation in P3HT/PCBM blends," *Macromolecules*, vol. 46, pp. 4002–4013, 2013.

[116] K. Sun, Z. Xiao, E. Hanssen, M. F. G. Klein, H. H. Dam, M. Pfaff, D. Gerthsen, W. W. H. Wong, and D. J. Jones, "The role of solvent vapor annealing in highly efficient air-processed small molecule solar cells," *J. Mater. Chem. A*, vol. 2, p. 9048, 2014.

[117] E. Verploegen, C. E. Miller, K. Schmidt, Z. Bao, and M. F. Toney, "Manipulating the morphology of P3HT–PCBM bulk heterojunction blends with solvent vapor annealing," *Chem. Mater.*, vol. 24, pp. 3923–3931, 2012.

[118] J. H. Jeon, H. K. Lee, D. H. Wang, J. H. Park, and O. O. Park, "The role of non-solvent swelling in bulk hetero junction solar cells," *Sol. Energy Mater. Sol. Cells*, vol. 102, pp. 196–200, 2012.

[119] B. Jung, K. Kim, Y. Eom, and W. Kim, "High-pressure solvent vapor annealing with a benign solvent to rapidly enhance the performance of organic photovoltaics," *ACS Appl. Mater. Interfaces*, vol. 7, pp. 13342–13349, 2015.

[120] Y. Kim, S. A. Choulis, J. Nelson, D. D. C. Bradley, S. Cook, and J. R. Durrant, "Device annealing effect in organic solar cells with blends of regioregular poly(3-hexylthiophene) and soluble fullerene," *Appl. Phys. Lett.*, vol. 86, p. 063502, 2005.

[121] M. A. Ruderer and P. Müller-Buschbaum, "Morphology of polymer-based bulk heterojunction films for organic photovoltaics," *Soft Matter*, vol. 7, p. 5482, 2011.

[122] L. Li, G. Lu, S. Li, H. Tang, and X. Yang, "Epitaxy-assisted creation of PCBM nanocrystals and its application in constructing optimized morphology for bulk-heterojunction polymer solar cells," *J. Phys. Chem. B*, vol. 112, pp. 15651–15658, 2008.

[123] Y. Yang, C. Liu, S. Gao, Y. Li, X. Wang, Y. Wang, T. Minari, Y. Xu, P. Wang, Y. Zhao, K. Tsukagoshi, and Y. Shi, "Large [6,6]-phenyl C_{61} butyric acid methyl (PCBM) hexagonal crystals grown by solvent-vapor annealing," *Mater. Chem. Phys.*, vol. 145, pp. 327–333, 2014.

[124] G. Paternò, A. J. Warren, J. Spencer, G. Evans, V. G. Sakai, J. Blumberger, and F. Cacialli, "Micro-focused X-ray diffraction characterization of high-quality [6,6]-phenyl-C_{61}-butyric acid methyl ester single crystals without solvent impurities," *J. Mater. Chem. C*, vol. 1, p. 5619, 2013.

[125] S.Hu, "The impact of selective solvents on the structure and function evolution in solvent annealed organic photovoltaics," Master's thesis, University of Tennessee, Knoxville, US, 2013.

[126] K. W. Chou, B. Yan, R. Li, E. Q. Li, K. Zhao, D. H. Anjum, S. Alvarez, R. Gassaway, A. Biocca, S. T. Thoroddsen, A. Hexemer, and A. Amassian, "Spin-cast bulk heterojunction solar cells: A dynamical investigation," *Adv. Mater.*, vol. 25, pp. 1923–1929, 2013.

[127] M. J. Sobkowicz, R. L. Jones, R. J. Kline, and D. M. DeLongchamp, "Effect of fullerenes on crystallization-induced aggregation in polymer photovoltaics casting solutions," *Macromolecules*, vol. 45, pp. 1046–1055, 2012.

[128] W.-R. Wu, U.-S. Jeng, C.-J. Su, K.-H. Wei, M.-S. Su, M.-Y. Chiu, C.-Y. Chen, W.-B. Su, C.-H. Su, and A.-C. Su, "Competition between fullerene aggregation and poly(3-hexylthiophene) crystallization upon annealing of bulk heterojunction solar cells," *ACS Nano*, vol. 5, pp. 6233–6243, 2011.

[129] W. Yin and M. Dadmun, "A new model for the morphology of P3HT/PCBM organic photovoltaics from small-angle neutron scattering: Rivers and streams," *ACS Nano*, vol. 5, pp. 4756–4768, 2011.

[130] Y.-C. Huang, C.-S. Tsao, C.-M. Chuang, C.-H. Lee, F.-H. Hsu, H.-C. Cha, C.-Y. Chen, T.-H. Lin, C.-J. Su, U.-S. Jeng, and W.-F. Su, "Small- and wide-angle X-ray scattering characterization of bulk heterojunction polymer solar cells with different fullerene derivatives," *J. Phys. Chem. C*, vol. 116, pp. 10238–10244, 2012.

[131] C. J. Schaffer, C. M. Palumbiny, M. A. Niedermeier, C. Jendrzejewski, G. Santoro, S. V. Roth, and P. Müller-Buschbaum, "A direct evidence of morphological degradation on a nanometer scale in polymer solar cells," *Adv. Mater.*, vol. 25, pp. 6760–6764, 2013.

[132] A. Swinnen, I. Haeldermans, M. vande Ven, J. D'Haen, G. Vanhoyland, S. Aresu, M. D'Olieslaeger, and J. Manca, "Tuning the dimensions of C_{60}-based needlelike crystals in blended thin films," *Adv. Funct. Mater.*, vol. 16, pp. 760–765, 2006.

[133] S. T. Turner, P. Pingel, R. Steyrleuthner, E. J. W. Crossland, S. Ludwigs, and D. Neher, "Quantitative analysis of bulk heterojunction films using linear absorption spectroscopy and solar cell performance," *Adv. Funct. Mater.*, vol. 21, pp. 4640–4652, 2011.

[134] H.-W. Liu, D.-Y. Chang, W.-Y. Chiu, S.-P. Rwei, and L. Wang, "Fullerene bisadduct as an effective phase-separation inhibitor in preparing poly(3-hexylthiophene)–[6,6]-phenyl-C_{61}-butyric acid methyl ester blends with highly stable morphology," *J. Mater. Chem.*, vol. 22, p. 15586, 2012.

[135] R. Colle, G. Grosso, A. Ronzani, M. Gazzano, and V. Palermo, "Anisotropic molecular packing of soluble C_{60} fullerenes in hexagonal nanocrystals obtained by solvent vapor annealing," *Carbon*, vol. 50, pp. 1332–1337, 2012.

[136] N. D. Treat, C. G. Shuttle, M. F. Toney, C. J. Hawker, and M. L. Chabinyc, "In situ measurement of power conversion efficiency and molecular ordering during thermal annealing in P3HT:PCBM bulk heterojunction solar cells," *J. Mater. Chem.*, vol. 21, p. 15224, 2011.

[137] W. Wang, S. Pröller, M. A. Niedermeier, V. Körstgens, M. Philipp, B. Su, D. Moseguí González, S. Yu, S. V. Roth, and P. Müller-Buschbaum, "Development of the morphology during functional stack build-up of p3ht:pcbm bulk heterojunction solar cells with inverted geometry," *ACS Appl. Mater. Interfaces*, vol. 7, pp. 602–610, 2015.

[138] W. Wang, C. J. Schaffer, L. Song, V. Körstgens, S. Pröller, E. D. Indari, T. Wang, A. Abdelsamie, S. Bernstorff, and P. Müller-Buschbaum, "In operando morphology investigation of inverted bulk heterojunction organic solar cells by gisaxs," *J. Mater. Chem. A*, vol. 3, pp. 8324–8331, 2015.

[139] J. You, L. Dou, K. Yoshimura, T. Kato, K. Ohya, T. Moriarty, K. Emery, C.-C. Chen, J. Gao, G. Li, and Y. Yang, "A polymer tandem solar cell with 10.6% power conversion efficiency," *Nat. Commun.*, vol. 4, p. 1446, 2013.

[140] L. Dou, J. You, J. Yang, C.-C. Chen, Y. He, S. Murase, T. Moriarty, K. Emery, G. Li, and Y. Yang, "Tandem polymer solar cells featuring a spectrally matched low-bandgap polymer," *Nat. Photon.*, vol. 6, pp. 180–185, 2012.

[141] C.-C. Chen, W.-H. Chang, K. Yoshimura, K. Ohya, J. You, J. Gao, Z. Hong, and Y. Yang, "An efficient triple-junction polymer solar cell having a power conversion efficiency exceeding 11%," *Adv. Mater.*, vol. 26, pp. 5670–5677, 2014.

[142] C.-H. Hsieh, Y.-J. Cheng, P.-J. Li, C.-H. Chen, M. Dubosc, R.-M. Liang, and C.-S. Hsu, "Highly efficient and stable inverted polymer solar cells integrated with a cross-linked fullerene material as an interlayer," *J. Am. Chem. Soc.*, vol. 132, pp. 4887–4893, 2010.

[143] Z. Xu, L.-M. Chen, G. Yang, C.-H. Huang, J. Hou, Y. Wu, G. Li, C.-S. Hsu, and Y. Yang, "Vertical phase separation in poly(3-hexylthiophene): fullerene derivative blends and its advantage for inverted structure solar cells," *Adv. Funct. Mater.*, vol. 19, pp. 1227–1234, 2009.

[144] S. Lattante, "Electron and hole transport layers: Their use in inverted bulk heterojunction polymer solar cells," *Electronics*, vol. 3, pp. 132–164, 2014.

[145] S.-H. Liao, H.-J. Jhuo, Y.-S. Cheng, and S.-A. Chen, "Fullerene derivative-doped zinc oxide nanofilm as the cathode of inverted polymer solar cells with low-bandgap polymer (PTB7-Th) for high performance," *Adv. Mater.*, vol. 25, pp. 4766–4771, 2013.

[146] R. Lampande, G. W. Kim, J. Boizot, Y. J. Kim, R. Pode, and J. H. Kwon, "A highly efficient transition metal oxide layer for hole extraction and transport in inverted polymer bulk heterojunction solar cells," *J. Mater. Chem. A*, vol. 1, p. 6895, 2013.

[147] S. K. Hau, H.-L. Yip, N. S. Baek, J. Zou, K. O'Malley, and A. K.-Y. Jen, "Air-stable inverted flexible polymer solar cells using zinc oxide nanoparticles as an electron selective layer," *Appl. Phys. Lett.*, vol. 92, p. 253301, 2008.

[148] T. Hu, F. Li, K. Yuan, and Y. Chen, "Efficiency and air-stability improvement of flexible inverted polymer solar cells using ZnO/poly(ethylene glycol) hybrids as cathode buffer layers," *ACS Appl. Mater. Interfaces*, vol. 5, pp. 5763–5770, 2013.

[149] K. Norrman, M. V. Madsen, S. A. Gevorgyan, and F. C. Krebs, "Degradation patterns in water and oxygen of an inverted polymer solar cell," *J. Am. Chem. Soc.*, vol. 132, pp. 16883–16892, 2010.

[150] F. Hou, Z. Su, F. Jin, X. Yan, L. Wang, H. Zhao, J. Zhu, B. Chu, and W. Li, "Efficient and stable planar heterojunction perovskite solar cells with an MoO_3 /PEDOT:PSS hole transporting layer," *Nanoscale*, vol. 7, pp. 9427–9432, 2015.

[151] M. C. Scharber, D. Mühlbacher, M. Koppe, P. Denk, C. Waldauf, A. J. Heeger, and C. J. Brabec, "Design rules for donors in bulk-heterojunction solar cells—towards 10 % energy-conversion efficiency," *Adv. Mater.*, vol. 18, pp. 789–794, 2006.

[152] D. Chi, S. Qu, Z. Wang, and J. Wang, "High efficiency P3HT:PCBM solar cells with an inserted PCBM layer," *J. Mater. Chem. C*, vol. 2, p. 4383, 2014.

[153] C. J. Brabec, M. Heeney, I. McCulloch, and J. Nelson, "Influence of blend microstructure on bulk heterojunction organic photovoltaic performance," *Chem. Soc. Rev.*, vol. 40, pp. 1185–1199, 2011.

[154] Y. Zhang, D. Deng, K. Lu, J. Zhang, B. Xia, Y. Zhao, J. Fang, and Z. Wei, "Synergistic effect of polymer and small molecules for high-performance ternary organic solar cells," *Adv. Mater.*, vol. 27, pp. 1071–1076, 2015.

[155] J. B. Kim, P. Kim, N. C. Pégard, S. J. Oh, C. R. Kagan, J. W. Fleischer, H. A. Stone, and Y.-L. Loo, "Wrinkles and deep folds as photonic structures in photovoltaics," *Nat. Photon.*, vol. 6, pp. 327–332, 2012.

[156] E. Metwalli, S. Couet, K. Schlage, R. Röhlsberger, V. Körstgens, M. Ruderer, W. Wang, G. Kaune, S. V. Roth, and P. Müller-Buschbaum, "In situ GISAXS investigation of gold sputtering onto a polymer template," *Langmuir*, vol. 24, pp. 4265–4272, 2008.

[157] G. Li, V. Shrotriya, Y. Yao, and Y. Yang, "Investigation of annealing effects and film thickness dependence of polymer solar cells based on poly(3-hexylthiophene)," *J. Appl. Phys.*, vol. 98, p. 043704, 2005.

[158] Y. Zhao, A. Sugunan, T. Schmidt, A. Fornara, M. S. Toprak, and M. Muhammed, "Relaxation is the key to longer life: suppressed degradation of P3HT films on conductive substrates," *J. Mater. Chem. A*, vol. 2, p. 13270, 2014.

[159] M. T. Lloyd, C. H. Peters, A. Garcia, I. V. Kauvar, J. J. Berry, M. O. Reese, M. D. McGehee, D. S. Ginley, and D. C. Olson, "Influence of the hole-transport layer on the initial behavior and lifetime of inverted organic photovoltaics," *Sol. Energy Mater. Sol. Cells*, vol. 95, pp. 1382–1388, 2011.

[160] S. Guo, C. Brandt, T. Andreev, E. Metwalli, W. Wang, J. Perlich, and P. Müller-Buschbaum, "First step into space: Performance and morphological evolution of P3HT:PCBM bulk heterojunction solar cells under AM0 illumination," *ACS Appl. Mater. Interfaces*, vol. 6, pp. 17902–17910, 2014.

[161] M. T. Lloyd, D. C. Olson, J. J. Berry, N. Kopidakis, M. O. Reese, K. X. Steirer, and D. S. Ginley, "Enhanced lifetime in unencapsulated organic photovoltaics with air stable electrodes," in *2010 35th IEEE Photovoltaic Specialists Conference*, Institute of Electrical & Electronics Engineers (IEEE), 2010.

[162] M. Rawolle, M. A. Niedermeier, G. Kaune, J. Perlich, P. Lellig, M. Memesa, Y.-J. Cheng, J. S. Gutmann, and P. Müller-Buschbaum, "Fabrication and characterization of nanostructured titania films with integrated function from inorganic–organic hybrid materials," *Chem. Soc. Rev.*, vol. 41, p. 5131, 2012.

[163] V. Puddu, H. Choi, D. D. Dionysiou, and G. L. Puma, "TiO_2 photocatalyst for indoor air remediation: Influence of crystallinity, crystal phase, and UV radiation intensity on trichloroethylene degradation," *Appl. Catal., B*, vol. 94, pp. 211–218, 2010.

[164] S. B. Darling and F. You, "The case for organic photovoltaics," *RSC Advances*, vol. 3, p. 17633, 2013.

[165] M. A. Niedermeier, M. Rawolle, P. Lellig, V. Körstgens, E. M. Herzig, A. Buffet, S. V. Roth, J. S. Gutmann, T. Fröschl, N. Hüsing, and P. Müller-Buschbaum, "Low-temperature sol-gel synthesis of nanostructured polymer/titania hybrid films based on custom-made poly(3-Alkoxy thiophene)," *ChemPhysChem*, vol. 14, pp. 597–602, 2013.

[166] E. Senses and P. Akcora, "Mechanistic model for deformation of polymer nanocomposite melts under large amplitude shear," *J. Polym. Sci. B Polym. Phys.*, vol. 51, pp. 764–771, 2013.

[167] D. Tahk, H. H. Lee, and D.-Y. Khang, "Elastic moduli of organic electronic materials by the buckling method," *Macromolecules*, vol. 42, pp. 7079–7083, 2009.

[168] M. Iuga, G. Steinle-Neumann, and J. Meinhardt, "Ab-initio simulation of elastic constants for some ceramic materials," *EPJ B*, vol. 58, pp. 127–133, 2007.

[169] *[Online]. Available: http://www.azom.com/article.aspx?ArticleID=1179.*

[170] K. Miyake, N. Satomi, and S. Sasaki, "Elastic modulus of polystyrene film from near surface to bulk measured by nanoindentation using atomic force microscopy," *Appl. Phys. Lett.*, vol. 89, p. 031925, 2006.

[171] *"Elastic Properties and Young Modulus for some Materials". The Engineering ToolBox. Retrieved 2012-01-06.*

List of publications

Publications related to the dissertation

- W. Wang, S. Guo, E. M. Herzig, K. Sarkar, M. Schindler, D. Magerl, M. Philipp, J. Perlich, P. Müller-Buschbaum, "Investigation of morphological degradation of P3HT:PCBM bulk heterojunction films exposed to long-term host solvent vapor", *J. Mater. Chem. A*, vol. 4, pp. 3743–3753, 2016.
- W. Wang, M. A. Ruderer, E. Metwalli, S. Guo, E. M. Herzig, J. Perlich, P. Müller-Buschbaum, "Effect of methanol addition on resistivity and morphology of PEDOT:PSS layers on top of carbon nanotubes for use as flexible electrodes", *ACS Appl. Mater. Interfaces*, vol. 7, pp. 8789–8797, 2015.
- W. Wang, C. J. Schaffer, L. Song, V. Körstgens, S. Pröller, E. D. Indari, T. Wang, A. Abdelsamie, S. Bernstorff, P. Müller-Buschbaum, "In operando morphology investigation of inverted bulk heterojunction organic solar cells with GISAXS", *J. Mater. Chem. A*, vol. 3, pp. 8324–8331, 2015.
- W. Wang, S. Pröller, M. A. Niedermeier, V. Körstgens, M. Philipp, B. Su, D. Moseguí González, S. Yu, S. V. Roth, P. Müller-Buschbaum, "Development of the morphology during functional stack build-up of P3HT:PCBM bulk heterojunction solar cells with inverted geometry", *ACS Appl. Mater. Interfaces*, vol. 7, pp. 602–610, 2015.
- W. Wang, T. Widmann, L. Song, P. Zhang, S. K. Vayalil, S. V. Roth, N. Hüsing, P. Müller-Buschbaum, "A low temperature route toward flexible nanostructured P3HT/TiO_2 hybrid films", to be submitted, 2016.
- W. Wang, L. Song, D. Moseguí González, D. Magerl, M. Philipp, J.-F. Moulin, P. Müller-Buschbaum, "Influence of solvent additive on P3HT:PCBM films", to be submitted, 2016.

- L. Song, W. Wang, V. Körstgens, D. Moseguí González, Y. Yao, N. K. Minar, J. M. Feckl, K. Peters, T. Bein, D. Fattakhova-Rohlfing, G. Santoro, S. V. Roth, P. Müller-Buschbaum, "Spray deposition of titania films with incorporated crystalline nanoparticles for all-solid-state dye-sensitized solar cells using P3HT", *Adv. Funct. Mater.*, vol. 26, pp. 1498–1506, 2016.

Further publications

- L. Song, A. Abdelsamie, C. J. Schaffer, V. Körstgens, W. Wang, T. Wang, E. D. Indari, T. Fröschl, N. Hüsing, T. Haeberle, P. Lugli, S. Bernstorff, P. Müller-Buschbaum, "A low temperature route toward hierarchically structured titania films for thin hybrid solar cells", *Adv. Funct. Mater.*, DOI: 10.1002/adfm.201603867, 2016.
- M. Al-Hussein, E. M. Herzig, M. Schindler, F. Löhrer, C. M. Palumbiny, W. Wang, S. V. Roth, P. Müller-Buschbaum, "Comparative study of the nanomorphology of spray and spin coated PTB7 polymer:fullerene films", *Polym. Eng. Sci.*, vol. 56, pp. 889–894, 2016.
- S. Guo, B. Cao, W. Wang, J.-F. Moulin, P. Müller-Buschbaum, "Effect of alcohol treatment on the performance of PTB7:PC71BM bulk heterojunction solar cells", *ACS Appl. Mater. Interfaces*, vol. 7, pp. 4641–4649, 2015.
- M. Philipp, V. Körstgens, D. Magerl, C. Heller, Y. Yao, W. Wang, G. Santoro, S. V. Roth, P. Müller-Buschbaum, "Sorption of water and initial stages of swelling of thin PNIPAM films", *Langmuir*, vol. 31, pp. 9619–9627, 2015.
- V. Körstgens, S. Pröller, T. Buchmann, D. Moseguí González, L. Song, Y. Yao, W. Wang, J. Werhahn, G. Santoro, S. V. Roth, H. Iglev, R. Kienberger, P. Müller-Buschbaum, "Laser-ablated titania nanoparticles for aqueous processed hybrid solar cells", *Nanoscale*, vol. 7, pp. 2900–2904, 2015.
- S. Guo, C. Brandt, T. Andreev, E. Metwalli, W. Wang, J. Perlich, P. Müller-Buschbaum, "First step into space: performance, and morphological evolution of P3HT:PCBM bulk heterojunction solar cells under AM0 illumination", *ACS Appl. Mater. Interfaces*, vol. 6, pp. 17902–17910, 2014.
- K. Sarkar, M. Rawolle, M. A. Niedermeier, W. Wang, E. M. Herzig, V. Körstgens, A. Buffet, S. V. Roth, P. Müller-Buschbaum, "A quantitative approach to tune metal oxide network morphology based on grazing incidence small angle x-ray scattering investigations", *J. Appl. Cryst.*, vol. 47, pp. 76–83, 2014.

- K. Sarkar, M. Rawolle, E. M. Herzig, W. Wang, A. Buffet, S. V. Roth, P. Müller-Buschbaum, "Custom-made morphologies of ZnO nanostructured films templated by a P(S-b-EO) diblock copolymer via sol-gel technique", *ChemSusChem*, vol. 6, pp. 1414–1424, 2013.

Award

- TUM.ENERGY THIRD-GRADE PRESENTATION AWARD 2015, in recognition of the poster, "Evolution of the morphology during functional stacks build-up of P3HT:PCBM inverted solar cells", 5th Colloquium of the Munich School of Engineering, Garching (Germany), 09.07.2015.

Scientific reports

- W. Wang, C. J. Schaffer, L. Song, V. Körstgens, S. Pröller, E. D. Indari, T. Wang, A. Abdelsamie, S. Bernstorff, P. Müller-Buschbaum, "In operando morphology investigation of inverted P3HT:PCBM solar cells by GISAXS", *Lehrstuhl für Funktionelle Materialien, Annual Report*, 2015.
- W. Wang, S. Pröller, M. A. Niedermeier, V. Körstgens, M. Philipp, B. Su, D. Moseguí González, S. Yu, S. V. Roth, P. Müller-Buschbaum, "Morphology investigation during functional stack assembling of P3HT:PCBM inverted solar cells", *Lehrstuhl für Funktionelle Materialien, Annual Report*, 2014.
- W. Wang, S. Guo, J. Perlich, P. Müller-Buschbaum, "The influence of solvent atmosphere on bulk heterojunction solar cells", *Lehrstuhl für Funktionelle Materialien, Annual Report*, 2013.
- W. Wang, M. Philipp, D. Magerl, J.-F. Moulin, P. Müller-Buschbaum, "The influence of processing additives on themorphology of bulk heterojunction films", *Lehrstuhl für Funktionelle Materialien, Annual Report*, 2012.
- W. Wang, M. Philipp, D. Magerl, J.-F. Moulin, P. Müller-Buschbaum, "The influence of processing additives on the morphology of bulk heterojunction films", *FRM II Annual Report*, 2012.
- W. Wang, E. Metwalli, S. Guo, K. H. Scherer, M. A. Ruderer, E. M. Herzig, M. Al-Hussein, C. M. Palumbiny, V. Körstgens, J.C. Heller, Y. Yao, J. Perlich, S. V. Roth, P. Müller-Buschbaum, "Effect of Different Electrodes on PEDOT:PSS Layer", *HASYLAB Annual Report*, 2012.

- W. Wang, M. A. Ruderer, P. Müller-Buschbaum, "Modified surface of CNT electrodes for flexile all polymer solar cells", *Lehrstuhl für Funktionelle Materialien, Annual Report*, 2011.
- W. Wang, E. Metwalli, S. Guo, K. H. Scherer, M. A. Ruderer, J. Perlich, S. V. Roth, P. Müller-Buschbaum, "Modified surface of CNT electrodes for flexible all polymer solar cells", *HASYLAB Annual Report*, 2011.
- W. Wang, M. A. Ruderer, P. Müller-Buschbaum, "Exploring different substrates for functional photoactive thin polymer films", *Lehrstuhl für Funktionelle Materialien, Annual Report*, 2010.

Conference talks

- W. Wang, S. Guo, "Polymer based solar cells", *E13 Summer School*, Rudolfshütte, Uttendorf (Austria), June 2012.
- W. Wang, D. Moseguí González, "Polymer based solar cells", *E13 Summer School*, Bergheim, Obertauern (Austria), June 2014.

Conference poster presentations

- W. Wang, S. Pröller, V. Körstgens, M. Philipp, B. Su, S. Yu, S. V. Roth, P. Müller-Buschbaum, "Evolution of the morphology during functional stacks build-up of P3HT:PCBM inverted solar cells", *5th Colloquium of the Munich School of Engineering*, Garching (Germany), July 2015.
- W. Wang, S. Pröller, M. A. Niedermeier, V. Körstgens, M. Philipp, B. Su, S. Yu, S. V. Roth, P. Müller-Buschbaum, "Evolution of the Morphology during Functional Stacks Build-up of P3HT:PCBM Inverted Solar Cells", *DPG Frühjahrstagung*, Berlin (Germany), March 2015.
- W. Wang, M. Philipp, D. Magerl, J.-F. Moulin, P. Müller-Buschbaum, "The influence of processing additives on the morphology of P3HT:PCBM BHJ photoactive layer ", *MLZ User Meeting*, Ismaning (Germany), February 2015.
- W. Wang, S. Guo, K. Sarkar, M. Schindler, D. Magerl, M. Philipp, J. Perlich, P. Müller-Buschbaum, "The influence of solvent atmosphere on bulk heterojunction solar cells", *DPG Frühjahrstagung*, Dresden (Germany), April 2014.

- W. Wang, M. Philipp, D. Magerl, E. M. Herzig, J.-F. Moulin, P. Müller-Buschbaum, "The influence of processing additives on the morphology of bulk heterojunction films in organic photovoltaics", *Nanosystems for Solar Energy Conversion*, Munich (Germany), July 2013.
- W. Wang, M. Philipp, D. Magerl, E. M. Herzig, J.-F. Moulin, P. Müller-Buschbaum, "The influence of processing additives on the morphology of bulk heterojunction films in organic photovoltaics", *3rd Colloquium of the Munich School of Engineering*, Garching (Germany), July 2013.
- W. Wang, M. Philipp, D. Magerl, J.-F. Moulin, P. Müller-Buschbaum, "The influence of processing additives on the morphology of bulk heterojunction films", *6th FRM II Science Meeting*, Grainau (Germany), June 2013.
- W. Wang, M. Philipp, D. Magerl, J.-F. Moulin, P. Müller-Buschbaum, "The influence of processing additives on the morphology of bulk herterojunction films", *DPG Frühjahrstagung*, Regensburg (Germany), March 2013.
- W. Wang, M. A. Ruderer, P. Müller-Buschbaum, "Modified surface of CNT electrodes for flexible all polymer solar cells", *2nd Colloquium of the Munich School of Engineering*, Garching (Germany), June 2012.
- W. Wang, M. A. Ruderer, E. Metwalli, S. Guo, K. H. Scherer, S. V. Roth, J. Perlich, P. Müller-Buschbaum, "The morphology of flexible all polymer solar cells", *DPG Frühjahrstagung*, Berlin (Germany), March 2012.
- W. Wang, M. A. Ruderer, E. Metwalli, S. Guo, J. Perlich, S. V. Roth, P. Müller-Buschbaum, "Investigation of the morphology of photoactive polymer layers for flexible solar cells", *GISAXS 2011 Workshop*, Hamburg (Germany), October 2011.
- W. Wang, M. A. Ruderer, S. Guo, Q. Zhong, C. Birkenstock, P. Müller-Buschbaum, "Morphology of photoactive polymers on flexible substrates", *1st Colloquium of the Munich School of Engineering*, Garching (Germany), July 2011.
- W. Wang, M. A. Ruderer, S. Guo, E. Metwalli, K. H. Scherer, P. Müller-Buschbaum, "Morphology of bulk heterojunction systems for polymer-based photovoltaics", *5th FRM II Science Meeting*, Burg Rothenfels (Germany), June 2011.
- W. Wang, M. A. Ruderer, P. Müller-Buschbaum, "Effect of annealing processes on morphology of photoactive polymer layers for solar cell applications", *DPG Frühjahrstagung*, Dresden (Germany), March 2011.
- W. Wang, M. A. Ruderer, S. Guo, Q. Zhong, C. Birkenstock, P. Müller-Buschbaum, "Organic solar cells with carbon nanotube electrodes", *1st Tag der Physikerinnen*, Garching (Germany), February 2011.

Acknowledgments

I would like to thank Prof. Dr. Peter Müller-Buschbaum to give me the opportunity to work in the field of polymer-based photovoltaics. I appreciate all his advice and guidance throughout my whole Ph.D. period. His foresight, solid knowledge about science, and open mind help me complete my Ph.D. and continuously develop my interests in scientific research. Especially, I am grateful for his encouragement, patience, and trust in me, which strengthen my self-confidence and personality. I believe I will benefit from all these in my future life.

I am also thankful to the China Scholarship Council for offering me the scholarship, which supported me financially during my Ph.D. studies in Germany.

I would further like to thank Dr. Matthias A. Ruderer for his kind guidance at the beginning of my Ph.D. studies. He introduced me into the topic of organic photovoltaics, taught me the basics of sample preparation and instruments' operation, and helped me get integrated into the E13 community. He set me a great example of being a senior Ph.D. candidate.

Many thanks go to my master students Tobias Widmann and Edoardo Barabino for their excellent work. I wish both of them have a bright future ahead. Tobias's highly attentive and efficient work impressed me a lot. We both are quite content with the outcome of the project we worked together. Edoardo showed his serious attitude towards research. We had many thorough discussions, which stimulated us to think and gradually deepened our knowledge. Apart from this, his wonderful sense of humor led us a joyful time.

The successes of all beamtimes at large scale facilities in Hamburg, Garching, Trieste, and Bejing would not be achieved without the support from many experienced beamline scientists, technicians, and all the colleagues' participation and strong support. I appreciated the collaborations with everyone of them. Many thanks go to Dr. Jan Perlich, Dr. Gonzalo Santoro, Dr. Adeline Buffet, Dr. Shun Yu, Dr. Peng Zhang, Dr. Sarathlal Koyiloth Vayalil, and Dr. Stephan V. Roth from DESY, Dr. Jean-François Moulin and Dr. Martin Haese-Seiller from REFSANS, Dr. Sigrid Bernstorff from Elettra, Dr. Zhonghua Wu and Dr. Guang Mo from BSRF, Dr. Ezzeldin Metwalli Ali, Dr. Shuai Guo, Dr. Eva

M. Herzig, Dr. Monika Rawolle, Dr. Kuhu Sarkar, Dr. Volker Körstgens, Dr. Yuan Yao, Bo Su, Stephan Pröller, Dr. Claudia M. Palumbiny, Prof. Dr. Mahmoud Al-Hussein, Jan Christoph Heller, David Magerl, Dr. Markus Schindler, Johannes Schlipf, Edoardo Barabino, Lin Song, Christoph Schaffer, and Dr. Martine Philipp from our chair. In addition, I want to thank Prof. Dr. Alexander W. Holleitner and Peter Weiser from WSI for providing me the access to SEM, as well Dr. Oliver Schneider and Dr. Sladjana Martens from ECRG for the support of QCM measurements.

Furthermore, I would like to thank the whole workshop team, especially to Raffael Jahrstorfer and Reinhold Funer for their help to construct the measure box of EQE and the bending-test setup.

I am sincerely grateful to Lin Song, Franziska Löhrer, Dr. Volker Körstgens, Nitin Saxena, Johannes Schlipf, Dr. Konstantinos Raftopoulos, Nuri Hohn, Daniel Moseguí González, Stephan Pröller, Lorenz Bießmann, Dr. Ezzeldin Metwalli Ali, and Dr. Martine Philipp for proofreading my thesis. All your corrections significantly improved my thesis.

I also want to thank the former and present colleagues from our chair, who have built a very friendly and joyful atmosphere: Prof. Dr. Christine M. Papadakis, Dr. Anatoly Berezkin, Dr. Konstantinos Raftopoulos, Dr. Margarita Dyakonova, Xiaohan Zhang, Bart-Jan Niebuur, Natalya Vishnevetskaya, Michael Bahr, Erik Braden, Dr. Shuai Guo, Dr. Sebastian Jaksch, Christian Jendrzejewski, Dr. Konstantinos Kyriakos, Anna Magerl, David Magerl, Dr. Robert Meier, Dr. Martin Niedermeier, Dr. Martine Phillipp, Sofia Ramirez Bernini, Dr. Monika Rawolle, Dr. Qi Zhong, Dr. Matthias Ruderer, Dr. Kuhu Sarkar, Dr. Markus Schindler, Gregory Tainter, Dr. Jianqi Zhang, Dr. Claudia M. Palumbiny, Dr. Alexander Diethert, Wei Liu, Minglong He, Dr. Yuan Yao, Bo Su, Tobias Widmann, Edoardo Barabino, Felipe Martinez, Rosa Maria Torrademé, Lorenz Bießmann, Nuri Hohn, Dr. Volker Körstgens, Franziska Löhrer, Dr. Ezzeldin Metwalli Ali, Daniel Moseguí González, Lukas Oesinghaus, Lin Song, Nitin Saxena, Christoph Schaffer, Simon J. Scharper, Johannes Schlipf, Richard Stockhausen, Senlin Xia, Dan Yang, Hong Xu, and Kun Wang. I also want to thank the Herzig group for working and partying together: Dr. Eva M. Herzig, Stephan Pröller, Mihael Čorić, and Jenny Lebert. I greatly appreciate the wedding gift from E13 for Lin and me.

I am also grateful to our secretaries Petra Douglas, Susanna Fink, and Marion Waletzki to help me a lot with administration and Visa extension. In addition, many thanks go to Dr. Martin Niedermeier who helped me several times for measuring my samples till late evening and taught me to ski. I want to thank my officemate Dr. Volker Körstgens who was always willing to help me in short notice and give his comprehensive suggestions for all aspects. Specially, I would like to thank Dr. Qi Zhong, Wei Liu, and Senlin Xia for their excellent dishes they cooked for me. I do enjoy them a lot. I also want to thank Dr.

Shuai Guo. I could not imagine my Ph.D. studies without your encouragement, advice, and kind help.

I am very grateful to my close friends Dr. Chen Liu and Dr. Ming Jin in Munich. They were always the first ones whom I would like to share my joy and success. They were also always there to comfort me in times of sorrow. One of the most pleasant things in Munich is to spend all my birthdays with your accompany. Great thanks to Chen for her amazing photography, which helped me remember all delightful and memorable moments. I also want to thank all my good friends in China: Yanpei Wu, Lin Tang, and Xin Duan. Despite long distances between their cities and mine, they visited me every year during my vocations in China. I enjoyed my time so much with them all. I wish a happy and successful life for them all.

I owe tons of gratitude to my parents, grandparents, and parents-in-law for their great supports. I could not come this far without their care and help. There would be no place in the world that is as reliable as home. I love my family so much. I wish all of them a healthy, happy, and long life.

Finally, I would like to thank my beloved husband Lin Song. He left his job in Beijing and came to Munich for me without a doubt. I was grateful for his support at my work and decisions. He understood me so well that he was able to help me get aware of where I was standing and where to go for future. I really appreciate his sense of humor which made our lives very pleasant.